THE UNIVERSITY OF HULL

COMPUTER MODELLING OF THE DEVELOPMENT OF THE TRABECULAR ARCHITECTURE IN THE HUMAN PELVIS

being a Thesis submitted for the Degree of

in the University of Hull

by

Peter James Watson, MEng (Hons)

October 2011

ABSTRACT

The influence of mechanical loading upon bone growth and remodelling has been widely studied. It has been suggested that functional bone growth is evident within the human adult pelvis, where the internal trabecular structure is purported to align to the principal strain trajectories induced during bipedal locomotion. Ontogenetic studies of the juvenile pelvis have observed that trabecular bone growth becomes progressively ordered from an initial randomised patterning. This has lead to theories linking the gradual structural optimisation of trabecular bone to the mechanical forces associated with the development of juvenile locomotion. However, recent studies have observed partially optimised trabecular structures within the human fetal and neonatal pelvis, in contrast to previous observations. The possible genetic and mechanical factors which cause the *in utero* formation of these trabecular structures, which are usually associated with a weight bearing function, remains unknown. Therefore, this thesis aimed to investigate the influence of the mechanical strains associated with juvenile movements, upon the growth of pelvic trabecular bone.

Biomechanical analyses were performed on digitised models of juvenile pelvic specimens belonging to the Scheuer collection. Digitised models of a prenatal, 1 year, 8 year and 19 year old pelvis were constructed through processing mirco-computed tomography scan data. A geometric morphometric reconstruction technique was devised which enabled the creation of hemi-pelvic models from originally disarticulated bone specimens. This reconstruction technique was validated through a close morphological comparison between a reconstructed hemi-pelvis, and its originally articulated CT data. The muscular and joint forces associated with *in utero* movements and bipedal locomotion, were computed through musculoskeletal simulations. A prenatal musculoskeletal model was constructed to replicate the *in*

utero mechanical environment, and simulated interactions between the fetal leg and the womb wall. The forces associated with bipedal locomotion were evaluated through analysis of a pre-defined subject-specific musculoskeletal model. An attempt was made to validate the modelling technique of altering generic musculoskeletal models to create subject-specific representations. However, comparisons between computed and experimentally recorded muscle activities proved inclusive, although this was attributed to uncertainties in the accuracy of the experimental data. A series of finite element analyses computed the strain distributions associated with the predicted musculoskeletal loading. A range of load regimes were applied to each juvenile pelves, and were based upon the computed musculoskeletal forces and the maximum isometric force capabilities of the pelvic muscles. However, despite the differences between the applied load regimes, the predicted von Mises and compressive strain distributions displayed similarities for all the ages analysed. All the predicted distributions were characterised by high strains within the inferior ilium, which correlated to a region of high trabecular organisation. The high strain magnitudes then travelled superiorly in either a gradual or rapid dissipation, both of which did not produce a distribution which correlated to the pelvic trabecular histomorphometry. Therefore, no strain distribution was predicted with divergence of the inferior strains to the anterior and posterior regions of the ilium, as observed with the trabecular trajectories within the pelvis.

As the predicted von Mises and compressive strain distributions failed to match the complete iliac trabecular histomorphometry, it was suggested that the *in utero* formation of partially optimised trabecular growth is possibly due to generic factors. This thesis provided initial investigations into the musculoskeletal and mechanical loading of the juvenile pelvis, although future work is required to develop the applied modelling techniques to fully determine the influence of the mechanical strains.

ACKNOWLEDGEMENTS

I would like to express my gratitude Catherine Dobson and Michael Fagan for their continuous advice and support throughout this study. I would also like to thank all those who I have worked with in the Medial and Biological Engineering Research Group, University of Hull, for their help and support. I also like to thank Paul O'Higgins for his help and knowledge regarding geometric morphometrics. Additional acknowledgements are made to Sue Black and Craig Cunningham, whose initial work laid the foundations for this study and for providing access to the Scheuer collection. I would also like to thank the University of Hull for funding my attendance at two conferences.

Finally, I would like to thank for my family for their continuous support and encouragement throughout everything I have done.

TABLE OF CONTENTS

LIST OF FIGURES

LIST OF TABLES

GLOSSARY

AIIS	Anterior inferior iliac spine
AMMRV1.2	AnyBody Managed Model Repository Version 1.2
ar	Acetabular roof
at	Anterior trajectory
ASIS	Anterior superior iliac spine
BW	Body weight
CDC	Centres for Disease Control and Prevention
CT	Computed tomography
Cortex	The outermost or superficial layer
D	Density
DOF	Degrees of freedom
E	Young's modulus
EMG	Electromyography
FE	Finite element
GMM	Geometeric morphometric methods
HJC	Hip joint centre
iMVC	Isometric maximal voluntary contration
Kilograms	Kg
L	Length
M	Mass
MIF	Maximum isometric force
ML	Muscular and ligamentous
mm	Millimeter
MRI	Magnetic resonance imaging
MS	Musculoskeletal

N	Newton
NPA	Averaged patient data
PC1	First principal component
PC2	Second principal component
PC3	Thrid principal component
PCA	Principal component analysis
PCSA	Physiological cross-sectional area
PD	Pelvic depth
PH	Pelvic height
PIIS	Posterior inferior iliac spine
PSIS	Posterior superior iliac spine
pt	Posterior trajectory
PW	Pelvic width
tc	Trabecular chiasma
TFL	Tensor fascia latae
THR	Total hip replacement
R	Radius
SIJ	Sacro-iliac joint
SD	Standard deviation
sn	Sciatic notch
sm	Superior medial
UX	Displacement in the x-axis
UY	Displacement in the y-axis
UZ	Displacement in the z-axis
yr/s	year/s
°	Degree

με	Micro-strain
μCT	Micro-computed tomography
υ	Poissons ratio
2D	Two-dimensional
3D	Three-dimensional

1. INTRODUCTION

Bones are constructed through the integration of cortical and trabecular bone, and are structurally optimised to fulfil their functional requirements. The growth and remodelling of trabecular bone has been widely studied, developing the understanding of Wolff's Law. This proposes that the structure of trabecular bone matches the principal stress distributions associated with common load regimes (Wolff, 1892). This observation has lead to the identification of functionally adapted bone growth within the human femur (Ryan and Krovitz, 2006) and hominid pelvis (Macchiarelli et al., 1999; Rook et al., 1999), where the trajectories of trabecular growth align to the mechanical strains induced during bipedal locomotion. Macchiarelli et al. (1999) reported that the pelvis displays distinct evidence of trabecular optimisation due to the large forces experienced throughout the structure, which can exceed 3 times body weight (BW) during walking (Bergmann et al., 2001). Functional adaptation has also been reported throughout ontogeny within the bones of the lower extremity (Ryan and Krovitz, 2006; Volpato, 2008; Gosman and Ketchman, 2009). Such studies have identified randomised trabecular patterning until the development of bipedal locomotion, after which structural optimisation occurred. Trabecular bone was observed to continue remodelling after the onset of initial juvenile bipedalism, producing growth into identifiable trajectories by around 8 years of age, which coincides with the development of mature bipedal gait (Sutherland, 1997). However, Cunningham and Black (2009b) identified trabecular trajectories within the human fetal pelvis which are comparable to those observed within an adult. Fetal specimens at an estimated 18-22 weeks gestation displayed trabecular organisation into identifiable trajectories, which became progressively defined with gestational age. Therefore, it was suggested that these trajectories form a genetic blue

print from which further remodelling is based (Cunningham and Black, 2009a). However, the factors which instigate the formation of these trabecular trajectories are unclear, as this type of bone growth is usually associated with a weight bearing function. Consideration must be given to the possibility that a genetic blueprint is pre-determined within the bone cells, thus causing the initial trabecular formation (Cunningham and Black, 2009a). Although, the influence of the *in utero* mechanical environment has been observed to influence bone growth (Miller, 2005), and therefore should also be considered a factor.

The understanding of the relationship between bone growth and mechanical loading has been aided by developments in the methods of evaluating the forces throughout the musculoskeletal (MS) system during movement. Commercial software packages have the capabilities to generate subject-specific MS models using motion capture and ground reaction force data, and predict muscular and joint forces (Damsgaard et al., 2006; Delp et al., 2007). Computerised models have been developed which have analysed the MS system of both healthy (Pedersen et al., 1997; Heller et al., 2001, 2005) and pathological subjects (Arnold et al., 2005). Although these techniques are predominately applied to model the adult MS system, they provide a means of analysing the juvenile during the development of bipedal locomotion, and even *in utero* environments. Advances within finite element (FE) methods have enabled the computation of the mechanical stresses/strains of skeletal bones induced by MS loading. In relation to the human pelvis, a large amount of research has been conducted within the medical industry to design and test components of hip prostheses (Korhonen et al., 2005; Cilingir et al., 2007; Coultrup et al., 2010). Consequently, literature reporting the mechanical response of the pelvis in relation to normal physiological loading is not extensive. These limited studies have analysed

the pelvis under the MS loading associated with bipedal locomotion and during standing (Dalstra and Huiskes, 1995; Majumder et al., 2005; Phillips et al., 2007). However, they did not relate their findings to the theories of bone remodelling, and only analysed the stress distribution throughout the pelvis. Therefore, although pelvic strain distributions for normal physiological conditions have not been previously reported, they can be computed through FE methods and compared to the known trabecular trajectories (Macchiarelli et al., 1999; Rook et al., 1999).

This study aimed to analyse the influence of mechanical loading associated with juvenile locomotion, upon the trabecular growth and remodelling within the human pelvis. The study was based on computational modelling of pelvic specimens belonging to the Scheuer collection (Cunningham and Black, 2009b), which is a unique repository of skeletal remains. Four specimens were selected whose ages each marked a significant stage in the development of juvenile locomotion, or growth of the pelvis, namely; prenatal (*in utero* movements); 1 year (yr) (development of initial bipedalism; 8 years (development of a mature gait); 19 years (fusion of the pelvic bones). Analysis of the juvenile pelvis was categorised into three sections, initiated by the digitisation of the specimens from computed tomography (CT) and micro-computed tomography (μCT) data (Chapter 3). Unfortunately, the majority of the specimens within the Scheuer collection are dry bones, resulting in the pelvic specimens to be presented as disarticulated structures. This is due to the growth of the juvenile pelvis as separate bones articulating around a cartilaginous acetabulum, until fusion during late adolescence. Therefore, a reconstruction technique was created which utilised geometric morphometric methods (GMM), to facilitate the re-articulation of the pelvic bones and reconstruct the omitted cartilaginous features (Chapter 4). The muscular and joint forces associated with *in utero* and bipedal

movements were computed within MS simulation software (Chapter 5). The mechanical response of the juvenile pelves to the predicted MS loading was subsequently calculated through a series of FE analyses (Chapter 6). The predicted stress and strain distributions for each pelvis were compared to the trabecular trajectories observed through histomorphometric analyses (Macchiarelli et al., 1999; Rook et al., 1999; Cunningham and Black, 2009b). Comparisons between the positioning of the computed strains and the known trabecular trajectories, were used as a measure to evaluate the influence of the mechanical loading on the growth of the juvenile pelvis.

2. LITERATURE REVIEW

Medical engineering uses the theories of various scientific fields to increase the understanding of medical and biological problems. In studying juvenile bone growth in relation to the age related MS loading, knowledge from biological and mechanical engineering disciplines were integrated. Therefore, this literature review is categorised into the areas of anatomy, MS modelling and FE modelling. A review of the knowledge and research performed within each subject area is provided, and presents information considered relevant to this study.

2.1. SKELETAL ANATOMY

The human skeleton is a composition of numerous individual bones which interact through a series of articulations, creating rigid and robust structures for internal organ protection, providing a reservoir for biological interactions and enabling locomotive movement (Skerry, 2000). This structural stability is supplemented by an extensive network of ligaments, tendons and muscles which span between independent bones to form the MS system.

The skeletal structure is categorised into axial and appendicular sections, which are based on geometric bone features and functions (Moore and Agur, 2002). The appendicular skeleton comprises of *"long"* bones which are weight bearing structures providing the necessary stability for locomotion (Gray, 1987), such as the femur and tibia. The axial skeleton consists of *"flat"* bones which either provide broad attachment sites for muscles and ligaments, or protect internal organs such as the cranium and ribs. Bones which cannot be classified into the above are referred to as *"irregular"* (or *mixed*), and are structurally optimised for their specific function, such as the pelvis (Gunn, 1984).

Both axial and appendicular bones are composed through the integration of two types of bone structure; cortical (or compact) and trabecular (or cancellous) bone. Bone morphology varies throughout the skeletal system as structural composition is based upon functional requirements. The weight bearing function of *"long"* bones often causes the formation of hollow cylindrical cortical structures, such as the intramedullary canal within the femur (see Figure 2.1).

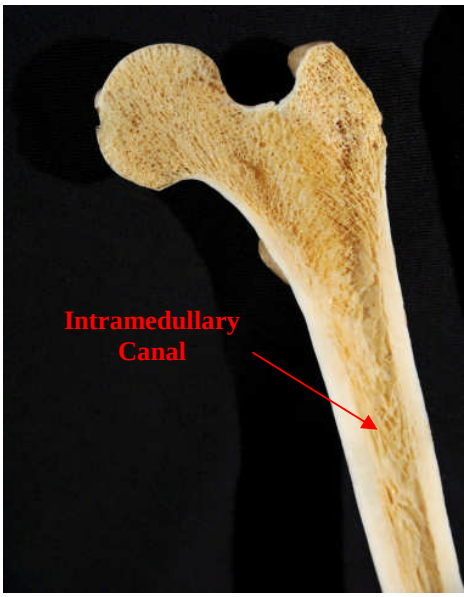

Figure 2.1. Cross section of the proximal femur showing the hollow intramedullary canal and the dense trabecular network within the femoral head.

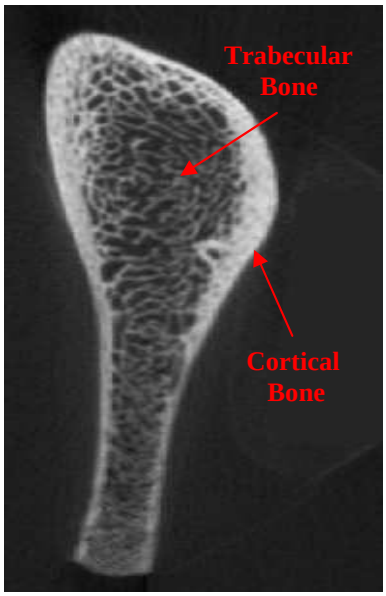

Figure 2.2. Cross section of the pelvic bone showing the two blades of cortical bone separated by an internal trabecular network.

In contrast, *"flat"* bones consist of two closely spaced cortical layers which are separated by a network of connecting trabecular rods and plates, as illustrated in Figure 2.2. A significant proportion of the muscular loading experienced by *"flat"* bones is transmitted through the stronger cortical bone, while the internal trabecular network serves to ensure structural integrity and provide additional mechanical support. Trabecular bone is also evident within the greater trochanter and the head of the femur (as shown in Figure 2.1), providing additional support to the mechanical loads experienced through the hip joint. Therefore, *"flat"* bones are optimised with

additional trabeculae to counteract compressive loading, while the hollow shaft of "*long*" bones resists bending and shear stresses (Einhorn, 1996). The total mass of the skeletal system is typically comprised of approximately 80% cortical and 20% trabecular bone (Hadjidakis and Androulakis, 2006).

2.1.1. Bone growth

The biological and mechanical factors which instigate and regulate bone growth have been widely studied. Trabecular bone has received significant attention based upon the theory of Wolff's Law, which proposes that trabecular structures align to the principal stress trajectories induced by mechanical loading (Wolff, 1892). The mechanical loading experienced within the skeleton is predominately generated through the functioning of the MS system and impact loading (Miller, 2005). The combined loading produced by BW and muscular contractions, continually loads the skeletal system, even when muscle state is passive (Rauch and Schoenau, 2001; Miller, 2005). Therefore, as muscles are considered to be the main contributors to the peak forces exerted on bone (Schoenau, 2006), the loading environment produced by normal activity is suggested to be the stimulus for bone growth (Ehrlich and Lanyon, 2002). However, Wolff's Law was based on observation and did not suggest the mechanism by which mechanical strain instigates bone remodelling.

Frost (1987) developed a link between bone growth/remodelling and mechanical loading via a regulatory feedback loop termed the "*mechanostat*", which monitors structural deformation in terms of mechanical strain. When strains fall outside a genetically determined threshold range, the loading is transmitted into biological signalling to activate either bone growth or resorption (see Figure 2.3). Therefore, bone mass and architecture are continually adapted when bone stability is

challenged, in order to maintain accepted strains (Rauch and Schoenau, 2001). The thresholding range is suggested to be subsequently regulated by the endocrine environment, which adjusts the accepted strain limits (Schoenau, 2006). Consequently, strain values of the thresholding range can vary in relation to anatomical location, although Martin (2000) reported the mechanostat range was between 50-1500 micro-strain (με). Ward et al. (2006) reported comparative values and stated that bone remodelling occurred when loading exceed 1500-2000με.

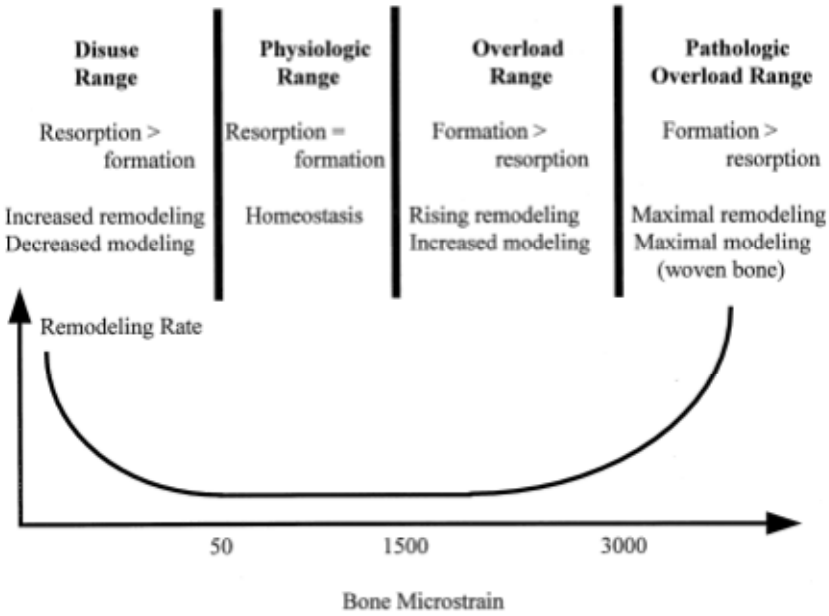

Figure 2.3. Bone remodelling in response to mechanical loading, showing an increase in remodelling when experiencing strains beyond the threshold range of 50-1500με (reproduced from Martin, 2000).

A genetic blueprint contained within bone cells is proposed to initiate *in utero* skeletal growth, producing initial bone morphologies with generalised internal structures (Turner, 1998). The mechanostat then forms a secondary system to optimise the internal structure (Rauch and Schoenau, 2001) in response to the mechanical loading experienced. This adaptive remodelling of trabecular bone has been observed in load bearing lower limbs throughout ontogeny (Ryan and Krovitz, 2006; Valpato, 2008; Gosman and Ketcham, 2009). Trabecular organisation during

fetal and neonatal growth has been reported to display fairly randomised structures, which become progressively ordered within early juvenile development. Evidence of trabecular remodelling has been reported to coincide with the onset of juvenile motion, leading to theories linking structural optimisation to the mechanical loading induced by the development of bipedal locomotion. Cunningham and Black (2009b) have reported contradictory findings within the pelvis, although this is discussed in more detail within Section 2.1.5.

The theory of the *"mechanostat"* illustrated in Figure 2.3 has been criticised as an over simplification of the actual process (Ehrlich and Lanyon (2002)). For example, dynamic loading has been observed to be associated with a greater level of bone growth in comparison to static loading (Turner, 1998). Consequently, the remodelling response has been suggested to be governed by strain-rates rather than singular strain values (Lanyon and Rubin, 1984). Turner (1998) stated that bone adaptation is driven by abnormal dynamic loading over small durations, while customary loading regimes evoke less response, and prolonged time frames have a diminishing effect. This challenges the theory relating trabecular organisation to strains resulting from normal activities, although these rules were based on mathematical equations and not histomorphometric observations.

The influence of mechanical forces upon bone growth and remodelling is demonstrated in instances of abnormal or absent loading. In cases of cerebral palsy, the undeveloped MS system is thought to attribute to the growth of thin cortical shells and generalised trabecular networks, which are often too weak to withstand daily or reasonable impact loading (Ward et al., 2006). Similarly, bone strength reduction within neonates has also been attributed to the *in utero* mechanical environment (Miller, 2005). The hypothesis that fetal bone development is driven by

mechanical forces is not extensively documented (Rauch and Schoenau, 2001; Nowlan et al., 2007). However, the action of the fetus kicking against the wall of the womb will exert mechanical forces upon the developing bone, although the magnitudes of these forces are unknown. As the fetus floats within amniotic fluid in the womb, it is unclear if these forces are sufficient to activate remodelling, although they have been reported to result in the fracture of diseased bones, as observed in osteogenesis imperfecta (Rauch and Schoenau, 2001). Consequently, cases of decreased fetal bone strength have been attributed to limited *in utero* movement (Miller, 2005).

Preterm births are often characterised by lower bone strength in comparison to full-term infants, which is accredited to the reduced duration of the higher *in utero* mechanical loading (Land and Schoenau, 2008). Moyer-Mileur et al. (2000) reported that passive range of motion exercises aids in the increase of bone mineral mass in preterm infants. Congenital neuromuscular diseases have been associated with the impairment of fetal movement and muscle strength, and the subsequent formation of diminished bone structures (Rodriguez et al., 1988a, 1988b). Such findings have been experimentally tested through purposely disrupting the MS system via chemical intervention within animal fetuses (Rodriguez et al.,1992; Nowlan et al., 2010). Fetal growth with abnormal muscle function was observed to produce weaker bone structures in comparison to control groups.

The theory of bone adaption has enabled the evaluation of a bone's mechanical function based upon its structure. In relation to the lower extremities, the trabecular architecture of the pelvis and femur has been used to determine the directionality of the experienced loading. For example, analysis of the trabecular structure within the primate femoral head has identified species capable of performing leaping motions

(Ryan and Ketcham, 2002a, 2002b, 2005). Functional bone growth was also observed by Volpato et al. (2008) when comparing pelvic and femoral trabecular growth between bipedally trained and wild macaques. Early homimins have also been documented to display pelvic trabecular structures which are related to load transfers during bipdal locomotion (Macchiarelli et al., 1999; Rook et al., 1999). Macchiarelli et al. (1999) stated that due to the uniqueness of mechanical loading induced during bipedal locomotion, strain related trabecular growth is evident within the pelvis. Therefore, the histomorphometric analyses of the modern human adult (Martinon-Torres, 2003) and the prenatal and neonatal (Cunningham and Black, 2009a, 2009b) pelvis have identified comparative trabecular organisation. The cortical shell of the pelvis has also received attention, again linking morphology with structural optimisation in response to locomotive mechanical loading (Cunningham and Black, 2009c).

2.1.2. The pelvic anatomy

The pelvic girdle is formed through a composition of individual bones, and provides a connection between the vertebral column and the lower extremities. As illustrated in Figure 2.4, the girdle is formed through the integration of the two hip (innominate) bones, sacrum and coccyx via the articulations at the sacro-iliac joint (SIJ) and pubic symphysis (Moore and Agur, 2002). The sacrum is located at the base of the spine, and is formed through the fusion of five sacral vertebrae to create a large triangular shaped structure. The assembly enables the sacrum to interlock between the two innominate bones and transfer axial forces to the lower limbs (Bogduk, 1997).

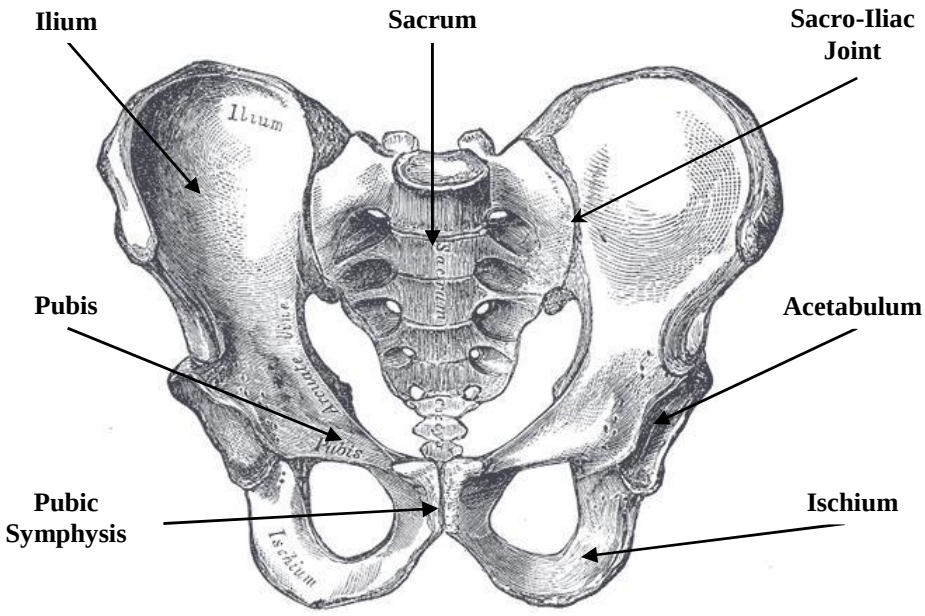

Figure 2.4. The pelvic girdle formed through the articulation of the two hip (innominate bones) and the sacrum at the SIJ and pubic symphysis (adapted from Gray, 1987).

The innominate bone (or hemi-pelvis) is further classified into the three separate components of the ilium, ischium and pubis (as illustrated in Figure 2.5). The ilium is the largest pelvic bone, joining the ischium and pubis inferiorly to form the acetabulum (for definitions of anatomical terminology see Appendix I). A rough articular surface within the posterior ilium marks the location of the SIJ. The ischium is located within the posterio-inferior region of the innominate, and fuses with the ilium and pubis to form the posterio-inferior quadrant of the acetabulum (see Figure 2.6). The pubis arises from the anterio-medial region of the innominate, fusing superiorly to form the anterio-inferior acetabular quadrant. Medially, the pubic symphysis forms an articulation with the contralateral pubis.

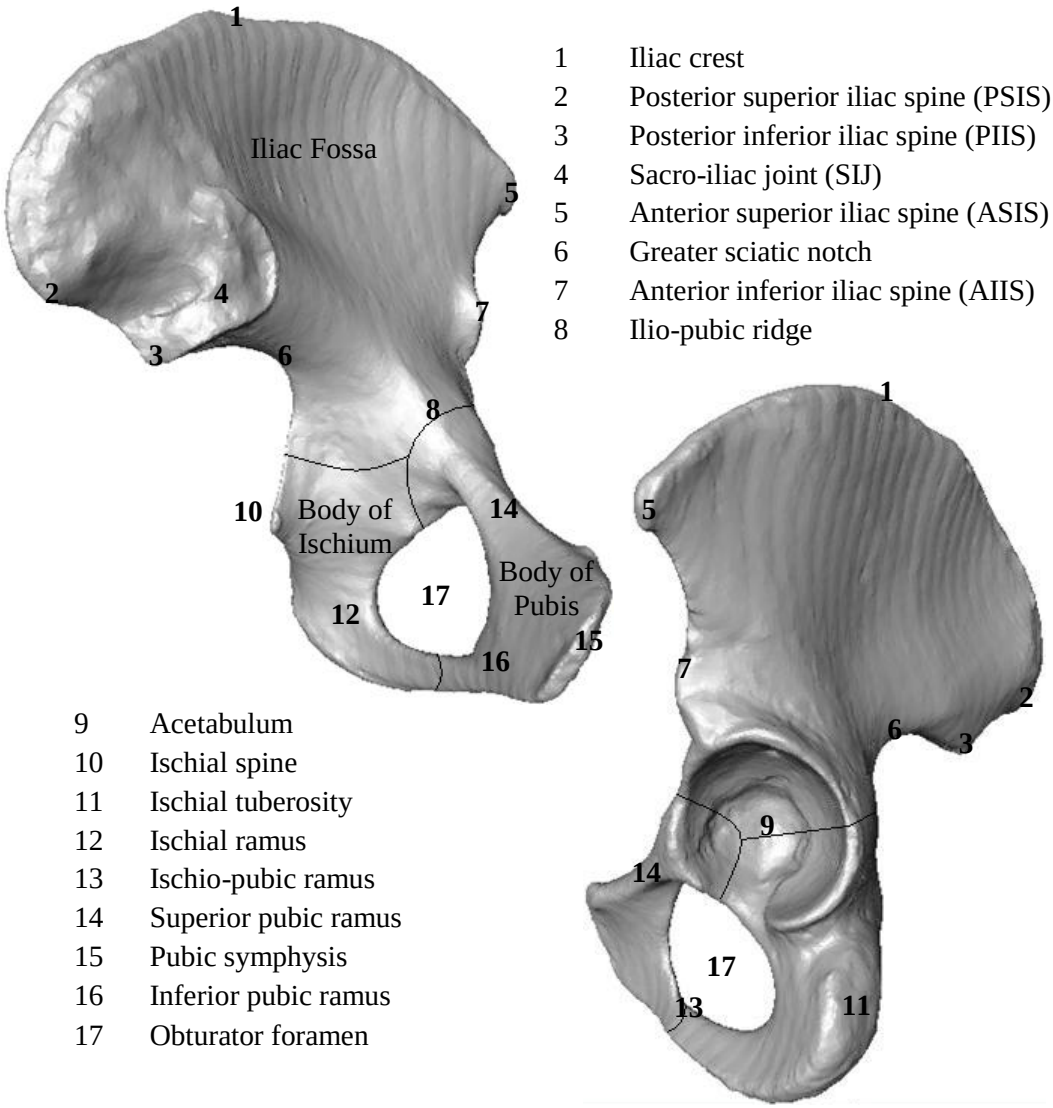

Figure 2.5. Bony landmark features of the adult innominate.

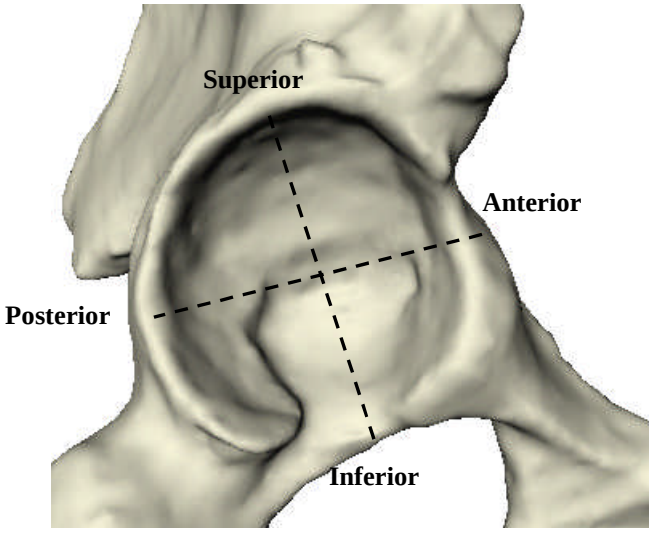

Figure 2.6. Fusion of the individual innominate bones to form the acetabulum and the structural division into quadrants.

The pelvic girdle is connected to the upper body through the SIJ, which is a synovial joint comprising of articulating fibro and hyaline cartilage, attached respectively to the ilium and sacrum (Gunn, 1984). The thickness of the cartilage varies between individuals, although the sacral cartilage is generally thicker than that of the iliac (Walker, 1992; Kampen and Tillmann, 1998; McLauchlan and Gardner, 2002). The articulation sites on the ilium and sacrum are characterised by rough and irregular bony surfaces, which display an increasing degree of irregularity with age (Walker, 1992). The resulting terrain of ridges and depressions cause the joint to partially inter-lock into position, which with the addition of interosseous and sacro-iliac ligaments, primarily limit SIJ movement to rotation in the median plane (Gunn, 1984). Excessive joint movements are prohibited to prevent the sacrum from dislocating inferiorly under the load of the upper body. However, joint movements have been measured to range between 0.5-8 degrees (°) in rotation and -0.3-8 millimetres (mm) in translation within a single plane (Goode et al., 2008). Fusion of the joint reduces the range of motion, although it increases the rigidity and likelihood of fracture (Bogduk, 1997).

The pubic symphysis forms an articulation between the two innominates, through a fibro-cartilaginous inter-pubic disc. The disc attaches to the medial surface of the pubis via a lining of hyaline cartilage (Becker et al., 2010). The fibro-cartilaginous composition of the symphysis aids its ability to withstand shear and tensile forces (Gamble et al., 1986), while four pubic ligaments provide additional joint stability. Therefore, movements are resisted to maintain the structural integrity of the pelvic girdle, although inferio-superior shear and anterio-posterior rotation has been reported (Walheim and Selvik, 1984). However, despite the mechanical strength of the inter-pubic disc, it is still able to widen during pregnancy to increase the volume within the pelvic girdle. Consequently, anatomical differences of the pubic

symphysis are present between sexes, with the female symphysis being shorter and broader (Li et al., 2006).

The hip joint facilitates interaction between the pelvis and the lower extremities, through articulation of the femoral head within the acetabulum. The cup shaped depression of the acetabulum and spherical head of the femur form to create a conventional ball and socket joint, permitting three dimensional (3D) movement in flexion/extension, adduction/abduction and medial/lateral rotation (Gunn, 1984). The acetabulum is deepened by a fibrocartilaginous rim (acetabular labrum) which encompasses the lateral circumference (Portinaro et al., 2001), increasing coverage of the femoral head (Ferguson et al., 2000). Through ensuring a secure fit of the femoral head, the labrum is considered to enhance the joint stability and assist in the even distribution of applied forces over the cartilaginous surface (Ferguson et al., 2000; Tan et al., 2001). Deformity of the acetabular depth often leads to hip dysplasia, where insufficient coverage of the femoral head results in discomfort caused by excessive wear and dislocation (Klaue et al., 1991).

The articulating surfaces are covered with a layer of hyaline cartilage and encompassed by a fibrous capsule, which attaches between the medial edge of the acetabulum and the femoral neck (Gunn, 1984). Articular cartilage thickness varies throughout the acetabulum (Wyler et al., 2007), producing a structure suggested to be optimised for hip contact stress distribution (Daniel et al., 2005). The fibrous capsule is subsequently surrounded by supporting ligaments which aids stability of the hip under loading.

2.1.3. Mechanical function of the pelvis

The pelvis is considered to be one of the most important structures within the MS system (Majumder et al., 2005), due to its role in protecting vital internal organs and facilitating locomotion. Therefore, one of the main functions of the pelvis is to transfer the weight of the connecting upper body through the lower extremities, for effective force dissipation during locomotion. Consequently, the pelvis is one of the largest weight bearing structures in the MS system, withstanding forces of up to three times BW during bipedal locomotion (Bergmann et al., 2001). Forces increase further during running and jogging and have been recorded to exceed seven times BW during stumbling (Bergmann et al., 2004).

Bipedal locomotion is characterised by a gait cycle, which is defined by consecutive heel strikes of the same leg. Figure 2.7 illustrates a gait cycle of the right leg, which initially undergoes a stance phase, while the opposite leg performs an unloaded swing phase. During the second half of the gait cycle these roles are switched, producing pelvic loading which is transversely alternated to produce one highly stressed hemi-pelvis, while the contralateral side is predominately passive.

Spinal loading is transferred from the sacrum to the pelvis through the SIJ, where it passes onto the posterio-superior ilium and then inferiorly towards the acetabulum (Dalstra and Huiskes, 1995; Majumder et al., 2005; Philips et al., 2007). During gait large stresses concentrate around the acetabulum as the loading converges towards the anterio-superior acetabular quadrant (Dalstra and Huiskes, 1995), and they then transfer through the hip joint and onto the femoral head. In instances of high mechanical loading, excessive stress magnitudes are dissipated along the superior pubic ramus, and the through the pubic symphysis into the contralateral hemi-pelvis.

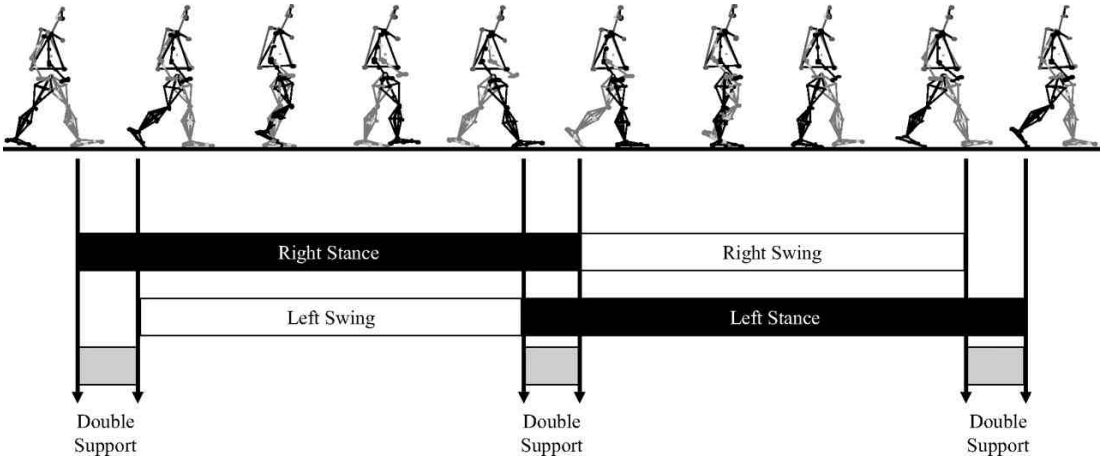

Figure 2.7.The standardised gait cycle defined between two consecutive heel strikes, and consisting of single leg and double support phases (left leg is illustrated in black, right leg is illustrated in grey) (reproduced from Wood et al. (2009)).

In addition to the cyclic torsional forces induced by the gait cycle, the pelvis also experiences axial and lateral forces caused by impact with the ground. Therefore, the pelvis is optimally designed to resist and oppose varied stress states, and ensure safe and efficient transfer of experienced loading. Load transfer is also aided by the MS system which assists in maintaining balance about a single hip joint during the single leg support phase of the gait cycle (Phillips et al., 2007). The large surface area of the ilium provides ideal attachment sites for powerful muscles such as the glutei, contributing to a complicated muscular complex. In total 22 muscles and 6 ligaments originate from each innominate, ensuring structural integrity of the pelvic girdle and reducing the risk of separation at the pubic symphysis and SIJ (Philips et al., 2007).

2.1.4. Pelvic bone structure

The ability of the pelvis to withstand mechanical loading is also enhanced by its structural composition, which is characterised by a thin cortical shell structure separated by trabecular bone. This is illustrated in the iliac blade displayed in Figure 2.2, resulting in the structure which has been likened to a “sandwich” construction,

which combines high strength with low weight (Dalstra et al., 1993). The pelvic trabeculae are predominately orientated perpendicular to the cortical shell to provide strong resistance against shear stresses (Dalstra et al., 1993). As trabecular histomorphometry is strongly correlated to experienced biomechanical strains (Turner et al., 1990), highly dense closed cell plate-like trabecular structures are found within regions that resist high loading. Conversely, regions under a lower loading contain low density open cell rod-like trabeculae (Gibson, 1985). The resulting trabecular structure is therefore highly anisotropic, although this is considered to reflect the anisotropy of daily loading (Turner, 1992).

Pelvic trabecular trajectories have been previously observed and classified through the use of radiographs (Macchiarelli et al., 1999; Rook et al., 1999; Cunningham and Black, 2009a, 2009b). Figure 2.8 shows the classification of the iliac trabecular organisation through the definition of six regions. A strongly defined structure is observed to travel anterio-inferiorly from the SIJ, forming a posterior trajectory (pt). Another structure travels posterior-inferiorly from the region around the anterior superior iliac spine (ASIS), producing an anterior trajectory (at). These orientations are believed to be structured to oppose loads induced by striding gait, and are termed the compressive and tensile trajectories respectively (Macchiarelli et al., 1999; Rook et al., 1999). As both trajectories travel inferiorly, they converge superior to the acetabulum and form the trabecular chiasma (tc). A poorly defined superio-medial structure (sm) is produced when the gluteal and pelvic cortical shells fuse without formation of trabecular bone (Cunningham and Black, 2009b). Additional regions of dense trabecular organisation are observed within the greater sciatic notch (sn) and acetabular roof (ar).

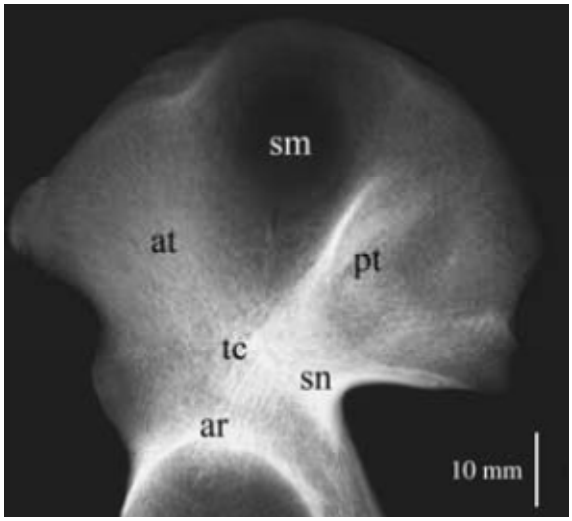

Figure 2.8. Trabecular bone organisation within the adult ilum, showing the regions of the posterior trajectory (pt), anterior trajectory (at), superior medial region (sm), trabecular chiasma region (tc), sciatic notch region (sn) and acetbular roof (ar) (reproduced from Cunningham and Black, 2009b).

In comparison to trabecular bone, knowledge of the cortical bone morphology is reported less frequently reported (Cunningham and Black, 2009c). However, cortical bone is known to be thicker in regions which experience high loading (Macchiarelli et al., 1999), and contain large muscle attachments. Consequently, a thick cortex is observed around the acetabulum and follows the pt towards the SIJ. To withstand forces exerted by muscles with large attachment sites, the cortex is correspondingly thicker around the glutei.

As pelvic bone growth is related to experienced mechanical stresses, varying histomorphometries can be observed between individuals (Dalstra et al., 1995; Anderson et al., 2005). In the analysis of a male cadaver, Dalstra et al. (1995) observed high trabecular densities at the acetabular rim and extending up to the SIJ. Cortical thicknesses were measured ranging between 0.5-3.2mm, with the greater sciatic notch and superior acetabular rim displaying a more robust cortex. Regions with the lowest thickness were located within the SIJ and the pubic symphysis. In contrast, Anderson et al. (2005) found high trabecular densities around the

acetabulum and near muscle attachments within a female pelvis. The SIJ contained a low trabecular density, along with the inferior ilium, contrasting with the trajectories in Figure 2.8. The cortex was reported to range between 0.44-4mm, with the iliac crest, pubic ramus, gluteal surface and around the acetabular rim being the thickest regions. The thinnest cortices were within the acetabular cup and the iliac fossa. The variance between the morphologies is attributed to the differing sex and age of the cadavers analysed, and the possibility of unknown medical conditions such as osteoporosis.

2.1.5. Juvenile osteology

The pelvis forms *in utero* from the lower limb bud through appositional ossification centres located within the ilium, ischium and pubis (Scheuer and Black, 2000). These centres expand and fuse to form a shallow acetabulum, forming the cartilaginous pelvis at the beginning of the third intra-uterine month. Subsequent primary endochondral ossification centres appear at the anatomical locations shown in Figure 2.9, with the ilium ossifying first at ~3 months, followed by the ischium (4-5 months) and pubis (5-6 months). The three primary ossification centres develop to form part of the bony acetabular wall, producing identifiable pelvic bones at birth (Avisse et al., 1997; Scheuer and Black, 2000). Despite an initial growth period after birth, the morphology of the pelvic bones displays limited variation within the first few juvenile years. Growth rates rise during the neonatal period, although their relative increase becomes progressively smaller until ~2-3 years old, after which they decrease until puberty. The first fusion between the separate bones occurs at the rami of the ischium and pubis at ~5-8 years, although they remain separated at the acetabulum by triradiate cartilage (Scheuer and Black, 2000; Portinaro et al., 2001).

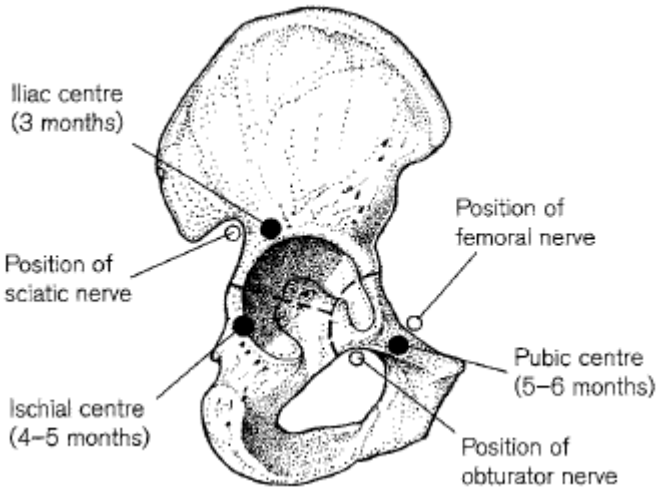

Figure 2.9. Locations of the primary ossification centres of the developing pelvis (reproduced from Scheuer and Black, 2000).

As illustrated within Figure 2.10, the triradiate cartilage is composed of growth cartilage, encompassed within epiphyseal cartilage at the bone surfaces. The structure is deepened laterally by articular cartilage, forming three flanges; the anterior flange between the ilium and pubis; the posterior flange between the ilium and ischium; and the vertical flange between the ischium and pubis (Ponseti, 1978; Scheuer and Black, 2000; Portinaro et al., 2001). Epiphyses which occur within the triradiate cartilage cause the fusion of the pelvic bones, commencing with the anterior acetabular epiphysis (located within the anterior flange) between 9-10 years old. The posterior epiphysis forms between 10-11 years, and is followed by the superior epiphysis (originating from the upper acetabular rim) which occurs between 12-14 years. Acetabular fusion is reported to vary between sexes, with the onset and completion occurring earlier in females (~11-15 years) compared to males (~14-17 years) (Scheuer and Black, 2000).

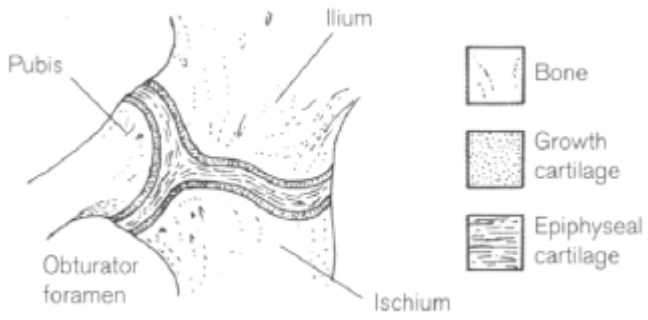

Figure 2.10. Composition of the triradiate cartilage which separates the juvenile pelvic bones (reproduced from Scheuer and Black, 2000).

Secondary epiphyses develop after fusion of the acetabulum, forming first at the posterior inferior iliac spine (PIIS) and expanding inferiorly to join the superior acetabular epiphysis. The iliac crest epiphysis follows at ~12-13 years in females and a year later in males, forming a cap over the superior ilium which fuses by 23 years of age (Scheuer and Black, 2000). The ischial tuberosity epiphysis is evident from ~13-16 years, expanding superiorly towards the ischial spine and inferiorly to the ramus. Partial fusion occurs between 16-18 years and remains incomplete until the rami reach the pubis at 20-21 years. Finally, the pubic epiphysis forms on the symphysis between 23-27 years and does not complete fusion until 35 years of age (Scheuer and Black, 2000).

The juvenile morphology of pelvic trabecular bone is considered to undergo adaptive remodelling in response to gait related MS loading, from an initial genetic blueprint. Ryan and Krovitz (2006) and Gosman and Ketchman (2009) both reported primary cancellous bone to be progressively remodelled with fewer, thicker trabecular struts within the juvenile femoral head and tibia respectively. Both the trabecular number and bone volume fraction were observed to decrease rapidly until 12 months of age, after which they were seen to be reasonably stable. The trabecular structure was recorded as relatively isotropic within the first year and diverged to anisotropy

thereafter. The juvenile ilium has been observed to display comparative trabecular structures to those of adults, by ~1-2 years of age (Valpato, 2008). This development of an ordered trabecular structure coincides with the juvenile development of unassisted bipedal locomotion (Sutherland, 1997). The high remodelling rates between birth and 1 year of age, may reflect the drastic changes in the experienced mechanical environments. Within this time frame, loading initially decreases rapidly from the *in utero* mechanical environment, until it increases again at the onset of crawling and bipedalism.

In contrast to the above, Cunningham and Black (2009b) witnessed structural alignment of iliac trabeculae comparable to that of an adult (see Figure 2.8), within fetal specimens as young as 18-22 weeks gestation. The initial generalised patterning displayed high density at the greater sciatic notch and inferior ilium, extending into the anterior and posterior regions. The definition of these trabecular trajectories increased with gestational age, producing adult-like alignment by 40 weeks. Adaptive remodelling has also been reported within the neonatal ilium (Cunningham and Black, 2009a), where regions experiencing higher forces were found to contain a more organised trabecular network. Regions which experience limited intrinsic forces, such as along the iliac crest, were observed to contain primary organisation through a high bone volume of tightly packed thin trabeculae. In contrast, increased organisation was observed inferior to the iliac crest, which was characterised with a slight reduction in trabecular bone volume and number. Further organisation was found superior to the acetabulum through a low number of moderately spaced trabeculae, attributed to possible MS loading during limb movement. Additionally, trabecular organisation was also observed within the greater sciatic notch, which is possibly caused by the sciatic nerve producing neurogenic influences (Cunningham and Black, 2009b).

Cortical bone morphology has been observed to be thicker in regions which are located near the primary ossification centres (Cunningham and Black, 2009c). The thinnest regions match those with limited trabecular organisation, while the gluteal cortex is thicker due to possible activation of the gluteal muscles. The thick cortex adjacent to the tc suggests that the cortical bone is important in protecting the underlying low bone volume fraction (Cunningham and Black, 2009c). The region of high trabecular organisation at the sn was also matched by an increased shell thickness, implying that the cortical bone undergoes similarly early adaptive growth.

Therefore, the prenatal pelvis has been observed to contain a partially optimised template for a load bearing function, from which future remodelling is based (Cunningham and Black, 2009a, 2009b, 2009c). As prenatal bone growth cannot be attributed to direct stance-related weight transfer, consideration must be given to potential genetic influences. The *in utero* mechanical environment is also thought to be a factor, as neurological firing of muscles and interactions with the womb wall can transmit loading through the cartilaginous acetabulum to the constituent bones. However, the contribution of genetic influences and mechanical loading to the adaptive growth of juvenile bone remains unknown.

2.2. MUSCULOSKELETAL MODELLING

Biomechanical analyses of anatomical structures aid the understanding of MS functioning, and enable prediction of muscular and joint forces throughout various locomotive movements. Analytical techniques in MS modelling have advanced from early mathematical methods (Seireg and Arvikar, 1973; Crowninshield, 1978; Crowninshield and Brand, 1981; Rohrle et al., 1984; Pedersen et al., 1987) to computerised simulations which replicate complex anatomical arrangements (Arnold et al., 2001; Blemker and Delp, 2005, 2006). Programming of the mathematical

principles which determine MS loading (Pedersen et al., 1987) has enabled the development of computational software for subject-specific modelling (Damsgaard et al., 2006; Delp et al., 2007).

Computational models which replicate the normalised gait pattern have provided an insight into the MS characteristics during common daily activities (Pedersen et al., 1997; Hoek van Dijke et al., 1999; Heller et al., 2001, 2005). Understanding of the MS system during locomotion has also aided diagnosis and treatment of conditions associated with pathological gait. For example, Arnold et al. (2005) observed that weak hip and knee extensors, along with ankle plantar flexors, contributed to excessive hip and knee flexion within cerebral palsy. In association with normalised gait, it has been reported that the declining strength of the gluteal and iliopsoas muscles is a cause of hip joint pain and instability (Lewis et al., 2007). Therefore, MS modelling can provide clinicians with an indication of which exercises should be prescribed to aid rehabilitation from injury or gait abnormalities (Lewis et al., 2009).

Modelling of locomotive movement before and after a total hip replacement (THR), has also captured the kinematical changes of the lower extremity post operatively (Lenaerts et al., 2009b). Computation of MS characteristics such as joint loading, has provided a means of testing prosthetic joint replacements and enabling refinement of their design (Stansfield and Nicol, 2002; Stansfield et al., 2003).

The above MS models are all associated with lower body modelling under normal daily activities, such as walking, sitting, stair climbing etc (Morlock et al., 2001). However, MS modelling techniques have also been applied to the upper extremity (Garner and Pandy, 2001; Blana et al., 2008), along with isolated anatomical features (Wu et al., 2009b; Saraswat et al., 2010), to replicate a variety of loading regimes (Van Drongelen et al., 2005; Dubowsky et al., 2008; Wu et al., 2009a). Although, as

this study is primarily concerned with the loading of the juvenile hip joint, this review focuses on MS modelling of the lower extremity.

2.2.1. Mathematical and experimental modelling

Initial attempts to analyse the mechanics of the hip joint mainly consisted of *in vivo* experimentations, comprising of strain gauge readings from implanted telemeterised total hip prostheses (Rydell, 1966; English and Kilvington, 1979; Davy et al., 1988). Such studies predominately recorded strains over a short term, within one or two patients during walking or stair climbing (Bergmann et al., 2001). However, Hodge et al. (1986) reported data collected post-surgery and during rehabilitation for a period exceeding 1 year after implantation.

Seireg and Arvikar (1973) provided the first attempt to quantify MS loading through non-invasive methods, through the use of a linear mathematical programme. Predicted muscle activity was found to provide a close correlation to that measured experimentally through electromyography (EMG). Crowninshield (1978) calculated intersegmental force and joint moments through a developed technique based on inverse dynamics, which integrated experimentally recorded kinematic and kinetic data. A further optimisation technique was devised by Pedersen et al. (1987) which included linear and non-linear calculations. Non-linear methodology was reported to produce muscle forces which were closer to those recorded through EMG, and reduced the high joint forces observed with linear modelling. Similarly, Crowninshield and Brand (1981) used non-linear optimisations to predicted muscle activity which was close to those measured through EMG.

These studies generally predicted higher joint forces than those measured experimentally, especially for the second half of the stance phase. This was possibly

due to the applied optimisation strategies and the anatomic assumptions and simplifications made (Bergmann et al., 1993). Brand et al. (1994) performed the first direct comparison between previous mathematical formulae and experimental data. Predicted peak joint forces were reported to exceed those measured *in vivo*, although the overall force patterns were similar. Comparative magnitudes were achieved through modifications to the applied mathematical methods. However, the theoretical values were based on kinematical data which was recorded at a longer post-operative period than the *in vivo* joint forces. Therefore, a cycle-to-cycle comparison was not achieved (Heller et al., 2001).

A long term experimental study performed by Bergmann et al. (1993), recorded telemeterised prosthetic strains within two patients over an 30 and 18 month post-operative period. The physical condition and ability of the patients contrasted, with one considered healthy and active (despite a bilateral THR), while the other suffered from a neuropathic disease. During walking at normal speed ($4Kmh^{-1}$) both patients produced comparable resultant hip joint force reaction profiles, characterised by two peaks during the stance phase, followed by a force reduction in the swing phase (similar to that of Figure 2.11). This generalised force pattern was also observed during increased walking speeds and jogging, although the relative height of the second peak (occurring at the instance of toe off) decreased.

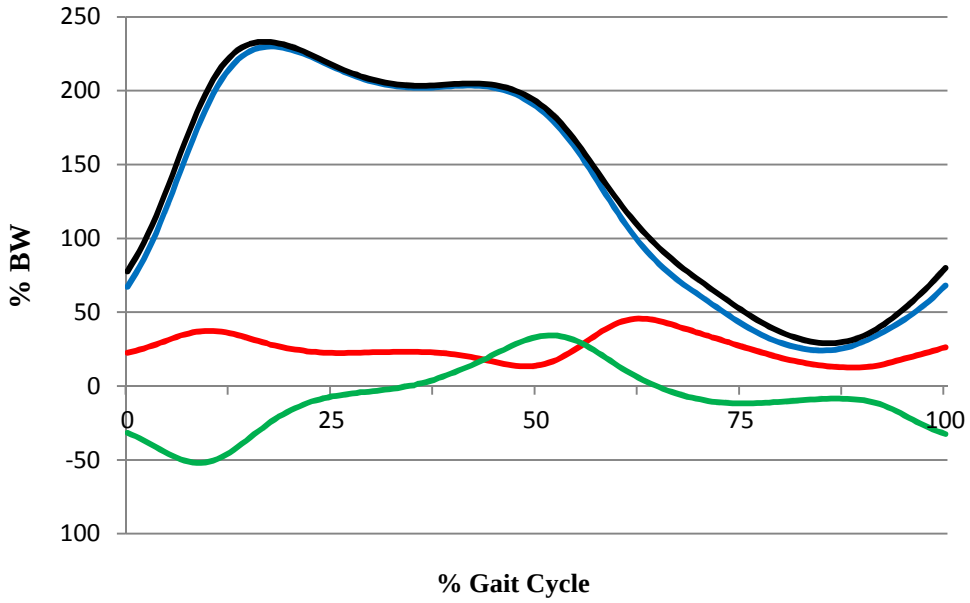

Figure 2.11. Hip joint reaction forces during the gait cycle calculated for a typical patient by Bergmann et al. (2001), showing the resultant reaction (black) and the orthogonal force components which are positive medially (red), anteriorly (green) and superiorly (blue) (data taken from Bergmann et al. (2001)).

A larger inter-patient variation was observed in the force magnitudes, which was highlighted through the average peak values associated with walking, measured at ~325% and ~380% BW. Higher reactions occurred within the neuropathic patient, which was suggested to be symptomatic of the disrupted MS system. The peak resultant forces within both patients increased significantly with a faster walking speed and during jogging, with magnitudes exceeding 584% BW. Similar to that of Figure 2.11, the minimal resultant forces occurred during the swing phase and despite variation at increased speeds, did not exceed 40% BW.

The gradual acquisition of a normalised gait pattern post-operatively did not produce uniform changes in the peak reaction values. The general trend displayed a constant peak magnitude within the first 4-5 months, followed by an increase and subsequent decrease until the force plateaued. Disturbance of gait after implantation was also evident within the swing phase, where higher minimal forces of 60-80% BW were

recorded within the first few weeks. The post-operative gait changes were attributed an improvement in walking ability (causing increased reactions) and the influence of training (causing decreased reactions). The final consistent peak magnitudes achieved were expected to be representative to those experienced pre-operatively, while the overall force reaction profiles did not deviate throughout.

Bergmann et al. (1993) reported the recorded general force patterns matched those of previous experimental data (Rydell, 1966; English and Kilvington, 1979; Davy et al., 1988), although comparison of peak forces was hampered by the variation in the walking speeds and the post-operatively period analysed within the literature. However, Bergmann et al. (1993) did observe a slightly more pronounced peak at toe off, which was either significantly smaller or absent in the preceding literature. This was comparable with predicted joint behaviour through theoretical calculations, although previous mathematical techniques often estimated a larger second peak.

Taylor et al. (1997) reported the axial forces within the shaft and tip of the intramedullary stem of instrumented femoral prostheses in two patients. The forces in the tip of the stem were comparable to those of Bergmann et al. (1993) at three times BW, despite measurements being taken distal to the hip joint and one patient having disrupted abductor muscles. However, an abnormal gait pattern was observed within this patient during the early months after implantation, adjusting the moment arms of the abductors, thus compensating for their initial abnormality. A post-operative increase in cadence was suggested to cause a rise in measured force within the first 18 months, although it stabilised thereafter. Force increases were reported to be greatest within the initial 1-6 months as the walking speed developed, preceded by more modest increments. A subsequent study reported the forces within the distal

femur, and provided the first account of reactions within the knee joint during various locomotive activities (Taylor et al., 1998).

To further their previous work, Bergmann et al. (2001) recorded telemetering prosthetic strains within four patients, with the aim of creating a unique data base of hip joint contact forces. Strain readings were recorded along with motion capture and force plate measurements during numerous locomotive activities, throughout an 11-31 month post-operative period. Patient mobility was deemed good after implantation, while the motion capture data did not detect any gait abnormalities.

Intra-patient hip joint reaction and gait pattern deviations during the various trials were reported as minimal, although more significant differences existed in the inter-patient comparison. This was highlighted within the hip joint reaction force profile during walking, where only two patients produced the generalised two peak trend during the stance phase (as shown in Figure 2.11). Within the remaining patients, the second peak either exceeded that of the first or was absent. Inter-patient variations were observed to increase through non-cyclic movements, such as standing on one leg or rising from a chair. The average peak reaction force measured during walking at normal speed ($4Kmh^{-1}$) ranged between 211-285% BW. These peak forces were lower than those recorded within slightly more immobile patients by Bergmann et al. (1993). A similar observation was made during fast walking, providing evidence linking muscle dysfunction to an increase in joint reaction forces. Bergmann et al. (2001) stated that a disrupted MS system activates muscles with short lever arms to perform joint movement, thus generates high joint forces.

Kinetic data was collated and used to calculate an average hip joint behaviour for a *"typical"* patient (NPA) during walking at various speeds, stair and chair ascent/descent, standing and knee bending. Despite the presence of an inter-patient

variation, all patients were identified as healthy which justified their inclusion within the NPA calculation. Figure 2.11 shows the hip joint reaction for the NPA patient during walking at normal speed, characterised by two peaks during the stance phase and a maximal magnitude of 234% BW. This averaged maxima is lower than those of previous mathematical predictions but similar to one of the subjects reported by Rydell (1966). However, Bergmann et al. (2001) stated that calculation of the NPA patient data was made with respect to the inter-patient variation, and that the inclusion of a larger data set would caused a change in the average forces.

Muscle activations during gait have also been measured *in vivo* through EMG and kinesiological electromyography, relating muscular electrical activity to joint movement (Sutherland, 2001). Initial studies utilising EMG were deemed invasive, involving the insertion of fine wire electrodes into the muscular anatomy (Andersson et al., 1997). However, wider application of surface electrodes has also reduced the intrusiveness of such methods, and enabled muscle activation measurement for an increased range locomotor activities and speed (Hof et al., 2002; Ivanenko et al., 2004; Gazendam and Hof, 2007). The ease of measurement and painless nature of such procedures has enabled analysis of the juvenile MS system during the development of a mature gait (Chang et al., 2007; Agostini et al., 2010). However, surface EMG is limited to superficial muscles and can detect electrical signalling from neighbouring anatomy, while muscle volume movement relative to attached electrodes can compromise accuracy (Masso et al., 2010). Therefore, fine wire electrodes are still used to measure the activity of deep lying muscles such, as the rectus femoris (Nene et al., 2004).

2.2.2. Computational inverse dynamics

Inverse dynamics is used to calculate kinetics through a series of static optimisations, based on either linear or non-linear programming. Net joint moments are initially determined through combining kinematic and ground force reaction data, preceded by prediction of the muscle forces which contribute to the calculated joint kinetics (Erdemir et al., 2007). The redundancy issues associated with the numerous muscle force combinations possible, are solved by minimising a cost objective function such as the total maximal force (Heller et al., 2001) or stress (Pedersen et al., 1997).

Pedersen et al. (1997) used inverse dynamics to calculate joint contact and pelvic muscle forces within a patient with a telemetering prosthesis. Analyses were based on a MS model developed by Brand et al. (1982), which was scaled to the anthropometrics of the patient. A non-linear optimisation was used to compute the associated kinetics of recorded motion capture data, with the objective function defined to minimise the sum of the muscle stresses (Crowninshield and Brand, 1981). Predicted peak joint contact magnitudes were similar to those measured experimentally, although the general force pattern throughout the gait cycle showed greater variance. However, laboratory recording of telemetering forces and motion capture data was taken on separate post-operative occasions, therefore a cycle-to-cycle comparison was not possible.

Heller at al. (2001) used the patient data published by Bergmann et al. (2001) to create subject-specific lower extremity MS models for each walking and stair climbing trial. Each model was driven via the recorded kinematical data to replicate gait movements, while the accompanying force plate reactions enabled inverse dynamics to calculate joint and muscular loading. Comparisons between the computed and measured hip joint contact forces provided a means for a cycle-to-

cycle validation for each model. Skeletal segments were extracted from the Visible Human Project (NLM, Bethesda, United States) and scaled to fit the proportions of the body markers within the motion capture data. As illustrated in Figure 2.12(a), a total of 95 lines of actions were modelled to represent the muscles and ligaments, with their maximum isometric force (MIF) based on a product of physiological cross sectional area (PCSA) and muscle stress. Inverse dynamics was based on a linear optimisation algorithm which minimised the sum of the total muscle force (Crowninshield, 1978), although muscle forces were restricted to 85% of their PCSA to prevent calculation of 100% activation. A close agreement was found between calculated and measured hip contact forces for all gait walking trials at each time step, with a minimal deviation of 0.3% occurring at the peak force of the stance phase. In contrast, the highest disparity was reported at 33%, although the average error produced through pooling of all the patient trials was 12%. Similar findings were observed during the stair climbing trials, producing an average deviation of 14%, with the calculated forces tending to overestimate the joint forces.

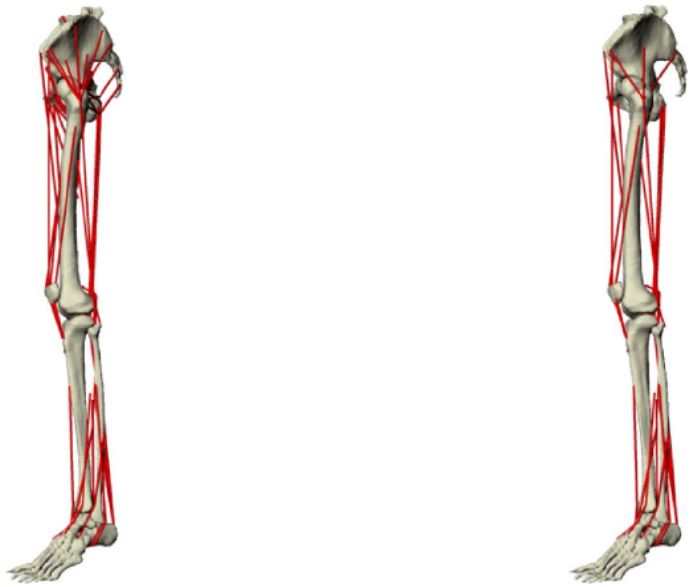

(a) **(b)**

Figure 2.12. Lower extremity MS modelling of the (a) complex muscular anatomy performed by Heller et al. (2001) and (b) the simplified muscle grouping devised by Heller et al. (2005) (reproduced from Heller et al. (2005)).

Heller et al. (2005) used the previously developed model to replicate the physiological loading of the typical NPA patient calculated by Bergmann et al. (2001), reporting a 1% (walking) and 4% (stair climbing) difference between computed hip joint contact forces and experimental data. Modelling of the hip joint muscular architecture was subsequently reduced in complexity, with the aim of obtaining a simplified load profile across the proximal femur for the use within *in vitro* testing. Initially, single joint muscles were combined to group the individual abductors and adductors into single lines of action, while lower strength muscles were progressively removed until unphysiological hip joint loading was produced. A simplified model which predicted hip joint forces that differed by 7% to experimental data during walking, consisted of 3 muscles spanning the joint (see Figure 2.12(b)). Further simplification of the muscle architecture was found to produce variances of up to 200% of the experimental data.

Similar techniques have been applied that combine kinematic and kinetic data to create subject-specific MS models. This has lead to the development of software programmes such as OpenSim (Delp et al., 2007) and AnyBody (AnyBody Technology, Alborg, Denmark), where pre-defined MS models can be modified to replicate subject-specific anthropometrics (see Figure 2.13). Lenaerts et al. (2008) used experimental data to generate subject-specific MS models from the generic model created by Delp et al. (1990), which consisted of 86 muscles throughout the lower extremity. Inverse dynamics performed within SIMM (Musculographics, Motion Analysis, United States) determined joint moments and muscle moment arms over a gait cycle, while muscle activations were calculated within Matlab (MathWorks Inc, United States). Subsequent studies used the same methods to examine the influence of modelling exact hip joint geometry upon the computed joint contact forces (Lenaerts et al., 2009a, 2009b). In identifying which muscles

contributed to the progression of gait movement, Steele at el. (2010) altered the same generic model within OpenSim to analyse children with crouch gait. Individual models were validated through comparison between computed joint kinetics and muscle activations, with experimental recordings. Arnold et al. (2010) recently constructed a new generic MS model using muscular anthropometric data published by Ward et al. (2009), detailing 88 muscles throughout the lower extremity.

Figure 2.13. The generic MS Lower Extremity Model within AnyBody.

Similar modelling techniques were performed by Manders et al. (2008) within AnyBody, through creating subject-specific models using gait data published by Vaughan et al. (1992). The calculated hip joint reactions for the generic (see Figure 2.13) and subject-specific models were compared to the *in vivo* measurements of Brand et al. (1994) and Bergmann et al. (2001). Saraswat et al. (2010) analysed the muscles within the foot through altering the same generic model, and performed validation through comparing computed forces with EMG recordings in literature.

Inverse dynamic calculations are based on net joint moments calculated superiorly from the ankle, which can result in initial inaccuracies in joint kinetics to be carried through to the knee and hip. It is also suggested that use of net joint moments is

unable to determine the mechanical contribution of bi-articular muscles (Neptune et al., 2001). In addition, calculation of muscle functioning does not compensate for energy expenditure (Zajac et al., 2002; Seth and Pandy, 2007), thus can potentially over estimate performance.

Although modification of generic MS models has enabled the evaluation of subject-specific kinetics, the incorporated isotropic or anisotropic scaling does not compensate for inter-individual variability in muscle geometry (Scheys et al., 2008). Likewise, scaling of bone segments to corresponding marker positions is unable to compensate for the possible structural variations within pathological subjects. For example, in cases of cerebral palsy the deformed proximal femur will caused an alteration of the muscular paths spanning the hip joint (Arnold et al., 2001; Scheys et al., 2008). The modelling of muscles through single or multiple lines of action, is also criticised for over simplifying the actual architecture (Blemker and Delp, 2005). Generic models assume that individual muscle fibres are comparative in characteristics, and thus group them together (Blemker and Delp, 2006). However, individual fibres of the rectus femoris and vastus intermedius have been reported to produce varying moment arms, suggesting true muscle behaviour can only be captured through more complex 3D modelling (Blemker and Delp, 2006).

Advances within magnetic resonance imaging (MRI) have linked the digital extraction of bone and muscle geometries, to create personalised MS models (Blemker and Delp, 2005, 2006). This has enabled greater accuracy in replicating the MS system, particularly in capturing muscle excursions around bony and soft tissue (see Figure 2.14). Morphing of FE meshes, which contain individual fibres, onto segmented muscle volumes provides a means of modelling numerous fibres per muscle. Blemker and Delp (2006) reported that such 3D muscle modelling produced

varying moment arms in comparison to techniques which assumed isotropic fibre properties.

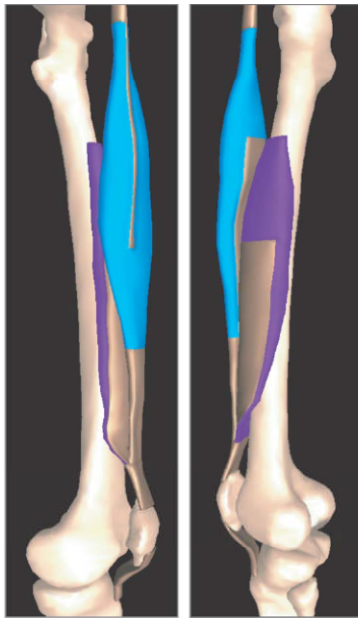

Figure 2.14. Modelling of the 3D geometries of the rectus femoris (blue) and vastus intermedius (purple) performed by Blemker and Delp (2006) (reproduced from Blemker and Delp (2006).

Application of personalised models for analysis of MS loading during gait is significantly hampered by computational power, and the time required for their construction. Therefore, personalised models tend to represent only a limited number of muscles (Blemker and Delp, 2005, 2006), although Oberhofer at al. (2009) combined motion capture with a personalised MS model containing 20 volumetric muscles. However, the model was constructed with deformation as the only measurable output, thus limiting its analytical capabilities. Additionally, the data required to define all the parameters required for 3D muscle modelling is currently unavailable within literature for each muscle (Blemker and Delp, 2005). As acquiring MRI data for patients is not always possible, subject-specific modelling through altering generic MS models is generally the most feasible option. Arnold et al. (2001) combined the two techniques via altering generic models based upon anthropometric

data taken from MRI scans, and reported an improvement in the accuracy of the muscle representation.

2.2.3. Computational forward dynamics

To overcome the problems associated with inverse dynamics, a forward based modelling method can be applied in which MS models are driven by known muscle activations. Forward dynamic MS models define muscles with contractile elements which are controlled by EMG signalling. Consequently, simulated muscle contractions excite joint movement and propel segments in a coordinated manner. Validation of this technique is achieved through comparing computed joint kinematics to those observed during the initial EMG acquisition (Buchanan et al., 2005; Barrett et al., 2007). However, as only superficial muscles can be measured accurately through EMG, such methods are only capable of representing a few muscles, limiting modelling of the gait cycle to either the swing or stance phase.

To eliminate the complications relating to EMG, parameter optimisation techniques have been devised in which muscle activations are continuously altered through a series of iterations, until physiological joint movements are achieved (Anderson and Pandy, 2003; Neptune at al., 2001). The complexity of this method renders it unsuitable for general application, due to the computational power and time required to perform analyses (Seth and Pandy, 2007). Therefore, despite the discussed limitations, inverse dynamics can be considered the most applicable modelling technique to determining subject-specific kinetics.

2.3. FINITE ELEMENT MODELLING

The structural behaviour of the pelvis in response to MS loading has been evaluated through the use of FE analysis by a number of researchers. Observation of the

mechanical stresses induced in the pelvis by the loading of the healthy MS system, has aided the development of theories linking bone growth optimisation to load transfer. However, analyses of normal pelvic MS loading are less common than those used in researching orthopaedic products. Such analyses utilise FE methods to optimally design and test THR or hemi-arthroplasty components (Korhonen et al., 2005), through calculating fracture risk and wear and fixation properties (Coultrup et al., 2010), hence reducing the reliance on expensive prototypes.

Analytical techniques to examine the structural mechanics of the pelvis and hip joint have developed from early experimental efforts, comprising of strain gauge measurements, to complex mathematical and FE modelling. Through the availability of increased computational abilities, the complexity of FE models has also increased from initial two-dimensional (2D) and axisymmetric studies, to 3D modelling.

2.3.1. Strain gauge experiments

Prior to the availability of computational FE software, experimental studies provided a means of analysing the pelvis under customised load conditions. Through the placement of strain gauges upon the cortical surface and applying external loading, strain values were measured to provide an indication of the mechanical response at specific locations. Early experimentations were often used as a sole measure to assess the alterations in pelvic strain distribution post implantation of acetabular prostheses (Petty et al., 1980; Lionberger et al., 1985; Finlay et al., 1986; Ries et al., 1989). However, FE modelling provides an accurate method of evaluating a number of mechanical measures (i.e. compressive, tensile, shear stress/strain) across the whole structure, thus providing a significant advantage over experimental measurements. Although, strain gauge experiments are still currently performed as a

method of validating FE models (Dalstra et al., 1995; Anderson et al., 2005; Korhonen et al., 2005; Majumder et al., 2008b; Shim et al., 2008; Leung et al., 2009; Shim et al., 2010).

Jabob et al. (1976) performed initial strain gauge experiments on an epoxy model of the pelvis, which replicated hip joint loading in a standing position. However, epoxy models cannot replicate the complex internal trabecular bone structure, thus fail to capture the true mechanics of the pelvis. Therefore, subsequent experimental modelling was performed on cadaveric pelves (Petty et al., 1980; Lionberger et al., 1985; Finlay et al., 1986; Ries et al., 1989). Photoelastic analyses have also been performed to examine the stress distribution within a healthy pelvic structure (Yoshioka and Shiba, 1981), and one with a prosthetic hip joint (Miles and McNamee, 1989)

Dalstra et al. (1995) was the first to study and perform strain gauge experiments on the pelvis as a means of validating FE modelling. A cadaveric pelvic specimen was loaded in a similar configuration to Figure 2.15, with the iliac crest constrained within acrylic cement and the acetabulum loaded through a femoral shaped lever arm. Corresponding CT scan data was used to determine the trabecular and subchondral bone density, along with the cortical shell thickness throughout the pelvis. The scan pixel intensity of the bone was converted into a calcium equivalent density using previously developed relationships (Dalstra et al., 1993), which in turn was used to calculate Young’s modulus (E). An FE model was created of a separate cadaveric hemi-pelvis which was meshed with 8-noded parametric brick elements to model trabecular and subchondral bone, and membrane elements to represent cortical bone. The hemi-pelvic mesh was mirrored to obtain the contralateral pelvis, and loaded in replication of the experimental procedure.

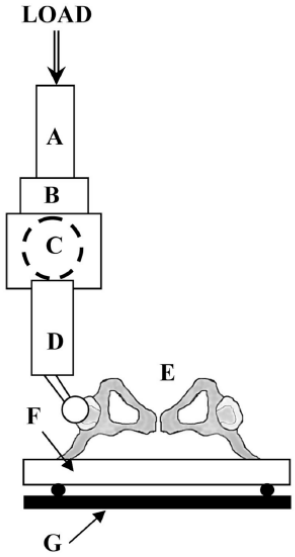

Figure 2.15. Experimental loading of a pelvis in which the iliac crest is submerged in resin, and the hip joint force is replicated through a prosthetic femoral head attached to a load cell (parts A-D) (reproduced from Anderson et al., 2005).

Two FE models were created; a realistic model with element-specific material properties based on the CT data; and a homogenous model with averaged material properties (for material properties see Table 2.1). Both FE models displayed similar compressive cortical stress distributions, although the magnitudes of the homogenous model were slightly larger in regions of high stress. This was linked to the increased flexibility at these locations due to an underestimation in the cortical thickness. Therefore, Dalstra et al. (1995) concluded that homogenous material properties can replicate pelvic mechanics, although histomorphometric data is more suitable if available and feasible to model. Minor variations between the experimental and FE predicted stresses were partially attributed to the use of a different sized femoral lever arm within the computational analyses. Although, comparison between two different pelvic morphologies and assignment of material properties obtained from another specimen, may have also attributed to the discrepancies. Additionally, the coarse FE mesh (consisting of 2602 elements) forced averaging of material properties over large areas, thus failing to capture the histomorphometry accurately.

A similar experimental protocol was adopted by Anderson et al. (2005) in assessing the sensitivity of material properties upon FE stress predictions. The study used the same cadaveric pelvis in histomorphometric, FE and experimental analyses. The employed experimental setup is illustrated in Figure 2.15, which loaded the hip joint through multiples of BW under single stance loading. A FE model was constructed using 4-noded tetrahedral elements to represent trabecular bone, and 3-noded shell elements to model the cortical bone and acetabular cartilage. A histomorphometric analysis determined the trabecular modulus (using similar methods to Dalstra et al. (1993)) and cortical thickness distribution across the pelvis. Histomorphometric data was used to assign element-specific material properties within the FE model, while another homogenous model was defined with averaged trabecular modulus and cortical thickness (for material properties see Table 2.1). Two further models were analysed which further assessed sensitivity to the material properties, each defined with parameterised trabecular and cortical moduli and cortical thickness. Magnitudes of each parameter were fluctuated by ±0, 0.5 and 1 standard deviation (SD), based on the collected histomorphometric data.

Modelling with element-specific material properties produced strain magnitudes which did not statistically vary from experimental measurements. In comparison, the homogenous model produced a stiffer structure, contrasting to the findings of Dalstra et al. (1995).

	Trabecular Bone E (MPa)	Subchondral Bone E (MPa)	Cortical Bone E (GPa)	Cortical Bone Thickness (mm)	Articular Cartilage E (MPa)
Dalstra et al. (1995)					
Realistic model	Element-specific (range 1-186) (υ = 0.2)	Element specific (range 132-2155) (υ = 0.3)	17 (υ = 0.3)	Element specific (range 0.7-3.1)	-
Homogeneous model	70 (υ = 0.2)	2 (υ = 0.3)	17 (υ = 0.3)	1	-
Dalstra and Huiskes (1995)	Element-specific (range 1-186) (υ = 0.2)	Element specific (range 132-2155)	17 (υ = 0.3)	Element specific (range 0.7-3.1)	-
Anderson et al. (2005)	Element-specific (range 2.5-3829) (υ = 0.2)	-	17 (υ = 0.3)	Element specific (range 0.44-4.0)	Mooney Rivlin Material C_1=4.1, C_2=0.41
Majumder et al. (2005)	70 (υ = 0.2)	-	17 (υ = 0.3)	2	-
Cilingir et al. (2007)	80(υ = 0.2)	-	17 (υ = 0.3)	1.5	-
Li et al. (2007)	70 (υ = 0.2)	-	19 (υ = 0.3)	-	Mooney Rivlin Material C_1=4.1, C_2=0.41
Phillips et al. (2007)	150 (υ = 0.2)	-	18 (υ = 0.3)	2	-
Shim et al. (2008)	Element-specific (υ = 0.2)	6900 (υ = 0.3)	17 (υ = 0.3)	Element specific	10.35 (υ = 0.4)
Leung et al. (2009)	Element-specific (υ = 0.2)	-	17 (υ = 0.3)	Element specific (range 0.44-4.0)	Mooney Rivlin Material C_0=0.1, C_1=0.45, C_2=1.67
Coultrup et al. (2010)	Element-specific (υ = 0.2)	-	17 (υ = 0.3)	1.5	-
Zhang et al. (2010)	Element-specific (range 2.4-3845) (υ = 0.2)	-	12 (υ = 0.3)	Element specific (range 0.5-4.0)	-

Table 2.1. Material properties of the pelvic bone used within literature.

Sensitivity studies varying the material parameters were made with respect to the subject-specific model, and observed that trabecular modulus did not produce a significant variation in predicted strains. Altering the cortical thickness produced a more distinct statistical difference, although strain variation increased further through altering the cortical modulus. Therefore, the cortical strains were 15 times more sensitive to changes in cortical modulus compared to the trabecular. Fluctuations of bone Poisson ratio (υ), cartilage modulus and cartilage thickness did not prove to be statistically different.

Anderson et al. (2005) also evaluated the validity of representing cortical bone through shell elements clad over the pelvic surface. The resulting overlap between shell and volumetric elements produces an overestimation of the cortex stiffness. However, analysis of a comparative model which defined a zero modulus to shell elements that intersected into the trabecular bone, did not produce a statistical different strain distribution.

In contrast to previous experimentations, Leung et al. (2009) examined the response of a cadaveric specimen which did not require a femoral implant to provide acetabular loading. In developing and validating an FE model for analysis of pelvic fractures, a cadaver with attached vertebra (up to L5) and femora (to the mid shaft) was used. Constraining the femoral shafts perpendicular to a mounting plate and applying compression through the vertebra, aimed to replicate loading during the stance phase. A corresponding FE model of the cadaver was constructed from CT data, with exact cortical geometry (eliminating need for shell elements) and incorporating cartilage, hip capsule and ligaments. The FE model, assigned with element-specific material properties (for material properties see Table 2.1), produced strains which closely correlated to experiment measurements. Changing the pelvic

bone properties suggested that decreasing the moduli produced larger cortical strains, while an increase caused the strains to plateau. Similar to Anderson et al. (2005), the surface strains where most sensitive to alterations in cortical modulus, and this sensitivity increased further when both trabecular and cortical moduli were altered together.

Shim et al. (2008) used experimental methods to validate a hybrid method of constructing FE models, based on sparse CT datasets (Shim et al., 2007). Three cadaveric pelves complete with intact articular cartilage and femoral heads were loaded in a similar configuration to that of Figure 2.15. Through CT scans of the cadaveric specimens, corresponding FE models were created with element-specific trabecular modulus and cortical thickness (for material properties see Table 2.1). Each model was then altered with four different meshes, which were based on varying parameters of the hybrid method. A close correlation was produced between FE and experimental strains, despite the FE modelling only incorporating the hemi-pelvis, thus not fully replicate the experimental setup.

Follow up experimental studies were performed on synthetic pelves constructed from Sawbone, using the same experimental protocol (Shim et al., 2010). The iliac crest of the pelves were constrained at a tilt which either replicated a standing or seated orientation, while a synthetic femoral head was used to load the acetabulum until fracture. A FE pelvic model was constructed through a CT scan of a Sawbones model, modelled through 4-noded volumetric elements and the non-linear material properties of the synthetic pelves. Predicted and experimental fracture loads were found to be in close agreement.

Experimental studies have also been performed to validate pelvic FE models which contain surrounding soft tissue (Majumder et al., 2008a, 2008b, 2009). An

experimental setup released a load cell from several heights and measured the peak force when it impacted two separate cadaveric specimens; one hemi-pelvis and one full pelvis with corresponding femurs (up to the mid shaft) and surrounding soft tissue. Previously developed pelvic FE models with element-specific material properties (Majumder et al., 2008a, 2009) were used to replicate the experimental protocol. The pubic symphysis and soft tissue were modelled using non-linear hyperelastic material properties (see Table 2.1). A correlation was found between experimental and computed peak impact forces, although the FE modelling tended to overestimate their magnitude and predicted them to occur earlier. Such variations are related to the construction of FE models that are based on differing cadaveric specimens to those used during the experimentation. Additionally, the experimental impact loading of the cadavers from several heights possibly contributed to fatigue of the cadaveric specimens.

2.3.2. Pelvic finite element modelling under physiological loading

Early attempts to capture pelvic mechanics through FE methods often examined acetabular prostheses, through reducing the complexity of modelling the pelvis via axisymmetric (Pedersen et al., 1982) or 2D modelling (Holm, 1981; Carter et al., 1982; Vasu et al., 1982; Rapperport et al., 1985). However, such approximations of the pelvic structure prove problematic, as axisymmetric models assume a 360° structure of the acetabulum. The opening at the acetabular notch proves this to be false, thus causing axisymmetric modelling to overestimate the stiffness. In comparison, 2D modelling cannot account for the out-of-plane stresses that are present within the acetabulum, thus prove to be too flexible. In fact, Vasu et al. (1982) reported that the maximum stress exceeded 30% of the yield stress (estimated at ~120MPa) in a 2D model, thus concluded that the modelling over estimated

stresses. Consequently, a large gap in predicted stresses is produced between the two modelling methods. This lead Dalstra et al. (1995) to conclude that the pelvis must be modelled as a 3D structure in order to capture the correct mechanics. Therefore, subsequent analyses of the pelvis aimed to eliminate these problems through 3D modelling (Oonishi et al., 1983). However, these either analysed the effects of components of hip prostheses or loading under side impact.

Dalstra and Huiskes (1995) made the first attempt to ascertain the 3D mechanical response of the pelvis to the physiological MS loading associated with gait. An FE model created through mirroring a hemi-pelvis about the sagittal plane, comprised of 8-noded brick elements and 4-noded membrane elements to represent trabecular and cortical bone respectively (see Figure 2.16). Element-specific trabecular modulus and cortical thickness was defined based on data of Dalstra et al. (1995) (for material properties see Table 2.1). Muscular and joint loading was determined at six phases during the gait cycle (see Table 2.2), through combining the optimisation techniques of Crowninshield and Brand (1981) and hip joint reactions from Bergmann et al. (1993). Muscular lines of action at the specific gait phases were resolved using the anthropometric data of Dostal and Andrews (1981). Loading was only applied to only one hemi-pelvis with constraints applied in all degrees of freedom (DOF) at the SIJ's.

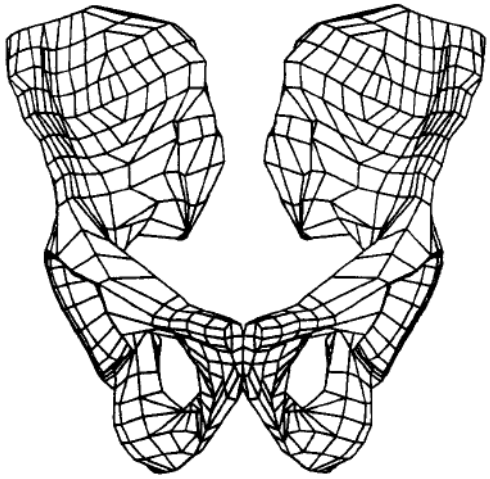

Figure 2.16. The pelvic FE model of Dalstra and Huiskes (1995), consisting of 2,662 8-noded brick and 4-noded membrane elements (reproduced from Dalstra and Huiskes (1995)).

Phase	Description	% of the gait cycle
1	Double support phase, beginning of the left stance phase	2
2	Beginning of the left single support phase	13
3	Halfway through the single support phase	35
4	End of the left single support phase	48
5	Double support, end of the left stance phase	52
6	Beginning of the left swing phase	63
7	Halfway through left swing phase	85
8	End left of the swing phase	98

Table 2.2. Description of the 8 phases during successive heel strikes of the left leg modelled by Dalstra and Huiskes (1995) and Majumder et al. (2005).

The highest predicted cortical and trabecular von Mises stresses were found to occur during the first half of the gait cycle, particularly during the single stance support. During these phases cortical stresses ranged between 0-30MPa, with large concentrations at the origin of the gluteus maximus, the greater sciatic notch and

along the superior pubic ramus. In contrast, trabecular stresses ranged between 0-0.6MPa, and were significantly concentrated within the central iliac wing and the anterior acetabular quadrants. Consequently, cortical stresses were typically around 50 times larger than in the underlying trabecular bone, with the regions of high stress concentrations not coinciding within the two. Acetabular stresses were predominately distributed along anterio-superior rim within both the cortical and trabecular bone. This was attributed to the applied hip joint loading, which was directed entirely towards the anterio-superior quadrant during the gait cycle (Bergmann et al., 1993).

Loading of the pelvis solely through hip joint forces significantly altered the cortical stress patterning, producing a concentration travelling directly between the SIJ and pubic symphysis. Therefore, Dalstra and Huiskes (1995) concluded that the muscles aided in stress relieving the pelvis through evening the distribution across the structure, and minimising changes in stress patterns during the gait cycle. This was considered to oppose possible fatigue failure associated with cyclic loading.

In comparison to histomorphometric analyses (Macchiarelli et al., 1999; Rook et al., 1999; Cunningham and Black, 2009a, 2009b), high trabecular stresses were observed within the central iliac blade, a region suggested as having sparse trabecular growth (see Figure 2.8). Therefore, the model validity must be considered, which is compromised by the limited number of elements and the use of two different sources to determine the MS loading. Additionally, sagittal rotation of the SIJ was not permitted and could have resulted in an over constrained model.

Despite these initial attempts of Dalstra and Huiskes (1995) to model the pelvis under normal gait loading, comparative studies were not published until Majumder et al. (2005) performed similar analyses. In this later study, an FE pelvic model

consisting of 71,674 elements representing trabecular and cortical bone through solid volumetric and shell elements respectively, was presented. Element selection ensured that six DOF could be modelled by both types, accounting for the out-of-plane loading of the pelvis, unlike the membrane elements adopted by Dalstra and Huiskes (1995). Homogeneous material properties were applied (see Table 2.1), and the right hemi-pelvis was loaded in the same method as Dalstra and Huiskes (1995). However, the hip joint reaction force was applied directly to the acetabulum, as opposed to through an incorporated femoral head. The SIJ's were constrained in translation movement (UX, UY and UZ) to simulate rotation of the joint.

The predicted von Mises stresses were greater during the single stance support phases, with cortical stresses ranging between 0-38MPa. Regions of high stress concentrations varied throughout the gait cycle, transferring between the superior pubic ramus, central inferior ilium and the posterio-superior ischium (a region virtually unloaded within Dalstra and Huiskes (1995)). In comparison, the largest trabecular stresses were reported to locate within the acetabulum for all phases, producing an overall range of 0-1.7MPa. Therefore, cortical stresses were observed to be around 20 times higher than that of trabecular bone, with regions of larger concentrations varying between the two.

Validity of the FE model was argued through the performance of a convergence test, which obtained an optimum mesh. Additionally, the experimental loading of Dalstra et al. (1995) was replicated, and resulted in von Mises stresses which agreed with those of the homogeneous model. However, the modelling performed by Majumder et al. (2005) was also subject to the validity of applying MS loading from different sources, while the effect of applying homogenous material properties was not analysed.

Phillips et al. (2007) employed a different method of replicating MS loading, through the use of spring and connector elements to model muscles and constraints. A pubic disc was also used to adjoin separate hemi-pelves, in contrast to a rigid connection as favoured by Dalstra and Huiskes (1995) and Majumder et al. (2005). A muscular and ligamentous (ML) model replicated 42 muscles and 7 ligaments (see Figure 2.17), with calculated tensile stiffness values based on a Hill type contraction model. Compressive spring stiffness was defined as negligible. As illustrated in Figure 2.17, muscles were modelled through several individual fibres with the femoral attachments based on the data of Dostal and Andrews (1981). Connector elements replicated the articulation of the SIJ and the pubic disc, through significant stiffness in compression and low stiffness in tension. The single stance hip joint loading reported by Bergmann et al. (2001) was applied through the centre of a spherical femoral head located within the acetabulum. The upper body was additionally considered as a load transferred to the pelvis through the lumbar spine.

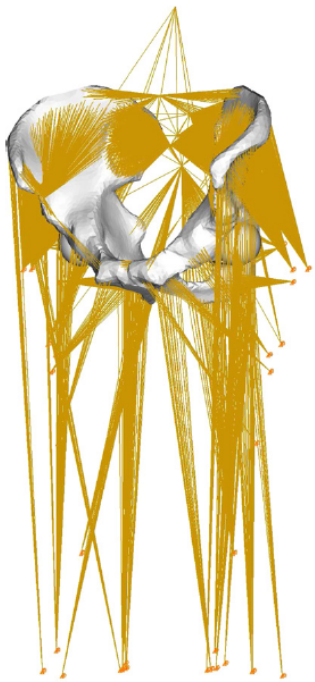

Figure 2.17. The ML boundary condition model of Phillips et al. (2007) which utilised spring and connector elements to represent soft tissue attachments and the SIJ respectively (reproduced from Phillips et al. (2007)).

A comparative fixed boundary condition model was also modelled which contained only two ligaments and was solely loaded through the hip joints. Constraining the SIJ in all DOF produced a similar loading regime to one adopted by Dalstra and Huiskes (1995). Noticeable variations in displacement patterns were observed between the two models, with the fixed boundary method producing a stiffer structure (displacement ranging between -0.05-0.2mm). Only the lateral ilium and ischium produced significant anterior movement, while the SIJ and contralateral hemi-pelvis remained stationary. In comparison, the ML model displayed increased movement ranging between -1.5-2mm, which exceeds that reported by Majumder et al. (2005). Displacement was reported throughout the whole structure, as the weight supporting hemi-pelvis moved posteriorly while the contralateral hemi-pelvis moved anteriorly.

Cortical von Mises stresses within the fixed boundary model were predominantly concentrated in a column between the superior acetabular rim and the SIJ. Although, this is similar to that of Dalstra and Huiskes (1995), the stress range of 0-70MPa is higher and the inclusion of a pubic disc produced an unloaded pubis. The largest trabecular von Mises stresses were located within the acetabulum, around the constrained SIJ and the central iliac fossa. As illustrated in Figure 2.18(a), the ML model produced a similar cortical von Mises stress distribution, although smaller magnitudes were reported (ranging between 0-30MPa). The lower stress state and a less dramatic stress reduction towards the lateral ilium, again highlighted the stress relieving role of the muscles to produce a more even distribution. Similar to Dalstra and Huiskes (1995), hip joint loading transferred from the rim of the superior acetabular quadrants (particularly the anterio-superior) towards the greater sciatic notch and SIJ. However, the pubis and ischium remained virtually unloaded which contrasts to the previous studies.

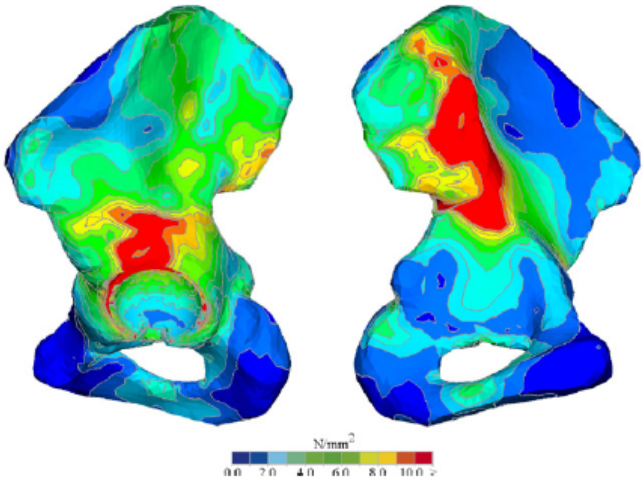

(a)

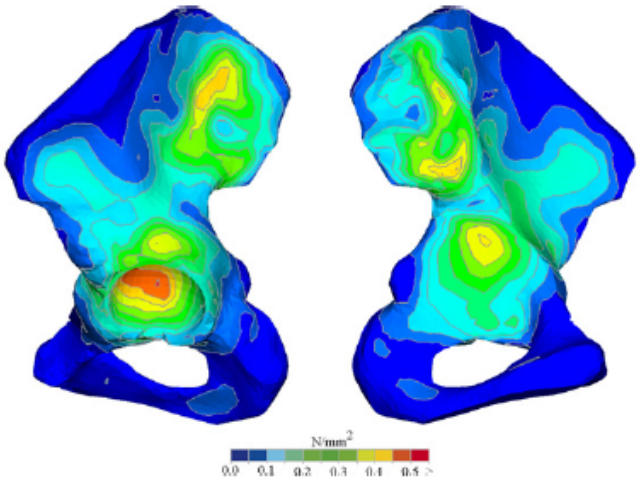

(b)

Figure 2.18. The medial and lateral von Mises stress distribution of the (a) cortical and (b) trabecular bone of the ML model of Phillips et al. (2007) (reproduced from Phillips et al. (2007)).

The largest trabecular stresses within the ML model were predominately concentrated within the acetabulum and around the SIJ (see Figure 2.18(b)). High stresses were also located towards the superior limit of the pt. Another defined concentration also originated from the superior acetabular region and was directed anterio-superiorly towards the ASIS. Consequently, these two concentrations roughly correspond to the at and pt. As both originate from the superior acetabulum, an additional concentration was created which is representative of the tc. In disagreement with the findings of Dalstra and Huiskes (1995), the central iliac fossa

remained unloaded in accordance with a poorly defined trabecular network within the sm region. However, the superior acetabular rim and sciatic notch did not contain the highest stress concentrations, as would be required to produce the well defined sn and ar trabecular trajectories. Therefore, although the stress distribution did not exactly match the trabecular trajectories in Figure 2.8, comparisons can be observed.

Phillips et al. (2007) also replicated the experimental loading of Dalstra et al. (1995) and Anderson et al. (2005), and found close agreement in cortical von Mises stresses. This validated the estimated pelvic geometry of the FE model, and the spherical femoral head used to load the acetabulum. The reported reaction forces of the glutei muscles in the ML model were also in accordance with the findings of Bergmann et al. (2001). Additionally, displacement within the pubic disc was similar to that measured experimentally by Walheim and Selvik (1984), providing additional validation.

2.3.3. Pelvic finite element modelling under alternative loading

The dynamic response of the pelvis under non-physiological conditions has also been studied, particularly under lateral impact to mimic the loading commonly associated with car accidents (Dawson et al., 1999; Majumder et al., 2004; Su et al., 2005; Salzar et al., 2009). However, loading is often applied directly to the pelvic bone and ignore the possible energy dissipation through the surrounding soft tissue. Comparatively, the analyses of the pelvis during simulated falling has assessed hip joint fracturing within the elderly (Majumder et al., 2007, 2008a, 2009). Li et al. (2007) also observed the mechanical response within the soft tissue, when modelling the pubic symphysis under lateral impact to accurately capture its non-linear hyperelastic nature (Li et al., 2006).

The performance of hip prosthesis components under *in vivo* loading environments has also been evaluated through FE methods. In relation to the pelvis, the stresses induced within acetabular prostheses (Korhonen et al., 2005), possible risk of failure (Coultrup et al., 2010) and loosening of bone (Zhang et al., 2010) have been analysed. However, the aim of such studies are often concentrated on the mechanics of the prostheses, thus do not report the post-operative effect on bone. Although, Cilingir et al. (2007) did observe the response of the pelvis and femur, along with the prostheses, after hemi- arthroplasty of the hip joint. Meanwhile, Kaku et al. (2004) reported the stress distribution throughout the pelvis after surgery to correct pubic fractures.

Analysis of prosthesis performance *in vivo* is often achieved using simplified FE loading, consisting solely of hip joint reactions. Additionally, pelvic movement is also simplified through constraining the SIJ and pubic symphysis in all DOF (Cilingir et al., 2007; Coultrup et al., 2010). Therefore, comparisons between pelvic mechanics pre and post-operatively under true physiological loading are hampered. However, Vaverka et al. (2006) compared the stress distribution of a juvenile hip joint which had a deformed femoral head. Partial physiological loading was also considered through incorporation of abductors muscles, which were modelled through the use of stiff cable elements. Although the findings of such studies are not fully applicable to this study due to the non-physiological loading applied, modelling methods and material properties provide useful data.

3. DIGITISED MODELLING

Digitised modelling involved the generation of computerised models from scan data, which could then be used for subsequent MS and FE analyses. In this study, digitised pelvic models were constructed of specimens obtained from the Scheuer collection, with their selection being based upon age and condition. All specimens were μCT scanned using an X-Tek HMX160 microCT system (X-Tek, Tring, UK) at the University of Hull, unless otherwise stated. Scan data was exported as a stack of .tiff (tagged Image File Format) images and imported into AMIRA Image Segmentation Software (TGS Inc, United States), for volumetric modelling and segmentation.

To simplify the digitised modelling procedure and to take advantage of the symmetrical nature of pelvis, only the hemi-pelvis was reconstructed for each specimen. Although Boulay et al. (2006) reported that the pelvis is not truly symmetric, only 15 of the 71 anatomical landmarks they studied displayed significant asymmetry. Therefore, the additional complexity in reconstructing the full pelvis was considered to outweigh the advantages of modelling its slight asymmetric nature. The complexity of the trabecular architecture is unrealistic to represent through conventional FE methods, therefore the innominate was modelled as a solid structure. The following modelling procedures were used to create digitised models of a prenatal, a 1yr, a 8yr and a 19yr old hemi-pelvis.

3.1. PRENATAL HEMI-PELVIS

A fetal pelvic specimen from the Scheuer collection was selected for biomechanical modelling based on its condition and approximate age. The chosen specimen (NP7) comprised of both innominate bones and the sacrum, as illustrated in Figure 3.1. The innominate bones were held in an articulated structure by the connecting cartilage of

the acetabulum and pubic symphysis, although due to the nature of the specimen, the cartilage had mummified. Therefore, the connecting cartilage held the constituent pelvic bones together, but it was unclear at this stage if their relative positioning had become distorted.

Figure 3.1. Prenatal specimen (NP7) of the Scheuer collection comprising of both innominate bones and mummified cartilage.

The prenatal specimen was μCT scanned with a slice thickness of 0.0588 x 0.0586 x 0.0588mm, and imported into AMIRA to observe the bone and soft tissue through varying grey scale values, based upon the apparent material density (see Figure 3.2 (a)). Differentiation between materials was highlighted by the higher grey scale value of bone, aiding image segmentation into separate bone and cartilage entities. As illustrated by Figure 3.2(a), bone was displayed through a bright white intensity which contrasted to the dull grey colour of the cartilage.

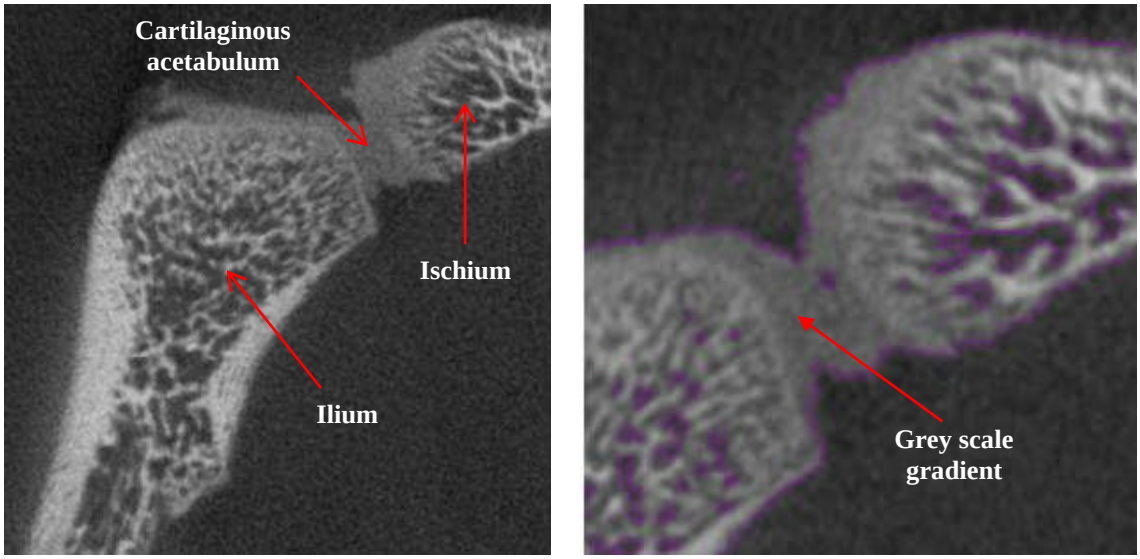

(a) **(b)**

Figure 3.2. A µCT slice through the prenatal ilium, cartilaginous acetabulum and ischium, showing (a) the grey scale variation between the bone and cartilage, and (b) thresholding of the grey scale gradient defining the whole structure as one material.

Interfaces between bone and soft tissue within mature anatomical structures are often clearly defined, with a layer of cortical bone forming a boundary with other materials. Therefore, in the case of the hip joint a layer of cortical bone around the acetabulum aids segmentation between the pelvis and articular cartilage. However, depending on gestation age, many prenatal bones do not have a continuous cortical shell around their structure. This is highlighted in Figure 3.2(a), where it is evident that the triradiate cartilage of the acetabulum is under ossification, therefore producing a material density which did not significantly differ from that of the developing iliac and ischial bone. This resulted in a gradual grey scale gradient from the trabecular bone through to the cartilage, producing an unclear boundary definition. Hence when thresholding of the grey scale values was applied, the triradiate cartilage was automatically detected within the same range as the trabecular and cortical bone (as highlighted in Figure 3.2(b)). Digitisation into a volumetric model with such thresholding techniques produced a structure where trabecular bone and cartilage was

defined through one material, as illustrated in Figure 3.3(a). Reducing the thresholding range until the triradiate cartilage detection was eliminated, produced the volumetric model shown in Figure 3.3(b) which highlighted the limited development of the innominate bone structure. This was particularly noticeable within the ilium, where there was no defined iliac crest, and indicated the level of reconstruction required to obtain a complete bone geometry.

The right innominate was selected for further modelling as it displayed slightly clearer definition between the bone and soft material (when compared to the left). Using the digitised volumetric model in Figure 3.3(b), the geometry of the ilium, ischium and pubis was manually reconstructed through specifying additional material in the regions of limited cortex development. Careful estimations of the bone exterior had to be made between consecutive slices to ensure the formation of a smooth and rounded bone geometry. All three individual innominate bones required additional material to be specified at the acetabulum, while the pubis and ischium required further reconstruction at the pubis symphysis. The reconstructed bone geometry of the right innominate is shown in Figure 3.3(c).

The cartilaginous acetabulum and pubic symphysis was constructed through defining the remaining grey scale values outside the newly formed bone borders, as a separate material. As illustrated in Figure 3.4, automatic thresholding detected the remaining unassigned grey scale values up to the bone border, enabling classification of a new material. This procedure ensured the bone and cartilage at the acetabulum and pubic symphysis was continuously adjoined, eliminating possible regions of disconnection. This modelling technique constructed the independent innominate bones, and the connecting cartilaginous acetabulum and pubis symphysis (see Figure 3.3(d)).

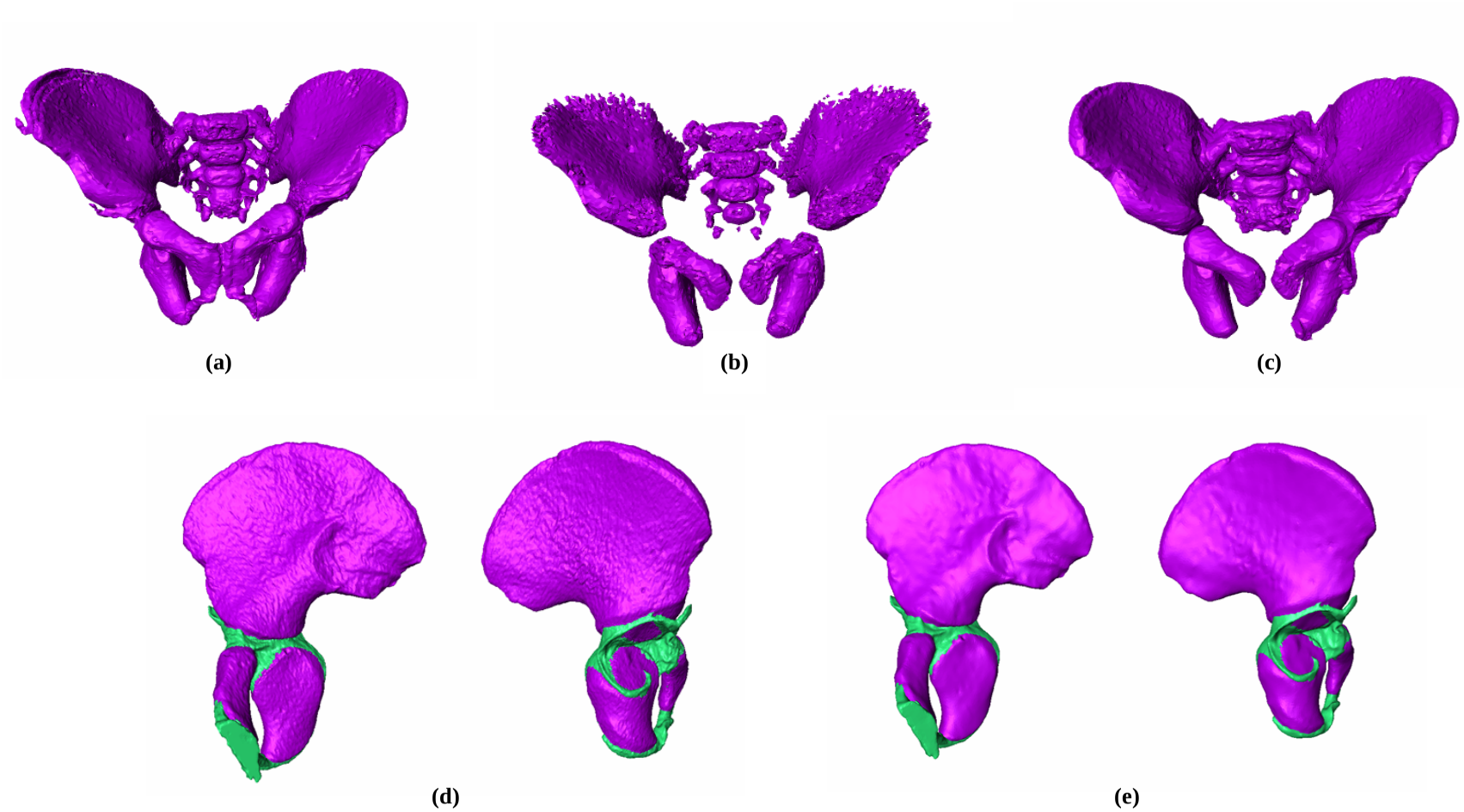

Figure 3.3. Digitised modelling of the right prenatal hemi-pelvis showing; (a) thresholding of all material comprising of both bone and cartilage, (b) reduction of the thresholding range to eliminate cartilage and highlight the limited development of the pelvic bone, (c) reconstruction of the pelvic bone of the right hemi-pelvis, (d) the medial and lateral view of the reconstructed right hemi-pelvis with connecting cartilage (shown in green) (e) and the medial and lateral view of the right hemi-pelvis after smoothing iterations to eliminate blemishes on the bone cortex.

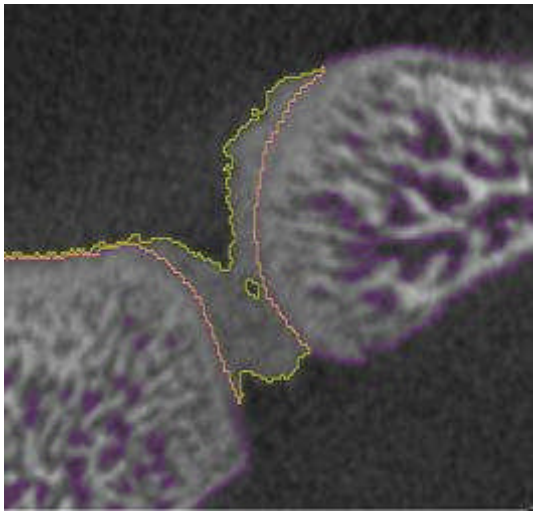

Figure 3.4. Manual segmentation of the pelvic bone border (purple outline) and the thresholding detection and definition of the triradiate cartilage (yellow outline).

The left innominate and sacrum were subsequently segmented and eliminated to produce the volumetric model of the right hemi-pelvis shown in Figure 3.3(d). Although the left-hemi pelvis could be erased through segmentation tools, the sacrum proved difficult as areas of connecting cartilage at the SIJ displayed similar grey scale values to that of the ilium. Consequently, further bone reconstruction of the ilium at the SIJ created a boundary from which the attached cartilage and sacrum could be eliminated. The pubis symphysis was then dissected in the median plane at the midpoint between the two hemi-pelves.

The hemi-pelvic model was completed through filling in the trabecular network to form a solid structure, and removing surface blemishes through a number of smoothing iterations. However, as illustrated in Figure 3.3(e), although the final prenatal model accurately presented the dimensions of the original specimen, the structure was still considered to be incomplete due to the absence of cartilage at the acetabulum. For further use within biomechanical analyses, the complete hemi-pelvic

geometry was required to faithfully replicate the upper body weight transfer through the hip joint.

3.2. 1 YEAR OLD HEMI-PELVIS

A specimen of an estimated 1yr age (P4), comprising of two disarticulated innominates, was selected based on the preservation of its anatomical features. After visual inspection of the specimen, the left innominate was chosen for digitisation, as its condition was considered to be slightly better than that of the right, thus requiring less reconstruction. The disarticulated ilium, ischium and pubis of the left innominate were μCT scanned with slice thicknesses of 0.0639 x 0.0639 x 0.0639mm, 0.0497 x 0.0497 x 0.0497mm and 0.0497 x 0.0497 x 0.0497mm, respectively.

Due to the specimen age, regions of limited cortical development and damage to the developed cortex were present, exposing the underlying trabecular bone. To maintain the integrity of the individual pelvic bones, regions with exposed trabeculae were manually segmented to reconstruct a continuous cortex. Through additional segmentation to fill the internal trabecular structure, solid volumetric models for each hemi-pelvic bone were created, as illustrated in Figure 3.5.

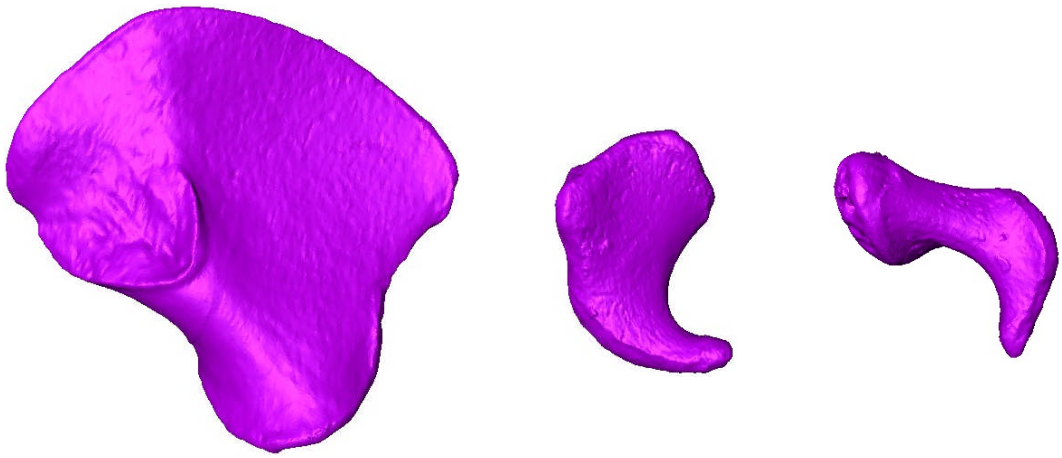

Figure 3.5. Digitised volumetric models of the 1yr old ilium (left), ischium (middle) and pubis (right) after manual segmentation to reconstruct a continuous cortex.

3.3. 8 YEAR OLD HEMI-PELVIS

An 8yr old pelvic specimen (STHB) also comprising of two disarticulated innominates, was μCT scanned with slice thickness of 0.1143 x 0.1143 x 0.1143mm (ilium), 0.1211 x 0.1211x 0.1211mm (ischium) and 0.1088 x 0.1089 x 0.1087mm (pubis). This specimen also displayed evidence of damage to the cortical shell, thus visual inspection was required to evaluate that the left innominate required less reconstruction. After manual reconstruction to repair the breaks in the cortex and fill in the internal trabecular network, solid volumetric models of each constituent bone were constructed, as illustrated in Figure 3.6.

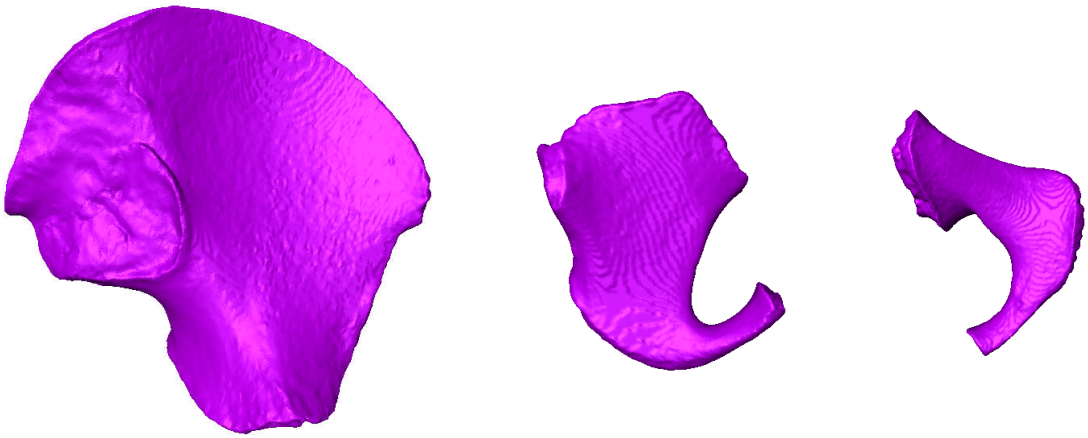

Figure 3.6. Digitised volumetric models of the 8yr old ilium (left), ischium (middle) and pubis (right) after manual segmentation to reconstruct a continuous cortex.

Due to the disarticulation of the pelvic bones shown in Figure 3.5 and Figure 3.6, there was little indication as to their relative anatomical positioning, while the geometry of the connecting cartilaginous material remained unknown. However, biomechanical modelling required the accurate representation of the hemi-pelvic morphology, consisting of articulating pelvic bones connected by cartilage at the acetabulum and obturator foramen. Consequently, a morphometric modelling technique was developed which facilitated the reconstruction of complete hemi-pelvic structures, including the geometry of missing soft tissue (Watson et al., 2011).

3.4. 19 YEAR OLD HEMI-PELVIS

The scan data of a 19yr old pelvis (P17) was supplied by Prof. S Black, Centre for Anatomy and Human Identification, University of Dundee, which comprised of fused innominates. The data was imported to AMIRA as a stack of .DICOM (Digital Imaging and Communication in Medicine) files, and segmented in volumetric models with a slice thickness of 0.488 x 0.488 x 0.25mm.

As shown in Figure 3.7, both innominates displayed damage to the anatomical features of the superior pubic symphysis on the left innominate, and the ASIS on the right innominate. The breaks in the cortex at these areas prevented the infill of the trabecular structure to obtain solid models. Consequently, as the complete hemi-pelvic structure was disrupted, neither hemi-pelves could be considered for further biomechanical modelling in their current form.

In contrast to previous attempts to repair breaks in the pelvic cortex within the other juvenile specimens, reconstruction of these missing anatomical features was more problematic. This was due to their irregular 3D geometries and because there was no indication as to the geometry of the original structure. Therefore, a morphometric modelling technique was required to reconstruct the complete morphology of the 19yr old innominates (Watson et al., 2011).

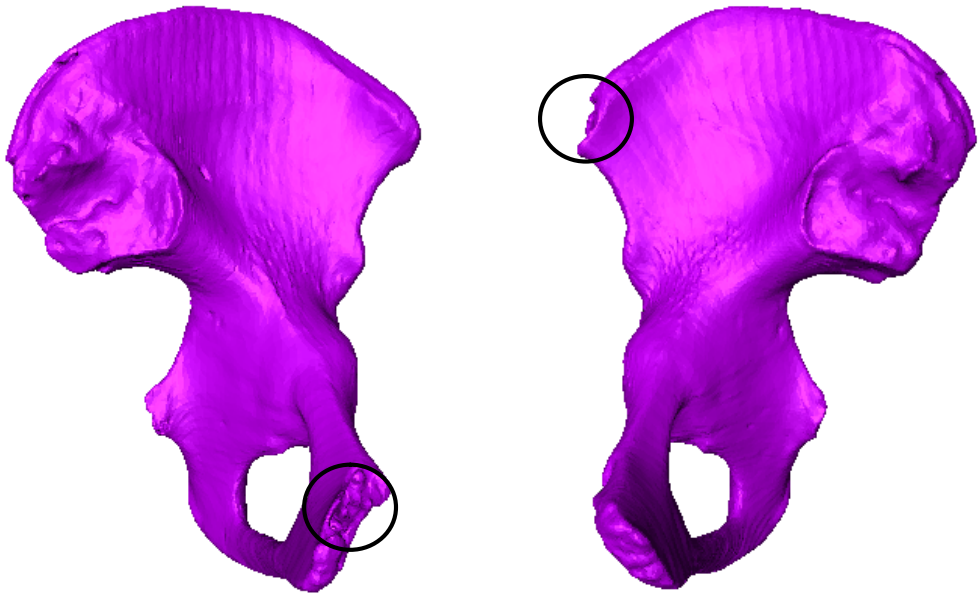

Figure 3.7. Digitised volumetric models of the 19yr left and right innominates, which displayed damage to the right ASIS and left superior pubic symphysis (indicated by the black circles).

4. GEOMETRIC MORPHOMETRIC MODELLING

To aid in the construction of complete hemi-pelvic structures, a morphometric modelling technique was created which estimated the relative positioning of the disarticulated pelvic bones, and the geometry of connecting cartilaginous features (Watson et al., 2011). This technique used GMM (Dryden and Mardia, 1998; O'Higgins, 2000; Zelditch et al., 2004) to facilitate comparison of landmark configurations between forms. Variations among landmark configurations can be represented through the use of thin plate splines (Bookstein, 1987) to warp associated volumes and surfaces. Such methods have been applied to reconstruct bone geometry in instances of damage to archaeological specimens (Benazzi et al., 2009), and where scan data has not captured complete anatomical features (Lapeer and Prager, 2000). This often comprises of warping a specimen without abnormalities to the form of a specimen requiring reconstruction, to determine the geometry of missing anatomical features.

Application of GMM to reconstruct damaged/incomplete specimens is often aided by the knowledge of the geometry to which complete structures are to be warped. This was more challenging when aiming to reconstruct the disarticulated juvenile hemi-pelves, as the exact original articulated forms was unknown. Therefore, a morphometric dataset of pelvic landmark configurations for numerous juvenile ages was used to obtain warped hemi-pelvic geometries. Consequently, the complete hemi-pelvic structure of a disarticulated specimen could be estimated and reconstructed without knowledge of its original articulated form.

The geometric morphometric modelling technique was validated through assessing the accuracy of a reconstructed hemi-pelvis in relation to its originally articulated

form, via morphometric and FE methods. The variance in created warped forms through using different initial complete specimens, was also analysed.

4.1. MODELLING PROCEDURE

The geometric morphometric modelling technique is demonstrated through reconstruction of a 9yr old hemi-pelvis from a state of disarticulation. The general reconstruction procedure can be described in four stages illustrated in Figure 4.1.

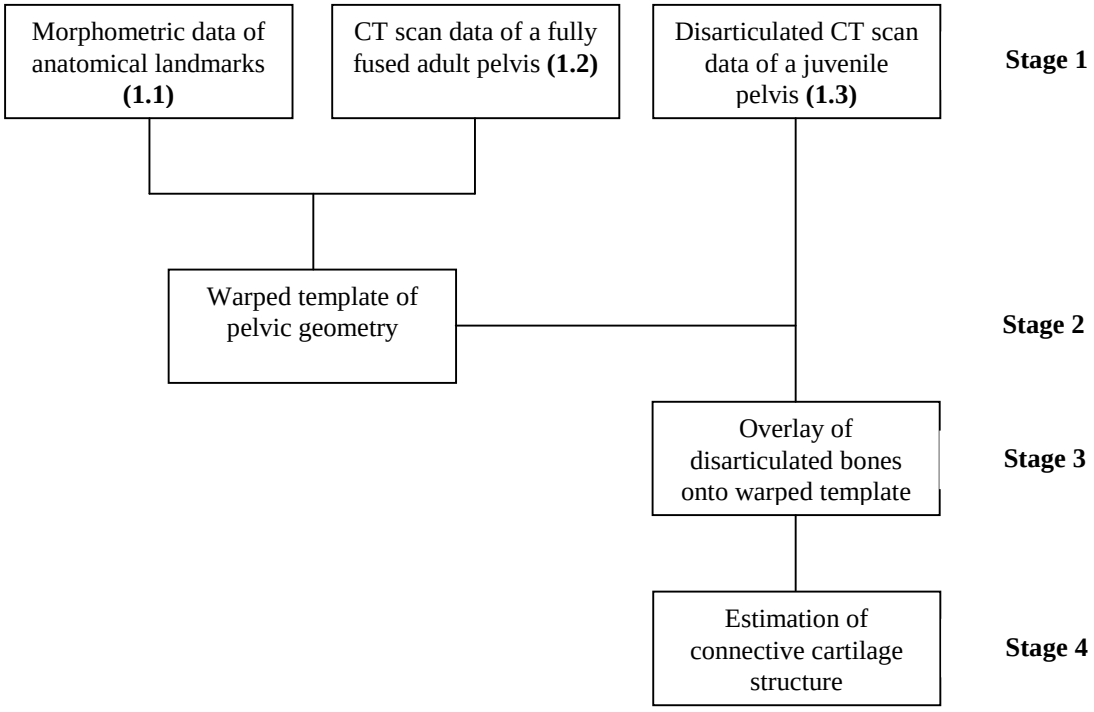

Figure 4.1. Flowchart of the four stages of the morphometric reconstruction modelling procedure.

Stage 1: A morphometric dataset comprising of 27 landmarks (identified on museum specimens; Natural History Museum) was gathered for juvenile pelves (see Table 4.1 and Figure 4.2) spanning infancy to adulthood (Stage 1.1 of Figure 4.1). Landmark configurations were taken from originally disarticulated juvenile specimens, which were manual positioned into a hemi-pelvic configuration as defined by anatomical features (i.e. articulating surfaces of the acetabulum).

Landmark	Anatomical description
1	Midpoint of the iliac crest between the ASIS and PSIS
2	Posterior superior iliac spine (PSIS)
3	Posterior inferior iliac spine (PIIS)
4	Upper (posterior) point of inflexion of the SIJ auricular surface
5	Junction of superior limit of the SIJ and iliac crest
6	Lower (anterior) point of inflexion of the SIJ auricular surface
7	Point of maximal curvature of the greater sciatic notch
8	Ischial spine
9	Anterior superior iliac spine (ASIS)
10	Anterior inferior iliac spine (AIIS)
11	Midpoint of the ilio-pubic ridge as it crosses the pelvic brim
12	Point at which the superior pubic ramus forming the border of the obturator foramen is the thinnest
13	Inferior point on the obturator foramen border closest to the ischial tuberosity
14	Inferior point on the obturator foramen border closest to the pubic symphysis
15	Inferior most point on the pubic symphysis
16	Superior most point on the pubic symphysis
17	Posterior point at maximum width of the pubic symphysis
18	Anterior point at maximum width of the pubic symphysis
19	Midpoint of the ilio-pubic epiphysis on the acetabular rim
20	Point directly opposite the midpoint of acetabular notch on the acetabular rim
21	Midpoint of the ilio-ischial epiphysis on the acetabular rim
22	Deepest central point in the acetabulum
23	Midpoint of the acetabular notch at the ischio-pubic epiphysis
24	Anterior limit of the ischial tuberosity towards the pubis
25	Medial point of the widest diameter of the ischial tuberosity
26	Superior limit of the ischial tuberosity
27	Lateral point of the widest diameter of the ischial tuberosity

Table 4.1. Description of the landmark locations used for the morphometric reconstruction.

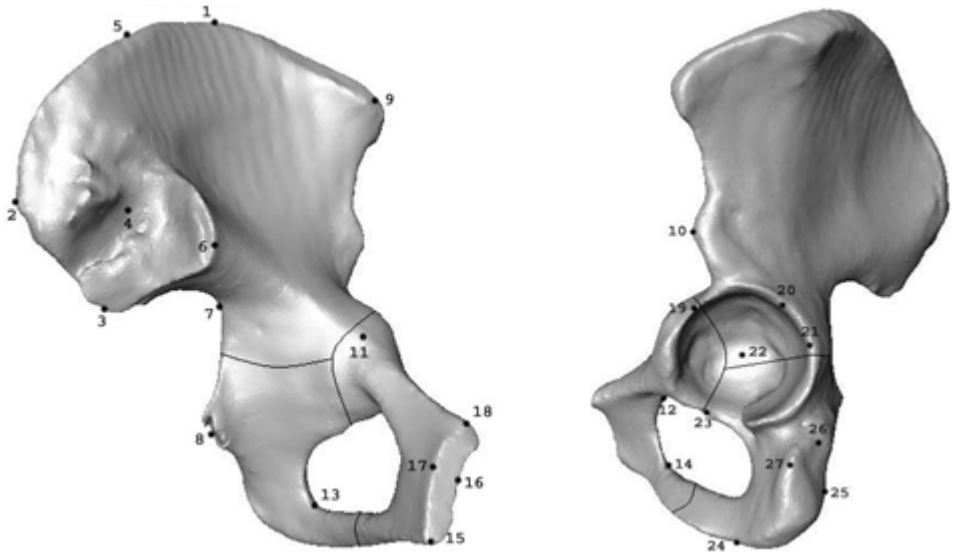

Figure 4.2. Landmark configuration of the morphometric dataset.

The digitised volumetric model of the 19yr old left hemi-pelvis detailed in section 3.4 (after reconstruction of the pubic symphysis (see section 4.6.4)) was selected as an appropriate specimen from which to perform warping (see Figure 4.3(a)). The same landmark configuration displayed in Figure 4.2 was manually defined upon the specimen (Stage 1.2 of Figure 4.1).

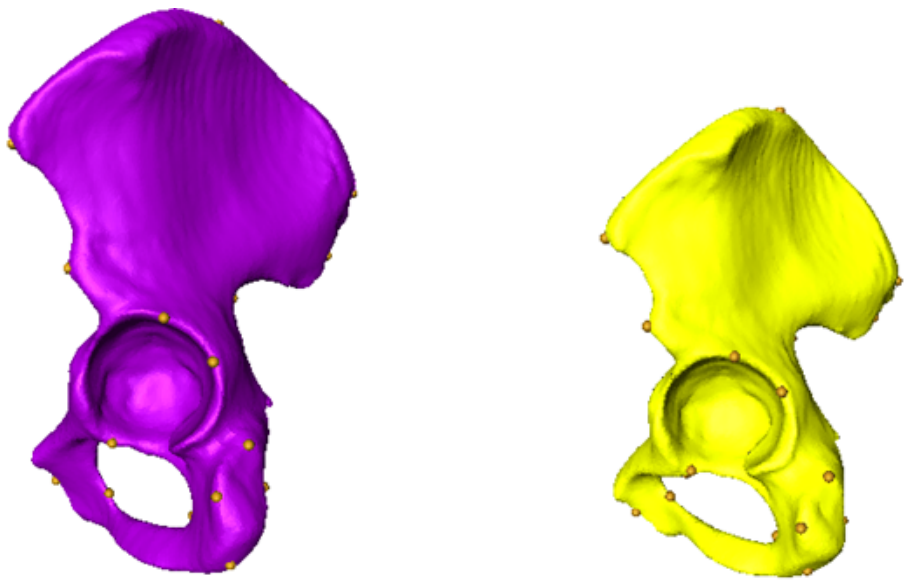

(a) **(b)**

Figure 4.3. Digitised modelling of the (a) 19yr old hemi-pelvis, which was (b) warped to an estimated mean landmark configuration with an iliac depth of 104mm (the spheres show the location of the 27 landmarks used in the morphometric analysis).

Clinical CT scan data of a 9yr old subject which included the pelvis was obtained from the research collection of Medizinische Universität Innsbruck, courtesy of Dr. W Recheis. The pelvis was segmented and a volumetric model of the left hemi-pelvis created in AMIRA with a slice thickness of 4.98 x 4.98 x 2.5mm. The volumetric model included the three bones of the hemi-pelvis, articulated around a thin layer of triradiate cartilage at the acetabulum and obturator foramen, as illustrated in Figure 4.4(a). For the purpose of applying and validating the reconstruction technique, the hemi-pelvic bones were then separated from the connecting cartilaginous material (see Figure 4.4(b)), to obtain disarticulation (Stage 1.3 of Figure 4.1).

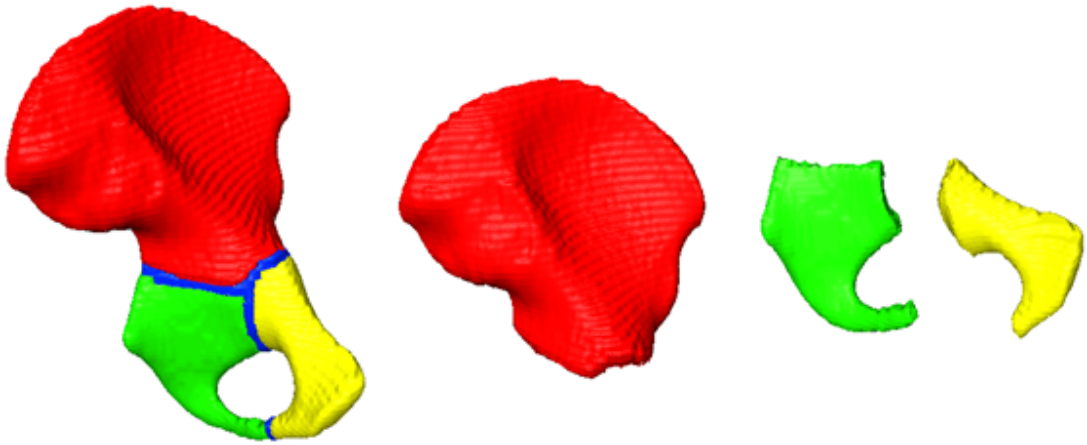

(a) **(b)**

Figure 4.4. Digitisation of the 9yr old left hemi-pelvis showing, (a) the originally articulated structure and (b) the disarticulated bones.

Stage 2: As the original articulated structures of the specimens detailed in Chapter 3 were unknown, warped templates were based upon an anatomical pelvic measurement. The pelvic depth (PD) was selected as a suitable parameter, which was defined as the vectoral distance between the ASIS and PSIS (Kirkwood et al., 1999). This was deemed appropriate as it could be measured from a single disarticulated bone and was determined between two easily identifiable features. The PD could also

be calculated for the specimens within the morphometric dataset, as the iliac spines where within the landmark configuration.

The original morphometric dataset was imported into GMM software Morphologika (O'Higgins and Jones, 1998), where the mean landmark configuration for an individual with a comparative PD (to that of the 9yr old) was estimated using a multivariate regression of Procrustes registered landmark configurations. Warping tools (a triplet of thin plate splines; 'Bookstein' function) within AMIRA were then used to warp the 19yr old hemi-pelvis to fit the form of the estimated landmark configuration (see Figure 4.3(b)). The result was an anatomical estimate of a continuous hemi-pelvic structure to be used as the template for subsequent stages of the reconstruction.

Stage 3: The disarticulated 9yr old hemi-pelvic bones were then manually sited within the warped template to estimate their relative positioning, as shown in Figure 4.5. Due to the age of the disarticulated bones, the ischio-pubic structure was expected to be close to fusion. Therefore, the ischium and pubis were initially positioned within the template with the spacing between the two representing the vertical acetabular flange. The ilium was subsequently positioned relative to this structure, paying particular attention to the ilio-pubic ridge and ilio-ischial and ilio-pubic articular surfaces, where the anterior and posterior acetabular flanges are located.

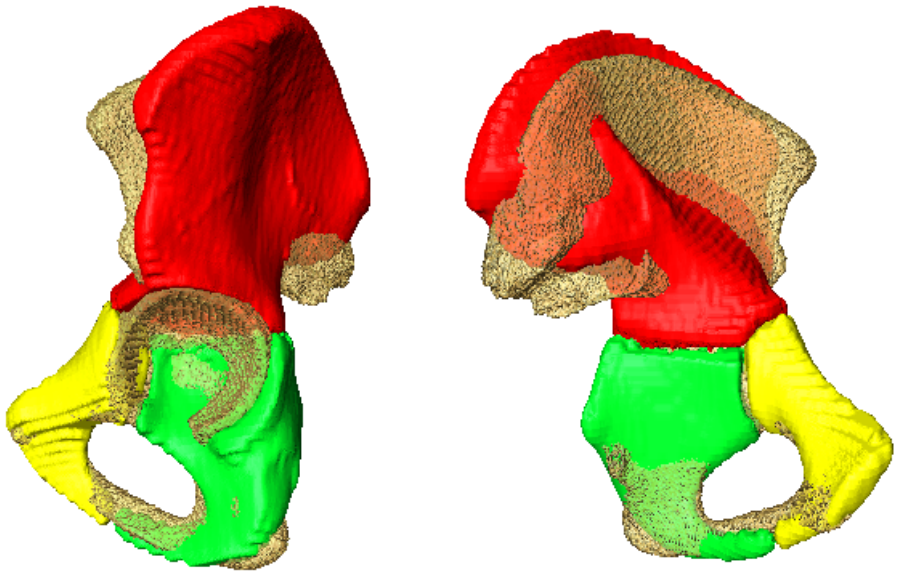

Figure 4.5. Overlay of the disarticulated 9yr old pelvic bones within the warped template.

Stage 4: The reconstruction technique was completed through re-creating the geometry of the connecting cartilaginous material. Using the contours of the template between the gaps of the repositioned bones, the curvature of the posterior, inferior and vertical acetabular flanges were reconstructed to produce a spherical joint (see Figure 4.6). Additional cartilage was defined to adjoin the ischial and pubic rami to complete the obturator foramen.

As illustrated in Figure 4.5, the estimated landmark configuration produced a warped template which was slightly smaller than the disarticulated bones. Therefore, reconstruction of the missing cartilaginous features required manual segmentation to ensure continuity of material between the pelvic bones. In regions where the warped template did not extend to the exterior of the disarticulated bones, additional material was created until it correctly adjoined the disarticulated bones. Similarly, in instances where the warped template protruded beyond the disarticulated bone edge, the contours were cropped until they were in profile.

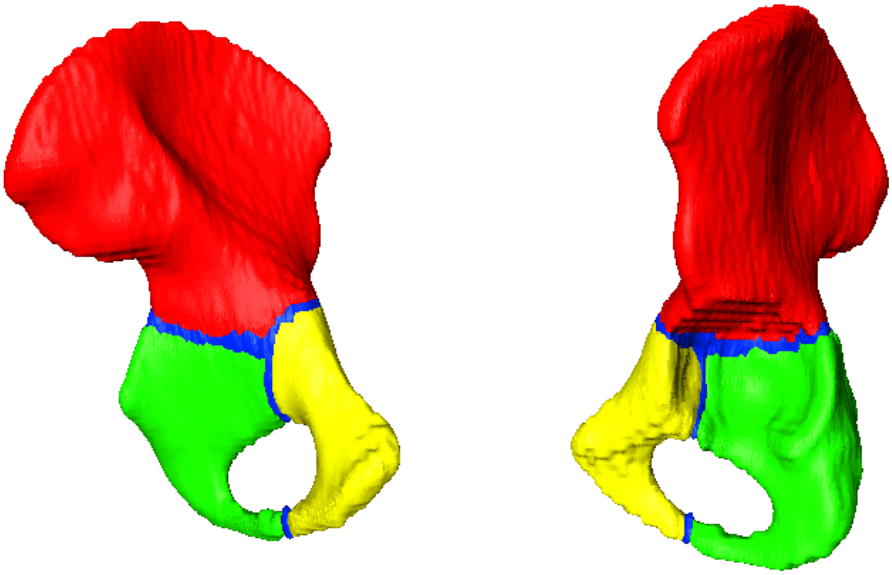

Figure 4.6. The reconstructed 9yr old hemi-pelvis.

4.2. VALIDATION OF THE MODELLING TECHNIQUE THROUGH MORPHOMETRIC METHODS

Validation of the morphometric reconstruction technique was determined by the comparison of the reconstructed 9yr old hemi-pelvic form, to that of the originally articulated CT data. The accuracy was assessed by two methods, firstly through a Principal Component Analysis (PCA) to examine the extent of variation in form, and then through an inter-model overlay to visually identify where geometric deviations occurred.

Initially the landmark configuration shown in Figure 4.2 was identified on both the originally articulated and reconstructed 9yr old hemi-pelves. These forms were then added to the original morphometric dataset (from Stage 1.1 of Figure 4.1) and input into Morphologika, where a multivariate regression analysis was performed to enable comparison between the forms. To observe an accurate reconstruction, the data points of the originally articulated and reconstructed hemi-pelves would be expected to be close to each other along all principal components.

Analysis of the PCA suggested an excellent agreement between the two hemi-pelves along all principal components. Through comparing the positioning between the two in Figure 4.7(a) and Figure 4.7 (b) to that of Figure 4.7(c), it was observed that the accuracy of the reconstruction decreased along the first principal component (PC1). Accuracy along the second principal component (PC2) and third principal component (PC3) was highlighted in Figure 4.7(c), where the originally articulated and reconstructed forms overlaid. However, although the accuracy of the reconstructed model appeared to be close to that of the original articulation, there was a slight difference between the forms. The morphological difference between the 9yr old pelvic bones and the warped template witnessed in Figure 4.5, was also observed within the PCA. This is highlighted in Figure 4.7(a) and Figure 4.7(c) where the warped template is within the data cluster while the reconstructed model falls outside.

The PCA also highlighted that the 9yr old form did not fit the generalised data cluster, particularly along PC1 and PC2. This implied that the landmark configuration of the 9yr old hemi-pelvis was not typical of the juvenile form, as suggested by the original morphometric dataset. A pathological growth could indicate evidence of a possible congenital disorder, such as hip dysplasia. However, visual inspection of the original CT scan did not indicate any presence of abnormalities. This also raised issues concerning the validity of the morphometric dataset, as the 9yr old hemi-pelvis was extracted from CT data, rather than through manual reconstruction of disarticulated bones.

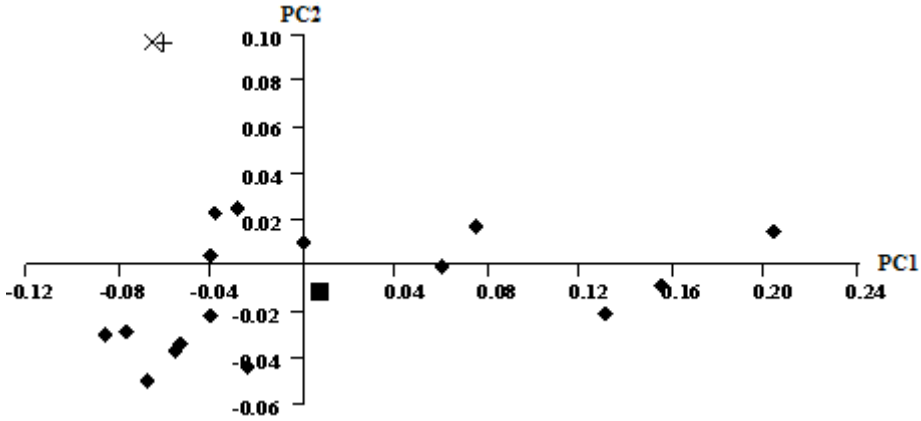

(a)

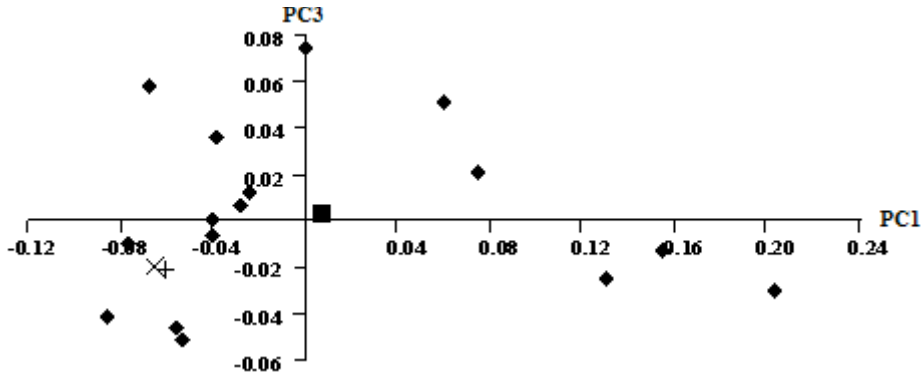

(b)

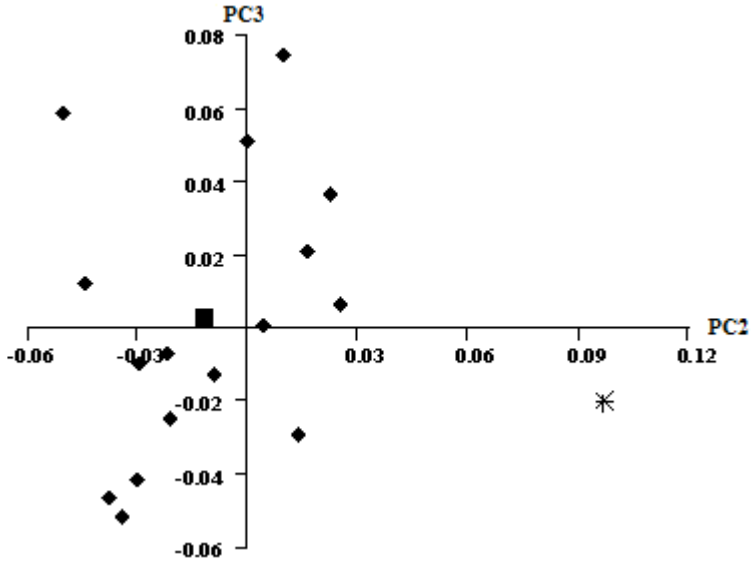

(c)

Figure 4.7. Multivariate regression analysis of the juvenile pelvic form, showing (a) PC1 vs PC2 (b) PC1 vs PC3 (c) PC2 vs PC3 (◆ = original morphometric dataset, ■ = warped template, + = original articulated hemi-pelvis, × = reconstructed hemi-pelvis).

To identify the locations where the original and reconstructed models differed, the ilia of both hemi-pelves were aligned in two planes; one axis defined through a line connecting the ASIS and PSIS; another axis defined between the PSIS and PIIS. Although the overlay shown in Figure 4.8 highlights the close match in form between the two models, the ischium and pubis of the reconstructed model appears to be more laterally rotated. To determine the magnitude of this misplacement, three anatomical features of the ischium (spine, superior symphysis and inferior foramen) and pubis (superior symphysis, inferior symphysis and inferior foramen) were selected based on their ease of manual identification. The vectoral distances between comparative points on both models was subsequently calculated to quantify the error in the reconstructed pelvic bone placement.

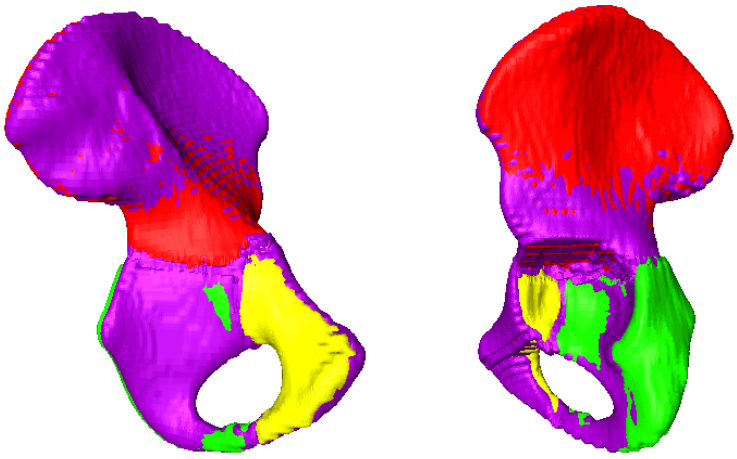

Figure 4.8. Overlay of the original and reconstructed 9yr old hemi-pelvic models through alignment of the ilium (the originally articulated model is shown in purple).

Figure 4.9 shows the extent to which the reconstructed ischium and pubis were misplaced, where the largest error occurred at the superior pubic symphysis, with a misplacement of 2.79mm. However, in relation to overall size of the 9yr old hemi-pelvis, this was found to be only 2.69% of the PD. In contrast, the smallest error was found at the ischial spine where a displacement of 2.22mm was observed (2.14%

PD). The average error in the ischial and pubic landmarks of the reconstructed model was only 2.5mm (2.41% PD), with a SD of 0.2mm.

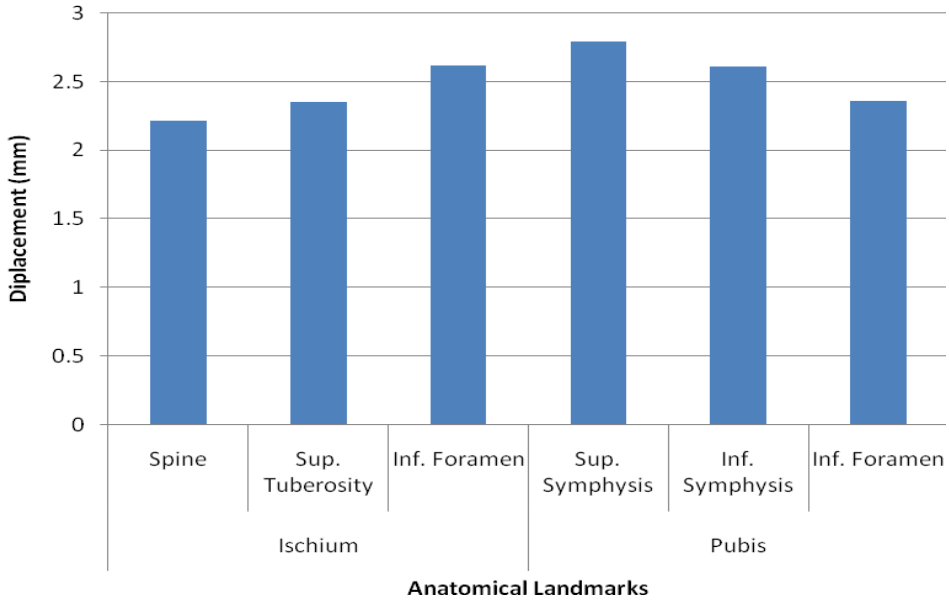

Figure 4.9. Displacement between specific ischial and pubic landmarks on the originally articulated and reconstructed 9yr old hemi-pelves.

The small range between the errors in Figure 4.9 suggested that the relative positioning between the ischium and pubis was close to that of the original. This was examined further through calculating two vectoral distances between the ischium and pubis on both models; one between the superior ischial tuberosity and pubic symphysis; and another between the inferior ischial and pubic foramen. An inter-model comparison of these distances showed that the error in the relative positioning between the reconstructed ischium and pubis was minimal (0.83mm and 0.04mm respectively). Therefore, this implied that it was the alignment of the ilium to the ischio-pubic structure which was slightly inaccurate. Therefore, although the reconstructed model contained a slight variance in the estimated form, the magnitude was minimal.

4.3. VALIDATION OF THE MODELLING TECHNIQUE THROUGH FINITE ELEMENT ANALYSIS

To examine the influence of the slight variation of the reconstructed hemi-pelvic form upon further biomechanical modelling, a series of FE analyses were performed. This aimed to examine possible variations in strain distributions between the originally articulated and reconstructed hemi-pelves when identical loading was applied.

To help quantify the differences observed between the original and reconstructed models, a third comparative hemi-pelvis which contained a greater variance in form, was also modelled. The comparative hemi-pelvis was created through altering the morphology of the reconstructed model, while still maintaining a general physiological form. This was achieved through further laterally rotating the ischio-pubic structure relative to the ilium, and altering the geometry of the connecting cartilage to maintain a complete structure. This procedure served not only to change the morphological form, but also distorted the shape of the acetabulum. The extent to which the comparative model varied from the originally articulated and reconstructed forms was highlighted through a PCA. The PCA of the three models within the pelvic morphometric dataset confirmed that the comparative model had greater variance, particularly along PC2 (see Appendix II).

4.3.1. Model meshing and material properties

The digitised hemi-pelves were converted into polygon surface models within AMIRA, from which 10-noded volumetric tetrahedral meshes were generated to represent the trabecular bone and triradiate cartilage. The tetrahedral element

parameters were adjusted to aspect ratios and tetrahedral qualities suggested by the software, in order to achieve an appropriate mesh quality. The meshes were then imported into ANSYS® (ANSYS, Inc, United States) where 4-noded shell elements (Shell 63) were clad onto the surface of the trabecular bone to represent the cortical exterior. Due to the age of the pelvis, the acetabulum was assumed to be undergoing ossification. Therefore, the interface between the triradiate cartilage and trabecular bone was maintained, so that it was not separated by a cortical shell.

A convergence test was performed to determine an appropriate number of elements to accurately capture the mechanical response of the complex pelvic geometry. A total of 10 meshes which ranged between ~117,000-2 million elements were analysed on the originally articulated hemi-pelvis, through application of identical loading regimes. Comparisons of the von Mises strains at specific anatomical locations concluded that convergence was achieved through a mesh containing ~200,000 elements (see Appendix III). Therefore, the three FE models used during this validation were meshed with ~220,000 elements, as illustrated in Figure 4.10.

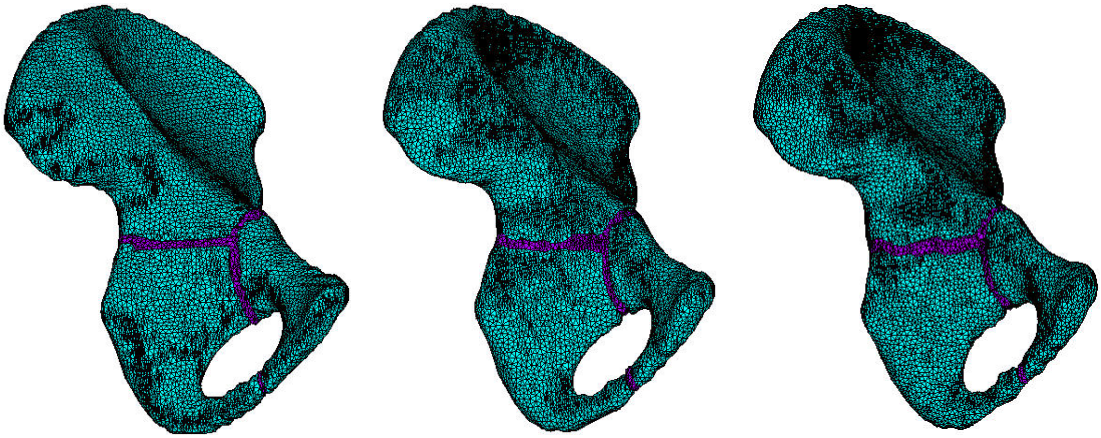

(a) **(b)** **(c)**

Figure 4.10. The FE models of the (a) originally articulated, (b) reconstructed and (c) comparative hemi-pelves, each meshed with total of ~220,000 elements.

Material properties were based on values cited in literature for previous pelvic FE analyses. The trabecular and cortical bone moduli were modelled at 70MPa ($\nu = 0.2$) and 17GPa ($\nu = 0.3$) respectively (Dalstra et al., 1995; Dalstra and Huiskes, 1995; Majumder et al., 2005). Unfortunately, data for the triradiate cartilage modulus is not as easily available, therefore the mid range value for articular cartilage ($E = 5$MPa, $\nu = 0.4$) reported by Anderson et al. (2005) was applied. Although, as the triradiate cartilage is under ossification to produce bone, it is expected to display a higher stiffness then that of articular cartilage. However, the layer of acetabular cartilage was relatively thin, thus the pelvic structural integrity was expected to be maintained even with a low cartilage stiffness.

The morphology of the pelvic cortex could not be determined from the original CT data, consequently a homogeneous thickness was applied to the shell elements. Histomorphometric analyses detailing the morphology of the juvenile pelvic cortex are limited, with the majority of relevant literature examining the thicknesses of biopsies taken from the iliac crest (Glorieux et al., 2000; Parfitt et al., 2000; Rauch et al., 2006; Schnitzler et al., 2009). Such data primarily concerns regions surrounding the ASIS, and thus is unable to provide an indication of the cortical morphology through the whole pelvic structure. However, as the FE models were only intended for validation purposes, it was not considered essential to model an exact cortical morphology. Therefore, data published by Glorieux et al. (2000) was used to apply a homogeneous cortical thickness of 1mm.

4.3.2. Model loading

The hemi-pelves were modelled with five individual loading regimes, aimed at analysing validity under various pelvic strain distributions. Initially, the models were

loaded through a partially physiological loading regime which constrained the SIJ in all DOF, and loaded the acetabulum with hip joint reactions associated with the gait cycle. To obtain differing mechanical responses of the pelvis, four separate hip joint reaction forces experienced during gait (see Figure 4.11) were applied:-

1. Heel strike;
2. Point of maximal reaction;
3. Toe off;
4. Point of minimal reaction.

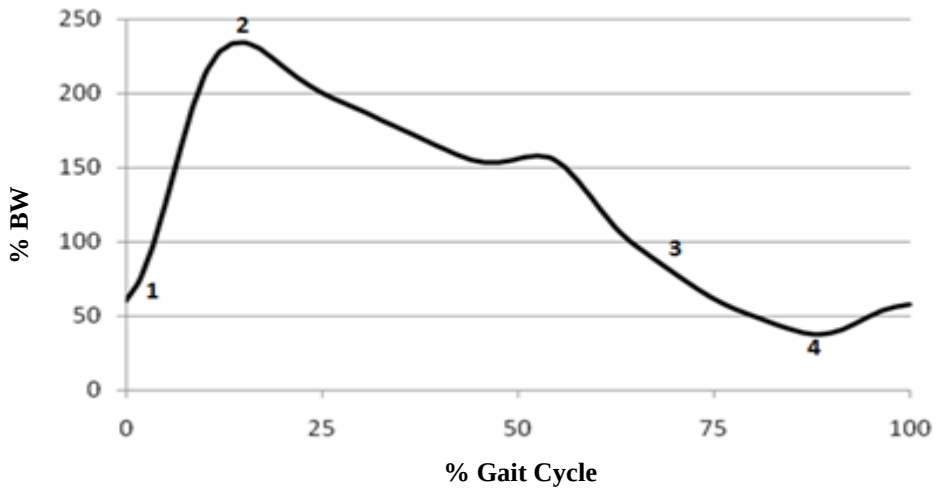

Figure 4.11. The resultant hip joint reaction force of the averaged patient reported by Bergmann et al. (2001) (1 = point of heel strike, 2 = point of maximal force, 3 = point of toe off and 4 = point of minimal force) (data taken from Bergmann et al. (2001)).

Reaction force magnitudes at these phases were taken from the NPA patient calculated by Bergmann et al. (2001), which were expressed as a percentage of BW. The average weight for a 9yr old was taken from growth charts of the Centres for Disease Control and Prevention (CDC) (Ogden et al., 2002), and used to calculate the resultant in terms of Newtons (N). The hip joint loading was then distributed among the nodes of the acetabulum, as performed by Majumder et al. (2005).

A more simplistic loading regime was also applied which comprised of constraining four nodes within the superior ilium (two on the medial side; and two on the lateral side) and applying a negative load on two nodes along the obturator foramen (one towards the pubis and another towards the ischium) (see Figure 4.12). This was designed to contrast from the previous regimes, and aimed to induce a different mechanical response of the pelvis. The total force was assigned an arbitrary magnitude of 12N, which aimed to cause acceptable deformation and induce sufficient strain. Although this total force was lower than those of hip joint reactions, higher magnitudes could cause excessive inferior movement of the obturator foramen due to the low modulus of the acetabular cartilage.

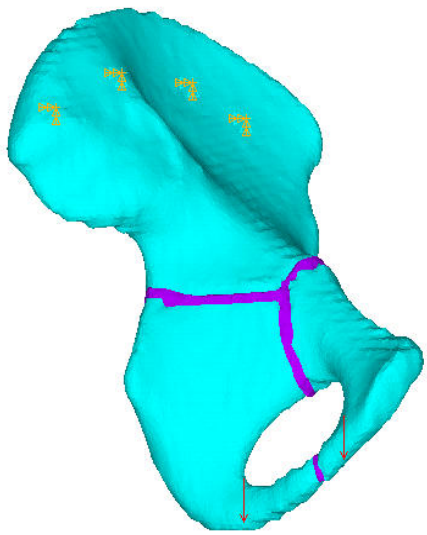

Figure 4.12. The simplistic loading regime which comprised of constraining the superior ilium through four nodes (2 nodes medial; 2 nodes lateral) and loading the obturator foramen through two nodes (one at the point closest to the ischial tuberosity; one at the point closest to the pubic symphysis).

4.3.3. Comparisons between predicted strains

As the morphometric modelling technique was utilised to reconstruct models for the investigation into trabecular bone growth and remodelling, it was considered appropriate to analyse its sensitivity in terms of mechanical strain. As a significant

proportion of the hip joint resultant force was directed superiorly towards the constraints at the iliac crest (see Figure 2.11), the majority of the ilium was placed under compression. Therefore, the mechanical response of the three hemi-pelves were compared in terms of the minimum principal component (i.e. compressive). Although compression within the ischio-pubic region was reduced in comparison, an inter-model variation in the strain distribution was still expected in these regions, due their differing morphologies. For continuity, the simplistic loading regime was also analysed in terms of the minimum principal strain component, despite the hemi-pelves being placed primarily under tension. Variations in strain distributions were made with respect to the originally articulated model.

The triradiate cartilage displayed significantly larger compressive strains in comparison to the trabecular bone, and remained at identical strain states between the different loading regimes (see Figure 4.13). Trabecular strains produced more noticeable inter-model distribution variations, although these were minimal and not consistent between the individual loading regimes. During heel strike there was evidence of strain relieving at the superior ischial tuberosity and medial ischial body (near the vertical acetabular flange), producing an altered distribution, particularly within the comparative hemi-pelvis (see Figure 4.13(a)). However, the changes in strain magnitude within these regions were relatively small in comparison to the magnitudes experienced throughout the structure. The largest variation occurred within the medial body of the ischium, which altered by a maximum of 5400$\mu\varepsilon$.

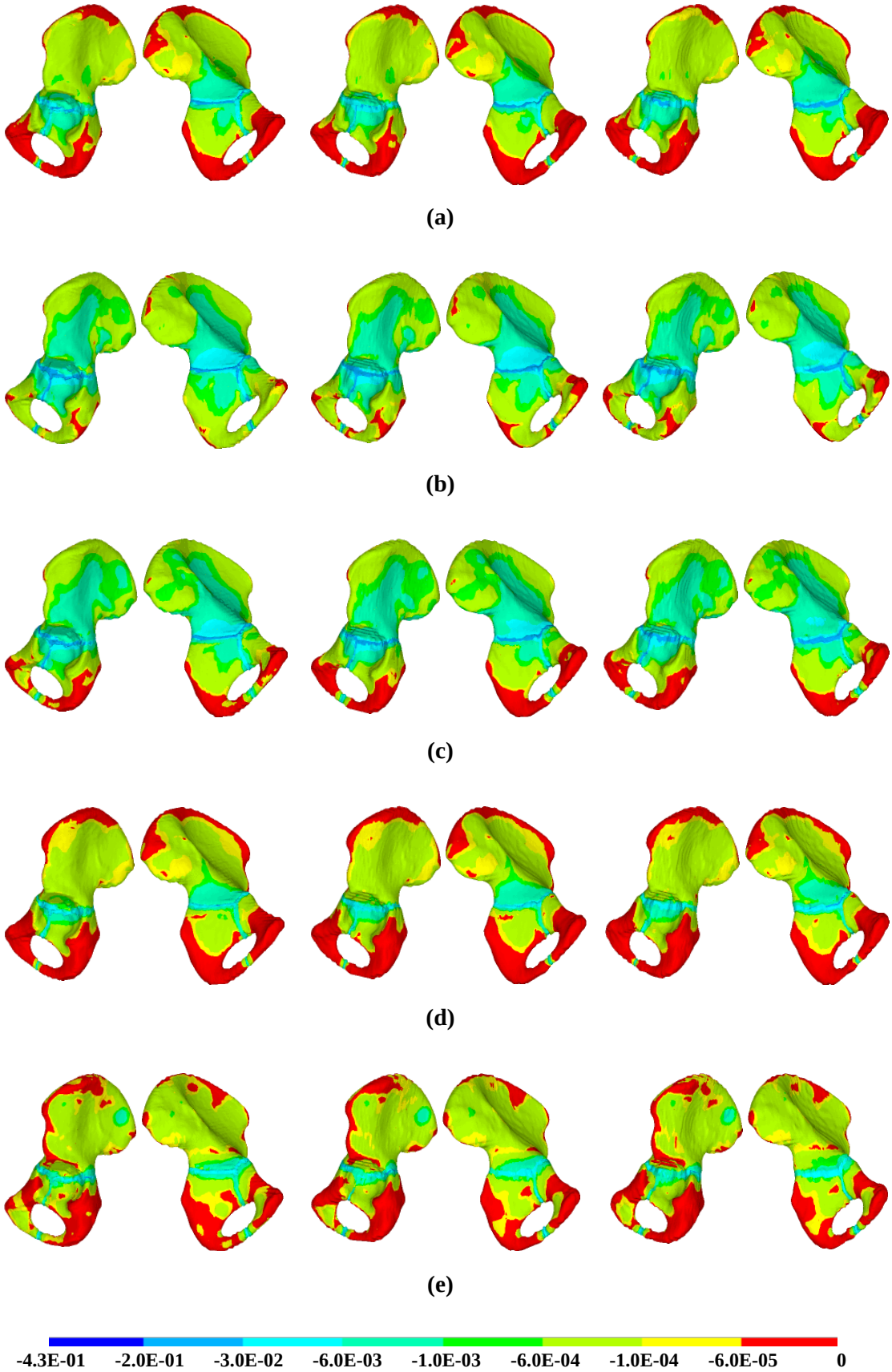

Figure 4.13. The minimum principal strain of the trabecular bone and cartilage for the originally articulated (left), disarticulated (middle) and comparative (right) hemi-pelves under hip joint loading at (a) heel strike, (b) point of maximal force, (c) toe off, (d) point of minimal force and (e) the simplistic loading regime.

The maximal hip joint reaction also caused strain relieving within the reconstructed and comparative hemi-pelves, around the pubic symphysis and the medial ischial body (see Figure 4.13(b)). A similar strain magnitude variation was present within the ischium near the obturator foramen and posterior acetabular flange, which produced a similar maximal deviation to that observed previously. The toe off loading regime produced a similar strain reduction along the superior pubic ramus and the pubic symphysis. However, a strain increase was also witnessed at the superior ischial tuberosity within the reconstructed hemi-pelvis (see Figure 4.13(c)). Although, a maximum increase of 100με was considered relatively small in magnitude. The minimal hip joint reaction produced a close match between the models, with no distinct strain distribution variation (Figure 4.13(d)).

A strain distribution variation was also caused by the simplistic loading regime, where the medial body of the ischium within both the reconstructed and comparative hemi-pelves displayed increased magnitudes (see Figure 4.13(e)). The comparative model displayed a maximal increase of 600με, while the reconstructed model produced an additional strain concentration within the gluteal iliac blade (near one of the constraints), which was not captured by the other models.

Figure 4.14(a) – Figure 4.14(d) showed similar small compressive strain variations within the cortical bone under the partially physiological regimes.

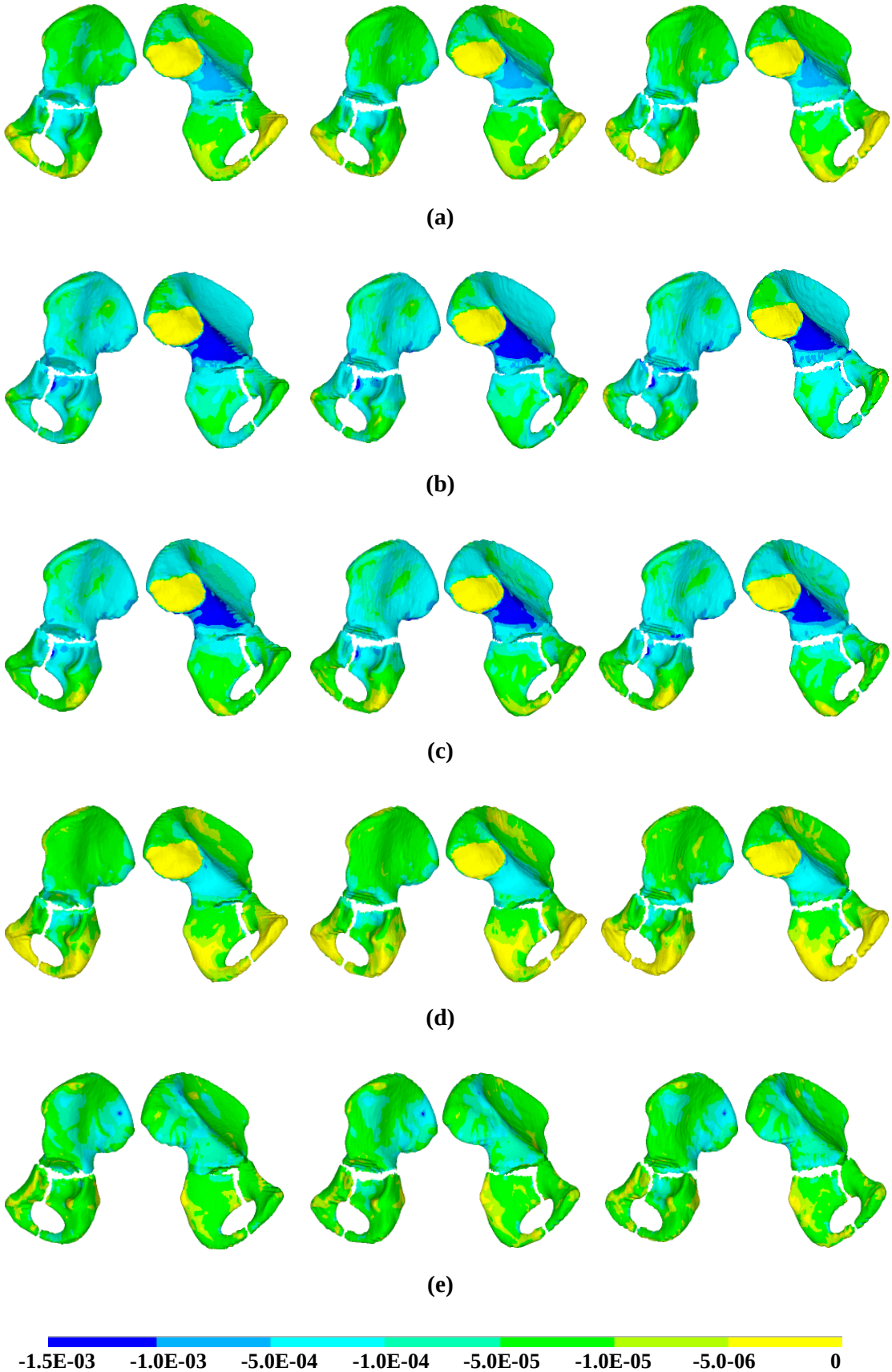

Figure 4.14. The minimum principal strain of the cortical bone for the originally articulated (left), disarticulated (middle) and comparative (right) hemi-pelves under hip joint loading at (a) heel strike, (b) point of maximal force, (c) toe off, (d) point of minimal force and (e) the simplistic loading regime.

The heel strike loading regime produced the greatest inter-model strain variation between the reconstructed and comparative hemi-pelves (see Figure 4.14(a)). The reconstructed model showed slight strain relieving within the medial ischial body, while the comparative hemi-pelvis produced lower strains in the ischial tuberosity. The comparative hemi-pelvis also displayed localised strain decreases within the lateral iliac blade (see Figure 4.14(a)), although the magnitudes were lower than associated with trabecular bone, differing by a maximum of 45με. Inter-model variations when applying maximal hip joint reaction and toe off loading were similar, producing slightly higher strains within the medial body of the ischium, and slightly relieving the pubic symphysis. As illustrated in Figure 4.14(b) and Figure (c), the comparative model produced the greatest deviation from that of the originally articulated model. As observed previously within the trabecular bone, no significant strain variation was caused through the minimal hip joint reaction force (see Figure 4.14(d)).

The simplistic loading regime produced the most uniform strain magnitudes throughout the cortical structure (see Figure 4.14(e)). Minimal inter-model variation was observed, although there was slight strain relieving within the ischial body for both the reconstructed and comparative hemi-pelves (see Figure 4.14(e)). However, the magnitudes of these strain reductions remained fairly small, varying by a maximum of 45με.

As illustrated in Figure 4.13 and Figure 4.14 the majority of the inter-model strain variation occurred within the lower strain ischium and pubis. In comparison, the higher strain ilium displayed less noticeable inter-model variation throughout the various loading regimes.

To quantify the inter-model strain distribution variation, comparative nodes were selected on each model, consisting of 7 iliac points (ASIS and 5 locations within the iliac fossa), 3 ischial points (ischial spine, superior ischial tuberosity and posterior obturator foramen) and 3 pubic points (superior pubic symphysis, inferior pubic symphysis and posterior obturator foramen). For the simplistically loaded models, two additional iliac points were selected (PSIS and PIIS) and the points along the obturator foramen were omitted. The ischial and pubic nodes locations were selected based on regions where large inter-model variation was observed, and due to their ease of identification.

The difference between the nodal von Mises strains of the reconstructed and comparative models to those produced by the original articulation, was analysed through a linear regression. Minimal deviation in the strain values of the two models was expected to be reflected through R^2 values within a 95% confidence interval. To eliminate possible inclusion of anomalous data, an average von Mises strain was calculated for each location using the nodes which encompassed the coordinate for each point.

The R^2 values produced by the linear regression of the trabecular nodal strains within the reconstructed and comparative hemi-pelves are shown in Table 4.2. A single regression performed on all nodes throughout the pelvic structure calculated that strains of both models were within a 95% confidence interval of the originally articulated hemi-pelvis (apart from the comparative model during heel strike). However, such observations were made with respect to the range of strain magnitudes experienced throughout the hemi-pelvis (see Figure 4.13). As this does not ascertain the inaccuracy within the individual bones, separate regressions were performed on the iliac, ischial and pubic nodes (see Table 4.2). Generally, the

reconstructed model produced a closer correlation to that of the original articulation. The iliac nodes for both models produced the highest R^2 values, while the pubis generated the largest level of variance. The pubic nodes of the reconstructed model under the point of maximal hip joint loading generated the lowest R^2 value (0.04), suggesting no correlation to the strains of the original articulation. In contrast, the comparative model displayed a significantly higher correlation ($R^2 = 0.99$) under the same loading. The simplistic loading regime produced the highest level of correlation for both models, with only the iliac nodes falling below the confidence limit, although the regression values still remained high ($R^2 = 0.94$).

	Complete Pelvic Structure		Ilium		Ischium		Pubis	
	REC	COM	REC	COM	REC	COM	REC	COM
Heel Strike	0.99	0.90	0.97	0.77	0.96	0.89	0.72	0.63
Point of Maximum Force	0.99	0.96	0.98	0.94	0.97	0.91	0.04	0.99
Toe Off	0.99	0.96	0.98	0.92	1	0.86	0.68	0.66
Point of Minimum Force	0.99	0.95	0.98	0.86	0.97	0.48	0.99	0.64
Simplistic Loading	0.97	0.97	0.94	0.94	0.99	0.99	0.99	0.98

Table 4.2. The R^2 values of the trabecular nodal von Mises strains produced by a regression analysis of the reconstructed (REC) and comparative (COM) hemi-pelves with respect to the originally articulated hemi-pelvis (values in red indicate instances which were below a 95% confidence interval).

A closer correlation of the reconstructed and comparative hemi-pelves was observed within the nodal strains of the cortical bone (see Table 4.3). Once again, the greatest

accuracy was observed within the iliac nodes, where both models fell within the confidence interval under the partially physiological loading regimes. The low level of correlation between the pubic nodal strains observed in Table 4.2, significantly increased within the cortical bone. Consequently, only the maximum hip joint loading caused an R^2 value below the confidence limit in the reconstructed model (see Table 4.3). In contrast to previous observations, the simplistic loading regime produced the greatest variability within the two models, with only the iliac and pubic nodal strains of the reconstructed model within the confidence limit.

	Complete Pelvic Structure		Ilium		Ischium		Pubis	
	REC	COM	REC	COM	REC	COM	REC	COM
Heel Strike	0.99	0.98	0.98	0.99	0.99	0.81	0.99	0.81
Point of Maximum Force	0.99	0.97	0.99	0.98	0.88	0.85	0.98	0.99
Toe Off	0.99	0.99	0.99	0.99	0.97	0.65	0.97	0.90
Point of Minimum Force	0.99	0.99	0.99	0.99	0.99	0.99	0.91	0.83
Simplistic Loading	0.94	0.89	0.98	0.86	0.80	0.86	0.99	0.88

Table 4.3. The R^2 values of the cortical nodal von Mises strains produced by a regression analysis of the reconstructed (REC) and comparative (COM) hemi-pelves with respect to the originally articulated hemi-pelvis (values in red indicate instances which fall outside the 95% confidence interval).

4.4. SENSITIVITY OF THE WARPING PROCEDURE

Due to the irregular shape of the pelvis, varying morphologies can be witnessed among different subjects, particularly between males and females (Patriquin et al.,

2003). Therefore, further validation was required to observe if this variance in morphology was maintained throughout the warping process, thus producing hemi-pelvic templates which differ from the required estimated form. As the relative positioning of disarticulated bones is reliant on the warped templates, any inaccuracies in their morphology could have a significant effect on the reconstructed models.

Through warping a number of adult pelves to the same landmark configuration, the variance in warped morphology was examined. As the relative positioning of disarticulated bones is primarily based on the warped geometry of the acetabulum and obturator foramen, the geometric divergence of these features was analysed.

4.4.1. Warping of varying adult hemi-pelves

Scan data of eight hemi-pelves of mixed age and sex were obtained from various sources (six courtesy of Prof. S Black, Centre for Anatomy and Human Identification, University of Dundee; one from the Vakhum Project (van Sint Jan, 2001); one from anonymous scan data). The hemi-pelvic data supplied by the University of Dundee was taken from 3 individual pelves. Digitised volumetric models of each hemi-pelvis were created within AMIRA and concluded to have no clear abnormalities after visual inspection. The hemi-pelves were then warped to the three different landmark configurations illustrated in Figure 4.15:-

1. The form of an adult (landmark configuration of one of the existing hemi-pelves);
2. The form of a 9yr old (landmark configuration taken from the 9yr old hemi-pelvis used previously);

3. A juvenile form with a PD of 90mm (estimated landmark configuration taken from a regression analysis of the original morphometric dataset).

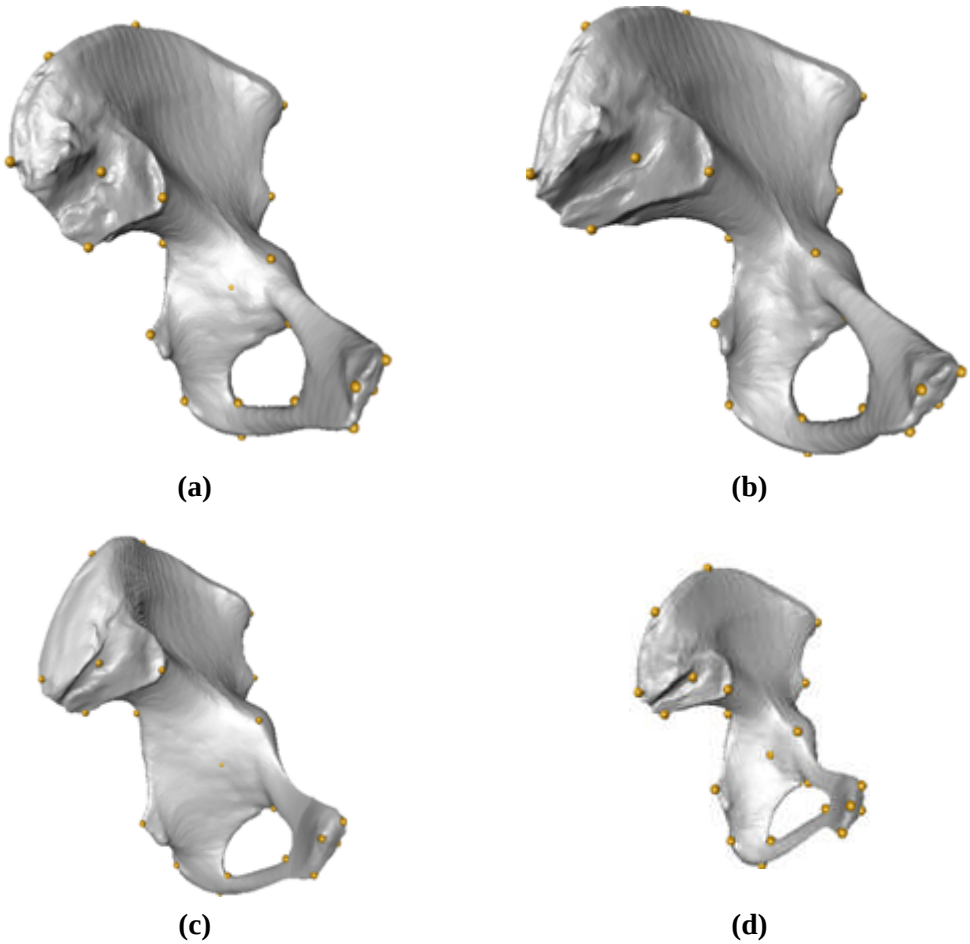

Figure 4.15. Morphometric warping of a (a) 19yr old hemi-pelvis to the morphologies of (b) another adult, (c) a 9yr old and (d) a juvenile with a PD of 90mm.

To examine the morphology of each warped template, 10 landmarks were manually defined around the acetabulum and obturator foramen, as shown in Figure 4.16. The configurations of the acetabular and obturator foramen landmarks for each warped hemi-pelvis were then pooled and analysed through a PCA within Morphologika. This aimed to determine if there was any significant statistical difference between the landmark configurations.

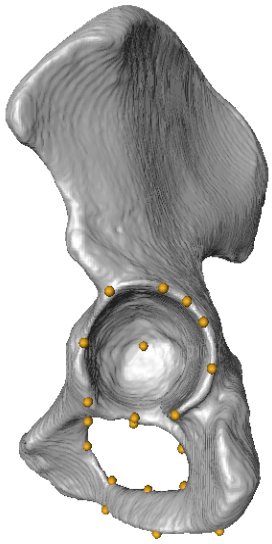

Figure 4.16. Positioning of the 10 landmarks around the acetabulum and obturator foramen of the warped hemi-pelves.

4.4.2. Principal component analysis of the warped landmark configurations

The PCA results of the acetabular and obturator landmark configurations are shown in Figure 4.17, where it was observed that the warped adult and 9yr old forms all had p values of above 0.05 (determined to be the limit of statistical significance). The statistical difference of all the warped morphologies significantly decreased along PC2, although the warped adult and 9yr old forms were still above the significance limit. The only significant statistical difference was observed for PC2 of the warped juvenile forms ($p = 0.008$), however all the remaining principal components displayed larger p values. As illustrated in Figure 4.17, the largest overall statistical difference in the morphologies was observed when warping to the 9yr old form.

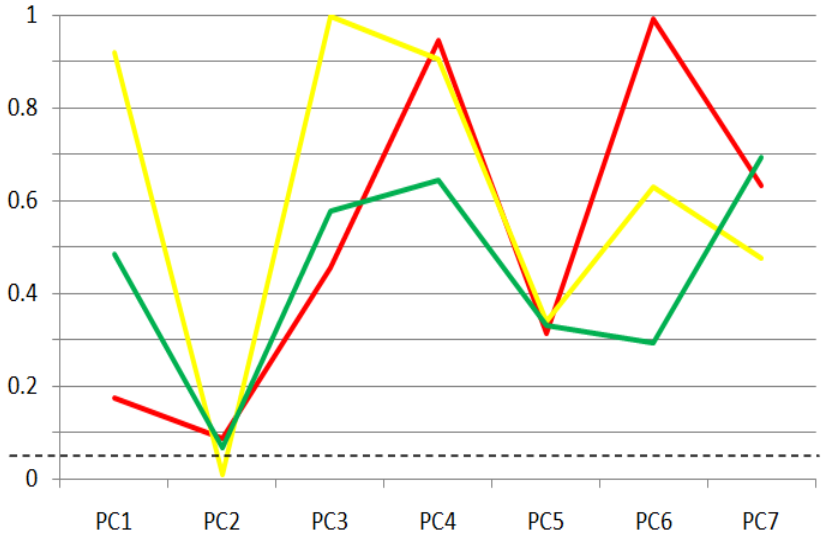

Figure 4.17. The p values of the PCA analysis of the warped adult (red), 9yr old (green) and juvenile (yellow) forms (the dotted line indicates a p value 0.05% where statistical difference was determined).

4.5. VALIDITY OF THE RECONSTRUCTION TECHNIQUE

A PCA displayed that the reconstructed 9yr old hemi-pelvis contained a similar morphology to that of the original articulation, as illustrated through the close proximity of their data points in Figure 4.7. Although the accuracy of the reconstruction decreased along PC1, this was suggested to be caused by the misplacement of the ilium relative to the ischio-pubic structure, as shown by the more laterally rotated obturator foramen in Figure 4.8. However, due to the observations of the PCA and the calculated misplacement errors in Figure 4.9, the magnitude of the slight inaccuracy of the reconstructed hemi-pelvis was considered to be minimal.

Figure 4.7 also highlighted the contrast in forms between the reconstructed hemi-pelvis and the warped template along all principal components. This morphological difference is visually evident in Figure 4.5, suggesting that reconstructions which are based solely on the warped template geometry, may produce greater morphological inaccuracies. This underlined the importance of identifying and correctly aligning

anatomical features such as the ilio-ischial, ilio-pubic and ischio-pubic articulation sites, to maintain physiological re-articulations.

The integrity of the warped template was governed by the accuracy of manually defining landmarks on the adult pelvis, and the estimated landmark configuration created from the morphometric dataset. Therefore, meticulous attention was paid to manually position the landmarks in accordance to the morphometric configuration of Figure 4.2. Accuracy could have been increased further through the application of additional landmarks, although their feasibility was limited by the fact that the bony features of adult pelves are not always identifiable on juvenile geometries. Determination of accurate landmark positioning was evaluated through the form of the warped template produced via the morphometrics. Generation of a warped template which displayed significant distortion of the generalised pelvic morphology, suggested refinement of the defined landmark configuration. As re-articulation and estimation of the connecting cartilaginous geometry was dependent on the shape of the acetabulum and obturator foramen, these features of the warped template were visually assessed. As illustrated in Figure 4.3(b), the morphologies of the warped acetabulum and obturator foramen were observed to maintain a physiological shape.

The reconstruction of the hemi-pelvic bone alignment and cartilaginous geometry was susceptible to operator variance. Unfortunately, as the reconstruction was a laborious activity, comparing the results from a range of operators would have proved to be prohibitively time-consuming. However, as the reconstruction process relied not only on the warped template but also through anatomical features, the operator variance was expected to be minimised.

Comparisons between the originally articulated and reconstructed hemi-pelves were made with respect to the manually defined anatomical landmarks. Determination of the exact positioning of anatomical features is often subject to the quality of the CT scan resolution and personal interpretation. Consequently, landmarks defined during the inter-model validation process were selected based on their ease of identification.

The influence of the slight variation in the reconstructed morphology upon FE strains was observed to be minimal. Constraining the SIJ in all DOF and applying hip joint loading through the acetabulum, produced only small differences in compressive strain distributions between the originally articulated and reconstructed hemi-pelves. Figure 4.13 and Figure 4.14 displayed that the strain distribution variations mainly occurred within the ischium and pubis, which were generally the lowest strained regions of the hemi-pelvis. In comparison, the regions of high strain concentrated within the ilium, did not display any noticeable inter-model variation. Strain variations caused by the different loading regimes were not found to be consistent between trabecular and cortical bone. The simplistic loading regime also produced negligible inter-model strain distribution variation, despite drastically altering the mechanical response of the hemi-pelvis. Consequently, as the magnitudes of the strain distribution variances were generally minimal (although a maximum variation of 5400με was observed), the slight variation of the reconstructed morphology was concluded to cause an insignificant affect upon FE modelling.

Strain distributions of the comparative model were also observed to be close to that of the original articulation, albeit not as accurate as the reconstructed hemi-pelvis. Therefore, despite a significant variation in the hemi-pelvic morphology, the mechanical response was comparable to that of the actual physiological form. Although this could suggest that the morphology of the comparative model may not

deviate too far from the original hemi-pelvis, the PCA analysis in Appendix II did confirm a variance in form.

The linear regression values shown in Table 4.2 and Table 4.3, confirmed that the reconstructed hemi-pelvis contained a greater accuracy than the comparative model. The majority of the trabecular nodal von Mises strains for the reconstructed model showed a close correlation to that of the original articulation, apart from the pubic nodes under the partial physiological regimes. In general, the cortical nodal von Mises strains displayed an increased correlation to those of the original articulation, particularly within the comparative model. The slight strain distribution variation within the ischium and pubis observed in Figure 4.13 and Figure 4.14 was also highlighted in the linear regressions. However, although the R^2 values in Table 4.2 suggested a large deviation of the nodal pubic strains, the relative inter-model variance was low in magnitude. The low regression values could have been an artefact of the nodal location being on curved surfaces, thus producing possible anomalous results. In comparison, the majority of the more accurate iliac nodes were situated on the relatively flat surface of the iliac fossa. This could imply the use of an inadequate mesh quality, however the regression values for the cortical bone displayed a significantly increased linearisation for all the hemi-pelvic bones. Therefore, the low correlation of the reconstructed pubic and ischial nodal trabecular strains were considered acceptable, but only with respect to the low strain magnitudes they recorded.

Although the magnitudes of the slight inter-model strain distributions were concluded to be minimal, it was recognised that only a limited level of loading complexity had been applied. Although transfer of the hip joint reaction force varied in all three models due to the distorted acetabular geometries, it would have been

more thorough to define complete physiological loading with muscle forces. For example, the contraction of the obturator externus and internus may have altered strain distributions around the obturator foramen. However, to maintain the integrity of any validation study, identical loading regimes must be applied to all models. Ensuring that muscular attachment areas were consistent between all hemi-pelves would have proved problematic and susceptible to inconsistencies. Therefore, when quantifying inter-model strain distribution variations it would have been impossible to discard deviations in muscle mapping. To eliminate this scenario, only hip joint loading was applied, which also enabled inter-model variation while the hemi-pelvis was under the highest strain distribution, as inclusion of muscles is shown to stress relieve the structure (Dalstra and Huiskes, 1995). This was considered to increase the possibility of detecting the strain distribution variations.

Warping of differing adult specimens to the same landmark configuration produced hemi-pelvic templates which did not vary significantly in terms of the acetabular and obturator foramen morphologies (see Figure 4.17). Although the form of the ilium may have varied more than that of the ischium and pubis, the accuracy of the superior hemi-pelvis was not considered imperative to reconstruction process. As the disarticulated ilium was positioned relative to the ischium and pubis once sited within the template, the iliac form of the warped hemi-pelvis was not completely followed during the reconstruction process (see Figure 4.5).

Evaluation of the warped morphologies could have been enhanced through definition of additional landmarks across the whole hemi-pelvic structure. However, this would have involved definition of anatomical features which are not easily identifiable, such as locations along the iliac crest and fossa. Therefore, incorporation of a landmark configuration with increased complexity would have made it difficult to maintain

continuity within the analysed dataset. Due to the statistical insignificance between the warped acetabular and obturator foramen geometries (see Figure 4.17), it was predicted that reconstructions created from the differing warped templates would not contain drastic morphometric discontinuities. Small deviations which may have occurred are likely to be in the order of magnitude witnessed in Section 4.1, which as further examination showed, does not influence FE results to any substantial extent. Consequently, creating warped templates from landmark configurations based on other specimens and multi-variant regression analyses, was concluded to be a valid method.

4.6. APPLICATION TO THE JUVENILE HEMI-PELVES

The morphometric reconstruction method was directly applied to create complete hemi-pelvic structures from the disarticulated bones of the 1yr and 8yr old innominates. The principle methods of the reconstruction technique were also used to reconstruct the missing cartilaginous material of the prenatal acetabulum and the damaged anatomical features of the 19yr old pelvis.

4.6.1. Reconstruction of the prenatal hemi-pelvis

A warped hemi-pelvic template was created to aid in the estimation of the geometry of the absent acetabular cartilaginous features. As the general hemi-pelvic morphology of the specimen could be retrieved from the μCT scan data (see Figure 3.1(a)), a warped template was created using a landmark configuration taken from the original volumetric model (see Figure 4.18(a)). A custom configuration was created which was based on that of the morphometric dataset (see Figure 4.2), although additional landmarks were identified around the acetabulum to fully morph the

template to an appropriate shape. A total of 34 anatomical landmarks were manually defined on both the prenatal and reconstructed 19yr left hemi-pelvis (see section 4.6.4), and used to create a warped template within AMIRA. As the 19yr old left hemi-pelvis was warped to the landmark locations of the prenatal specimen, the created template automatically overlaid the original model.

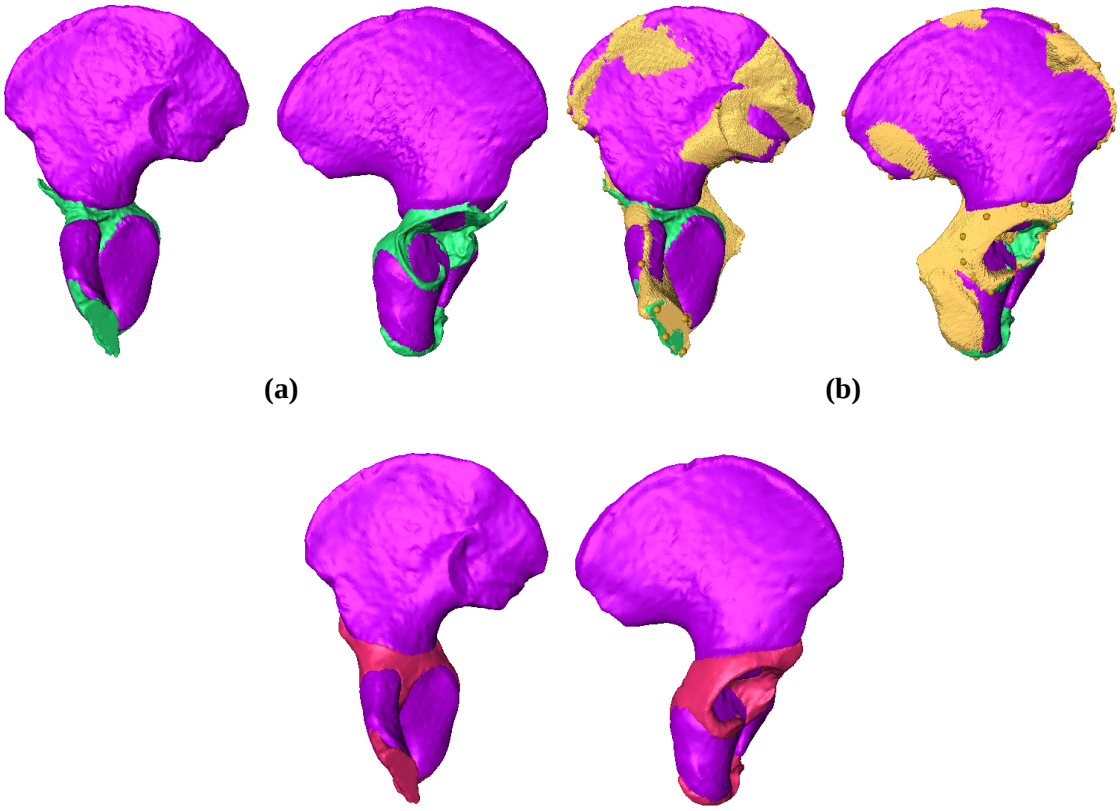

Figure 4.18. Procedure for reconstructing the cartilaginous prenatal acetabulum, showing (a) the original volumetric model, (b) overlay of the warped template to estimate the missing cartilage, and (c) the final reconstructed hemi-pelvis.

As illustrated in Figure 4.18(b), the warped template displayed a similar morphology to that of the prenatal hemi-pelvis, and highlighted the complete formation of the cartilaginous acetabulum. Through merging the individual models within AMIRA, the contours of the warped template in the regions which required reconstruction were indentified. The warped template was cropped to the boundary of the

acetabulum to focus solely on the cartilaginous features, and then merged to the prenatal hemi-pelvis. As the geometry of the warped acetabulum was not fully continuous with that of the original model (evident in Figure 4.18(b)), further manual segmentation was required to reconstruct the absent cartilage. Additional cartilage was also defined within the ilio-ischial, ilio-pubic and ischio-pubic articulations, and the volumes smoothed to produce the final reconstructed prenatal hemi-pelvis shown in Figure 4.18(c).

4.6.2. Reconstruction of the 1 year old hemi-pelvis

The morphometric reconstruction technique was subsequently applied to re-articulate the 1yr old hemi-pelvic bones, and estimate the geometry of the connecting cartilaginous features. Due to the disarticulation of the original specimen, a warped template was created based upon an estimated hemi-pelvic form with a comparative PD. After measuring the PD to be 62mm, an estimated landmark configuration was created through performing a multivariate regression of the morphometric dataset in Morphologika. This configuration was then used to warp the reconstructed 19yr left hemi-pelvis (see section 4.6.4) to the estimated juvenile form within AMIRA.

The disarticulated bones were sited within the template through initially aligning the ischio-pubic structure, and then relatively positioning the ilium to the ilio-ischial and ilio-pubic articulation sites (see Figure 4.19(a)). As the warped template was based on an estimated landmark configuration, its size was larger than those of the re-articulated bones. Therefore, using the warped template in its current form to estimate the geometry of the missing cartilaginous features was problematic. Consequently, further warping was performed to alter the morphology of the template.

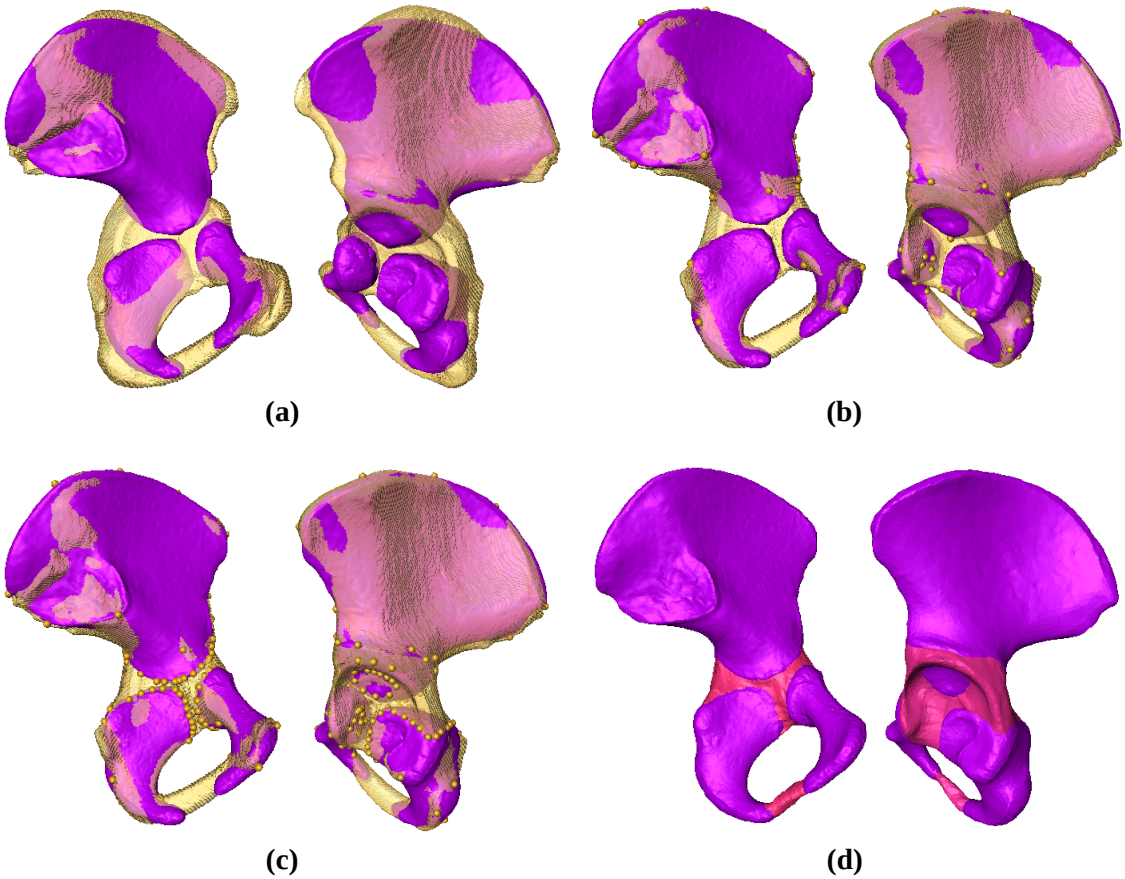

Figure 4.19. Morphometric reconstruction of the 1yr old specimen, showing the (a) siting of disarticulated bones within the original hemi-pelvic template, (b) initial alteration of the template to fit the morphology of the re-articulated bones, (c) further alteration to ensure continuity between the re-articulated bones and warped template, and (d) the final reconstructed 1yr old hemi-pelvis.

Using the morphology of the re-articulated 1yr old hemi-pelvic bones, a custom landmark configuration was created to re-warp the template. The re-warped template shown in Figure 4.19(b) illustrates extent to which the volume was altered to fit the morphology of the rearticulated bones. This was particularly evident in the regions of disarticulation, as the external contours of the re-warped template now adjoined those of the individual bones. Definition of additional landmarks, particularly in the acetabulum, improved the fit of the re-warped template to the morphology of the disarticulated bones (see Figure 4.19(c)).

Altering of the template morphology enabled direct use of the warped volume to reconstruct cartilaginous features, and significantly reduced the amount of manual segmentation required. Regions of the warped template which indicated the geometry of cartilaginous features were identified through merging of the models shown in Figure 4.19(c). Limited manual segmentation was required to ensure continuity between the hemi-pelvic bones and the newly defined cartilage. A final reconstructed 1yr old model was created with articulating hemi-pelvic bones, connected through cartilage at the acetabulum and obturator foramen (see Figure 4.19(d)).

4.6.3. Reconstruction of the 8 year old hemi-pelvis

An articulated hemi-pelvis of the 8yr old specimen was reconstructed using the same morphological techniques previously applied. An estimate landmark configuration with a PD of 90mm was created within Morphologika from a multivariate regression of the original morphometric dataset. The landmark configuration was then used to warp the reconstructed 19yr left hemi-pelvis (see Section 4.6.4) to the estimated form within AMIRA. The disarticulated bones were then sited within the template to gain an estimation of their relative positioning, as illustrated in Figure 4.20(a).

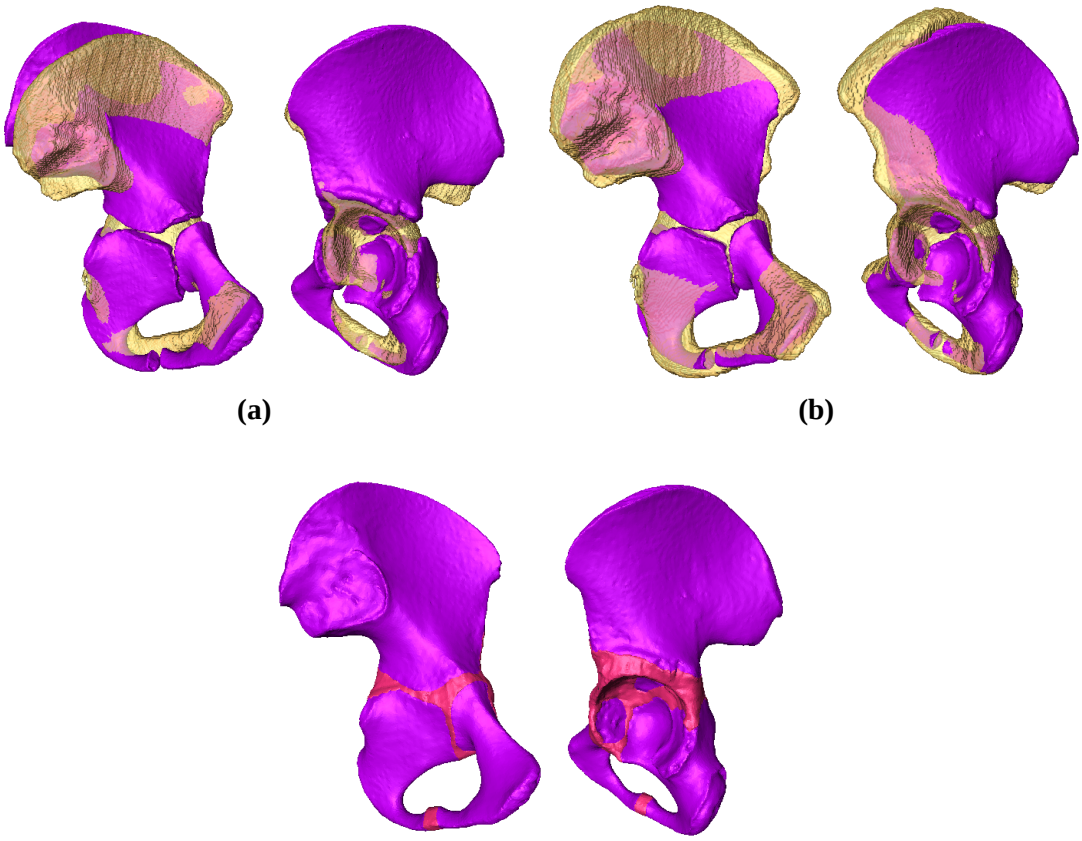

Figure 4.20. Morphometric reconstruction of the 8yr old specimen, showing the (a) siting of the disarticulated bones within the initial warped template, (b) scaled increase in the warped template size to fit the general shape of the acetabulum, and (c) the final reconstructed 8yr old hemi-pelvis.

Due to the use of an estimated hemi-pelvic form during the warping process, the created template was smaller than the morphology of the re-articulated bones (see Figure 4.20(a)). However, unlike reconstruction of the 1yr hemi-pelvis, the general shape of the acetabulum was similar to that of the disarticulated bones, albeit slightly reduced in size. Therefore, rather than re-warping the template, it was considered advantageous to enlarge its size. Through increasing the voxel size within AMIRA, the warped template was scaled while still maintaining its original shape. As shown in Figure 4.20(b), the morphology of the altered warped acetabulum produced a closer match to that of the disarticulated structure.

Merging of the volumetric models in Figure 4.20(b) was preceded by identifying the contours of the warped template which indicated the geometry of the missing cartilaginous features. Merging of these regions to the re-articulated bones, enabled subsequent manual segmentation to create a smooth and continuous morphology between the hemi-pelvic bones and the cartilage. The reconstructed geometry of the cartilaginous features of the acetabulum and obturator foramen, created the final model of the 8yr old hemi-pelvis illustrated in Figure 4.20(c).

4.6.4. Reconstruction of the 19 year old hemi-pelves

The principle methods of the morphometric reconstruction technique were also applied to reconstruct the missing anatomical features of the 19yr old hemi-pelves. The morphometric technique holds the capability of warping one innominate into the other, thus providing a template from which the omitted features can be reconstructed. However, the accuracy of this is dependent on manually defining an identical landmark configuration between each innominate. Due to the disruption to the geometry of the ASIS and pubic symphysis (see Figure 3.7), landmarks could not be defined within these regions. A configuration could have been used which omitted the details of these regions, although using landmarks which did not sufficiently define the hemi-pelvis may have failed to produce accurate warped templates. Conversely, additional features could have being defined, although they were not easily identifiable between innominates.

Alternatively, the landmark configuration of an innominate can be rotated about its centroid to produce a configuration of the same morphology, but for the opposite anatomical side (i.e. turning the morphology of the left hemi-pelvis into the right). The innominates can be warped to the rotated landmark configuration, producing a

hemi-pelvis of the opposite anatomical side. The method is advantageous as the original morphology is maintained during warping, thus providing a more accurate template from which anatomical features can be reconstructed. Therefore, this method was selected to reconstruct the 19yr old innominates.

A custom landmark configuration defined on each 19yr old hemi-pelvis was rotated about it's centroid within Morphologika. The rotated configurations were then used to warp the left hemi-pelvis into a right hemi-pelvis, and vice versa. Subsequently, warped models of the complete left pubic symphysis and right ASIS were created, and used as templates from which to reconstruct the original innominates. Figure 4.21 shows the reconstruction of the left innominate by initially cropping the superior pubic symphysis of the warped template, and positioning it into the void created by the missing anatomy (see Figure 4.21(b)). The two were then merged and manual segmented to reconstruct an appropriate morphology (see Figure 4.21(c)). The model was then smoothed to ensure a continuous profile around the pubic symphysis, as illustrated by Figure 4.21. The same process was applied to reconstructing the ASIS of the right innominate, as demonstrated within Figure 4.22. The final reconstructed volumetric models of the 19yr old specimens are illustrated in Figure 4.23.

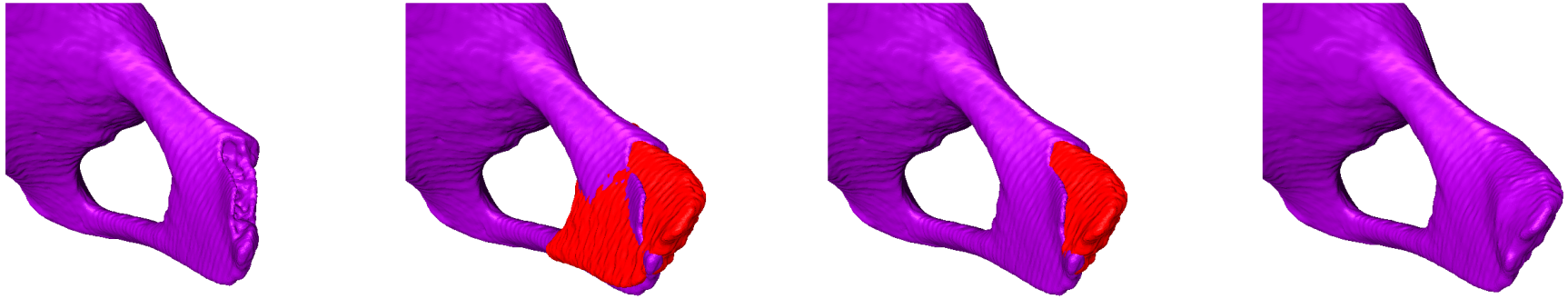

(a) (b) (c) (d)

Figure 4.21. Reconstruction of the pubic symphysis of the 19yr old left innominate, showing (a) the original volumetric model, (b) overlay of the reflected right pubic symphysis, (c) manual segmentation of the reflected right pubic symphysis to model the omitted material, and (d) the final smoothed model of the reconstructed left pubic symphysis.

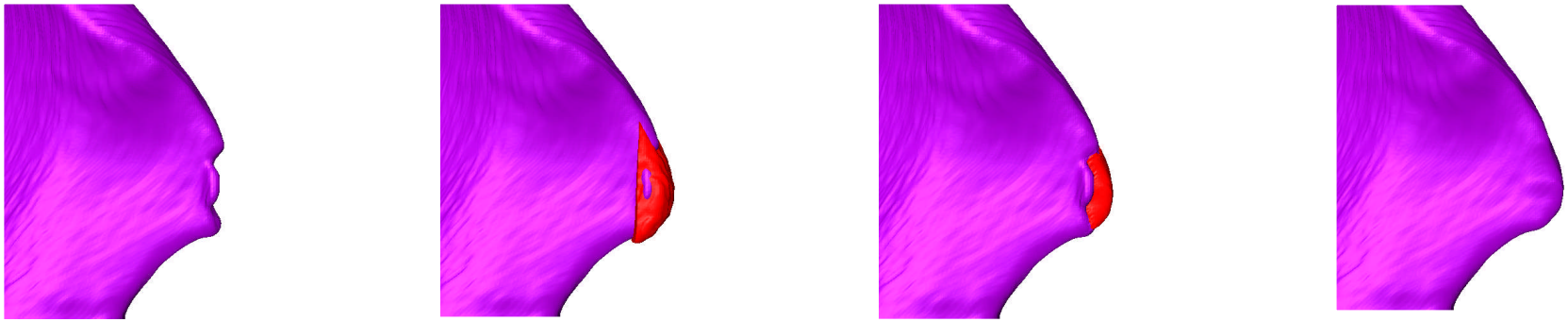

(a) (b) (c) (c)

Figure 4.22. Reconstruction of the ASIS of the 19yr old right innominate, showing (a) the original volumetric model, (b) overlay of the reflected left ASIS, (c) manual segmentation of the reflected left ASIS to model the omitted material, and (d) the final smoothed model of the reconstructed right ASIS.

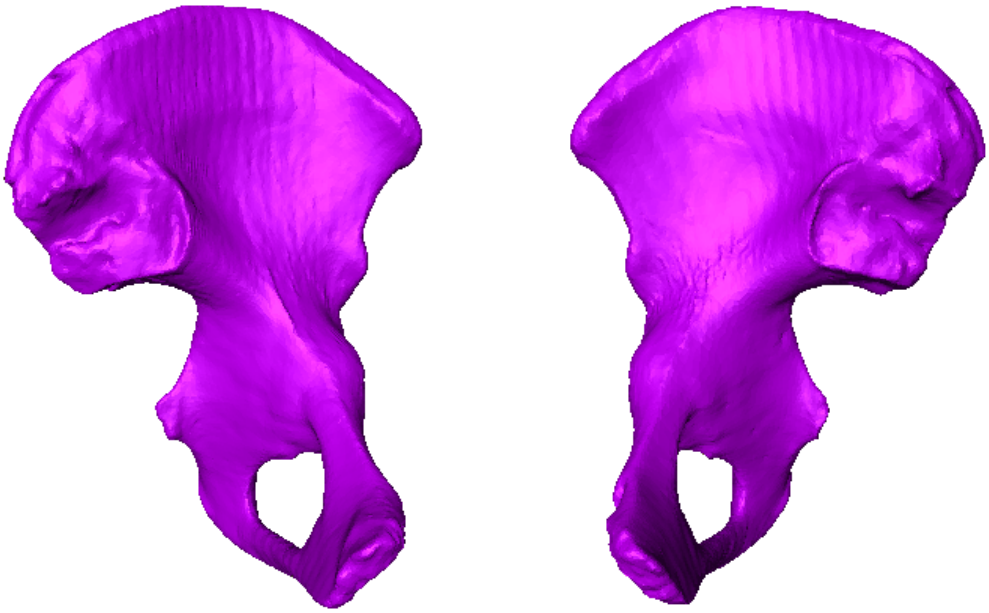

Figure 4.23. Reconstructed digitised volumetric models of the left and right 19yr old hemi-pelves.

5. MUSCULOSKELETAL MODELLING

The joint reaction and muscle forces of the pelvic system during locomotive activities were determined within the MS simulation software AnyBody. Two models were analysed which estimated the MS forces occurring within an *in utero* mechanical environment, and during bipedal locomotion. A custom built prenatal MS model aimed to replicate the interaction between the fetal leg and the womb wall. A pre-defined generic adult MS model was used to determine the loading throughout the gait cycle. These predicted forces produced an indication of the MS activity associated with a mature bipedal gait. A validation study was also performed which analysed the accuracy of creating subject-specific MS simulations from generic models. The validity was determined by comparing computed muscles forces to those measured through experimental methods.

5.1. PRENATAL MUSCULOSKELETAL MODELLING

A MS model of the prenatal hip joint was constructed which aimed to compute the mechanical loading associated with movements *in utero*. Determining the characteristics of *in utero* movements is difficult and dependent on the age of the fetus and it's positioning (e.g. breech position). Unfortunately, the history of the specimen was unknown, although the age could be estimated from its morphology. Through measurement of the iliac and ischial width and length, along with the pubic width, a gestational age of ~34-38 weeks was estimated using data of Fazekas and Kosa (1978). Consequently, the hemi-pelvic specimen was considered to be fairly close to term, and at an advanced stage of fetal development. As illustrated within Figure 5.1, the confinement within the womb combined with the fetal size at this gestational age, causes the positioning of the lower limb with a highly flexed hip and knee. Therefore, the main mechanical forces from *in utero* movements at this

gestational age are mainly from interactions between the leg and the womb wall. Consequently, the MS model of the prenatal hip joint aimed to replicate the twitching and kicking of the leg at a high hip joint flexion.

Figure 5.1. Fetal positioning at 38 weeks gestation characterised by a high hip and knee flexion (reproduced from Moore and Persaud, 2008).

To faithfully model the prenatal hip joint using the digitised hemi-pelvis constructed in section 4.6.1, an accompanying femur was also required. However, the corresponding femur to the prenatal specimen selected from the Scheuer collection was not available. In the absence of the actual fetal femoral form, a fully developed adult femur (obtained from the Vakhum Project (van Sint Jan, 2001)) was scaled down to an appropriate juvenile size, as determined by the morphometric data reported by Fazekas and Kosa (1978). Although this is likely to have a differing morphology to that of an actual prenatal femur, it provided an estimate of the femoral geometry.

5.1.1. Pelvic hip joint centre positioning

An important aspect of MS modelling is the positioning of the hip joint centre (HJC), as inaccurate estimation of its location can influence kinematic movement (Stagni et al., 2000) and the lengths and lever arms of muscles spanning the joint (Harrington et al., 2007). Due to their disarticulation, the HJC's of the prenatal pelvis and femur were determined separately. The point of articulation linking each bone was determined as the centre of the acetabulum and femoral head (Wu et al., 2002).

Techniques of estimating the HJC have developed from traditional predictive approaches to more functional methods, all which vary in terms of complexity. Functional methods are generally considered to provide greater accuracy in estimating the HJC, often comprising of fitting a sphere to a cluster of points plotted around the acetabulum or femoral head (Hicks and Richards, 2005). This technique is commonly applied when radiographic or CT data of the articulated hip joint is available. Algorithms have also been computed from kinematic data (Camomilla et al., 2006; Siston and Delp, 2006) to determine the HJC from the positioning of motion capture markers during gait. However, as these methods require detailed information of the hip joint in a state of articulation or during gait, their application to the cadaveric prenatal specimen was not possible.

Traditional predictive approaches were considered more applicable, as they use regression equations based upon anatomical landmarks of the pelvis (Andriacchi et al., 1980; Bell et al., 1989, 1990; Davis et al., 1991; Seidel et al., 1995; Leardini et al., 1999; Harrington et al., 2007). Through positioning the pelvis within a pelvic reference frame (Cappozzo et al., 1996), the anatomical landmarks illustrated in Figure 5.2 are identified and used to calculate the PD, pelvic width (PW) and pelvic height (PH). The distance of the HJC in each anatomical plane from a selected

reference point is then estimated as a percentage of one (or more) of the anatomical measures (see Table 5.1). However, the accuracy of such predictive techniques are hindered by the sample size and age of the subjects analysed.

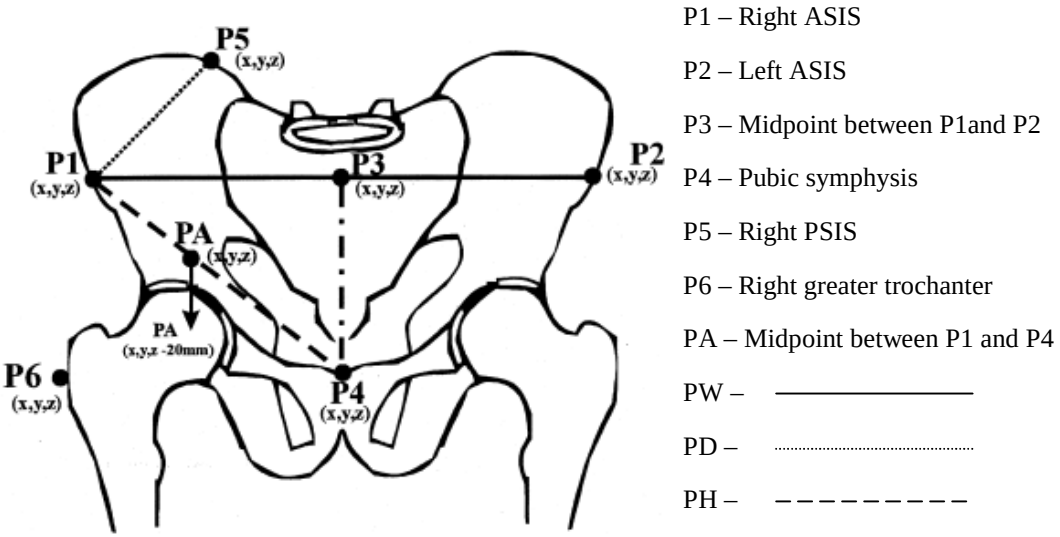

Figure 5.2. Pelvic landmarks and measures used for predictive HJC location techniques (adapted from Kirkwood et al. (1999)).

An early approach by Andriacchi et al. (1980) suggested that the HJC was located 1.5-2cm distal to the midpoint of a line interesting the ASIS and pubic symphysis in the frontal plane (see Figure 5.2). Bell et al. (1989, 1990) estimated the HJC as a percentage of the PW, which was found to be accurate to within 2.6cm of the true location. This technique was adapted by Davis et al. (1991) and located the joint centre using a combination of the PW and leg length. Seidel et al. (1995) performed direct measurements on cadaveric specimens and found the HJC in the frontal, median and horizontal planes as a function of the PW, PH and PD respectively. This method was found to produce lower errors, although its application is limited by the necessity to palpate the pubic symphysis.

Study	Magnitude	Direction	Located from
Andriacchi et al (1980)	1.5-2cm	Distal	Midpoint of line intersecting the ASIS and pubic symphysis
Bell et al. (1989)	22% PW 30% PW 14% PW	Posterior Inferior Medial	ASIS
Bell et al. (1990)	19% PW 30% PW 36% PW	Posterior Inferior Medial	ASIS
Davies et al. (1991)	0.95D+0.031LL-4mm 0.31D-0.096LL+13mm 0.5PW-0.055LL+7mm	Posterior Inferior Lateral	Midpoint between the left and right ASIS's
Siedel et al. (1995)	79% PH 34% PD 14% PW	Posterior Inferior Medial	ASIS
Leardini et al. (1999)	31% PD 9.6% LL 38% PW	Posterior Inferior Lateral	Midpoint between the left and right ASIS's
Harrington et al. (2007)	24% PD-9.9mm 30% PW-10.9mm 33%PW+7.3mm	Posterior Inferior Lateral	Midpoint between the left and right ASIS's
OrthoTrak (Motion Analysis Crop., CA., United States)	22% PW 34% PW 32% PW	Posterior Inferior Lateral	Midpoint between the left and right ASIS's

Table 5.1. Techniques of estimating the HJC (LL = distance between ASIS and homolateral medial malleolus; D = anterio-posterior component of the distance between a point approximating the hip centre and the homolateral ASIS).

Leardini et al. (1999) evaluated the accuracy of the predictive methods of Bell et al. (1990) and Davis et al. (1991), through comparing estimated HJC's to those found via Roentgen Stereophotogrammetric Analysis. The predictive methods were found to have a lower accuracy compared to the applied functional method, although the authors did suggest improved regression equations. A similar study by Harrington et al. (2007) compared the same predictive methods and software recommendations for OrthoTrak (Motion Analysis Crop., CA, United States), to a functional method of calculating the HJC via sphere fitting from MRI images. The authors also suggested new regression equations from which to estimate the HJC, using the PD in the frontal and the PW in the horizontal and median planes.

Various predictive techniques were used to estimate the HJC of the prenatal specimen (Andriacchi et al., 1980; Bell et al., 1989, 1990; Seidel et al., 1995; Harrington et al., 2007) (see Figure 5.3 and Figure 5.4). Techniques which utilise parameters of the lower extremity (Davis et al., 1991; Leardini et al., 1999) were not used due to the uncertainty in the accuracy of prenatal femoral morphology. The digitised prenatal model was rotated into the pelvic reference fame reported by Cappozzo et al. (1995), defined through the following:-

Origin:	Midpoint between the left and right ASIS's;
Z:	Parallel line passing through the ASIS's (positive laterally);
X:	A parallel line connecting the midpoint of the two ASIS's and the midpoint of the two PSIS (positive anteriorly);
Y:	Perpendicular to both the x and z-axis (positive superiorly).

The anatomical landmarks illustrated in Figure 5.2 were identified, with the location of the left ASIS taken from the volumetric model of the fully articulated prenatal pelvis (see Figure 3.3(a)). The pelvic distances were calculation through vector mechanics, as suggested by Kirkwood et al. (1999).

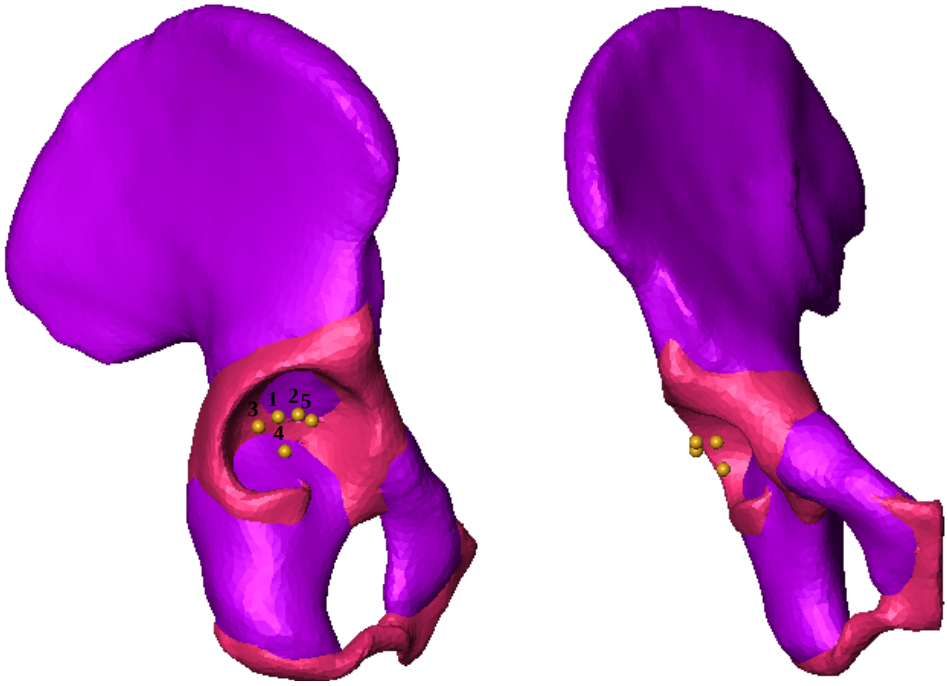

Figure 5.3. The estimated HJC locations of the prenatal pelvis using methods of (1) Bell et al. (1989), (2) Bell et al. *(*1990), (3) Seidel et al. (1995), (4) OrthoTrak and (5) Harrington et al. (2007).

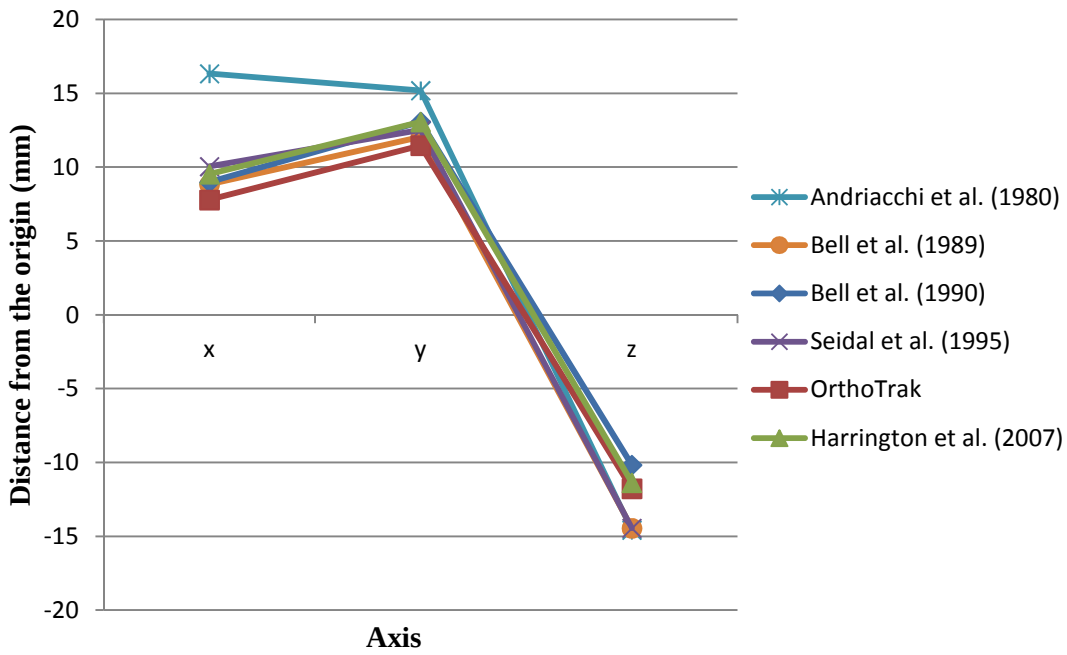

Figure 5.4. Estimated coordinates of the prenatal HJC produced by the predictive methods.

Through applying the predictive methods which were solely based on pelvic measurements, six estimated HJC coordinates were calculated from the defined origin. All methods produced estimated locations which were within the acetabular labrum (see Figure 5.3), apart from that suggested by Andriacchi et al. (1980). As this method was devised to estimate the HJC in the frontal plane, only the z coordinate fell within the range suggested by the other methods (see Figure 5.4). Consequently, the estimated joint positioning produced through this method was eliminated from further analysis.

Through visual inspection of Figure 5.3, the HJC's calculated via the methods of Seidel et al. (1995) and Harrington et al. (2007) were deemed to predict overestimations in the posterior and anterior positioning, respectively. Figure 5.3 also highlighted the excessively inferior estimation of the centre produced by the method of OthroTrak. The predicted coordinates estimated by Bell et al.(1989, 1990) and Seidel et al. (1995) were also deemed to be unrealistic within the z-axis (see Figure 5.4). This can be observed within Figure 5.3 where the more lateral estimation of the HJC placement exceeds the limit of the acetabular labrum. The remaining coordinates were assumed to provide a reasonable estimation of the region in which the HJC could have been located. As there was limited confidence in a singular method to estimate the HJC, the remaining coordinates were averaged to produce a single vector position. Therefore, an estimated location was calculated through combining a number of predictive techniques, and visual inspection of where the HJC should be positioned.

5.1.2. Femoral hip joint centre positioning

The centre of the femoral head was determined through the assumption that its shape was comparative to that of a sphere. A boundary box was initially created which roughly encompassed the femoral head, through adjusting its widths in the 2D anatomical planes until they were at the limit of the bone surface. As illustrated in Figure 5.5, this can be easily determined for the frontal and horizontal planes, although it is more problematic in the median plane due to the fusion between the femoral head and neck. Therefore, the limit of the boundary box in the lateral direction was estimated based upon visual inspection of the femoral head. The mid slice in each orthogonal direction was determined (as shown in Figure 5.5), and the point at which the three anatomical planes intersected was estimated as the joint centre.

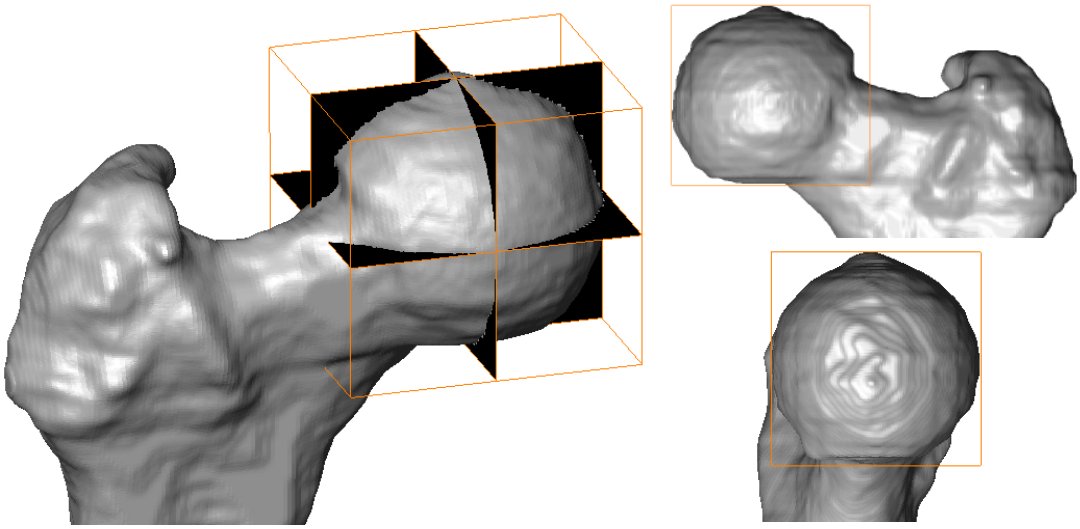

Figure 5.5. Estimation of the femoral HJC via defining a boundary box around the femoral head and determining the point of intersection of the three anatomical planes.

5.1.3. Articulation of the prenatal hip joint

An articulated hip joint was initially achieved through rotating the prenatal pelvis and femur into their relative reference frames, as detailed by Wu et al. (2002). The

pelvic reference frame was similar to that previously described, although the origin was positioned at the HJC as opposed to the midpoint of the ASIS's. The femoral reference frame was defined through the following:-

Origin:	Centre of rotation;
Y:	Line connecting the midpoint between the medial and lateral femoral epicondyles and the origin (positive superiorly);
Z:	Perpendicular line to the y-axis, lying in a plane defined by the origin and the femoral epicondyles (positive laterally);
X:	Perpendicular to the y and z-axis (positive anteriorly).

Through aligning the origins of both reference frames, the prenatal hemi-pelvis and femur were subsequently articulated about an estimated HJC (see Figure 5.6).

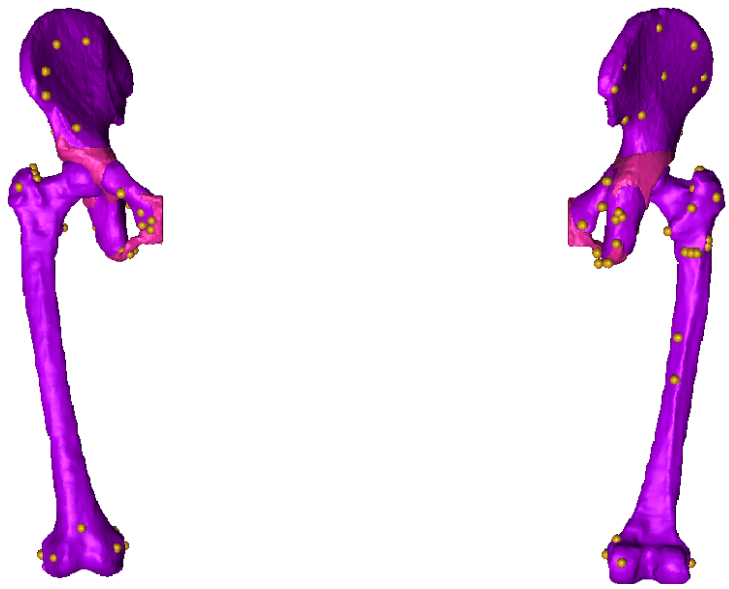

Figure 5.6. Articulation of the prenatal hip joint (the spheres represent the landmarks of the origin and insertion points of the muscles spanning the joint).

5.1.4. Prenatal muscle modelling

Modelling of the prenatal hip joint within AnyBody Version 3.1 required the construction of a program which defined the MS features, along with the *in utero*

loading and kinematical movements. The customised program was written in an AnyScript language (Damsgaard et al., 2006), which initially imported the volumetric models of the prenatal hemi-pelvis and femur as .stl (Stereolithography) files. These were automatically transformed into an .ANYSURF file format within AnyBody. The hemi-pelvis and femur were defined as separate segments and connected through a spherical joint at the estimated HJC.

The pelvic and femoral masses were calculated through anthropometric data of Winter (1990), in which the weights of individual skeletal segments are expressed as an percentage of overall BW. A fetal weight of 2.5 kilograms (Kg) was estimated from the data of Salomon et al. (2007), through selecting the mean weight recorded at 36 weeks gestation. The individual skeletal segment weights were subsequently calculated from this, providing estimated weights of the pelvis and femur at 0.36Kg and 0.25Kg respectively. The upper body weight which transfers through the pelvis was determined to be 1.34Kg, while the leg distal to the knee was calculated at 0.15Kg. Figure 5.7 shows the definition of the two masses as negative vertical forces acting through the HJC, and the midpoint between the medial and lateral femoral epicondyles. The moment of inertia for the femur was calculated through pre-defined formulas within AnyBody, and was based upon the femoral mass and length (for further information see Appendix IV). Unfortunately, AnyBody does not contain any formulae for determining the pelvic moment of inertia, favouring the use of constant values. However, as the pelvis was modelled as a constrained segment (for the purpose of kinematical determinacy), the inertia was set to zero as no velocities or accelerations were expected.

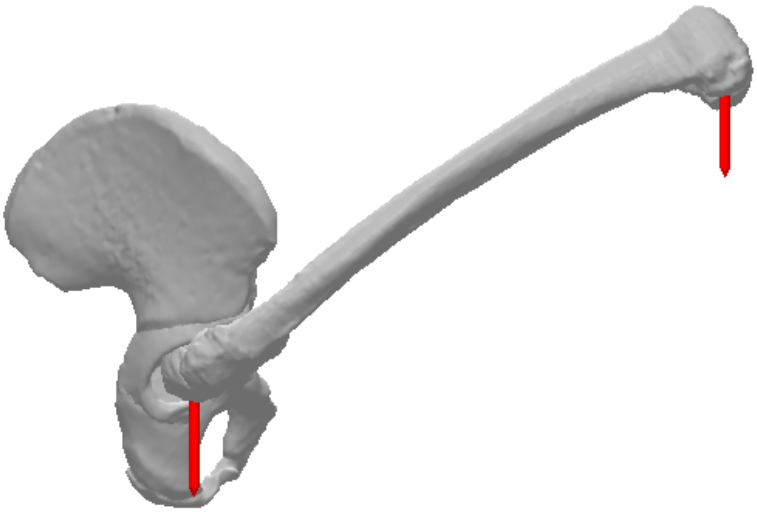

Figure 5.7. Modelling the weight of the upper body and the lower leg acting through the HJC and the midpoint between medial and lateral femoral epicondyles respectively.

The muscular architecture of the prenatal hip joint was initially constructed via mapping origin and insertion sites through landmarks within AMIRA (see Figure 5.6). The locations of the muscle attachments on the pelvis and femur were identified through combining the anatomical texts of Scheuer and Black (2000), Moore and Agur (2002) and Sobotta (2006). As the prenatal MS model only contained the hemi-pelvis and femur (see Figure 5.7), modelling muscles which span the hip joint and attach to the tibia (such as the gracilis and sartorious), proved problematic as the distal insertion point could not be determined. However, as such muscles wrap around the femoral epicondyles, the first point of contact with the femur was taken as the insertion point. Although this is not anatomically correct, it does estimate the muscle line of action originating from the pelvis. Muscles whose individual fibres travel in a uniform direction, for example the pectineus and tensor fascia latae (TFL), were deemed appropriate to model through singular lines of action (see Table 5.2). Broader groups of muscles, such as the iliacus and glutei, were split into three lines of action, to provide a more accurate representation of the *"fanning"* nature of the muscular geometry (see Figure 5.8).

Muscle	Lines of Action	PCSA (cm^2)
Adductor Brevis	1	3.5
Adductor Longus	1	15.1 *
Adductor Magnus	3	24.3
Biceps Femoris	1	27.2 *
Gemellus Inferior	1	4.1 *
Gemellus Superior	1	4.1 *
Gluteus Maximus	1	49.7
Gluteus Medius	3	49.35
Gluteus Minimus	3	8.5
Gracilis	1	4.9 *
Iliacus	3	9
Obturator Externus	2	24.6
Obturator Internus	2	25.4 *
Pectineus	1	6.8 *
Piriformis	1	8.1 *
Quadratus Femoris	1	14.6 *
Rectus Femoris	2	28.9 *
Sartorius	1	5.9 *
Semimembranosus	1	17.1 *
Semitendinosus	1	14.7 *
TFL	1	8.8 *

Table 5.2. The number of lines of action representing the prenatal muscular architecture and the defined PCSA's based on the data of Klein Horsman et al. (2007) (the values marked with an * indicate PCSA's taken directly from the literature, while the remaining values are averages of the individual fibre PCSA's reported within a single muscle).

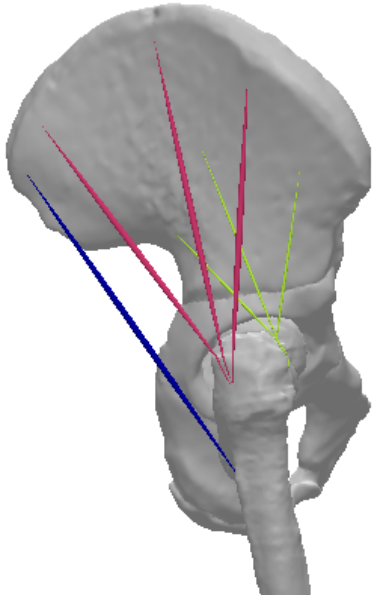

Figure 5.8. Modelling of the gluteal muscles, showing the single line representation of the maximus (blue), and the *"fanning"* of the medius (red) and minimus (green).

As the prenatal MS model aimed to replicate the hip rotation occurring *in utero*, muscle wrapping was employed to ensure that muscles did not intersect each other or bony features. Cylinders were defined on the exterior of the hemi-pelvis and femur, and the muscles were positioned to follow the path of the cylindrical surface to replicate muscles wrapping around bony features (see Figure 5.9(a)). Cylinders were additionally defined within the muscular architecture of the hip joint, so that muscles maintained a physiological path at high flexion angles and to ensure that they did not intersect each other (see Figure 5.9(b)). As illustrated in Figure 5.10, the completed prenatal muscular architecture contained 21 muscles which were modelled through 32 individual lines of action, and wrapped around a total of 104 cylinders.

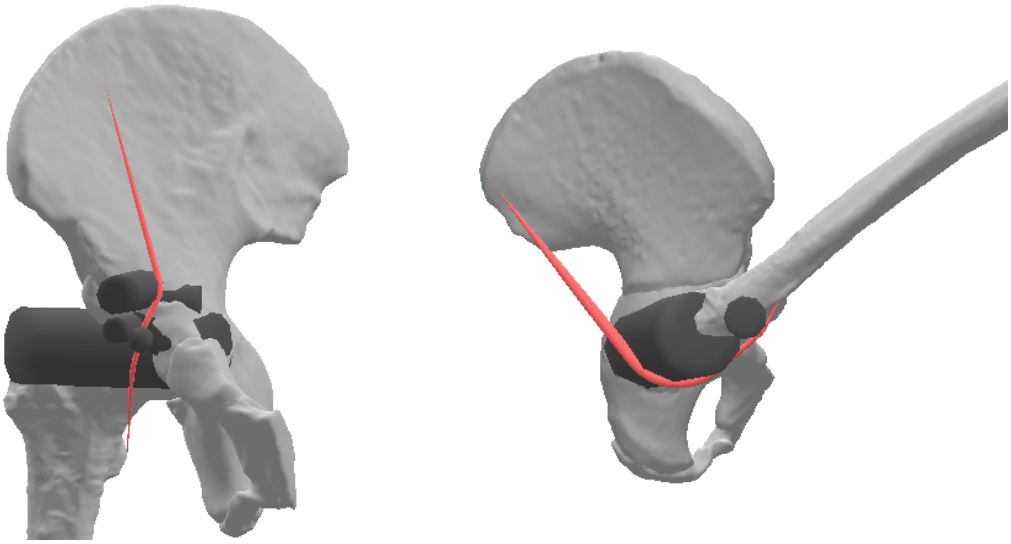

(a) (b)

Figure 5.9. Muscle wrapping of the (a) iliacus and (b) gluteus maximus around defined cylinders.

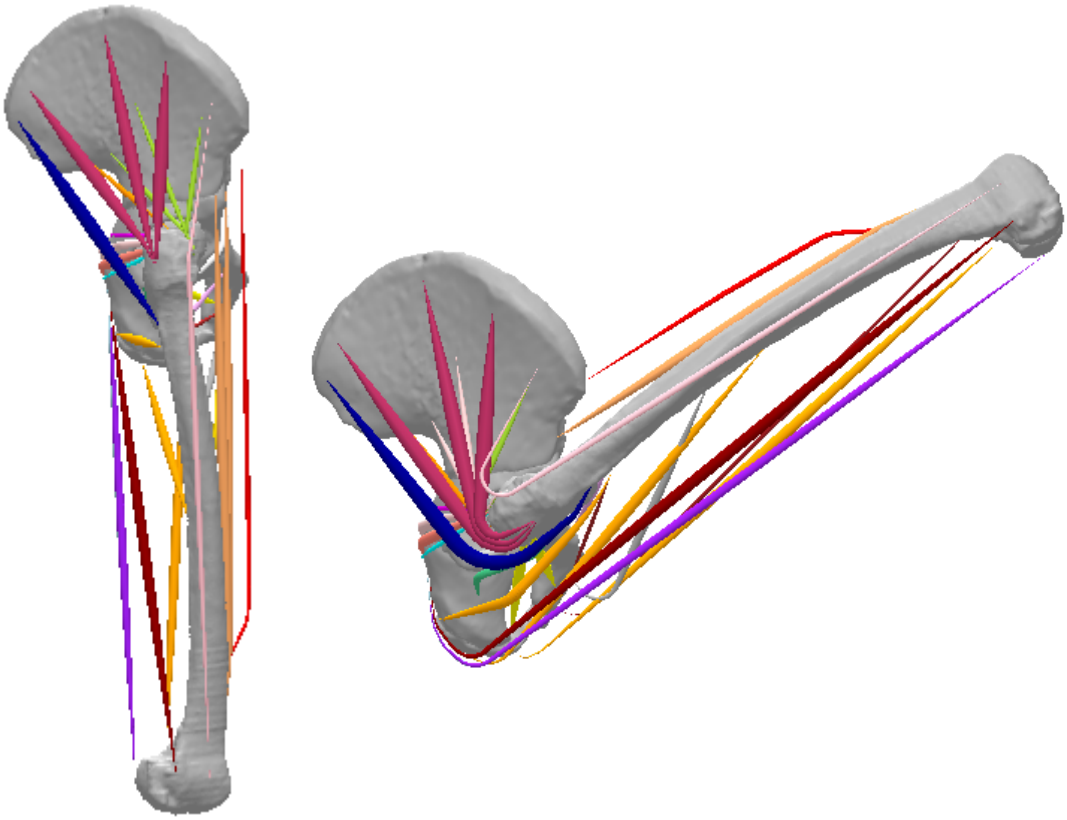

(a) (b)

Figure 5.10. The muscular architecture of the prenatal MS model at (a) 0° and (b) 120° hip joint flexion.

Each muscle was assigned a MIF capability to enable computation of inverse dynamics. Information detailing the MIF of all the hip joint muscles is limited, particularly pertaining to the prenatal anatomy. Therefore, they were determined by the proportional relationship between the PCSA and muscle stress, as performed by Heller et al. (2001). Anatomical studies examining the lower extremity muscle architecture have published details of muscle attachment sites (Dostal and Andrews, 1981; Brand et al., 1982; Duda et al., 1996) and muscle parameters (Pierrynowski, 1995; Klein Horsman et al., 2007; Ward et al., 2009). The muscle characteristics vary between studies due to the analyses being performed on separate single cadaveric specimens, although Ward et al. (2009) did report average values from a data set of 21 cadaveric lower extremities. However, such studies often failed to analyse the complete MS system of the lower extremity, or generalised muscles into single lines of action and only report singular muscle parameters values. Only Klein Horsman et al. (2007) dissected cadaveric muscles into several fibres, thus detailing larger muscles through numerous lines of action (e.g. anterior, mid and posterior). Therefore, due to the greater detail in characterising the muscular anatomy, the PCSA measurements of Klein Horsman et al. (2007) were selected and used to define the MIF's. The modelled PCSA's are shown in Table 5.2, with the majority of the values extracted directly from the literature. As Klein Horsman et al. (2007) dissected larger muscles into several lines of action, a PCSA value was reported for each individual fibre. In the instances where the PCSA of individual fibres did not vary extensively, an averaged value was calculated. However, the fibres of the gluteus maximus and obturator externus displayed a larger PCSA variation, therefore the values of the superior fibres were averaged. As the PCSA values were measured from an adult cadaver, they were not fully representative of the prenatal anatomy. Although, they did provide a means of representing the relative size of the muscles in

relation to each other. The muscle stress was taken as 1MPa, as performed by Heller at el. (2001).

To replicate the prenatal hip within an *in utero* environment, the joint positioning was initial rotated to a 120° flexion angle, as shown in Figure 5.10(b). To simulate twitching of the leg within the womb, two hip joint movements were modelled; one performing a further 2° flexion; and another producing an opposing 2° extension. Both movements were achieved through a rotational driver applied to the hip joint in the median plane. To represent interaction between the leg and the womb wall *in utero*, a cylindrical block was defined in close proximity to the femoral epicondyles. The femur and the block were separated by a spring, which provided a resistance to the hip flexion/extension movement. To maintain the kinematic determinacy of the model, a rigid constraint was applied at the SIJ. Joint and muscle kinetics were computed through an inverse dynamics analysis, using a pre-defined Min/Max optimisation solver (Rasmussen et al., 2001), which used linear programming to minimise the sum of the muscle activations (Wu et al., 2009b).

5.1.5. Inverse dynamic simulations

The forces generated within the prenatal muscles when undergoing contraction was initially observed through driving the hip joint to a 120° flexion angle, and then back again to a neutral position (taken as 0°). This aimed to identity which muscles contributed to the performance of either hip flexion or extension, or if they were involved in both. As observed in Figure 5.11 and Figure 5.12, six muscles were observed to contract solely during the flexion (gemellus, gluteus minimus, obturator internus, rectus femoris and TFL). In comparison, six muscles were found to only contribute to the hip extension movement (adductor magnus, bicep femoris, gluteus

maximus, gluteus medius, semitendinosus and semimembranosus). The remaining muscles contributed to both movements, as the modelled muscle paths caused them to undergo contraction and co-contraction during a single 120° rotation. As shown in Figure 5.11, the larger muscles of the rectus femoris and obturator internus (see Table 5.2) were the only muscles to generate a force exceeding 2.1N. Forces were generally lower during the extension movement, although the larger muscles once again produced the greatest forces, with the gluteus maximus and medius exceeding 1N (see Figure 5.12). Within the muscles which were modelled through more than one line of action (see Table 5.2), only the obturator externus produced differing forces between its individual fibres.

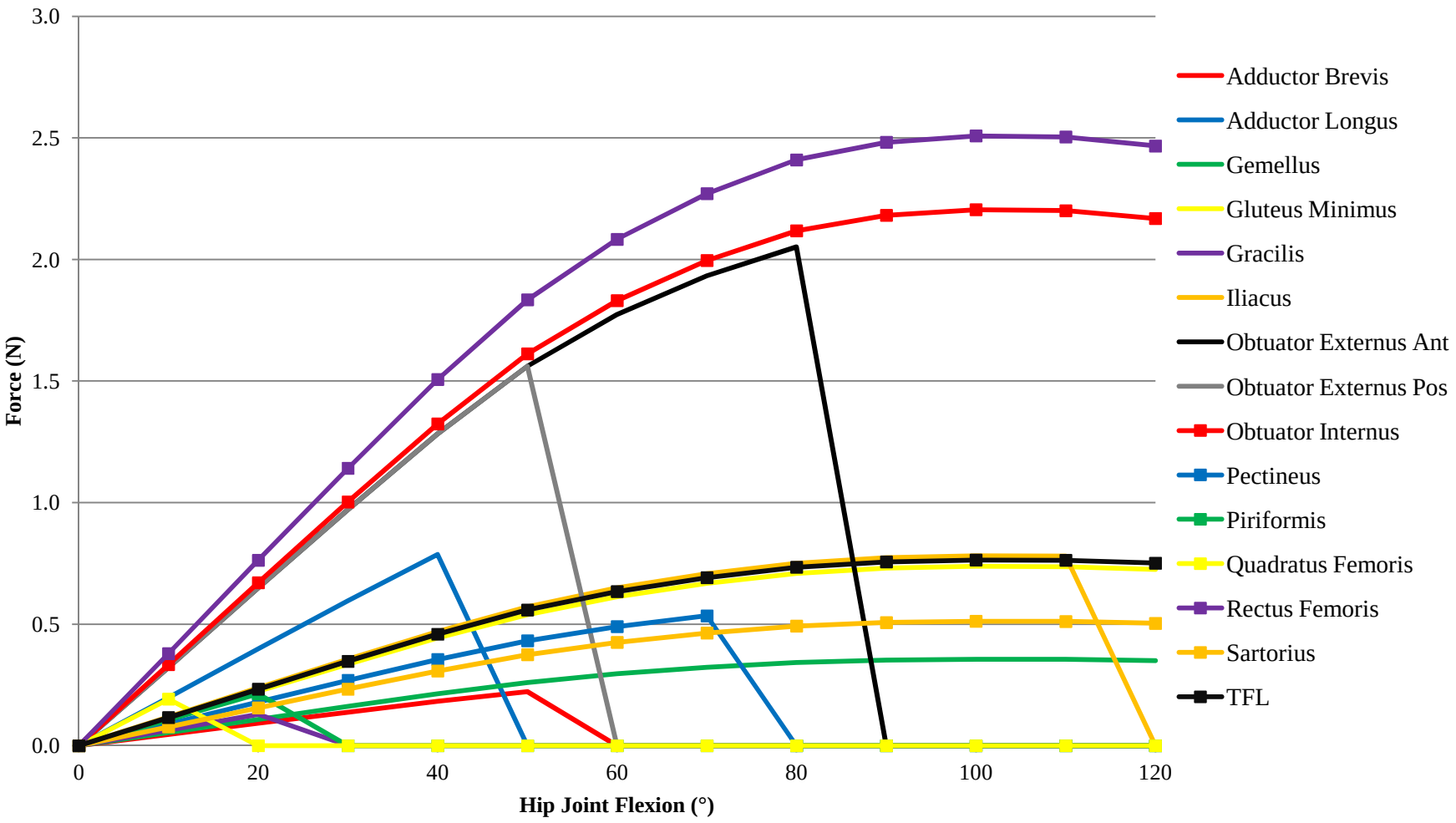

Figure 5.11. Muscle forces calculated by the prenatal MS model when the hip joint was rotated to a 120° flexion angle.

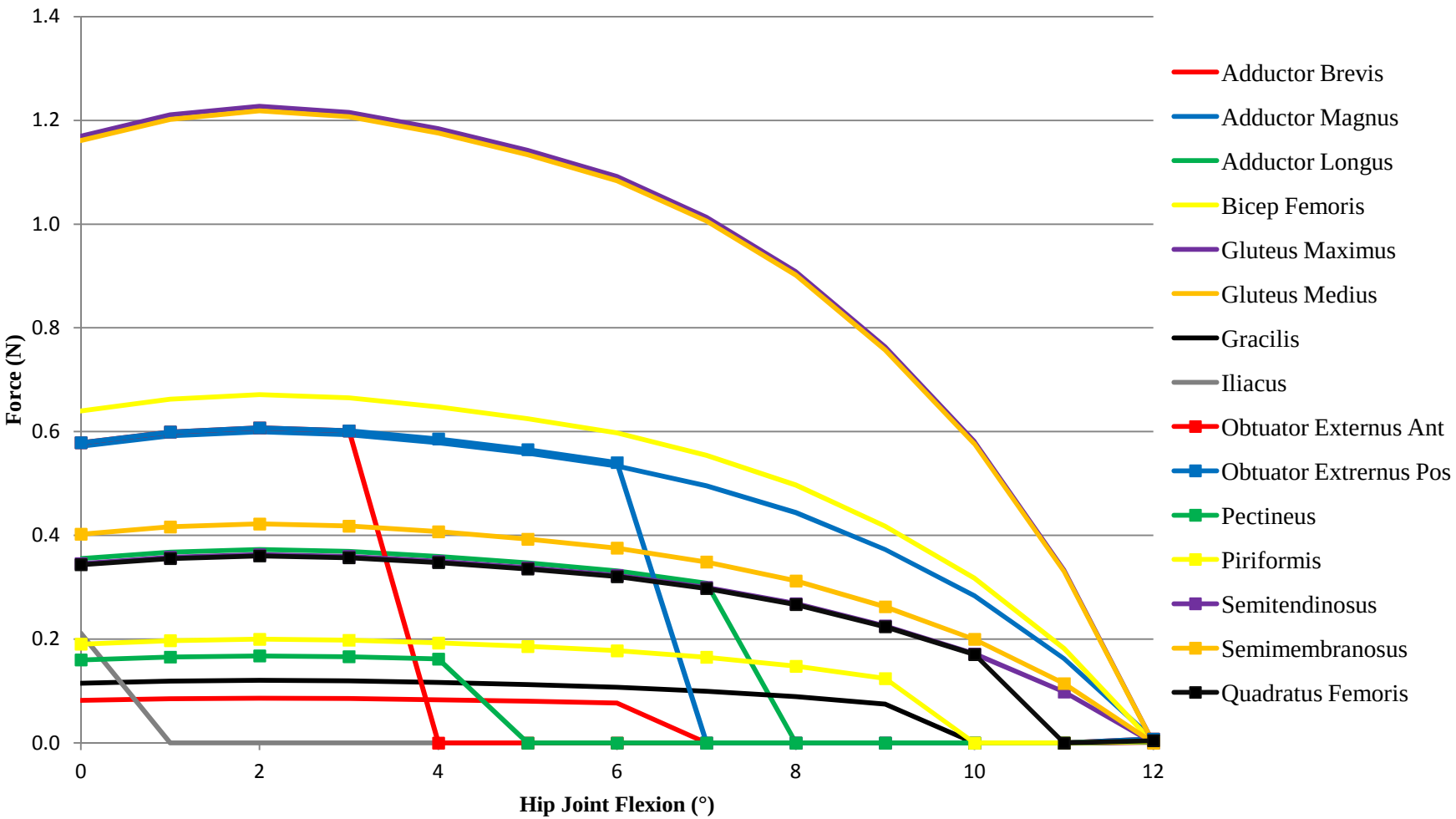

Figure 5.12. Muscle forces calculated by the prenatal model when the hip joint was rotated from a 120° flexion angle to a neutral position (0°).

The original calculation of the MIF for each muscle was based on that reported by Heller et al. (2001), therefore the defined maximal muscle strengths were the same as those used in adult MS modelling. As such values are unrealistically high for representing the prenatal MS system, the muscle strengths were lowered. This was achieved throughout continuously lowering the MIF's by a factor of 10, until there was insufficient strength within the hip joint muscular anatomy to perform the same joint movements previously described. This also aimed to investigate if differing muscle force combinations were calculated when reducing the maximal force generating capabilities.

As shown in Table 5.3, restricting the MIF's to 1% of their original values did not influence the maximal forces predicted during the modelled joint rotation. Consequently, even with a significantly reduced strength, the predicted behaviour of the MS system did not change and produced identical muscle force contributions. However, reducing the MIF's to 0.1% of their original values did cause an alteration to the muscle force combinations. This was highlighted within the gluteus minimus and iliacus, where their strength was reduced to a level which caused them to be passive. To compensate for the deactivation of some muscles, there was an increased contribution from others, as shown in the adductor longus and gluteus medius. The force increase within these muscles was fairly modest, causing the ratio between the maximum recorded force and the restricted MIF to remain low. However, the obturator externus, obturator internus and rectus femoris displayed more drastic increases, and produced maximal muscle forces which exceeded their force generating capabilities (see Table 5.3). Consequently, this was deemed as the point at which the hip muscular anatomy had insufficient strength to perform passive movements. As a result, modelling the MIF's at 1% of their original values was selected as an appropriate reduction from which to perform further analyses.

Although the majority of the ratios between the maximum force and the restricted MIF's were small (all below 9%) when modelling this muscle strength (see Table 5.3), these values only corresponded to a passive range of movement. Therefore, the MS model was considered to contain sufficient additional strength from which to overcome resisted motion.

		100%		10%		1%		0.1%	
	MIF (N)	Force (N)	% MIF	Force (N)	% of MIF	Force (N)	% MIF	Force (N)	% MIF
Adductor Brevis	350	0.22	0.063	0.22	0.63	0.22	6.3	0	0
Adductor Longus	1510	0.78	0.052	0.78	0.52	0.78	5.2	1.24	82.1
Adductor Magnus	2430	0.6	0.025	0.6	0.25	0.6	2.5	0.62	25.5
Biceps Femoris	2720	0.67	0.025	0.67	0.25	0.67	2.5	0.69	25.4
Gemellus	410	0.35	0.085	0.35	0.85	0.35	8.5	0	0
Gluteus Maximus	4970	1.23	0.02	1.23	0.25	1.23	2.5	1.26	25.4
Gluteus Medius	4935	1.22	0.025	1.22	0.25	1.22	2.5	1.27	25.7
Gluteus Minimus	850	0.73	0.086	0.73	0.86	0.73	8.6	0	0
Gracilis	490	0.13	0.026	0.13	0.26	0.13	2.6	0	0
Iliacus	900	0.8	0.089	0.8	0.89	0.8	8.9	0	0
Ob Externus Ant	2460	2.05	0.083	2.05	0.83	2.05	8.3	3.22	130.1
Ob Externus Pos	2460	1.56	0.063	1.56	0.63	1.56	6.3	4.48	182.1
Obturator Internus	2540	2.17	0.085	2.17	0.85	2.17	8.5	3.4	133.9
Pectineus	680	0.54	0.079	0.54	0.79	0.54	7.9	0	0
Piriformis	810	0.21	0.026	0.21	0.26	0.21	2.6	0	0
Quad Femoris	1460	0.2	0.014	0.2	0.14	0.2	1.4	0.37	25.3
Rectus Femoris	2890	2.47	0.085	2.47	0.85	2.47	8.5	3.86	133.6
Sartorius	590	0.5	0.085	0.5	0.85	0.5	8.5	0	0
Semimembranosus	1710	0.42	0.025	0.42	0.25	0.42	2.5	0.44	25.7
Semitendinosus	1470	0.36	0.024	0.36	0.24	0.36	2.4	0.38	25.8
TFL	880	0.75	0.085	0.75	0.85	0.75	8.5	0	0

Table 5.3. The maximum muscle forces generated by the prenatal MS model when flexing the hip joint to 120° and then back to 0°. Maximum forces are displayed which were generated through reducing the MIF's to 10, 1 and 0.1% of their original values.

The prenatal MS modelling was initially performed basing the MIF on a muscle stress of 1MPa. However, muscle definition within AnyBody uses a muscle stress of 0.27MPa, which is based on the dataset of Klein Horsman et al. (2007). To examine if modelling with this muscle stress caused differing observations to those of Table 5.3, the previous procedure was repeated with re-defined MIF's. However, identical maximal muscle forces to those in Table 5.3 were calculated when reducing the MIF's 1% of their original values (see Appendix V). When modelling the MIF's at 0.1% of their original values, a differing muscle combination was produced, although once again some forces exceeded their maximal strength. Therefore, the results in Appendix V confirmed that modelling muscle MIF's at 1% of their original values was appropriate. As the forces calculated through the differing methods were identical at this strength (see Table 5.3 and Appendix V), the muscle definition adopted by Heller et al. (2001) was chosen for further modelling.

To simulate resistance to the hip joint motion caused by interaction of the fetal leg with the womb wall, two methods of modelling can be applied. A resistive force applied directly to the hip joint causes an additional resistance to the rotation. However, a moment of inertia was already applied to the joint which aimed to resist joint motion. Although, the defined inertia properties (see Appendix IV) did not affect the calculated muscle forces, therefore it was turned off during further modelling. An alternative method of simulating interactions with the womb wall was through applying a stiffness to the spring created between the distal femur and the closely situated cylindrical block. To replicate the hip joint position illustrated in Figure 5.1, the hip joint was rotated to a starting position of 120° (as illustrated in Figure 5.10) and two independent movements simulated; a further flexion of 2°; and a 2° extension. As a spring stiffness that is representative of the resistance produced by the womb wall during fetal kicking is difficult to determine, the stiffness was

increased by 1N/mm increments until the hip musculature had insufficient strength to overcome the resistance.

As shown in Table 5.4, the majority of the hip joint muscles were under contraction during the extension movement. Once again the rectus femoris and obturator internus were the most significant contributors to the joint flexion, while the gluteus maximus and medius generated the greatest forces during extension. Table 5.4 also highlights that the muscle forces increased relative to each other when incrementing the spring stiffness. During the joint flexion and extension with the various spring stiffness', the increase in the ratio between the maximum force and the MIF was roughly the same for each muscle. Therefore, when a spring stiffness of 5N/mm was modelled, the muscles activated during the joint flexion all produced maximum forces at ~87% of their MIF. In comparison, maximum muscle forces during joint extension were ~29% of their MIF, apart from the iliacus (13% for the anterior and mid fibres and 6% for the posterior fibre). Consequently, at this spring stiffness the muscles contracting during joint flexion exceeded 85% of their MIF's. Following the protocol adopted by Heller et al. (2005), which aim to prevent muscles exceeding this level of their maximal strength, only the forces associated with the 4N resistive force was used within FE analyses.

	Spring Stiffness (N/mm)					
	0	1	2	3	4	5
Flexion						
Gemellus	0.3	1.0	1.6	2.3	2.9	3.6
Gluteus Minimus	0.7	2.1	3.4	4.7	6.1	7.4
Ob Internus	2.1	6.1	10.1	14.1	18.1	22.1
Rectus Femoris	2.4	7.0	11.5	16.1	20.6	25.2
Sartorius	0.5	1.4	2.4	3.3	4.2	5.1
TFL	0.7	2.1	3.5	4.9	6.3	7.7
Extension						
Adductor Brevis	0.1	0.3	0.5	0.7	0.9	1.0
Adductor Longus	0.4	1.2	2.0	2.8	3.7	4.5
Adductor Magnus	0.6	1.9	3.2	4.6	5.9	7.2
Biceps Femoris	0.7	2.1	3.6	5.1	6.6	8.1
Gluteus Maximus	1.2	3.9	6.6	9.4	12.1	14.8
Gluteus Medius	1.2	3.9	6.6	9.3	12.0	14.7
Gracilis	0.1	0.4	0.7	0.9	1.2	1.5
Iliacus A & Mid	0.2	0.4	0.6	0.8	1.0	1.2
Iliacus P	0.2	0.3	0.4	0.5	0.5	0.6
Ob Externus	0.6	1.9	3.3	4.6	6.0	7.3
Pectineus	0.2	0.5	0.9	1.3	1.7	2.0
Piriformis	0.2	0.6	1.1	1.5	2.0	2.4
Quad Femoris	0.4	1.2	2.0	2.8	3.6	4.4
Semimembranosus	0.4	1.3	2.3	3.2	4.2	5.1
Semitendinosus	0.4	1.2	2.0	2.8	3.6	4.4

Table 5.4. The maximum muscles forces of the prenatal MS model calculated when performing a 2° flexion and 2° extension movement of the 120° flexed hip joint, and applying a varying spring stiffness.

5.2. ADULT MUSCULOSKELETAL MODELLING

The hip joint loading associated with a mature adult gait was determined through analysis of an existing MS model within the repository of the AnyBody modelling system. The repository enables free accessibility to a range of models which vary in terms of complexity and performed activity. The Lower Extremity Model from the AnyBody Managed Repository Version 1.2 (AMMRV1.2) was selected for further analysis, which contains three separate motion capture trials of the same subject (weighing 62kg with a height of 1.73m) performing level walking across three AMTI force platforms (AMTI, MA, United States). Each trial was recorded in a .C3D (Coordinate 3D) file format, which contained the ground reaction forces and the motion analysis of a Helen Hayes marker setup. Although predominately a lower extremity model, the motion capture also recorded three additional markers on the upper body, in order to capture the angle between the trunk and the pelvis.

The Lower Extremity Model is based on a generic MS model which contains 55 muscles per leg, modelled through 159 individual lines of action (see Figure 5.13), with 11 muscles wrapping around bony features of other muscular anatomy (such as the gastrocnemius and iliacus). The origin and insertion sites of the lower extremity muscles are based on the data of Klein Horsman et al. (2007), and modelled through a Hill-Type 3 element muscle model. The muscle parameters reported by Klein Horsman et al. (2007) were also used to define the muscle strengths (see Appendix V). The hip joint was defined as a spherical joint, permitting flexion/extension, adduction/abduction and medial/lateral rotation, while the knee was defined through a revolute joint to enable flexion/extension. The ankle was modelled through both a revolute and subtalar joint, to allow for plantar flexion and eversion, respectively.

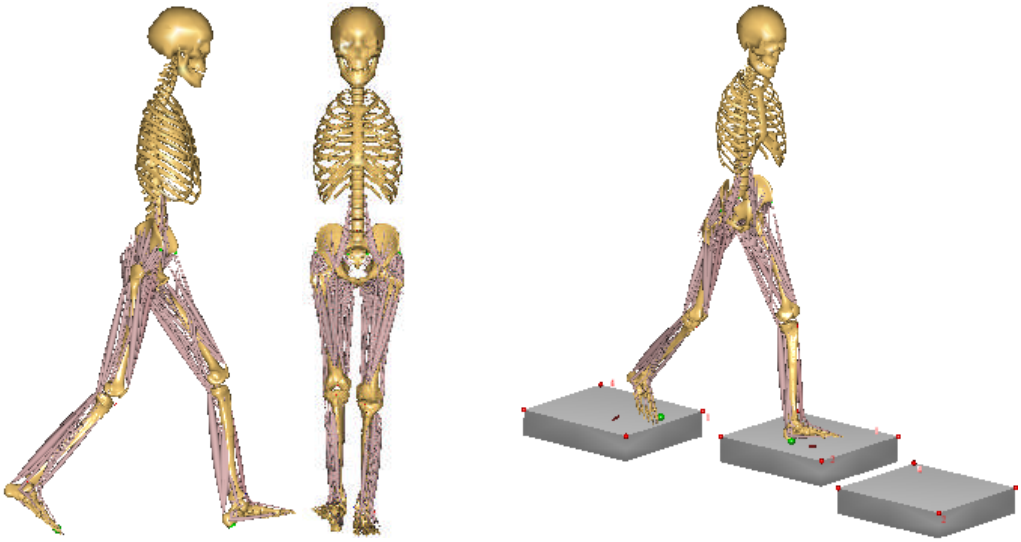

(a) **(b)**

Figure 5.13. Adult modelling within AnyBody, showing (a) the Lower Extremity Model of the AMMRV1.2 and (b) a subject-specfic model created in this study.

The "GaitNormal0003 – processed" trial was selected for analysis, and a motion and parameter optimisation performed on the generic MS model within AnyBody Version 4.1. This scaled the generic model to appropriate segment lengths based on the anthropometrics of the marker positioning in the motion capture data (see Figure 5.13(a)). The marker positioning subsequently drove the lower extremity joints through the appropriate angles, to replicate the kinematics of the recorded motion. A subsequent inverse dynamic analysis computed the associate joint and muscular loading in accordance with the recorded kinematics and ground force reactions.

A heel-to-heel strike gait cycle of the left leg was extracted from the resulting kinetics and used to estimate the joint and muscular loading associated with a normalised gait pattern. The predicted muscle forces are presented within the groups of the anterior, posterior and medial thigh muscles (see Figure 5.14 - Figure 5.16), and those of the gluteal region (see Figure 5.17), as suggested by Ward et al. (2009).

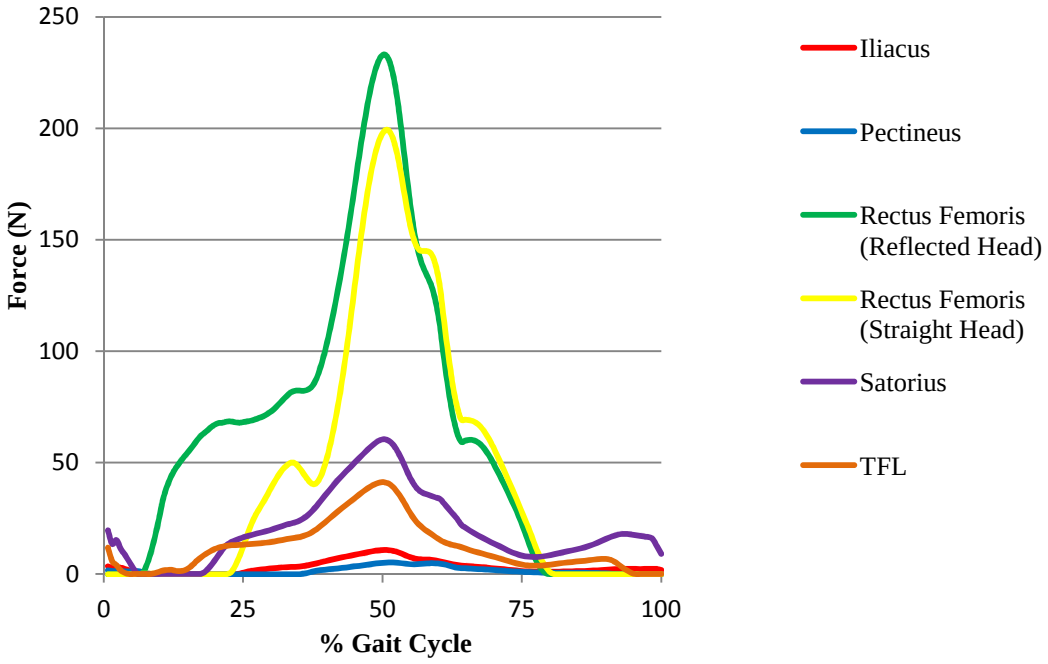

Figure 5.14. The forces of the anterior thigh muscles during the gait cycle predicted by the Lower Extremity Model.

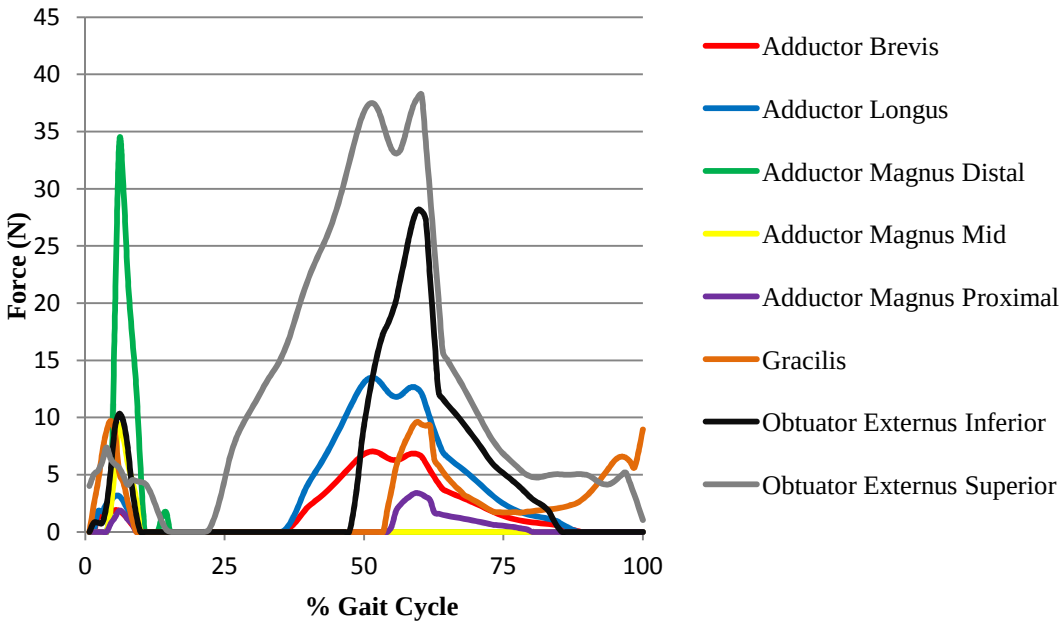

Figure 5.15. The forces of the medial thigh muscles during the gait cycle predicted by the Lower Extremity Model.

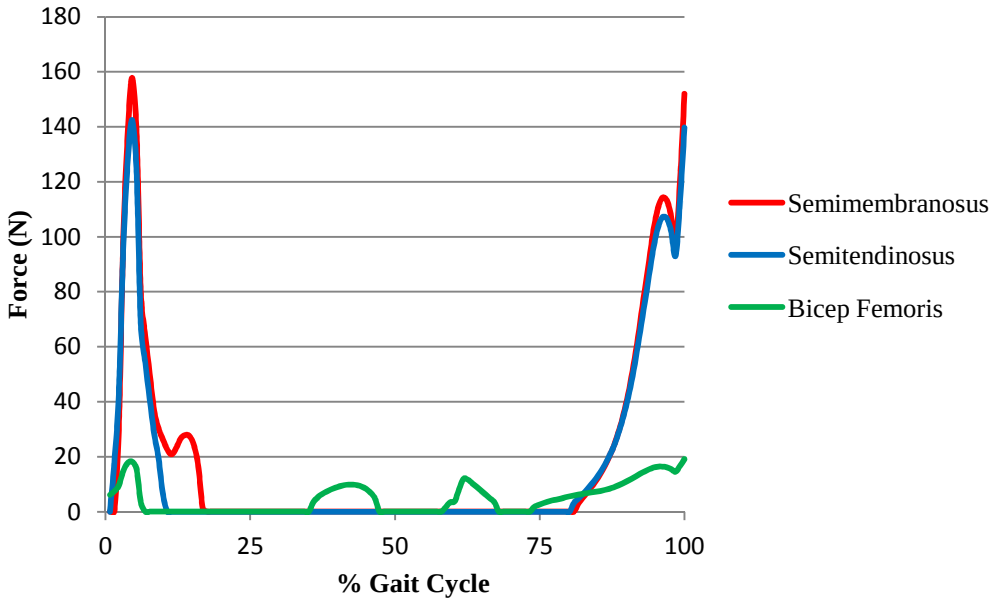

Figure 5.16. The forces of the posterior medial thigh muscles during the gait cycle predicted by the Lower Extremity Model.

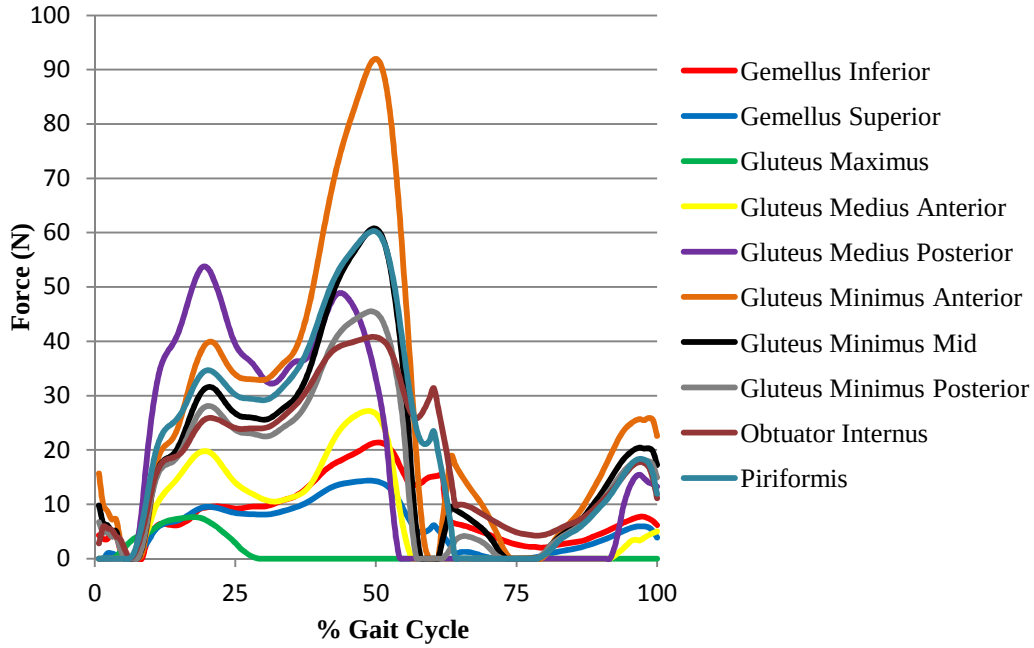

Figure 5.17. The forces of the muscles in the gluteal region during the gait cycle predicted by the Lower Extremity Model.

The computed hip joint reactions are illustrated in Figure 5.18, where the resultant displays the typical two peaks during the stance phase, although the second peak exceeded the magnitude of the first. Although this is not typical of the hip joint reaction shown in Figure 2.11, the excessive second peak has been reported within

the individual trials of Bergmann et al. (2001). However, in such cases the peak reaction of nearly 400% BW has not been previously reported during walking. However, the magnitude of the initial peak and the reactions during the swing phase are similar to those calculated for the NPA patient by Bergmann et al. (2001) (see 2.11).

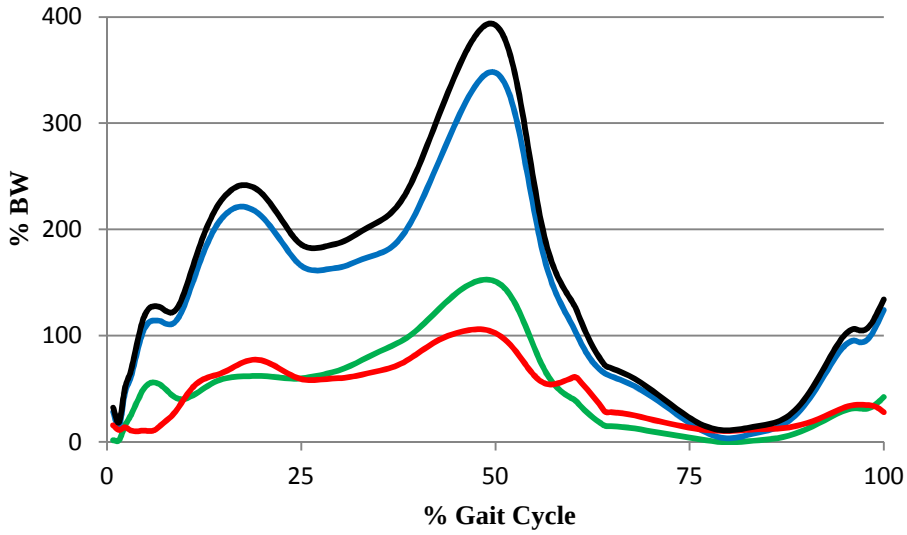

Figure 5.18. The hip joint reaction during the gait cycle predicted by the Lower Extremity Model, showing the resultant reaction (black) and the orthogonal force components which were positive medially (red), anteriorly (green) and superiorly (blue).

5.3. VALIDATION OF ALTERING GENERIC MUSCULOSKELETAL MODELS

The validity of altering generic MS models to perform subject-specific analyses was assessed through comparing predicted and experimentally measured muscle activities. A subject-specific model of a 24yr old male was created using experimentally recorded kinematical data, and the computed activity of the MS system directly compared to EMG signalling. A close correlation between the two would provide validity to the assumptions made within computational MS modelling.

5.3.1. Experimental data collection

The height and weight of a 24yr old male subject was measured using a stadiometer and SECA balance scales, respectively. Reflective markers were placed over anatomical landmarks within the lower extremity to a Helen Hayes setup, while additional markers were placed over the clavicle, sternum, and T10. Motion capture data of the subject performing a series of gait trials was collected using 10 ProReflex MCU 1000Hz cameras (Qualisys Medical, Gothenburg, Sweden), while kinetic data was obtained from three 600 x 900mm AMTI force platforms (Advanced Medical Technology, Inc, United States). The force platforms were configured in a manner which enabled capture of three consecutive foot contacts. Kinematic and kinetic data was collected using a sampling frequency of 100Hz and 1000Hz, respectively. EMG data was also collected during the trials, recorded unilaterally from the bicep femoris, rectus femoris, tibialis anterior and gastrocnemius medialis of the right leg, using an 8-channel portable, wireless EMG system (ME6000, MEGA Electronics Ltd, Finland). The origin and insertion of each muscle was identified in order to identify the appropriate muscle belly, to which two circular silver-silver chloride electrodes were placed (another electrode was placed over a bony landmark). Isometric Maximal Voluntary Contractions (iMVCs) were performed for each of the muscle in order to obtain a maximal signal, which was used to normalise the EMG readings recorded during the gait trials. All data was recorded using a 64-channel USB Analog Board, and synchronised via Qualisys Track Manager (Qualisys Medical, Gothenburg, Sweden).

5.3.2. Subject-specific musculoskeletal modelling

The experimental data was imported into Visual 3D (C-Motion, United States), a biomechanical analysis and modelling software package. A 3D model of the skeleton was constructed based on positioning of the motion capture markers during a static trial. The motion trials were cut down to identify a complete gait cycle of the right leg, and the kinematic data interpolated and filtered using a low-pass filter with a cut-off frequency of 6Hz. The kinetic data was also filtered using a low-pass filter with a cut-off frequency of 25Hz. The EMG data was rectified and filtered using a moving root mean square with a moving window of 25 frames, and subsequently normalised to the maximum signal obtained during the iMVC trials.

The processed kinematic and kinetic data from VIS 3D for each trial was then imported to AnyBody Version 4.2 as a .C3D file. A motion and parameter optimisation was performed on the generic model of the AMMRV1.2 (see Figure 2.13), to anthropometrically scale the skeletal segments to the motion capture marker positions. The marker positioning throughout the gait cycle was then used in a kinematical analysis, to drive the skeletal segments and replicate the recorded motion. Additional definition of the subject height and weight enabled subsequent inverse dynamical calculations to compute the kinetics of the subject-specific MS system. A total of four MS models of the subject were created which replicated four independent walking trials.

5.3.3. Comparisons between computed and experimental data

Comparisons between the kinematics of each gait trial did not display any significant variation. Therefore, the %iMVC of the EMG signalling and the computed forces of the bicep femoris, rectus femoris, tibialis anterior and gastrocnemius medialis for the

four gait trials were pooled and averaged. As shown in Figure 5.19 - Figure 5.22, a low level of correlation was observed between the predicted muscle forces and the experimentally measured activity. This was evidence within the biceps femoris, where during a phase of predicted muscle inactivity, the experimental recordings produced the highest %iMVC readings (see Figure 5.19). The opposite occurred in the rectus femoris, where during a time period of low measured activity, relatively high muscle forces were predicted (see Figure 5.20). Figure 5.21 displayed the greatest comparison between the predicted muscle forces and measured activity, where both produced a maximal high peak roughly occurring during the stance phase of the gait cycle. However, the maximal muscle activity was measured to occur before the computed maximum force, producing a time deviation between the two of ~20% of the gait cycle. The gastrocnemius medialis also produced similar profiles during the gait cycle (see Figure 5.22), although the EMG signalling was observed to display a delayed response in relation to the computed muscle activity.

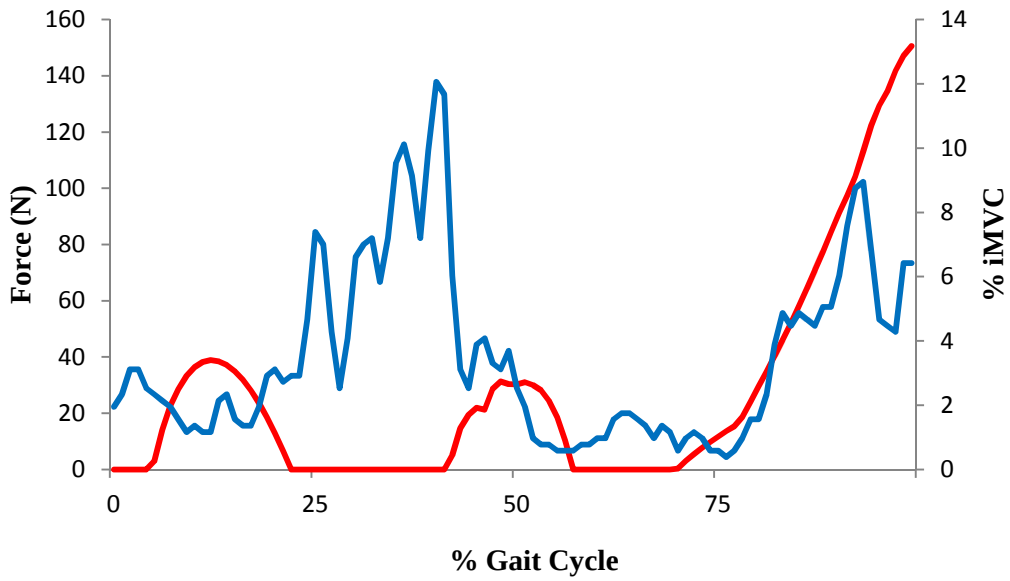

Figure 5.19. Comparison between the calculated muscle force of the subject-specific MS model (red) and the muscle activity measured through EMG (blue) for the biceps femoris.

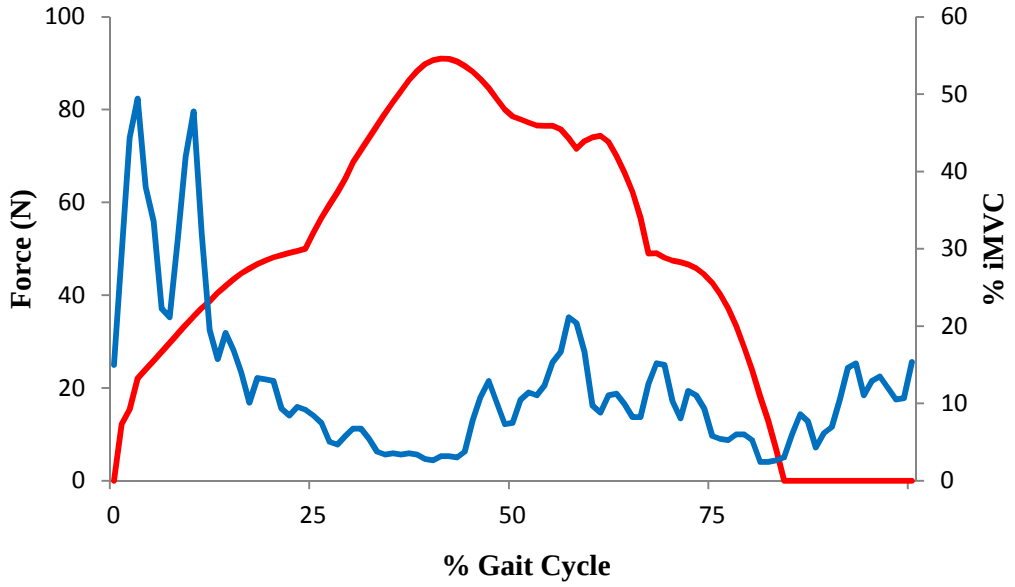

Figure 5.20. Comparison between the calculated muscle force of the subject-specific MS model (red) and the muscle activity measured through EMG (blue) for the rectus femoris.

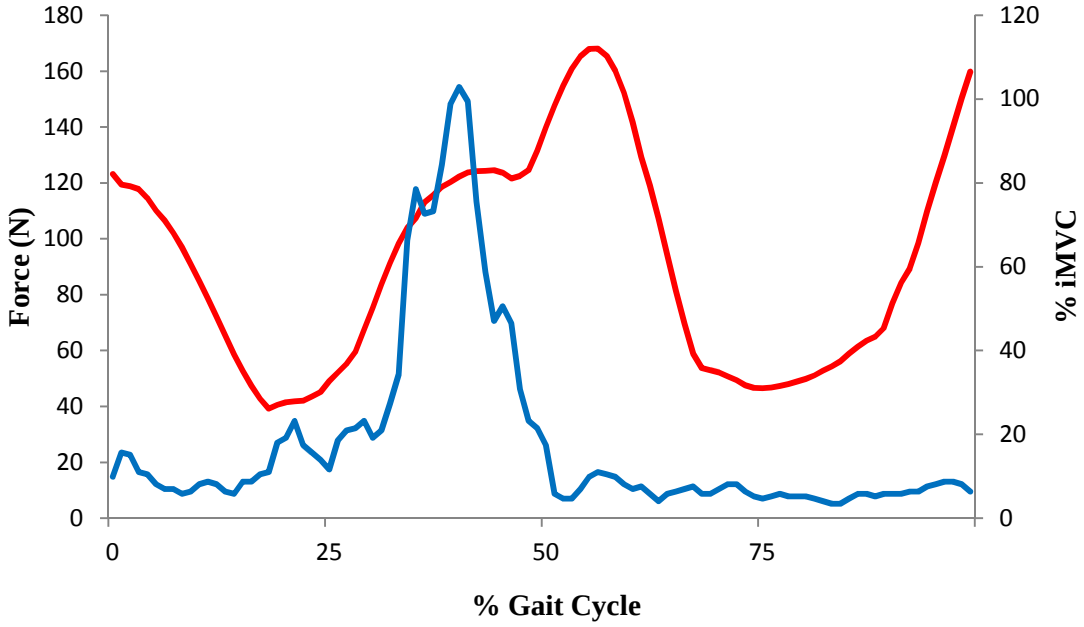

Figure 5.21. Comparison between the calculated muscle force of the subject-specific MS model (red) and the muscle activity measured through EMG (blue) for the tibialis anterior.

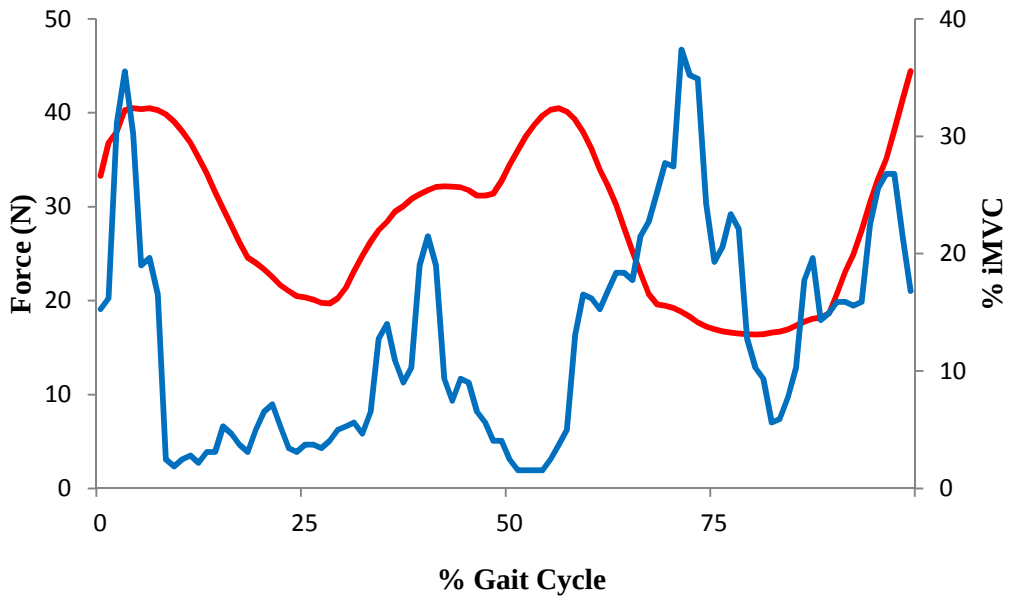

Figure 5.22. Comparison between the calculated muscle force of the subject-specific MS model (red) and the muscle activity measured through EMG (blue) for the gastrocnemius medialis.

Although the data displayed in Figure 5.19 - Figure 5.22 questioned the validity of the subject-specific MS model, it was determined that the limited complexity of the analysis was insufficient from which to base conclusions. The validity of the computerised simulations primarily concerned the accuracy of the anthropometric scaling from the generic model, and the representation of the MS system. An incorrect estimation of segment lengths by the motion and parameter optimisation, can cause a subsequent error in the modelled joint positioning. Therefore, the joint angles produced when replicating the recorded motion, will not be representative of the subjects kinematics. This also results in muscular lines of action which do not truly reflect those of the subject. The combined effect of modelling incorrect kinematics and muscular excursions, would have resulted in inverse dynamics calculations which predicted inaccurate joint kinetics and muscle forces. However, the kinematical data of the subject-specific MS models during all trials were observed to be similar to those computed in Visual 3D, implying the kinematical movement was faithfully replicated.

Analysis of the EMG signalling raised issues concerning the validity of the recorded experimental data. As observed in Figure 5.19, the recorded muscle activity formed a series of fluctuations during the production of the maximal peak, rather than following a smooth profile. As this constant deviation of the muscle activity is not consistent with the functioning an efficient MS system, the experimental readings were presumed to be inaccurate. The possible inaccurate location of the muscle belly could have hampered the ability of the EMG to detect the muscle signalling, and have may resulted in cross signalling from other muscles.

The analysis of the subject-specific MS models validity proved fairly inconclusive, as the accuracy of the experimental data was comprised. Due to the complexity of performing EMG experimentation, analysing validity through this sole measure was not suitable. Further attempts to validate the subject-specific MS models through this method would also have to ascertain experimentally determined muscle forces (rather than activity alone). This would not only assess the accuracy of the muscle activity predicted by computer simulations, but also the magnitudes as well. Analysing only one subject was also a limitation of this study, as a greater dataset is required from which to base conclusions.

6. FINITE ELEMENT MODELLING

The mechanical response of the juvenile hemi-pelves constructed in section 4.6, when experiencing the MS loading detailed in Chapter 5, was computed through a series of FE analyses. The predicted pelvic strain distributions were then used to evaluate the role that mechanical strain plays within the formation of the juvenile pelvic trabecular histomorphometry.

All FE analyses were performed within ANSYS, and based on tetrahedral meshes generated within AMIRA, which were created through converting the digitised hemi-pelvic reconstructions into polygon surface models. In all cases, the tetrahedral element parameters were adjusted to the software recommended aspect ratio and tetrahedral quality, to ensure the highest mesh quality possible. Solid 10-noded tetrahedral elements (SOLID 92) were modelled to represent trabecular bone and triradiate cartilage (if present), while 4-noded shell elements (SHELL 63) clad around the structural exterior replicated cortical bone. Shell elements did not cover the pelvic exterior in regions where trabecular bone connected to triradiate cartilage. This aimed to faithfully replicate the ossifying pelvic bone, which would not have developed a cortical exterior in regions such as the acetabulum. The pelvic bone was represented as a linear elastic material with properties taken from literature, using moduli of 70MPa (υ = 0.2) and 17GPa (υ = 0.3) for trabecular and cortical bone, respectively (Dalstra et al, 1995; Dalstra and Huiskes, 1995; Majumder et al, 2005).

The muscle forces predicted by the prenatal and adult MS models (see Chapter 5), were defined as distributed loads over the surface nodes within muscular origin sites, which were identified using the descriptions of Scheuer and Black (2000), Moore and Agur (2002) and Sobotta (2006). For load regimes which were based on the forces of the adult MS model, the muscular line of actions were calculated through

vector mechanics between the point of origin and insertion (or nearest via point). As the adult MS model contained numerous fibres for muscles with broad attachment sites (see Figure 5.13), the line of action for the fibre representing the midpoint of the muscle origin was selected. Large muscles were defined in the same arrangement as the adult MS model, dividing the gluteus medius, gluteus minims and iliacus into three separate areas, and the obturator internus and externus into anterior and posterior segments. The FE modelling of the prenatal muscular architecture replicated that of the prenatal MS model. The hip joint forces were also modelled as distributed loads, and applied to the exterior nodes within the acetabulum. The BW for the juvenile ages modelled was estimated from CDC growth charts (Ogden et al., 2002). The constraints applied to each FE model are described for the individual juvenile pelves, and were based on the results of a validation study into the differing methods of constraining the pelvis.

The trabecular bone was analysed in terms of the von Mises and minimal principal strains (i.e. compressive), to distinguish any correlations between predicted distributions and the trabecular trajectories described by Macchiarelli et al. (1999) (see Figure 2.8). Strain magnitudes were also analysed to observe if they exceed the remodelling thresholds suggested within literature (Martin, 2000; Ward et al., 2009). The compressive strain of the pelvis was deemed an appropriate measure to analyse, due to the limited movement of the SIJ (Gunn, 1984) and the predominantly superiorly directed hip joint loading during gait (see Figure 2.11). Therefore, such loading of the pelvis was expected to predominately place the pelvis under compression. Cortical stresses were also analysed to identify possible similarities between those reported within literature (Dalstra and Huiskes, 1995; Majumder et al., 2005; Phillips et al., 2007). As the reported histomorphometry of the pelvic trabecular bone is limited to the ilium (Macchiarelli et al., 1999; Rook et al., 1999;

Cunningham and Black, 2009a, 2009b; Volpato, 2008), this study only focused on the iliac stress/strain distributions, although the overall pelvic mechanics was documented.

6.1. VALIDATION OF THE METHODS OF CONSTRAINT

Numerous methods have been documented within literature of modelling the SIJ, with the level of complexity predominately determined by the anatomical features available. Studies which acquire CT scans of the pelvic girdle often model movement of the pelvis relative to a constrained sacrum, with the two connected through articular cartilage (Li et al., 2007; Majumder et al., 2007; Majumder et al., 2008a; Leung et al., 2009; Majumder et al., 2009). In instances where an articulated sacrum is not available, the SIJ has been modelled as a solely rotational joint through constraining the translation (Majumder et al., 2005). Alternatively, the pelvic interaction with the sacrum has also been presumed to be fixed, therefore the SIJ has been constrained in all DOF (Dalstra and Huiskes, 1995; Kaku et al., 2004; Cilingir et al., 2007; Zant et al., 2008; Coultrup et al., 2010). This may be a reasonable assumption when modelling the elderly, where the SIJ fuses to cause a decrease in the range of movement. However, its application to the juvenile anatomy is considered less valid as increased movement is expected due to the large amount of cartilage present.

Previous FE analyses of the pelvis have also modelled the physiological interaction between the two hemi-pelves via the pubic symphysis, which is often represented as either a rigid link (Phillips et al., 2007) or a hyperelastic material (Li et al., 2007; Majumder et al., 2007; Kim et al., 2009; Leung et al., 2009). This enables force dissipation from a loaded hemi-pelvis through the pubic symphysis and into the contralateral side. However, in cases where only the hemi-pelvis is modelled, the

pubic symphysis is considered as a rigid connection and constrained in all DOF (Kaku et al., 2004; Cilingir et al., 2007; Zant et al., 2008; Coultrup et al., 2010). Subsequently, rather than allowing force to be transferred onto the contralateral side, stress concentrations have been observed to form along the superior pubic ramus (Kaku et al., 2004). To evaluate the influence of the varying constraint methods upon the mechanics of the pelvis, four models were created which replicated constraints of both the pelvis and hemi-pelvis.

6.1.1. Construction of the validity models

The validation study was performed on the digitised 19yr old left hemi-pelvis created within section 4.6.4. The digitised model was initially rotated within AMIRA to the reference frame described by Wu et al. (2002). The hemi-pelvic rotation within the horizontal plane was unknown due to its original disarticulation from the sacrum, therefore a corresponding angle between the ASIS and PSIS was taken from the morphological dataset of Klein Horsman et al. (2007). Rotation of the left hemi-pelvis to a corresponding angle provided a means of physiologically representing the horizontal rotation. An FE model of the 19yr old pelvic girdle could not be created directly from the original specimen, due to the disarticulation between the two hemi-pelves (as shown in Figure 4.23). Therefore, the left hemi-pelvis was mirrored about the sagittal plane within AMIRA, to generate a digitised volumetric model of a contralateral hemi-pelvis. As illustrated in Figure 6.1, the two hemi-pelves were relatively positioned with a 2mm gap at the pubic symphysis (Phillips et al., 2007), and subsequently merged into one entity.

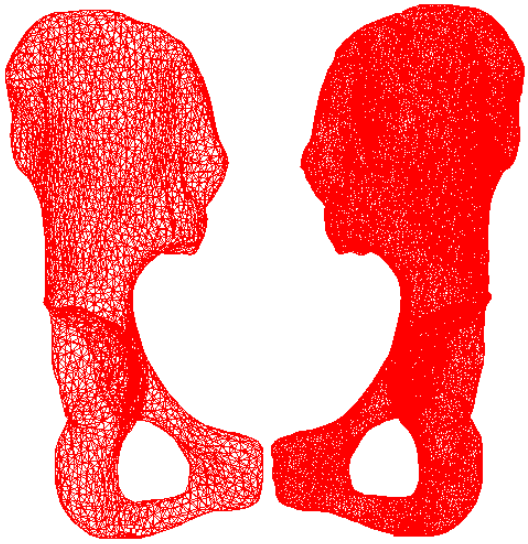

Figure 6.1. The mesh of the 19yr old pelvis within AMIRA, showing the mirrored contralateral pelvis with a lower element density compared to the left hemi-pelvis.

As the sole function of the reflected hemi-pelvis was to provide support for the left side, the number of surface faces used to replicate its geometric features was reduced to limit its mesh density (see Figure 6.1). This was performed to confine the total element number within the model and achieve an appropriate computation time for analyses. The meshed 19yr old pelvis contained a total of 208,655 volumetric and 36,396 shell elements to present the trabecular and cortical bone. A uniform thickness of 1.5mm was applied to the shell elements, as performed by Cilingir et al. (2007) and Coultrup et al. (2010). A pubic disc was incorporated into the pelvic FE model via creating a volume which connected the two symphyses within ANSYS, as shown in Figure 6.2(a). The volume was defined through four attachment sites which aimed to match the location of the anterior and posterior limits of the superior and inferior symphyses. The created volume was meshed with 60 20-noded brick elements (SOLID 186), and defined with hyperelastic material properties based on the Mooney-Rivlin parameters of C_{10} = 0.1MPa, C_{01} = 0.45MPa and C_{11} = 0.6MPa (Li et al., 2006; Kim et al., 2009).

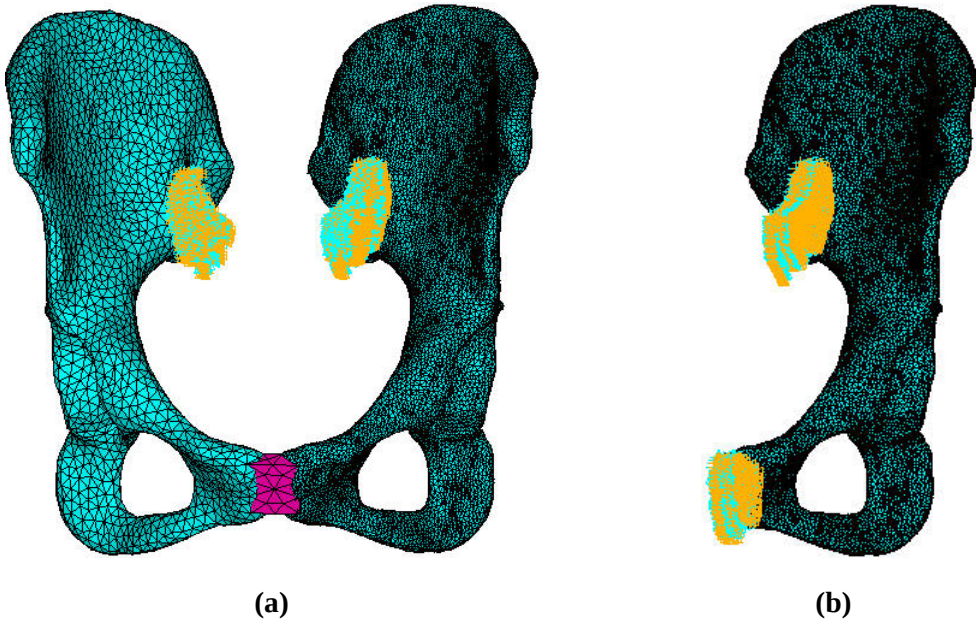

Figure 6.2. FE modelling of the 19yr old (a) pelvis with a hyperelastic pubic disc and constrained SIJ, and (b) left hemi-pelvis with a constrained SIJ and pubic symphysis.

Unfortunately, the solid tetrahedral elements only permitted translational movement, which proved problematic when attempting model rotation of the SIJ. Therefore, an artificial layer of cartilage was modelled through initially creating areas over the exterior elements within the SIJ articulation area. These were then extruded medially by a distance of 1mm to roughly represent a layer of the SIJ articular cartilage (McLauchlan and Gardner, 2002), as illustrated in Figure 6.3. The volumes were meshed with brick elements (SOLID 186), producing 8,433 elements on the left hemi-pelvis and 1,572 on the right.

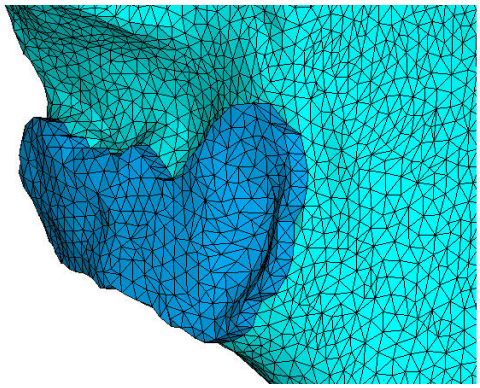

Figure 6.3. Modelling a layer of cartilage through defining volumes within the articulation area of the SIJ.

As brick elements permitted rotational deformation, constraining the nodes along the medial layer of the cartilage subsequently allowed for rotation of the pelvis. However, the extent of the rotation permitted was dependent on the material modulus applied to the SIJ cartilage elements. Definition of a linear elastic articular cartilage modulus, which can be as low as 5MPa (Anderson et al., 2005), would have produced excessive deformation under loading. Comparatively, modelling as a hyperelastic material increased the modelling complexity and the computational time required for analysis. As modelling of this nature has not been previously documented, there is no indication as to an appropriate modulus for this application. Therefore, the cartilage was modelled with a high material modulus (E = 200GPa, $\upsilon = 0.3$) to control the deflection.

Four FE models were created which aimed to replicate the differing methods employed to represent both the SIJ and pubic symphysis. The features of the individual models were as follows:-

Model 1 - The left hemi-pelvis constrained in all DOF at the SIJ and pubic symphysis, as shown in Figure 6.2(b);

Model 2 - The left hemi-pelvis constrained in all DOF at the SIJ, and in the inferio-superior and posterio-anterior translation at the pubic symphysis;

Model 3 - The pelvic girdle constrained in all DOF at the SIJ, as shown in Figure 6.2(a);

Model 4 - The pelvic girdle with the additional SIJ cartilage, to which the medial nodes were constrained in all DOF.

The SIJ constraints (except model 4) were applied to the nodes within the articulation area. All models were loaded with the muscular and hip joint loading predicted by the adult MS model (described in section 2.2), at the midpoint of the single leg

support phase (phase 3 of Table 2.1). This phase was selected as it marked a point of high MS activity (Dalstra and Huiskes, 1995), thus loading the pelvis to its maximal physiological state associated with the gait cycle. This aimed to aid inter-model comparison of the cortical and trabecular von Mises stresses. Pelvic stresses were selected for analysis as they enabled comparisons with the findings of literature, either at the same gait phase (Dalstra and Huiskes, 1995; Majumder et al., 2005) or under similar loading (Phillips et al., 2007).

6.1.2. Evaluation of the constraint methods

The different methods employed to replicate the 19yr old left hemi-pelvis and pelvic girdle produced comparative cortical von Mises stress distributions, although varying magnitudes were observed. As illustrated in Figure 6.4, the left hemi-pelvis of all models displayed significant stress concentrations within the superior acetabular quadrants, which emanated anteriorly towards the AIIS and posteriorly to the greater sciatic notch (on the lateral side). These distributions are similar to the findings of Dalstra and Huiskes (1995) and the ML model of Phillips et al. (2007) (see Figure 2.18). Medially, large stresses progressed inferiorly from a significant concentration around the SIJ, travelling along the ilio-pubic ridge and onto the superior pubic ramus. Additional high stresses were also observed along the obturator foramen and within the inferior quadrants of the acetabulum, of which the latter has not been previously reported.

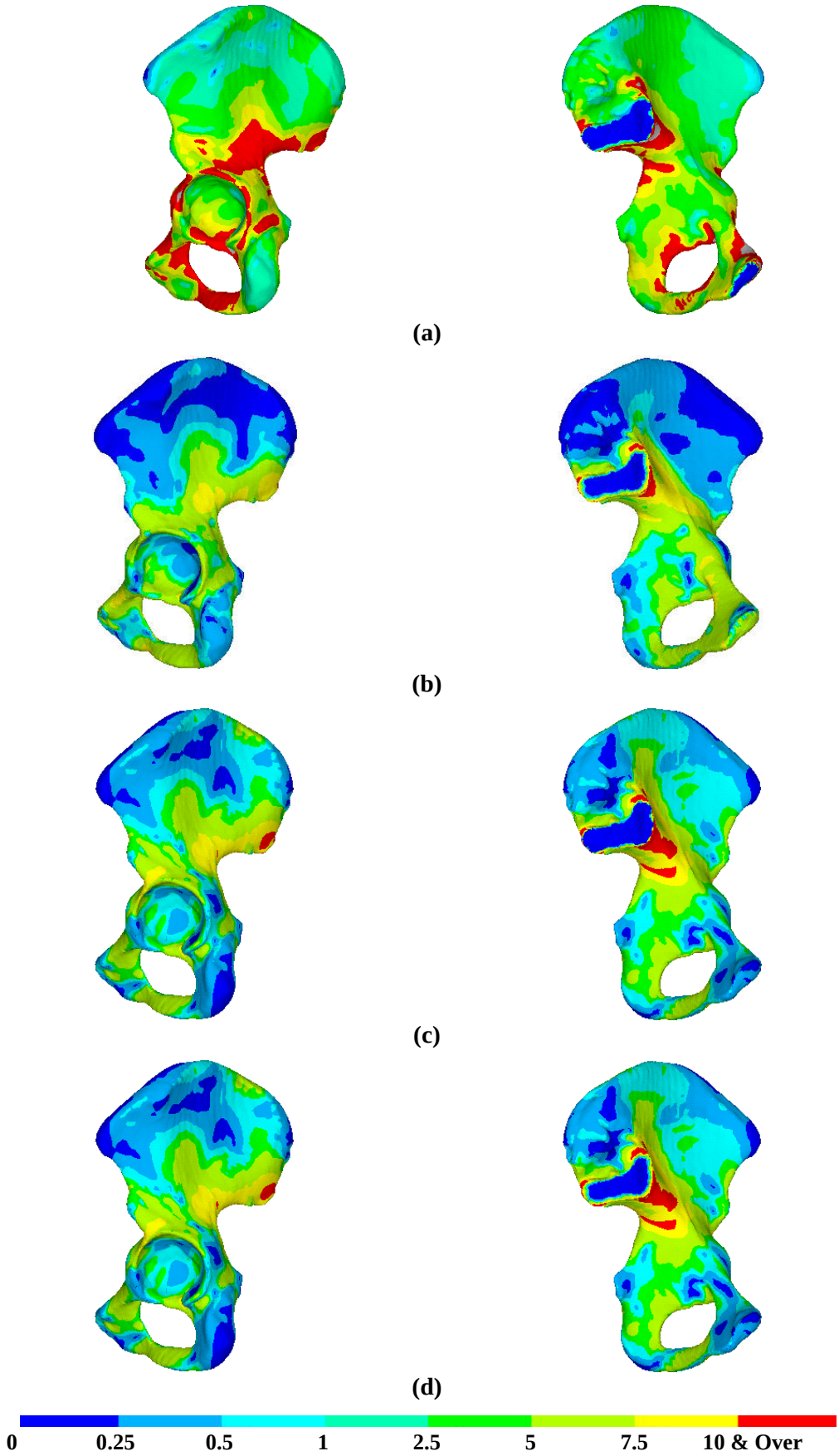

Figure 6.4. The cortical von Mises stress distribution (MPa) of the 19yr old left hemi-pelvis produced by the varying methods of constraining the pelvis, showing (a) model 1, (b) model 2, (c) model 3 and (d) model 4.

Constraining the hemi-pelvis in all DOF at the SIJ and pubic symphysis produced cortical stresses which exceeded 200MPa (see Figure 6.4(a)), significantly higher than those within literature. Such magnitudes are unrealistically high considering the cyclic loading that the pelvis experiences. Through permitting translation of the pubic symphysis, the entire cortical structure was observed to be stress relived, particularly at the SIJ and along the superior pubic ramus (as illustrated in Figure 6.4(b)). Consequently, maximal stresses significantly reduced in magnitude, and regions such as the superior ilium and ischium became virtually unloaded. The resulting magnitudes were more comparable to those reported within literature. Modelling of the pelvis with a hyperelastic pubic disc produced a slightly altered stress distribution, with larger magnitudes concentrated around the greater sciatic notch and SIJ (see Figure 6.4(c)). Inclusion of the contralateral hemi-pelvis also caused significant stress relieving of the pubic symphysis, similar to that reported by Phillips et al. (2007). As shown in Figure 6.4(d), inclusion of the SIJ cartilage did not alter the mechanical response of the pelvis in comparison to the fully constrained joint.

As illustrated in Figure 6.5, a greater inter-model variance was observed within the trabecular von Mises stresses of the left hemi-pelvis. However, the largest magnitudes were constantly located within the central acetabulum, consistent with findings of Phillips et al. (2007). A second concentration of lesser magnitude also travelled superiorly from the acetabular rim through the medial and lateral ilium. Within model 1, the ischium and pubis remained virtually unloaded, while the maximum stresses did not exceed 0.75MPa (see Figure 6.5(a)), both of which are comparable to literature.

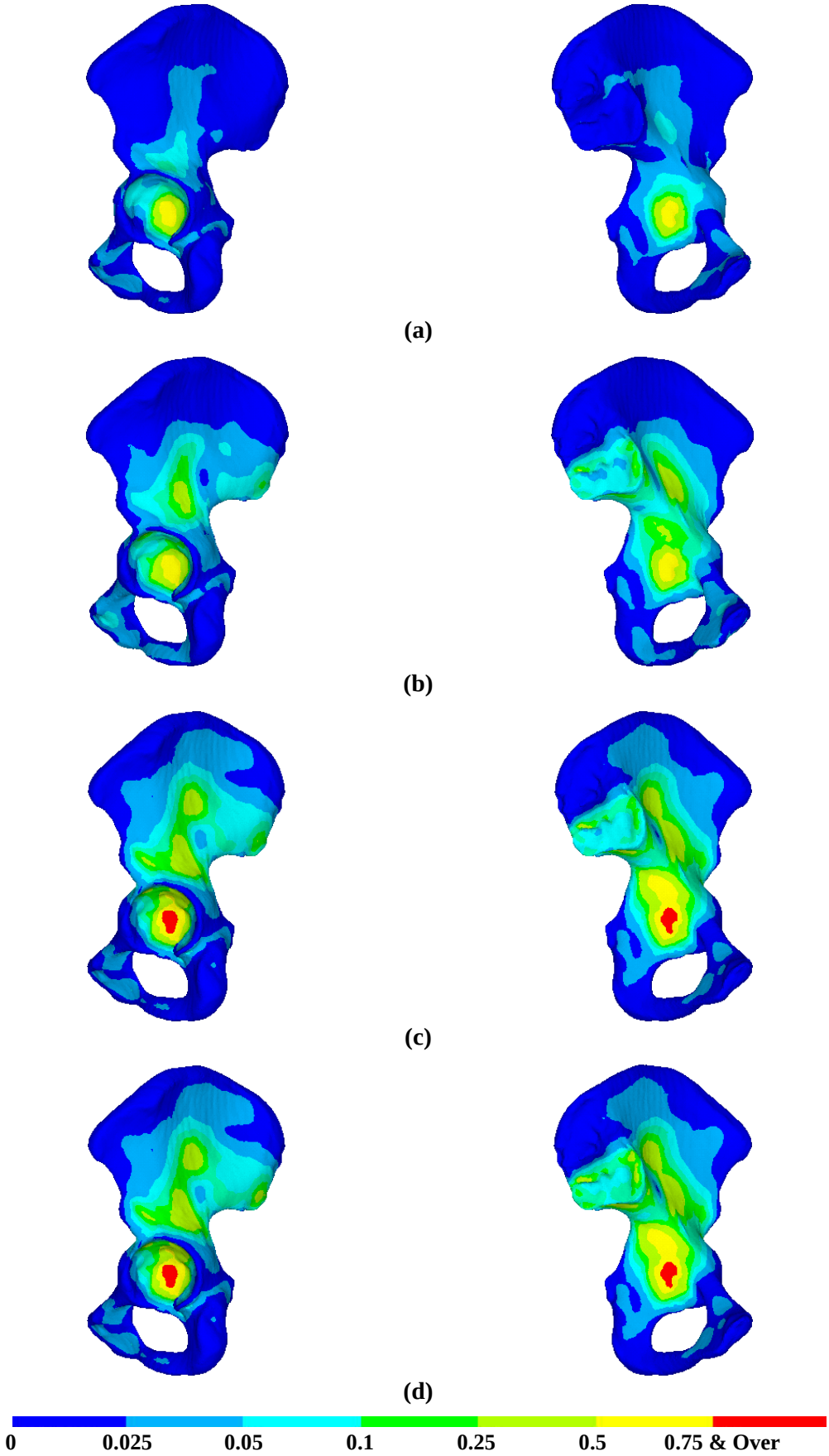

Figure 6.5. The trabecular von Mises stress distribution (MPa) of the 19yr old left hemi-pelvis produced by the varying methods constraining the pelvis, showing (a) model 1, (b) model 2, (c) model 3 and (d) model 4.

Trabecular stresses were observed to increase in model 2, particularly within the central medial and lateral iliac blade, where the magnitudes were similar to those located within the acetabulum (see Figure 6.5(b)). Stress concentrations also formed around the SIJ, similar to the ML model reported by Phillips et al. (2007) (see Figure 2.18), while the loading was greater along the obturator foramen and pubis ramus (although the relative increase remained small). The trabecular von Mises stress distribution did not produce magnitudes which were constant factors of the cortical von Mises stresses, as reported by Dalstra and Huiskes (1995) and Majumder et al. (2005).

Stress magnitudes increased further through modelling of the contralateral hemi-pelvis, producing acetabular stresses exceeding 0.75MPa and an additional concentration within the iliac fossa (see Figure 6.5(c)). Consequently, the overall stress state of the superior ilium increased, although the relative difference from Figure 6.5(b) remained small. Once again, the permitted rotation of the SIJ did not evoke any variation in the stress distribution, as shown in Figure 6.5(d).

Figure 6.4 and Figure 6.5 demonstrated that although inclusion of the contralateral hemi-pelvis slightly increased trabecular stresses, it proved successful in relieving regions of excessive cortical stresses, particularly at the pubic symphysis. Consequently, pelvic bone stresses were more consistent with the values of literature and more evenly distributed across the hemi-pelvis, favourable to maintaining structural integrity. Therefore, these results suggested that modelling of the pelvis with a hyperelastic pubic disc should be employed to accurately capture its physiological mechanical response. The identical response of the left hemi-pelvis in models 3 and 4 suggested that the modulus of the SIJ cartilage was too high to cause deformation under MS loading. Subsequently, model 4 failed to permit rotation of

the pelvis at the SIJ. The two models also produced the largest maximal displacement of 2.5mm, which was higher than those reported within literature. However, in instances when only hemi-pelvic modelling is possible, a degree of translation should be permitted at the pubic symphysis to alleviate high stresses and produce physiological stress/strain distributions.

6.2. MODELLING OF THE 19 YEAR OLD PELVIS

Due to the more uniform von Mises stress distribution created through inclusion of the contralateral pelvis, further modelling of the 19yr old pelvis was based on the previously developed model 4. The material properties and constraints remained the same, despite the high SIJ cartilage modulus proving unsuccessful in enabling pelvic rotation. The original modulus was maintained as modelling with either articular cartilage or hyperelastic properties, was predicted to cause excessive deformation. In addition, the application of higher loading compared to the previously modelled MS regime, was expected to have greater capabilities of enabling rotation at the SIJ.

The muscle and hip joint reaction forces predicted by the adult MS model (detailed in section 2.2), was recorded at the eight phases of the gait cycle described in Table 2.2, as modelled by Dalstra and Huiskes (1995) and Majumder et al. (2005), and applied to the 19yr old FE model. Two additional load cases were also modelled which cumulated the maximal forces exerted by the pelvic muscles and the hip joint throughout the gait cycle. However, modelling of such a scenario proved problematic when considering the lines of action to apply, as the maximal force of each muscle did not occur at the same time (see Figure 5.14 – Figure 5.17) Therefore, one model replicated the lines of action of each muscle at the instance when their maximum force occurred, while another modelled the lines of action associated with a standing position. As the adult MS model only replicated walking, muscular paths at a neutral

flexion angle could not be determined from this model. Consequently, muscular lines of action during standing were taken from Klein Horsman et al. (2007), while the hip joint reaction force was measured from the Standing Model of the AMMRV1.2 within AnyBody Version 4.1.

The cortical and trabecular von Mises stresses of the left hemi-pelvis were initially analysed to ensure that each model reacted in a physiological manner when compared to literature (Dalstra and Huiskes, 1995; Majumder et al., 2005; Phillips et al., 2007). Comparisons between the locations of the largest von Mises stresses and minimum principle strains, and the identifiable trabecular trajectories within the adult ilium (see Figure 2.8), were subsequently made.

6.2.1. Stress and strain distribution associated with the gait cycle

The cortical von Mises stress distributions shown in Figure 6.6, displayed the largest stresses occurring during the single support phases. During the initial gait cycle stages illustrated in Figure 6.6(a) - Figure 6.6(c), the highest cortical stresses were observed to concentrate around the SIJ and the ilio-pubic ridge on the medial side, and the greater sciatic notch and PIIS laterally. At the onset of the double support phase (see Figure 6.6(d) and Figure 6.6(e)) these concentrations spread, causing a subsequent increase in the overall stress state of the iliac fossa and crest. Additionally, stresses within the lateral body of the pubis, medial body of the ischium and along the obturator foramen, also become greater.

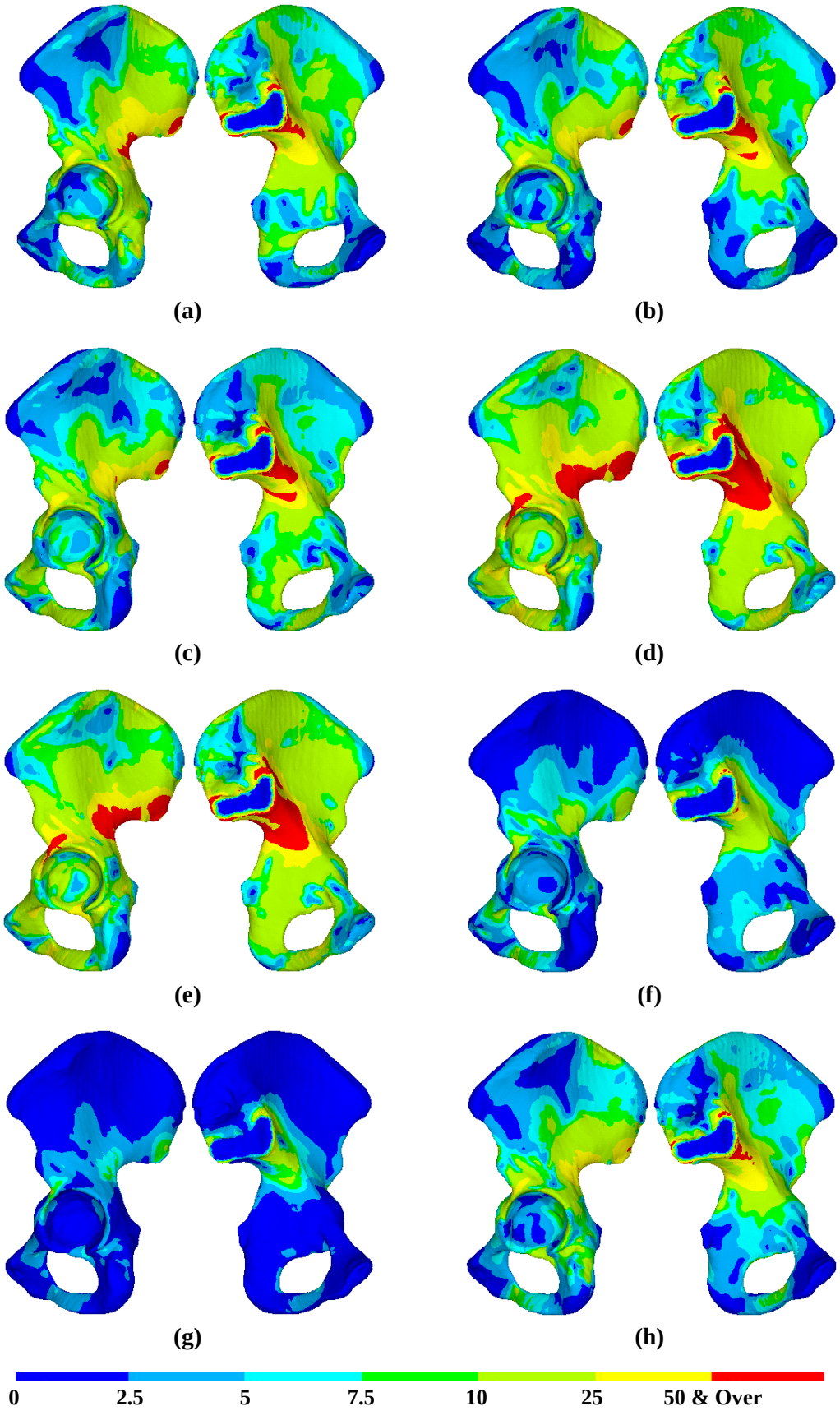

Figure 6.6. The cortical von Mises stress distribution (MPa) of the 19yr old left hemi-pelvis produced by the MS loading at the (a) 1st, (b) 2nd, (c) 3rd, (d) 4th, (e) 5th, (f) 6th, (g) 7th and (h) 8th phase of the gait cycle.

The stress concentrations which occurred during first half of the gait cycle displayed distinct comparisons to the findings of Dalstra and Huiskes (1995) and the ML model of Phillips et al. (2007). However, the cortical stress concentrations were observed to reduce significantly at the beginning of the swing phase (see Figure 6.6(f)), a stage which was still suggested to provide high loading by Dalstra and Huiskes (1995). Although, cortical stresses decreased to a minimum during the mid swing phase (see Figure 6.6(g)), and increased again at the next heel strike (see Figure 6.6(h)), consistent with literature. The overall cortical stress magnitudes within the 19yr old left hemi-pelvis were slightly higher than those within literature, with the largest concentrations ranging between 50-100MPa.

Cortical stresses within the acetabulum displayed greater variance from those within literature, which have been reported to predominately concentrate around the rim of the superior quadrants during the single support phases. Although, this is true for the acetabular stresses illustrated in Figure 6.6(a) - Figure 6.6(c), similar magnitudes were also observed around the acetabular notch. As the hemi-pelvic loading increased to the magnitudes displayed in Figure 6.6(d) and Figure 6.6(e), the acetabular stresses correspondingly rose to produce high magnitudes around the whole acetabular rim, and formed a similar concentration within the structure itself. Cortical loading within the acetabulum is not a previously reported occurrence, producing a pelvic mechanical response which is contradictory to that of literature.

A greater variation between the von Mises stress distribution of the 19yr old hemi-pelvis to those reported within literature was observed within the trabecular bone, as illustrated in Figure 6.7.

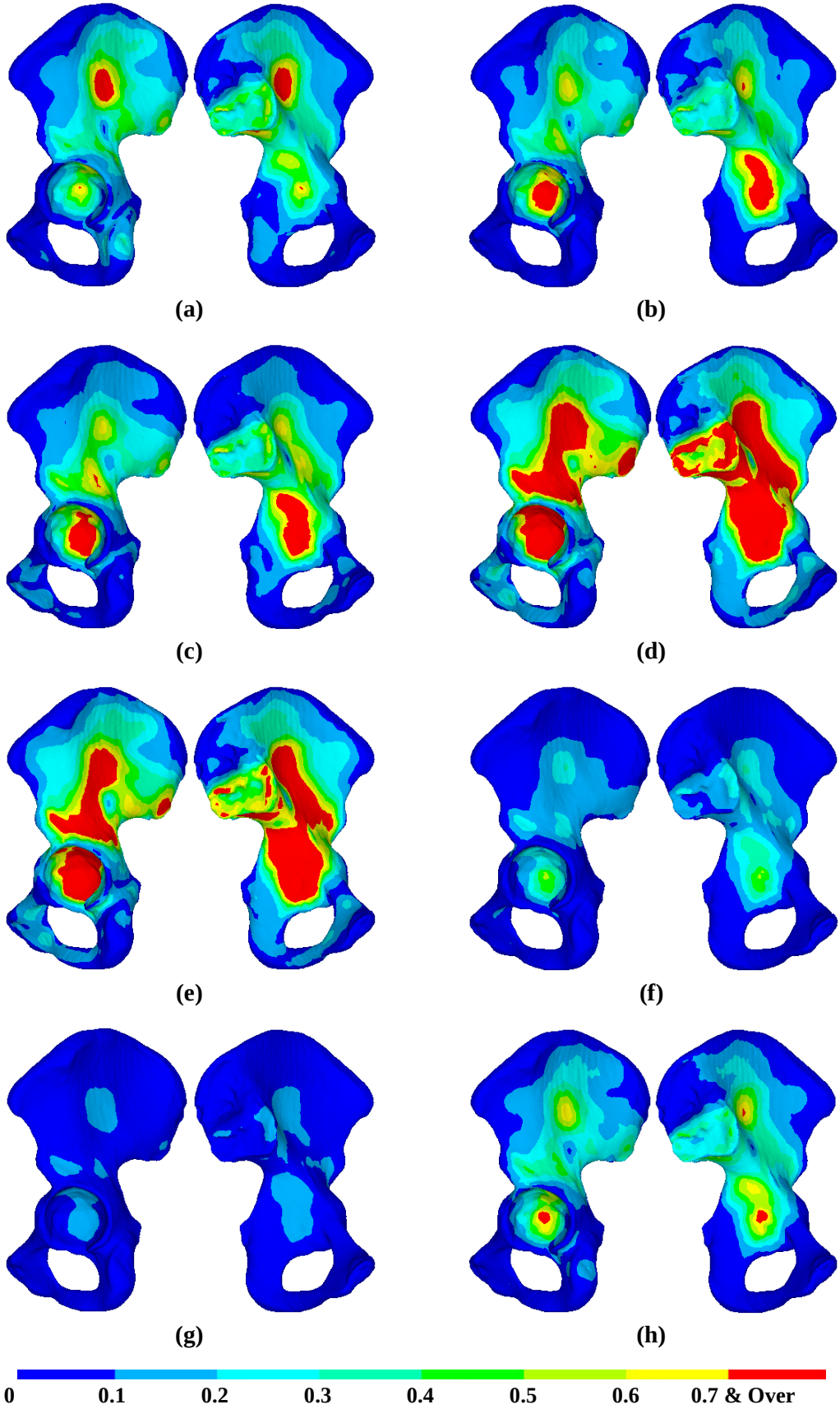

Figure 6.7. The trabecular von Mises stress distribution (MPa) of the 19yr old left hemi-pelvis produced by the MS loading at (a) 1st, (b) 2nd, (c) 3rd, (d) 4th, (e) 5th, (f) 6th, (g) 7th and (h) 8th phase of the gait cycle.

Once again, the most predominant stresses occurred during the single support stages, although they were initially confined to the central acetabulum and iliac fossa (see Figure 6.7(a) – Figure 6.7(c)), similar to that reported by Dalstra and Huiskes (1995). However, between the mid single support phase (see Figure 6.7(c)) and the double support phase (see Figure 6.7(e)), these stress magnitudes increased significantly to load the majority of the acetabulum to magnitudes over 0.7MPa. These high acetabular stresses then radiated superiorly through the medial and lateral ilium, and inferiorly towards the ischium and pubis. Consequently, stresses within the acetabulum and around the ilio-pubic ridge and greater sciatic notch, produced magnitudes which exceeded the values reported within literature. However, during the same loading regimes, the regions of the pubic symphysis, ischial tuberosity and obturator foramen remained relatively unloaded, consistent with the results of Dalstra and Huiskes (1995) and Phillips et al. (2007). As previously observed within the cortical bone, the stress magnitudes decreased dramatically during the swing phase (as shown in Figure 6.7(f) and Figure 6.7(g)) and subsequently rose again upon initiation of double support (see Figure 6.7(h)). Once again, the magnitudes of the trabecular von Mises stresses were slightly higher than those reported within literature.

Direct comparisons between the von Mises stress distribution of the 19yr old left hemi-pelvis could be made with those reported within literature. This was more evident within the cortical bone (with the exception of the acetabulum), as trabecular stress concentrations were larger than reported during the single stance phases. The observed stress distribution variation, along with the higher magnitudes, was attributed to the morphology of the younger specimen analysed and the application of loading from a newly developed MS model.

The maximum displacement which occurred during the gait cycle was 4.5mm (5th phase), which was higher than those reported in literature (Dalstra and Huiskes, 1995; Majumder et al., 2005; Phillips et al., 2007). This was possibly due to the applied MS loading being higher in magnitude than in previous pelvic modelling. However, as similarities could be identified between the von Mises stress distributions in Figure 6.6 and Figure 6.7 and those within literature, the model was concluded that the model behaved in an appropriately physiological manner. Therefore, the mechanical strains produced within the trabecular bone by the MS loading, was analysed.

The double and single stance phases produced the largest trabecular von Mises strains, as illustrated in Figure 6.8(a) – Figure 6.8(e). Initial strain distributions were similar to those observed within Figure 6.7, producing high concentrations within the central regions of the acetabulum and the medial and lateral iliac blade (see Figure 6.8(a) and Figure 6.8(b)). Within the ilium, the von Mises strains radiated from a central iliac concentration, although a secondary concentration formed laterally superior to the acetabulum (see Figure 6.8(b)). In relation to the trabecular trajectories, this inferiorly positioned concentration partially corresponds to the location of the tc and ar trabecular growth. Although the slightly larger superior concentration could be compared to the highly dense pt, it's fairly centralised positioning produces a closer correlation to the low density sm region. During the progression of the single support stages, as illustrated in Figure 6.8(c) and Figure 6.8(d), the volume of the high strain concentrations significantly increased to dominate the majority of the inferior ilium and acetabulum. Therefore, a fairly uniform strain distribution was produced, which failed to match the complexity of the iliac trabecular trajectories (see Figure 2.8).

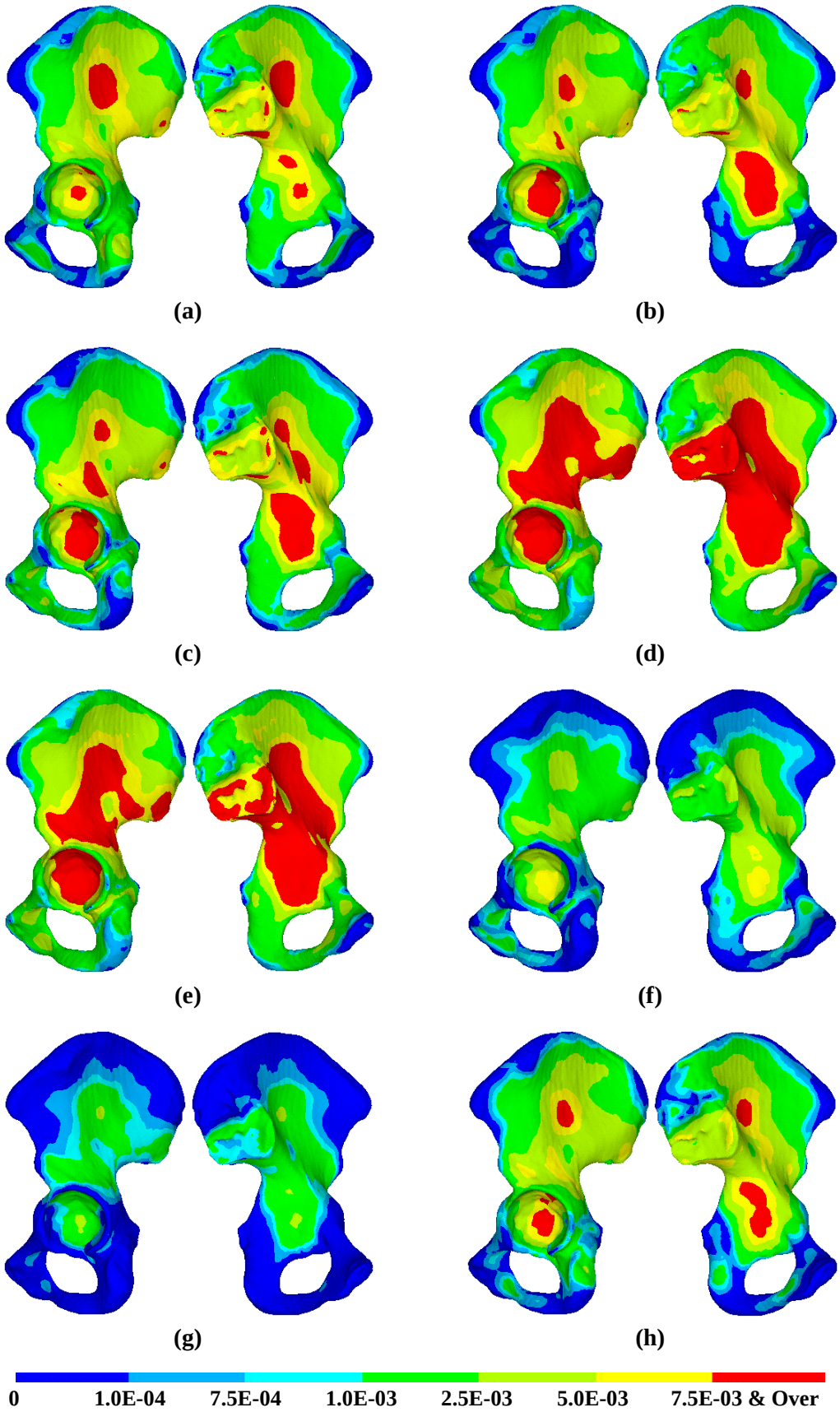

Figure 6.8. The trabecular von Mises strain distribution of the 19yr old left hemi-pelvis produced by the MS loading at the (a) 1st, (b) 2nd, (c) 3rd, (d) 4th, (e) 5th, (f) 6th, (g) 7th and (h) 8th phase of the gait cycle.

Even if such comparisons were suggested as evidence of strain related bone growth, the high concentrations observed within the mid and superior portions of the iliac blade, provided strong contrasting observations. Figure 6.8 illustrates that although the magnitudes of the high strain concentrations surpassed the suggested remodelling limits (Martin, 2000; Ward et al., 2009), areas such as the iliac crest also experienced values ranging between 1000-5000με. Such values were considered excessive considering the fairly low trabecular organisation in this region. The von Mises strains decreased during the swing phases, producing more ordered concentrations within the acetabulum and the central and inferior ilium. Therefore, due to the wide spread of the high magnitude von Mises strains, the distributions in Figure 6.8 were not considered to match the formation of the trabecular trajectories within the adult ilium.

Analysis of the minimum principal strains also failed to distinguish any clear correlations between regions of high compression, and the locations of organised trabecular growth. As illustrated in Figure 6.9, similar strain distributions were witnessed in compression during the early stance phases. As the gait cycle progressed, the areas of high strain increased in size to form a well defined concentration around the location of the tc. However, as previously observed, a concentration of similar magnitude also formed within the sm region. The compressive strains within the highest concentrations exceed those known to initiate trabecular remodelling. Although, regions around the iliac crest still experienced magnitudes up to 5000με, which was considered too high for the low trabecular definition in this location.

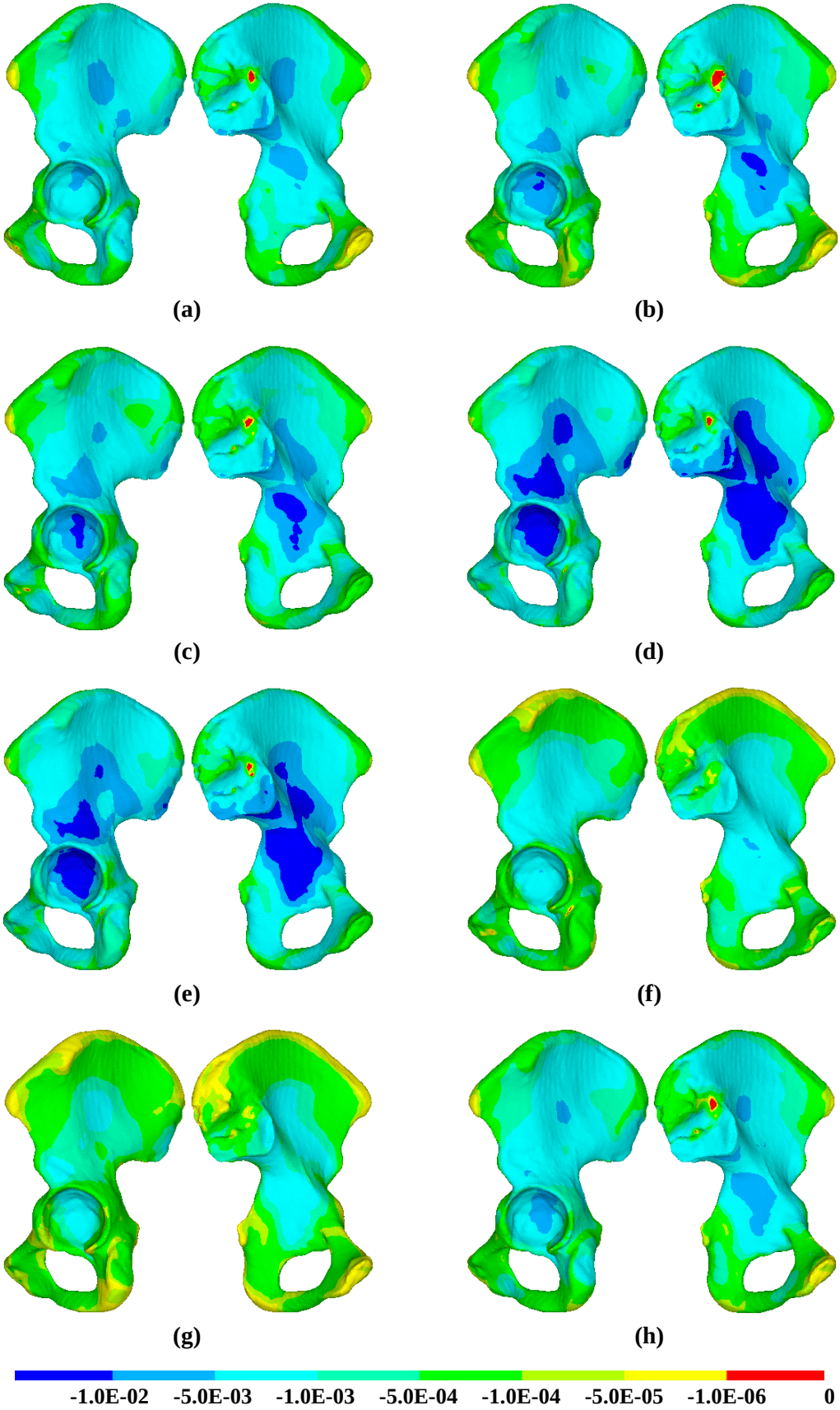

Figure 6.9. The trabecular minimum principal strain distribution of the 19yr old left hemi-pelvis produced by the MS loading at the (a) 1st, (b) 2nd, (c) 3rd, (d) 4th, (e) 5th, (f) 6th, (g) 7th and (h) 8th phase of the gait cycle.

Figure 6.8 and Figure 6.9 did not produce conclusive observations relating the von Mises and compressive stain distributions to the trabecular trajectories illustrated in Figure 2.8. However, it is unlikely that the entire pelvic trabecular network would remodel the strain distribution related to the MS loading associated with a single phase of the gait cycle. Consequently, it was presumed that the trabecular patterning is more likely to be produced in response to the cumulative loading of the gait cycle.

6.2.2. Stress and strain distribution associated with cumulative maximal muscle and hip joint forces

Figure 6.10 displays the stress and strain distribution of the left hemi-pelvis produced by the cumulative maximum muscular and hip joint forces, when modelled at the line of actions which corresponded to when they occurred. Within the cortical shell, a general von Mises stress distribution was observed which was similar to that of Figure 6.6 during the stance phases. However, although the distributions could be compared favourably with those of literature, strain magnitudes were significantly higher, and exceeded 100MPa in regions around the SIJ and greater sciatic notch (see Figure 6.10(a)). However, such magnitudes were expected due to the high level of loading applied.

The trabecular von Mises stress distribution (see Figure 6.10(b)) was comparable to those observed in Figure 6.7(a) - Figure 6.7(e), with the most noticeable concentrations within the central acetabulum and iliac blade. Once again the magnitudes were increased, and produced values exceeding 2MPa in the concentrations of high stress. Therefore, although the applied MS loading was significantly different from those related to the individual gait cycle phases, only the trabecular stress magnitudes altered significantly, and not the distribution.

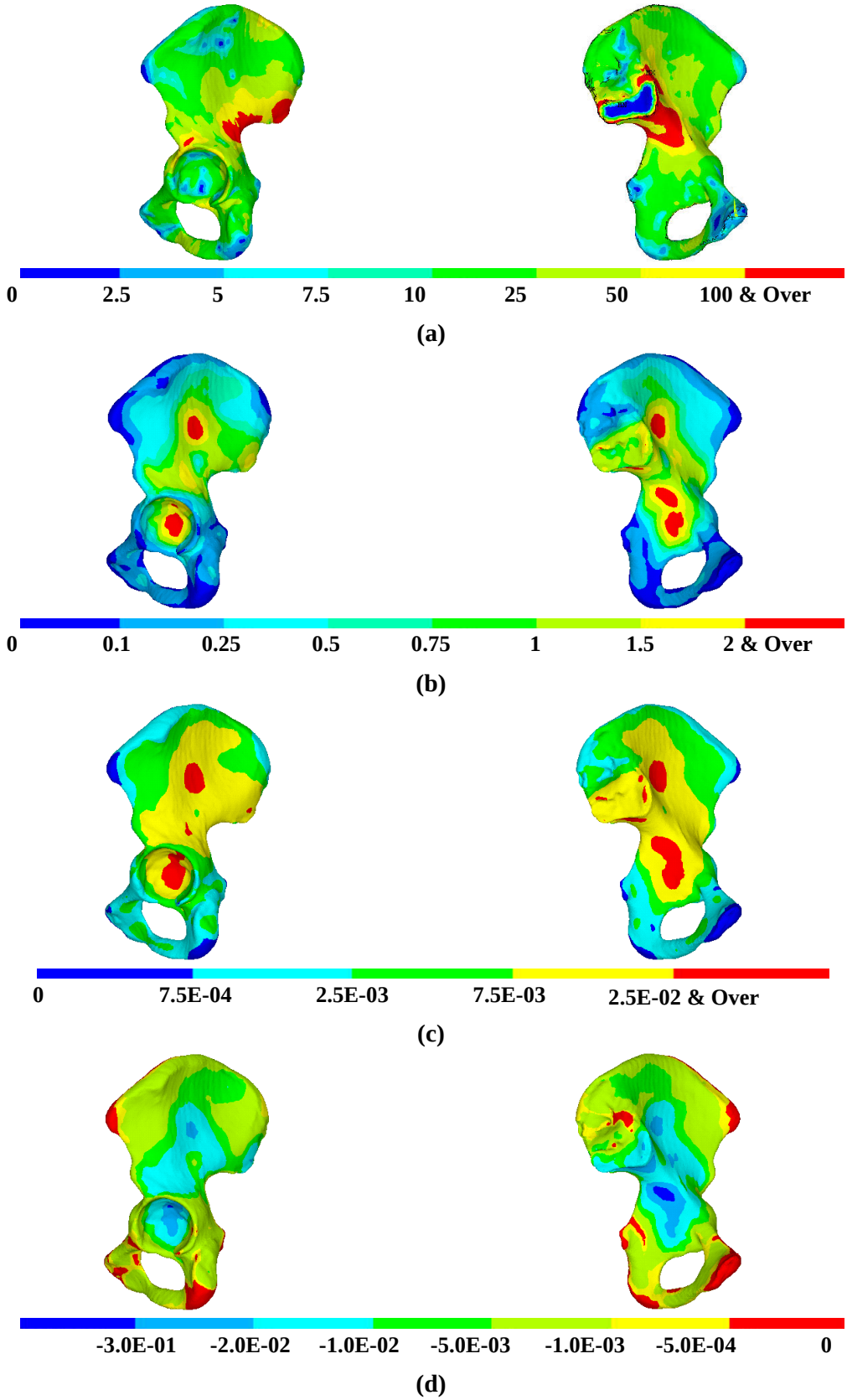

Figure 6.10. The mechanical response of the 19yr old left hemi-pelvis when loaded with cumulative maximal forces at their corresponding line of actions during the gait cycle; showing, (a) cortical von Mises stress (MPa), (b) trabecular von Mises stress (MPa), (c) trabecular von Mises strain and (d) trabecular minimum principal strain.

The trabecular von Mises strains primarily concentrated within the central acetabulum and iliac blade (see Figure 6.10(c)), producing a distribution not too dissimilar from those of Figure 6.8(a) and Figure 6.8(b). The increase in strain magnitudes caused the majority of the lateral ilium to experience strains exceeding 7500με, significantly above the remodelling threshold. High strains could be mapped to the location of the tc, sn, pt and ar regions, although the larger concentrations continued superiorly throughout the central ilium. Therefore, the resulting von Mises strain distribution did not produce any viable comparisons between the regions of high strain magnitudes, and the locations of known trabecular trajectories. Likewise the compressive strains illustrated in Figure 6.10(d) did not yield a distribution which correlated to the trabecular organisation within the adult ilium.

Application of the cumulative maximum muscle and hip joint forces at the lines of action associated with a standing position, did not significant alter the von Mises stresses of the hemi-pelvis, as shown in Figure 6.11(a) and Figure 6.11(b). Only minor stress relieving was observed in the regions of high magnitudes. Conversely, trabecular strain magnitudes displayed a marginal increase (see Figure 6.11(c) and Figure 6.11(d)). However the overall distributions remain consistent with those previously observed. Therefore, despite applying two variations of the cumulative maximal force loading regime, no further relationships between the mechanical strain and trabecular growth could be determined.

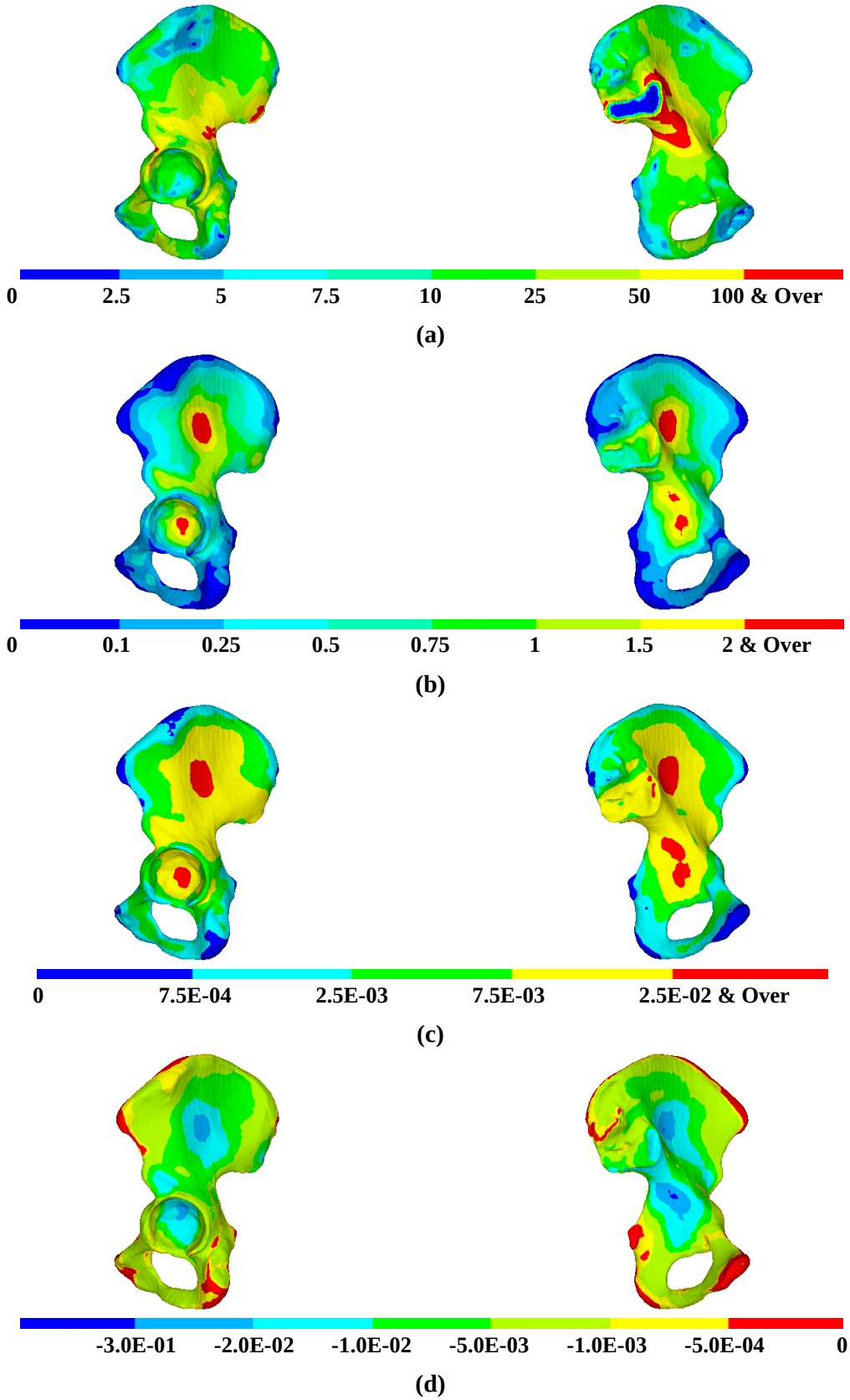

Figure 6.11. The mechanical response of the 19yr old left hemi-pelvis when loaded with cumulative maximal forces at lines of actions taken during a standing position; showing, (a) cortical von Mises stress (MPa), (b) trabecular von Mises stress (MPa), (c) trabecular von Mises strain and (d) trabecular minimum principal strain.

6.3. MODELLING OF THE PRENATAL HEMI-PELVIS

The prenatal specimen was analysed as a hemi-pelvic structure to eliminate the complexity of modelling the entire pelvic girdle. Although the original specimen was an articulated fetal pelvis (see Figure 3.1), reconstruction of both innominates would have proven to be extremely time consuming. Alternatively, the reconstructed right hemi-pelvis could have been mirrored within the sagittal plane, similar to the procedure detailed in 6.1.1. However, such modelling would have required the separate segmentation of the pubic disc and the triradiate cartilage, which was difficult due to fairly uniform grey scale values of the soft tissue within the pubic symphysis. Additionally, the material properties of the prenatal pubic disc are not documented within literature. Therefore, hemi-pelvic modelling was deemed to be the most feasible option, with the results from section 6.1.2 used to help alleviate possible high stresses/strains concentrating along the superior pubic ramus.

The prenatal FE model illustrated in Figure 6.12 contained a total of 185,512 and 18,871 volumetric tetrahedral elements to represent the trabecular bone and triradiate cartilage, respectively. Cortical bone was defined through a total of 17,446 shell elements, with a uniform cortical thickness of 0.6mm, which was based on the average values reported throughout the cortex of the neonate by Cunningham and Black (2009c). The properties of pelvic triradiate cartilage are not reported within literature, therefore assumptions concerning its modulus were made. The cartilage was defined as linear elastic material, over preference as a hyperelastic material, due to the computation expense of modelling the large volume with the latter. As the triradiate cartilage was under ossification to form bone, its modulus was presumed to be between articular cartilage and trabecular bone, producing a range between ~5-70MPa. Therefore, the modulus was set at 40MPa ($\upsilon = 0.4$) unless otherwise stated.

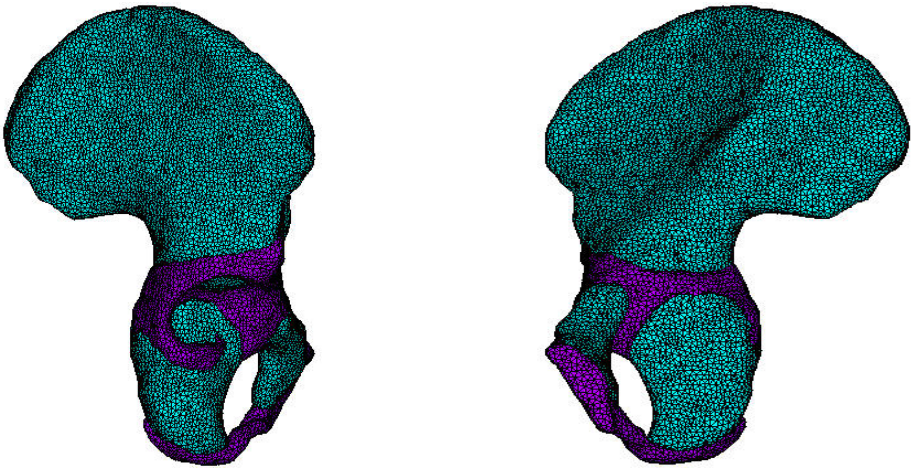

Figure 6.12. The FE model of the prenatal hemi-pelvis containing a total of 204,383 10-noded tetrahedral and 17,446 4-noded shell elements.

The FE model was initially loaded with the forces computed by the prenatal MS model during the passive 2° flexion and 2° extension of the 120° flexed hip joint (see Table 5.4). The muscular and hip joint forces for each movement were modelled independently to observe the effect of the muscles undergoing contraction and co-contraction in isolation (load regimes 1 and 2 of Table 6.1). The maximum force for each muscle during both movements was also collated into another load regime, along with the maximal hip joint reaction. Under this loading regime the modulus of the triradiate cartilage modulus was altered to 5, 20, 30 and 50MPa to observe any possible influences upon the pelvic mechanics (load regime 3 of Table 6.1). To analyse the mechanical stresses induced by opposition to the passive movement, the loading predicted by the MS with a 4N resistive force was also applied (see Table 5.4). Once again, three models were created to represent the two independent movements, and the cumulative maximal forces (load regimes 4-6 of Table 6.1).

Load Regime			
1	Passive hip joint movement at 120° flexion	2° extension	
2		2° flexion	
3		Cumulative maximal forces of each movement	Modelled with triradiate moduli of 5, 20, 30, 40 and 50MPa
4	Hip joint movement at 120° flexion with a 4N resistive force	2° extension	
5		2° flexion	
6		Cumulated maximal forces of each movement	
7	Adult gait loading	Cumulative maximal muscle and hip joint forces occurring throughout the gait cycle	Modelled with triradiate moduli of 5, 20, 30, 40 and 50MPa
8	Maximum isometric muscle force modelling	Maximum isometric muscle forces modelled at a 0° hip flexion	Modelled with 0, 1, 2, 5 and 10 times the prenatal BW
9		Maximum isometric muscle forces modelled at a 120° hip flexion	Modelled with 0, 1, 2, 5 and 10 times the prenatal BW
10	Validation of the pubic constraint	Load regime 3 with a fully constrained pubic symphysis and a triradiate cartilage modulus of 40MPa	
11	Validation of the SIJ constraint	Load regime 3 with rotation allowed at the SIJ and a triradiate cartilage modulus of 40MPa	

Table 6.1. Load cases applied to the prenatal FE model.

As the prenatal iliac trabecular trajectories reported by Cunningham and Black (2009b) are likened to that of mature structure with a weight bearing function, the MS loading associated with the gait cycle was also applied. The previously developed adult load regime which combined the maximum muscle and joint forces during the gait cycle was used (as detailed in section 6.2.2). The lines of action for each muscle were modelled to correspond to those which occurred at the point of the maximum force (load regime 7 of Table 6.1). As the adult loading was unrealistically high for the prenatal specimen, all forces associated with gait loading were restricted to 1% of their original values. Once again the triradiate cartilage modulus was altered to 5, 20, 30, 40 and 50MPa.

As the validity of the forces predicted by the prenatal MS was unknown, two further load scenarios were created which modelled each muscle to its MIF (based on the values in Table 5.3). The MIF's were initially modelled at the lines of action corresponding to a standing position (load regime 8 of Table 6.1) and then separately corresponding to a 120° hip flexion (load regimes 9 of Table 6.1). The lines of action for each scenario were taken from the prenatal MS model. However, there is no indication as to an appropriate hip joint reaction to model along with the MIF's. Therefore, various hip joint reactions were modelled at 0, 1, 2, 5 and 10 times the prenatal BW. To preserve the structural integrity of the prenatal pelvis, the MIF's were restricted to 0.01% of their actual values, while the triradiate cartilage modulus was maintained at 40MPa.

To prevent the excessive stresses within the superior pubic ramus due to the absence of the contralateral hemi-pelves, all models were constrained in all DOF at the SIJ and in inferio-superior and posterio-anterior translation at the pubic symphysis. Two further validation models were created (load regimes 10 and 11 of Table 6.1); one

which fully constrained the pubic symphysis; and another which provided the capability of SIJ rotation (modelled though the procedure detailed section 6.1.1). For the load scenarios incorporating the forces computed through the prenatal MS model, the muscular line of action for each node within the pelvic origin site was determined. This was possible in these load regimes only (in contrast to those associated with the MIF's) as the same hemi-pelvic geometry was modelled in both MS and FE analyses. Consequently, the fanning nature of the broad muscles, such as the glutei and iliacus, could be replicated within the FE modelling.

Due to the specimen age, the predicted trabecular von Mises and minimum principal strain distributions were compared to the trabecular trajectories reported by Cunningham and Black (2009b). The von Mises stresses of the cortical shell were compared to the histomorphometry reported by Cunningham and Black (2009c).

6.3.1. Stress and strain distribution associated with *in utero* loading

The cortical von Mises stress distribution produced by the MS loading during passive hip joint movements (load regimes 1-3 of Table 6.1), displayed higher magnitudes during flexion than extension, as illustrated in Figure 6.13. The combined maximal loading regime (see Figure 6.13(c)) produced distributions and magnitudes comparative to those of Figure 6.13(b). The locations of maximal stresses were similar in all models, which were generally concentrated at the SIJ and greater sciatic notch. In comparison to the histomorphometry of the prenatal cortical shell, Cunningham and Black (2009c) reported a relatively thin cortex within the medial surface at these locations. Correlations between high stress concentrations and regions of thick cortical bone were made within the lateral surface, particularly at the SIJ. Additionally, a band of high stress within the inferior ilium travelling anterio-

posteriorly also corresponded to a location higher cortical rigidity. However, where a thicker cortex was documented within the central iliac lateral blade, relatively low stress magnitudes were observed. These stress concentrations produced by load regimes 1-3 were comparable with those of displayed in Figure 6.6, although varied levels of stress reduction between the two was observed throughout the cortex.

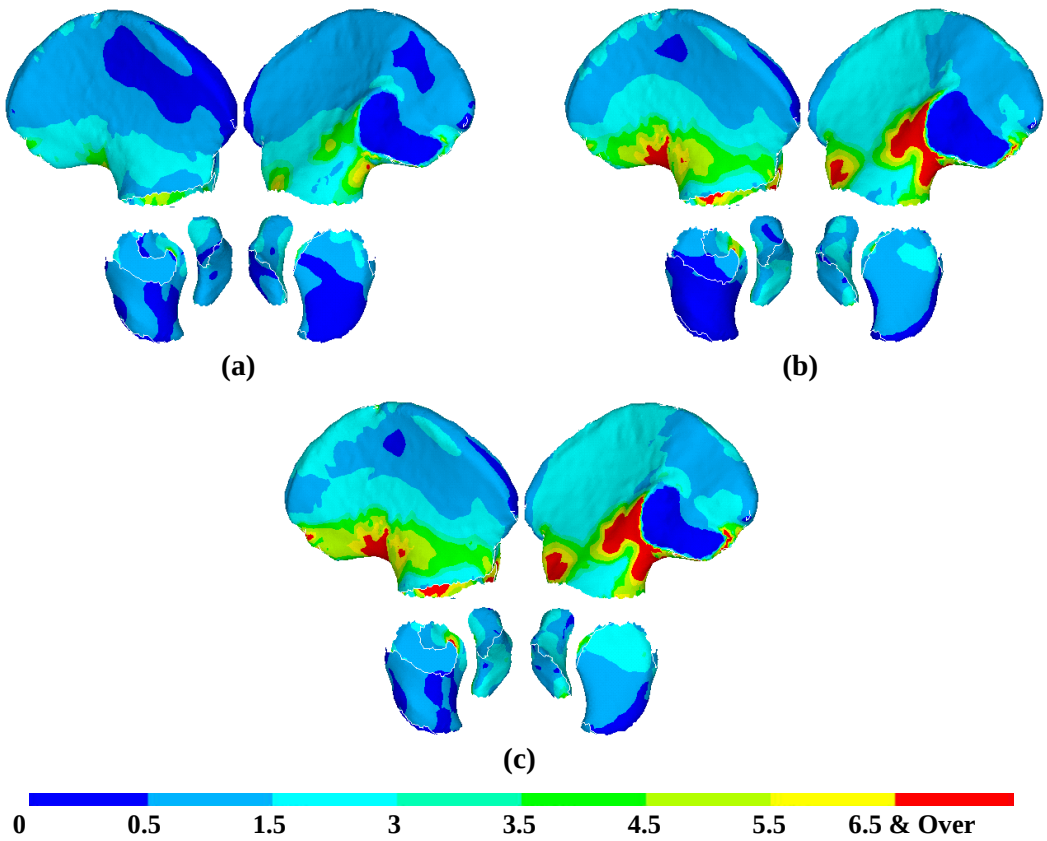

Figure 6.13. The cortical von Mises stress (MPa) distribution of the prenatal right hemi-pelvis produced by the MS loading associated with a passive (a) 2° extension, and (b) 2° flexion of the 120° flexed hip joint, and (c) the cumulated maximal loading.

Similar to the observations in Figure 6.13, the largest trabecular von Mises strains were also produced during the flexion and cumulative loading regimes (see Figure 6.14). In relation to the iliac trabecular growth within the prenatal innominate, all models displayed the highest strains within the inferior ilium, which correlated to the location of the well defined ar region. This concentration radiated superiorly and dissipated through to the iliac crest, as shown in Figure 6.14(b) and Figure 6.14(c).

Consequently, large stresses were also produced within the region of the tc, although these did not extend to the sn region. No loading regime produced significant evidence of a strain concentration travelling anteriorly towards the ASIS, to match the at. The radiation of strains superiorly from the inferior ilium produced additional concentrations along the ilio-pubic ridge. However, these did not extend to the superior region of the SIJ articulation site, therefore no concentration was formed to correspond to the pt. Relatively lower stresses were observed within the sm region (particularly in Figure 6.14(a)), although these expanded to the majority of the superior ilium.

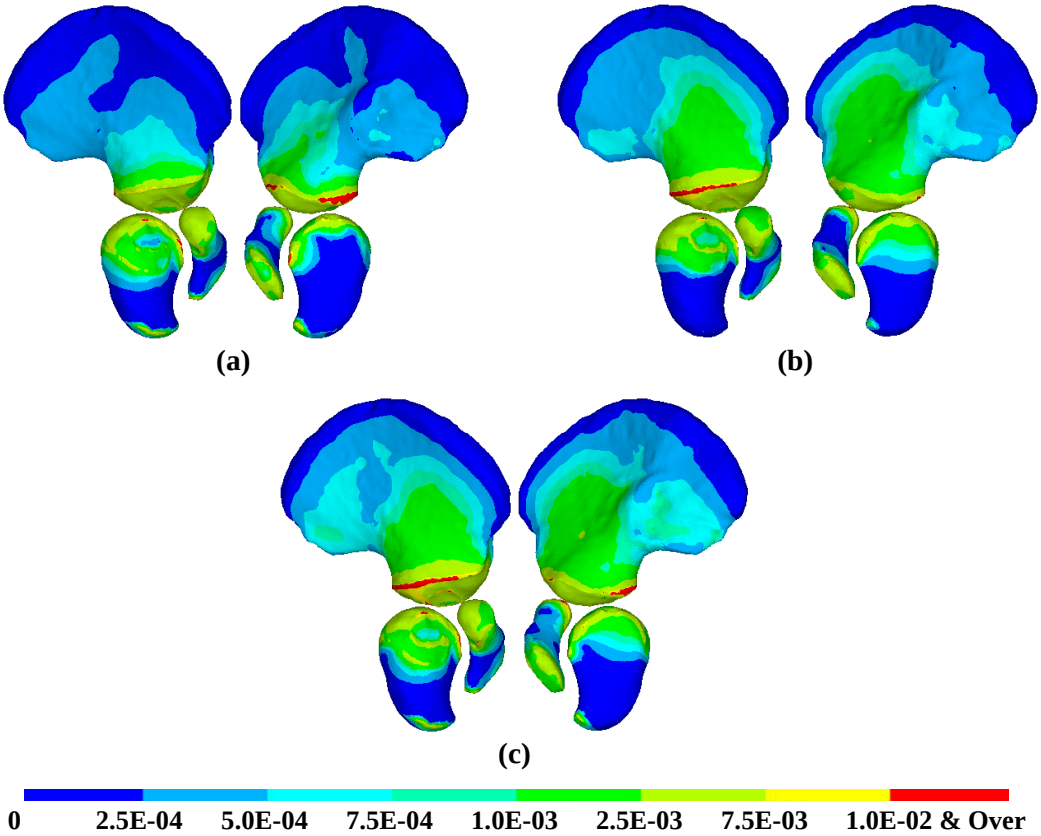

Figure 6.14. The trabecular von Mises strain distribution of the prenatal right hemi-pelvis produced by the MS loading associated with a passive (a) 2° extension, and (b) 2° flexion of the 120° flexed hip joint, and (c) the cumulative maximal loading.

The compressive strains within the trabecular bone showed similar distributions to those in Figure 6.14, with magnitudes dissipating in a superior direction from a high

concentration within the inferior ilium (see Figure 6.15). Compressive strain distribution was comparable to that of the von Mises, with magnitudes within the inferior ilium reaching above 7500με, significantly surpassing the remodelling threshold level. Strain magnitudes within the vicinity of the tc ranged between 750-2500με, which was again consistent with formation of a high level of trabecular organisation. These magnitudes continued in a posterio-superior direction to loosely correspond to the pt, although they also spread anteriorly into the lower density sm region. As observed within the 19yr old hemi-pelvis, compressive strains radiate superiorly in a uniform manner, thus no distinct concentrations where directed anteriorly. Strains around the sn ranged between 75–250με, which was considered too low to cause the high level of trabecular organisation in this area.

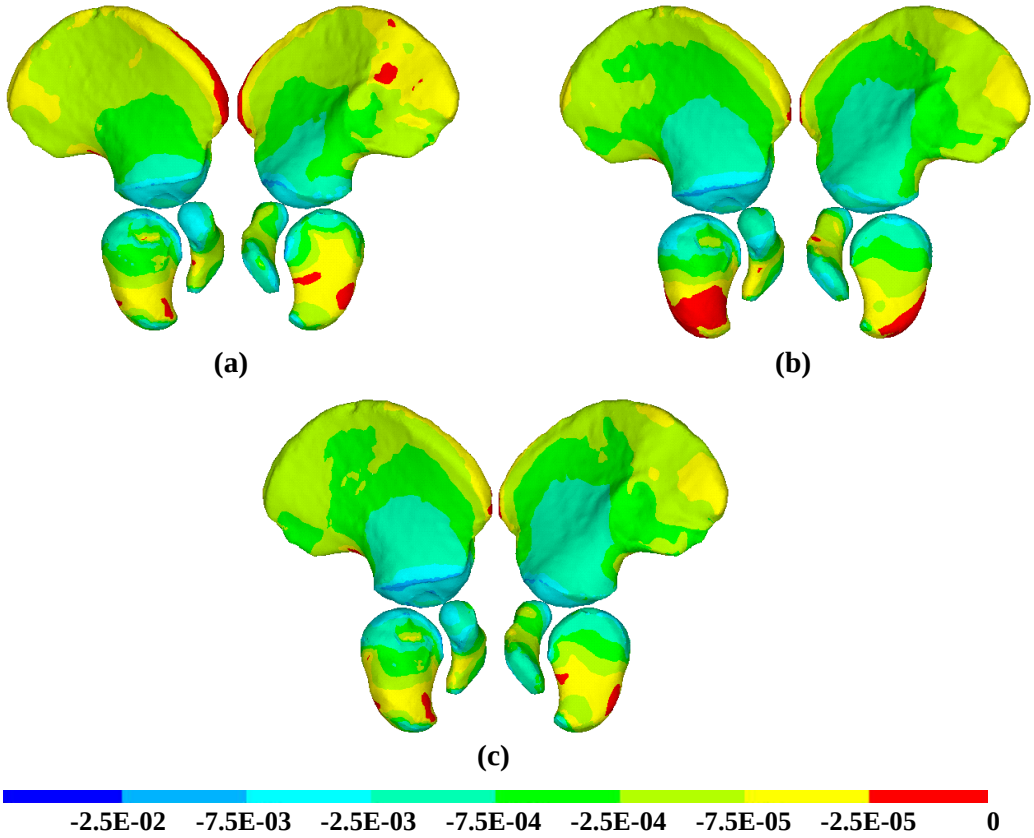

Figure 6.15. The trabecular minimum principal strain of the prenatal right hemi-pelvis produced by the MS loading associated with a passive (a) 2° extension, and (b) 2° flexion of the 120° flexed hip joint, and (c) the cumulative maximal loading.

Despite the cortical von Mises stresses and trabecular strains produced by load regimes 2 and 3 been comparative, differing maximal displacements were produced at 0.11mm and 0.22mm respectively. However, the largest displacement of 0.31mm was generated by the MS forces associated with hip joint extension, although this distance was still only 1% of the prenatal PD. In comparison to the physiological displacement observed during the gait cycle, the 19yr old hemi-pelvis produced a maximum displacement of 3% PD. Therefore, the deformation of the prenatal hemi-pelvis produced by load regimes 1-3, was not considered to be too excessive.

Similar cortical stress and trabecular strain distributions were observed through applying the MS loading associated with a 4N resistive force to the hip joint movement (see Figure 6.16 - Figure 6.18). However, cortical stress values were significantly increased (see Figure 6.16), producing magnitudes which were comparative to those observed within the adult pelvis under gait loading (Dalstra and Huiskes, 1995; Majumder et al., 2005). In comparison, trabecular von Mises and compressive strains both increased by around a factor of 10 from those induced by the passive loading. However, strains still continued to dissipate in a superior direction, rather than converging towards the anterior and posterior regions of the ilium. Therefore, applying MS loading associated with a resisted hip joint movement only served to increase the stress and strain magnitudes, rather than alter the distribution. However, this was expected as the prenatal MS model predicted uniform increases in muscle forces when a greater resistance was applied, thus did not produce a different muscle force combination (see Table 5.4).

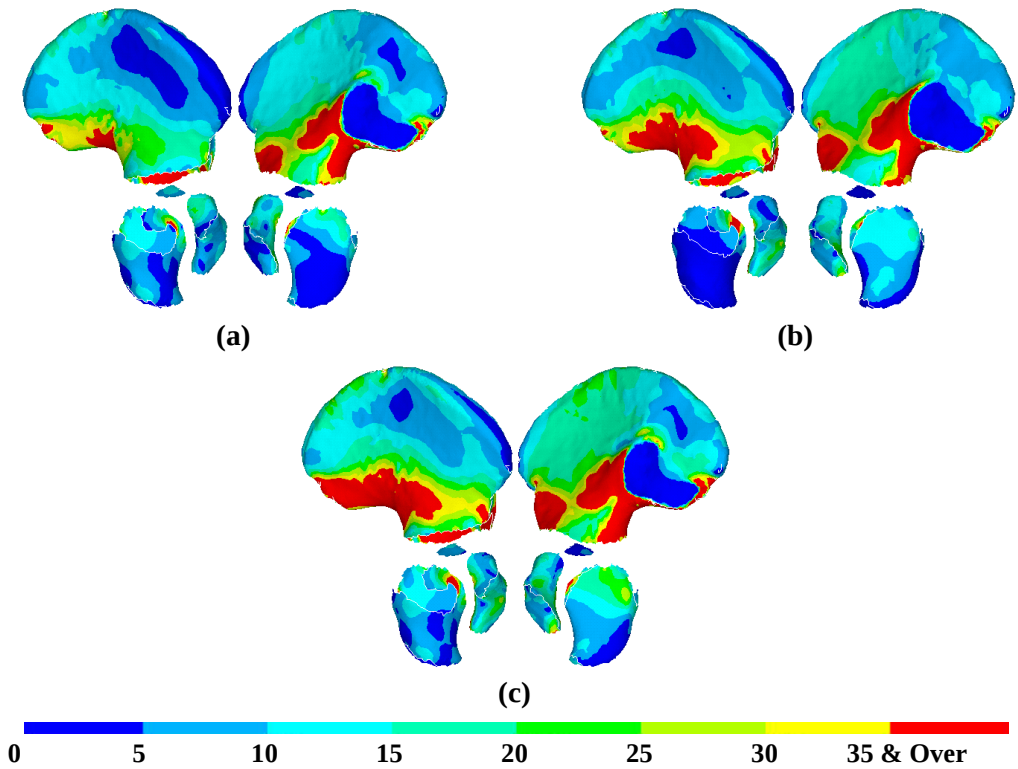

Figure 6.16. The cortical von Mises stress (MPa) distribution of the prenatal right hemi-pelvis produced by the MS loading associated with a resisted (a) 2° extension, and (b) 2° flexion of the 120° flexed hip joint, and (c) the cumulative maximal loading.

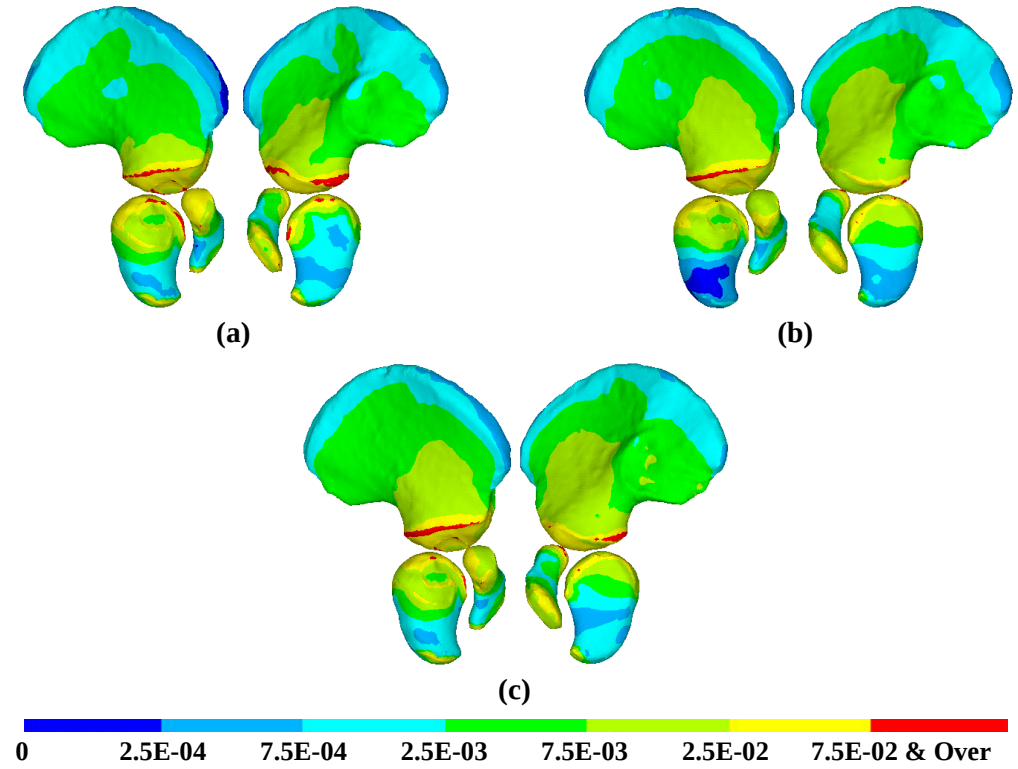

Figure 6.17. The trabecular von Mises strain distribution of the prenatal right hemi-pelvis produced by the MS loading associated with a resisted (a) 2° extension, and (b) 2° flexion of the 120° flexed hip joint, and (c) the cumulative maximal loading.

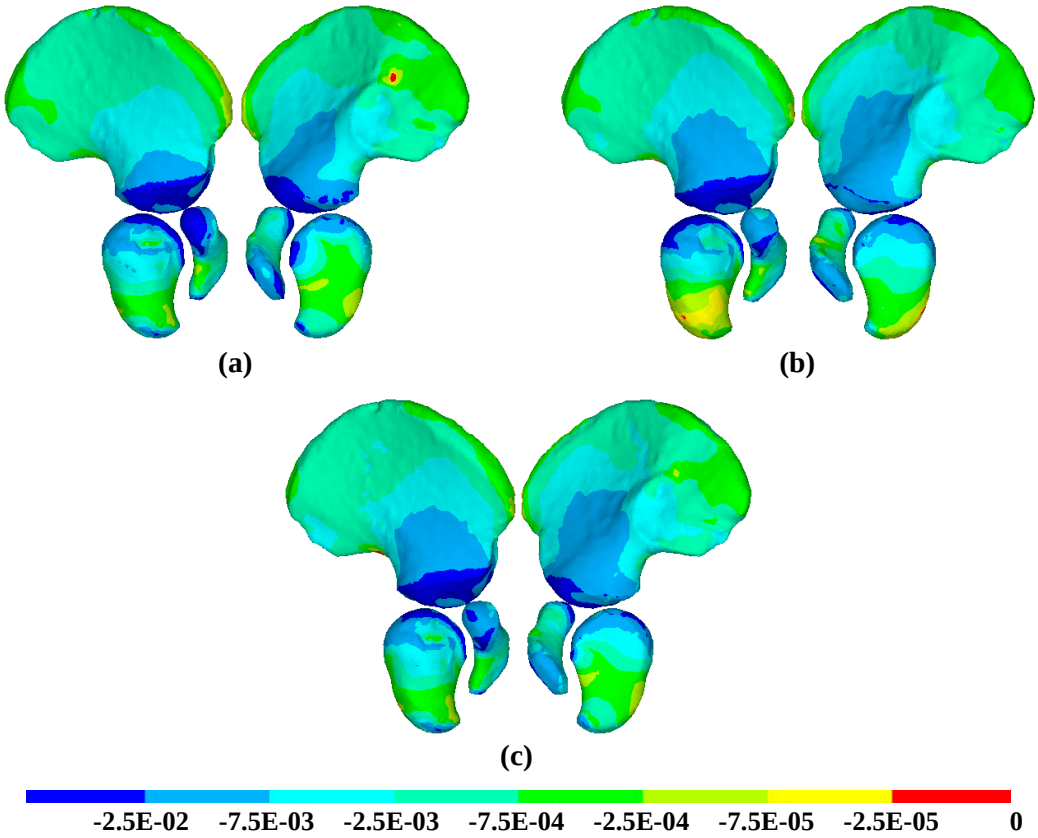

Figure 6.18. The trabecular minimum principal strain distribution of the prenatal right hemi-pelvis produced by the MS loading associated within a resisted (a) 2° extension, and (b) 2° flexion of the 120° flexed hip joint, and (c) the cumulative maximal loading.

Due to the large increase in stress and strain magnitudes, it was considered that load regimes 4-6 were unrealistically high for the prenatal structure. This was confirmed through analysis of the maximal displacement produced by these load cases, where the greatest displacement of 3.31mm (11% PD) occurred during hip extension. Although the lowest displacement of 0.8mm (2.77% PD) (caused by joint flexion) was more appropriate for the prenatal morphology, the cortical stresses in this instance remained high (see Figure 6.16(b)). Consequently, these load regimes were not considered to be representative of *in utero* MS interactions.

When load regime 3 (see Table 6.1) was applied and the triradiate cartilage modulus varied, no significant alteration to the trabecular compressive strains was observed (see Figure 6.19). Similar observations were made for the trabecular von Mises

strains and cortical von Mises stresses (see Appendix VI), showing there was no disturbance to the pelvic bone mechanics when varying the moduli. Although the maximal total displacement varied between the models shown in Figure 6.19 (0.21-0.97mm), the deformation solely related to the shape of the cartilaginous features. Additionally, the maximum displacement caused by modelling moduli between 30-50MPa only varied by 0.06mm. Therefore, these results suggested that modeling MS loading associated with passive joint movements with a triradiate cartilage modulus of 40MPa, was suitable for observing physiological pelvic behavior.

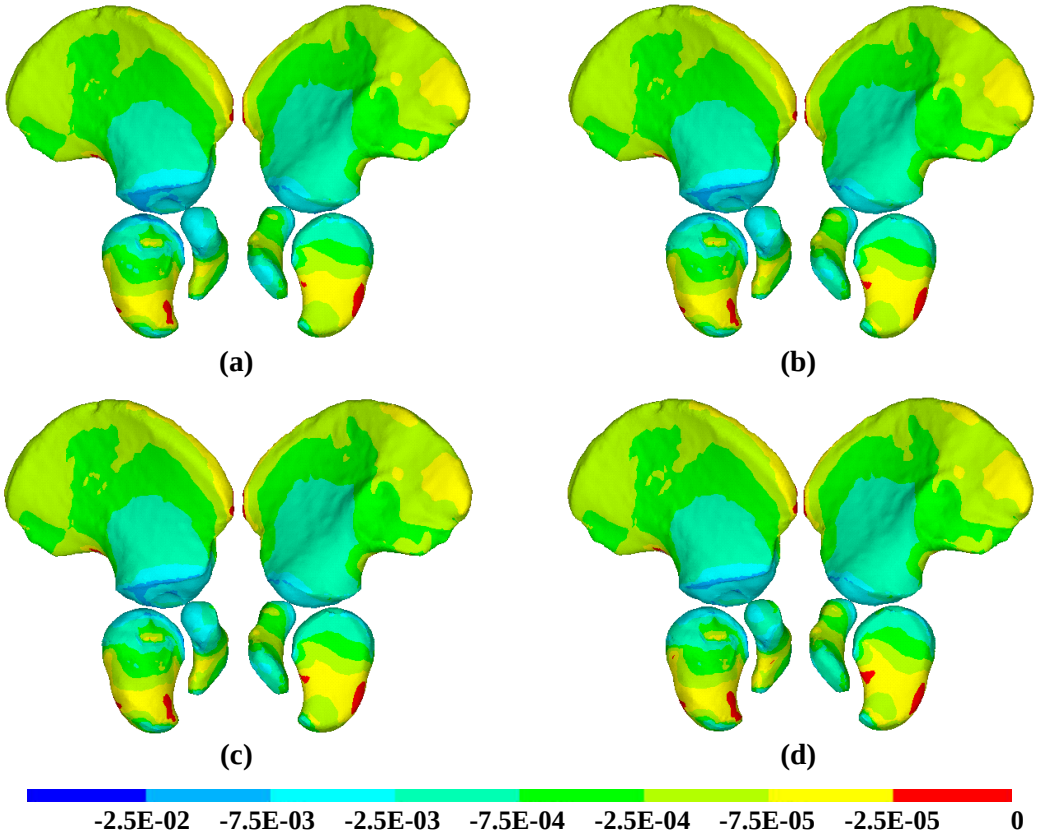

Figure 6.19. The trabecular minimum principal strain distribution produced when applying the cumulative maximal loading regime of the passive hip joint movement and varying the triradiate modulus to (a) 5MPa, (b) 20MPa, (c) 30MPa and (d) 50MPa.

6.3.2. Stress and strain distribution associated with gait and maximal isometric muscle force loading

The cortical von Mises stress distribution produced by the cumulative maximal forces associated with the adult gait cycle (load case 7 of Table 6.1), predicted high magnitudes around the greater sciatic notch and SIJ (see Figure 6.20(a)). Again, only the former of these stress concentrations correspond to observed regions of a thicker cortical shell (Cunningham and Black, 2000c), as did high concentrations within the lateral ilium. Therefore, a differing cortical stress distribution was observed in comparison to those predicted through *in utero* loading. The trabecular von Mises strains also displayed a variation in distribution and magnitude (see Figure 6.20(b)). The highest magnitudes were witnessed in the inferior ilium, with secondary concentrations observed within the iliac fossa medially, and anterior to the greater sciatic notch laterally. Unlike previous von Mises strain distributions produced through predicted *in utero* MS loading, the distribution in Figure 6.20(b) displayed higher loading on the lateral ilium in comparison to the medial side. The compressive trabecular distributions are illustrated in Figure 6.20(c), which shows high strain within the inferior ilium, but fairly randomised concentrations elsewhere. Although a large concentration within the medial and lateral iliac blade exceeded the remodelling limit at over 2500με, their locations could not be compared with regions of defined trabecular trajectories. Therefore, the predicted compressive strain distributions of Figure 6.20(c) showed no correlation to the locations of the known trabecular trajectories.

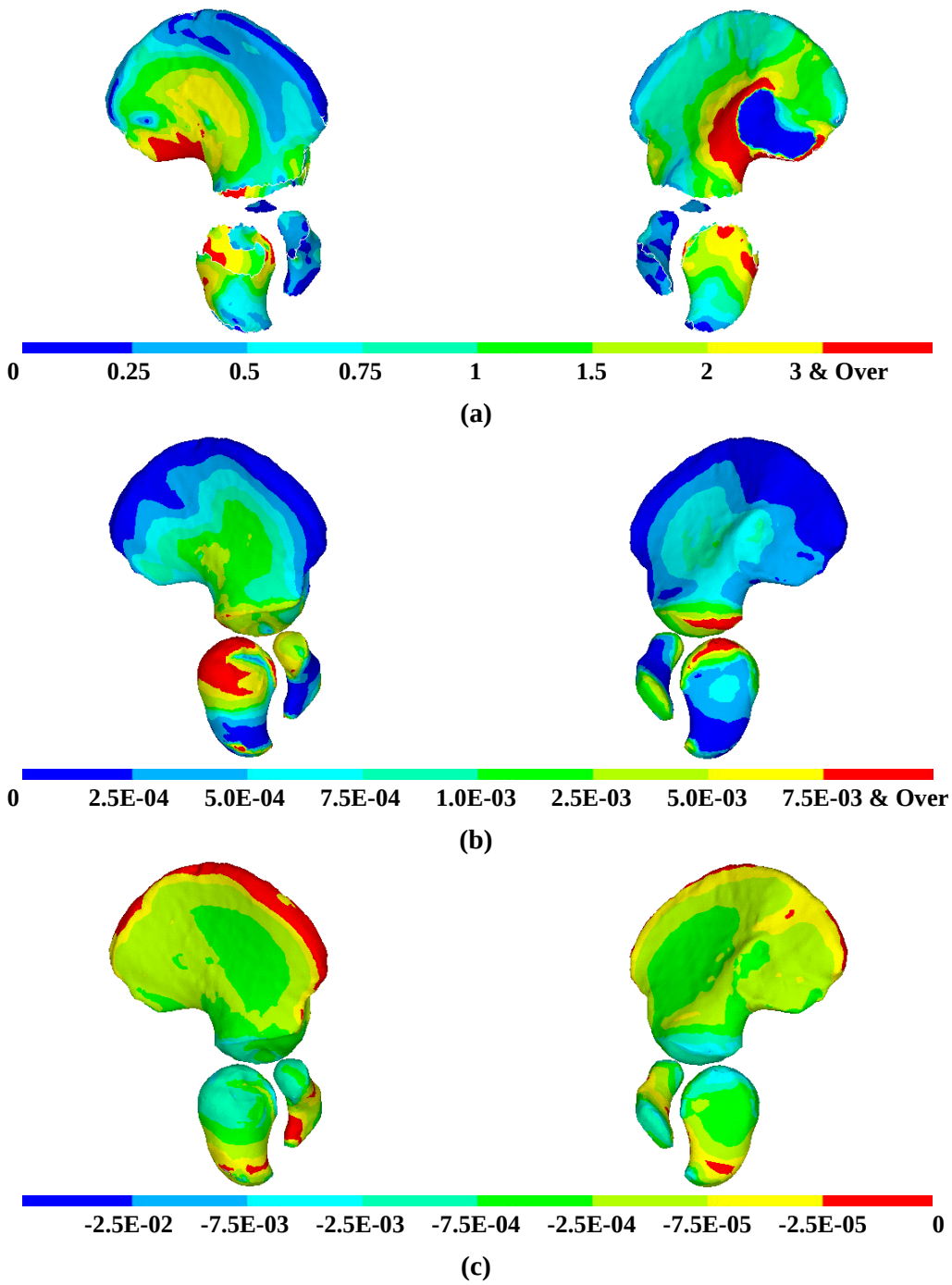

Figure 6.20. The mechanical response of the prenatal right hemi-pelvis when loaded with 1% of the cumulative maximum forces associated with the gait cycle; showing, (a) cortical von Mises stress (MPa), (b) trabecular von Mises strain and (c) trabecular minimum principal strain.

Restricting the muscle and joint forces to 1% of their actual values during the gait cycle, produced a maximum displacement of 0.13mm (0.43% PD), which did not cause excessive structural deformation. Similar to the observations in Figure 6.19,

perturbations to the triradiate cartilage moduli did not alter cortical stress or trabecular strain distributions significantly (see Appendix VI).

Compressive trabecular strains produced when applying muscle forces at 0.01% of their MIF's, at the lines of action associated with a standing position (load case 8 of Table 6.1), displayed slightly reduced maximal magnitudes compared to those seen previously (see in Figure 6.21). When a BW factor of 1 was loaded through the hip joint (see Figure 6.21(b)), the strains within the ar region exceeded the remodelling rate (over 2500με). Although these magnitudes dissipated quickly, values ranging between 750-2500με were still generated within the vicinity of the tc. The strain dissipation from the inferior ilium occurred in a column-like fashion, and therefore did not form any concentrations travelling anteriorly or posteriorly. When loading the acetabulum through various multiples of BW, the strain distribution within the inferior ilium remained fairly consistent, although there was a slight increase in the concentration size. In comparison, the high strains in the central iliac wing became progressively relieved (see Figure 6.21), producing a radiation of strains from the inferior ilium which dissipated more drastically. The maximal displacement ranged between 0.77-1.02mm (2.57-3.4% PD), which was considered relatively low since ten times the prenatal BW was applied in Figure 6.21(e). Therefore, Figure 6.21 displayed similar strain distributions between the different applied BW factors, with no increased likeness to the trabecular patterning in Figure 2.18.

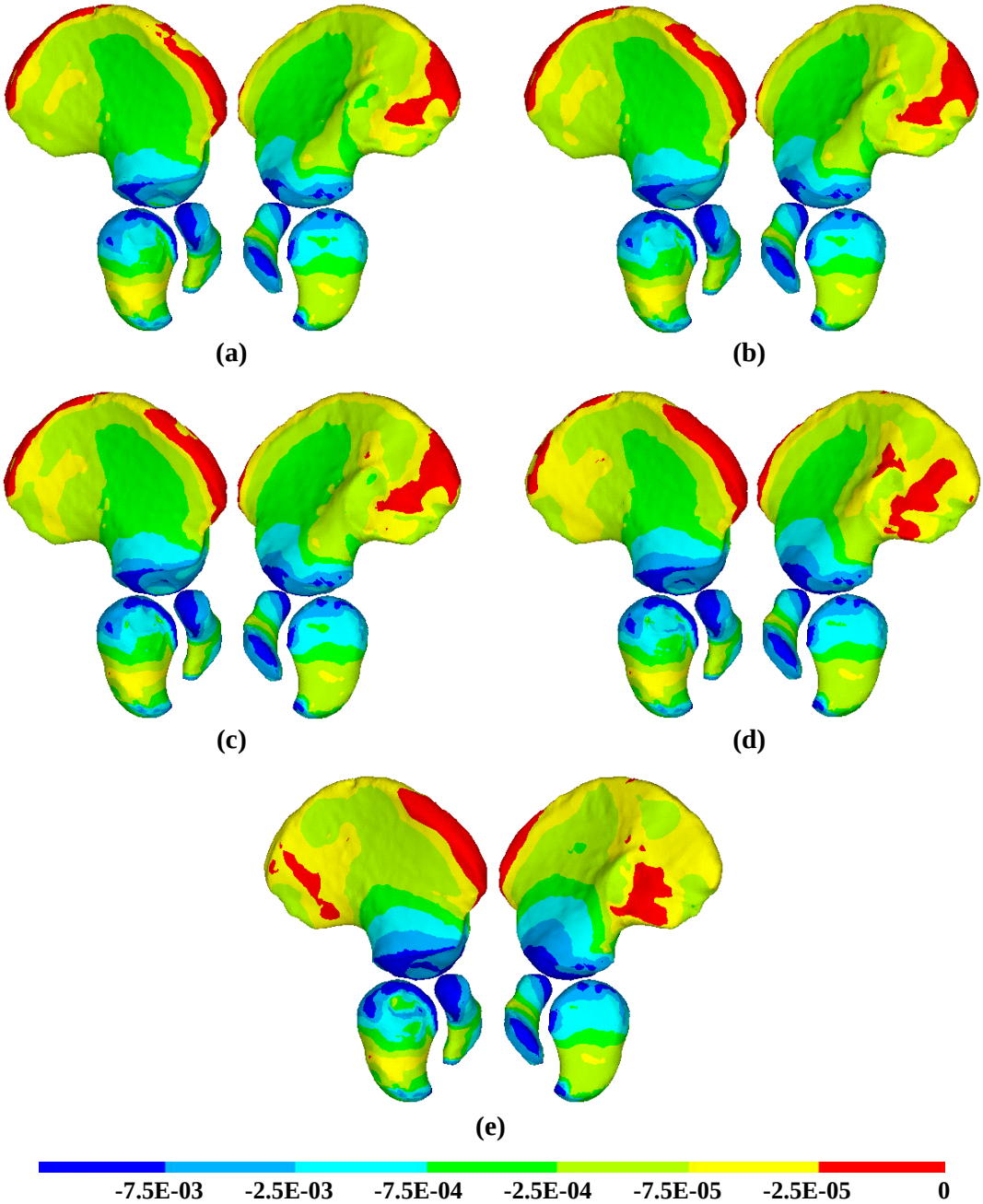

Figure 6.21. The trabecular minimum principal strain distribution of the prenatal right hemi-pelvis produced by 0.01% of the maximum isometric muscle forces and a hip joint force of (a) 0 BW, (b) 1x BW, (c) 2x BW, (d) 5x BW and (e) 10x BW at the lines of action corresponding to a standing position.

Significantly higher compressive strains were observed when the same forces were applied at a 120° hip flexion angle (load case 9 of Table 6.1), which predominately radiated in a superior direction from the inferior ilium (see Figure 6.22). Strains within the inferior ilium were larger than those observed in Figure 6.21, and they dissipated less efficiently to produce a higher loaded superior ilium. The strain

distribution in Figure 6.22(b) displayed magnitudes over 2500με within the locations of the tc and ar. The superior radiation of these high strains generated concentrations within the iliac fossa and towards the SIJ. Although the high strains within the posterior ilium matched the location of the pt, these magnitudes formed a large concentration which dominated the majority of the central ilium. Consequently, strains within the sm region were too high to correspond to a poorly defined trabecular organisation. When increasing the hip joint force, the concentrations of the inferiorly located strains rose significantly, producing magnitudes previously unseen with the other load regimes. Consequently, strains within the superior ilium increased as well, causing the distribution in Figure 6.22(e) to load the majority of the ilium over 2500με. A higher range of maximal displacement (0.28 – 3.19mm) was also produced at the 120° flexed hip joint.

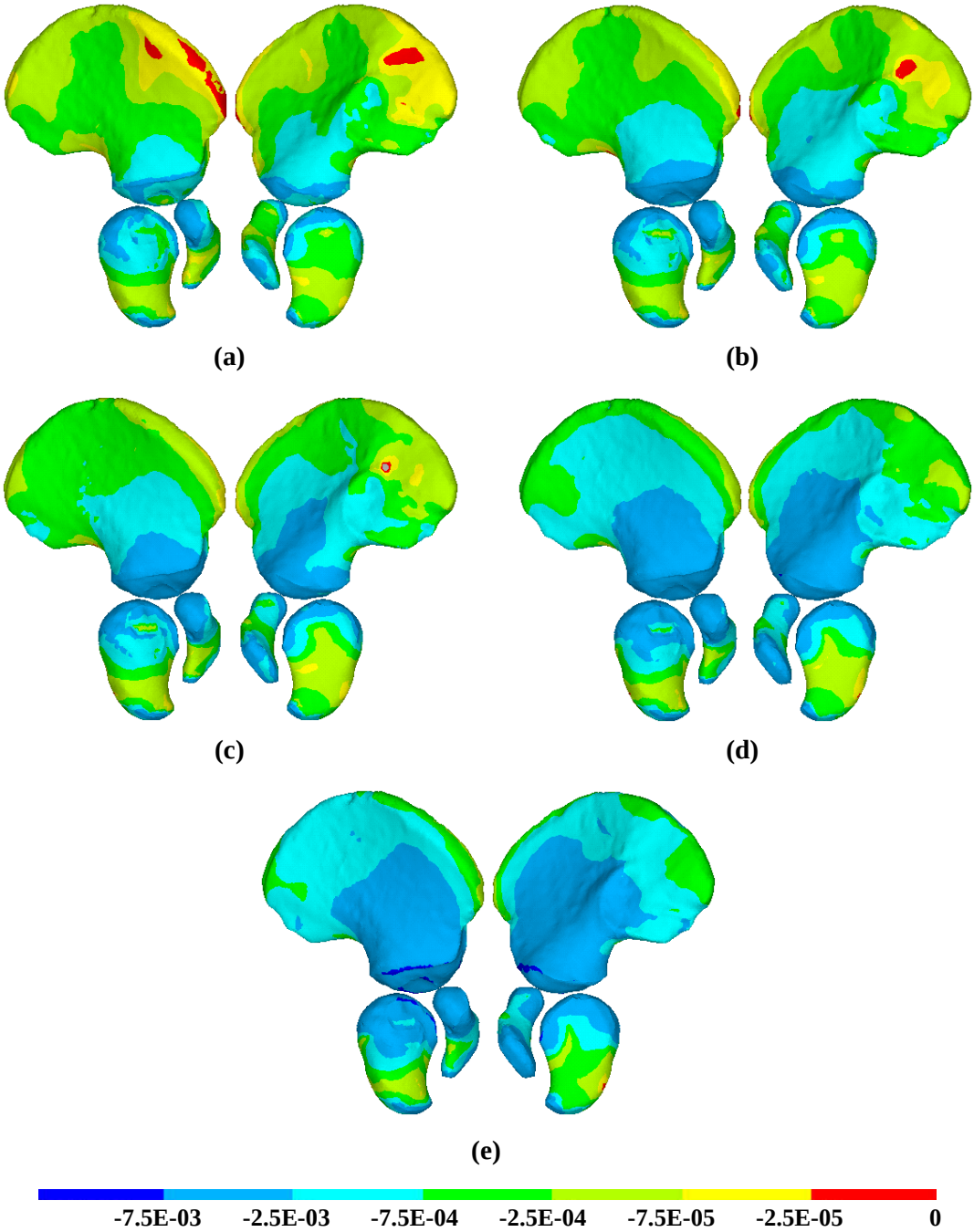

Figure 6.22. The trabecular minimum principal strain distribution of the prenatal right hemi-pelvis produced by 0.01% of the maximum isometric muscle forces and a hip joint force of (a) 0x BW, (b) 1x BW, (c) 2x BW, (d) 5x BW and (e) 10x BW at the lines of action corresponding to a 120° flexed hip joint.

6.3.3. Validation of the methods of constraints

Load cases 10 and 11 (see Table 6.1) produced only a limited variation to the trabecular compressive trabecular strain distribution and magnitudes, when enabling

rotation at the SIJ (see Figure 6.23(a)) and fully constraining the pubic symphysis (see Figure 6.23(b)). In comparison to the original trabecular compressive strain distribution (illustrated in Figure 6.15(c)), the only significant variations occurred within the superior ilium. However, these alterations were minimal and reflected the lower compressive strains predicted. The applied MS forces were possibly too low to cause pelvic rotation at the SIJ, as the maximal displacement only increased by 0.02mm (0.07% PD). The permitted translation at the pubic symphysis did not cause any fluctuation in the total displacement. Therefore, Figure 6.23 suggests that modelling the hemi-pelvis with a fully constraint SIJ and pubic symphysis was a valid method. However, this conclusion was made with respect to the singular load case applied.

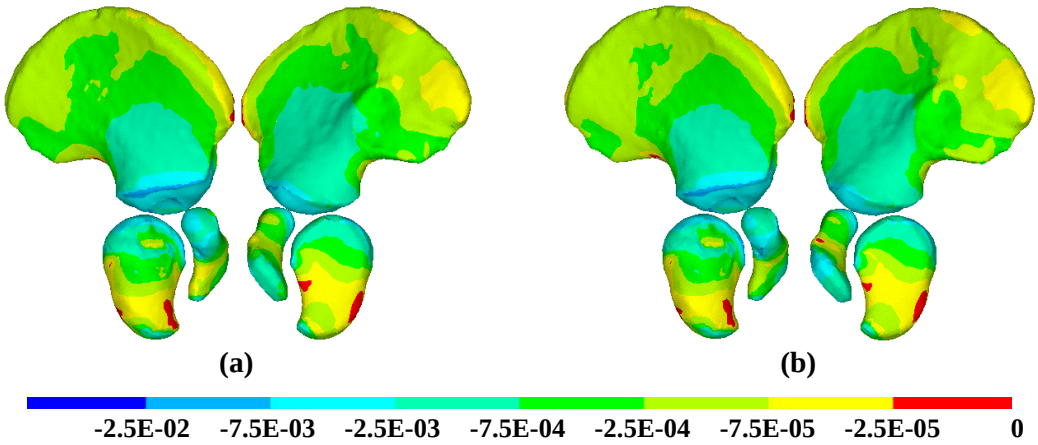

Figure 6.23. The trabecular minimum principal strain distribution of the prenatal right hemi-pelvis produced by identical MS loading and (a) enabling rotation at the SIJ, and (b) constraining the pubic symphysis in all DOF.

6.4. MODELLING OF THE 1 YEAR OLD HEMI-PELVIS

The 1yr old pelvis was modelled as a hemi-pelvic structure through 152,315 and 51,417 volumetric elements for trabecular and cartilage bone, respectively (see Figure 6.24). Cortical bone was modelled through 44,461 shell elements with a thickness of 0.71mm, based on data of Parfitt et al. (2000). The three load cases

detailed in Table 6.2 were applied to the FE model. These aimed to evaluate the hemi-pelvic mechanical response when experiencing MS loading associated with bipedal locomotion (load regimes 1 and 2), and muscle forces at their MIF's (load regime 3). The average weight of a 1yr old was defined as 10.4Kg, and the MIF's were based on those displayed in Table 5.3. The forces associated with gait loading were limited to 5% and 2% of their actual values, respectively, while the MIF's were limited to 0.25%. Each model was constrained in all DOF at the SIJ and in the inferio-superior and posterio-anterior translation at the pubic symphysis. A triradiate modulus of 40MPa was defined, unless otherwise stated.

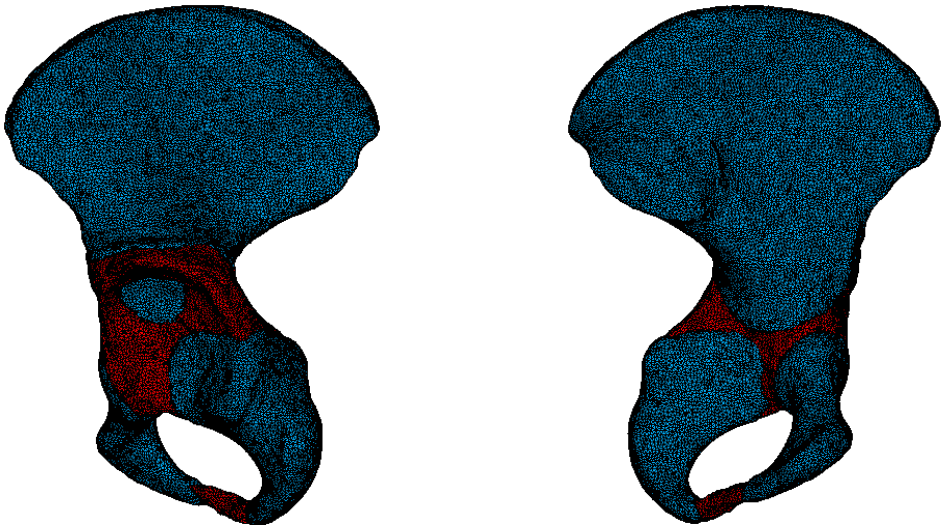

Figure 6.24. The FE model of the 1yr old left hemi-pelvis containing a total of 203,732 10-noded tetrahedral and 44,461 4-noded shell elements.

Load Regime		
1	The MS loading associated with the 5th phase of the gait cycle (taken from the adult MS model)	Modelled with a triradiate moduli of 5, 20, 30, 40 and 50MPa
2	The cumulative maximal muscle and hip joint forces associated with the gait cycle. Muscular lines of action modelled as those which occurred at the instance of the maximum force.	Modelled with a triradiate moduli of 5, 20, 30, 40 and 50MPa
3	The maximum isometric muscle forces, based on PCSA and a muscle stress of 1MPa. Muscular lines of action modelled to correspond to a standing position.	Modelled with 0, 1, 2, 5 and 10 times BW.

Table 6.2. The load cases applied to the 1yr and 8yr old FE hemi-pelvic models.

6.4.1. Stress and strain distribution associated with gait loading

As illustrated in Figure 6.25(a), the MS loading associated with 5th phase of the gait cycle (load regime 1 of Table 6.2) produced the highest cortical von Mises stresses around the SIJ medially, and the greater sciatic notch and inferior ilium laterally. As witnessed within the prenatal modelling, the largest trabecular von Mises strains were again located within the lateral inferior ilium, and dissipated superiorly through the iliac blade, as shown in Figure 6.25(b). However, high concentrations also radiated towards the PSIS, producing a highly strain posterior ilium, similar to that observed within the 19yr old hemi-pelvis at same phase of the gait cycle (see Figure 6.8(e)). The trabecular strain magnitudes in Figure 6.25(b) were lower than those generated within the 19yr old hemi-pelvis.

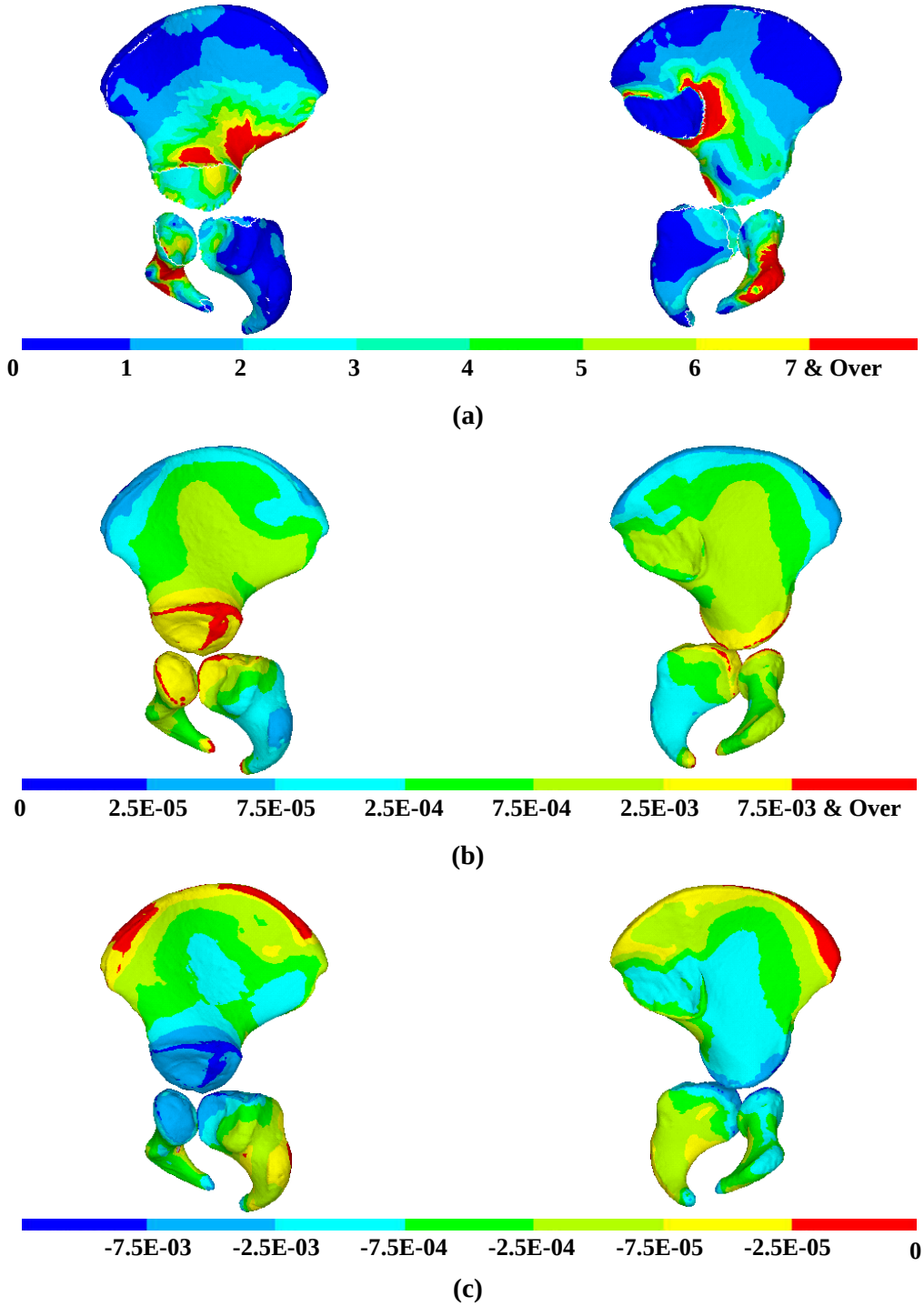

Figure 6.25. The mechanical response of the 1yr old left hemi-pelvis when loaded with 5% of the MS forces associated with the 5th phase of the gait cycle; showing, (a) cortical von Mises Stress (MPa), (b) trabecular von Mises strain, (c) trabecular minimum principal strain.

The trabecular compressive strains in Figure 6.25(c) also displayed similarities to those of the 19yr old (see Figure 6.9(e)), with high compression concentrated within the inferior ilium which radiated superiorly. However, the smaller maximal

compressive strains within the 1yr old hemi-pelvis dissipated quickly through the ilium, producing a lower relatively strained iliac crest. There was no defined strain distribution travelling anteriorly to match the at, while concentrations reduced around the greater sciatic notch to magnitudes insufficient to cause formation of the sn region. Strain magnitudes within the ar region exceeded 2500με, while in the locations of the tc and pt they were a minimum of 750με. Therefore, compressive strains in these regions were either above or close to the remodelling rate required to form the highly organised trabecular densities. However, high strains ranging between 750-2500με also transferred throughout the centre of the medial and lateral iliac blade. Such values in this region were possibly too high considering the lack of trabecular formation within the sm location. Restricting the muscle forces to 5% of their actual values proved successful in preventing excessive deformation of the hemi-pelvis. A maximal displacement of 0.67mm (1.1% PD) was considered to produce a physiological structural deformation.

As witnessed in modelling of the prenatal hemi-pelvis, varying the modulus of the triradiate cartilage did not cause a significant alteration of the trabecular compressive strain distribution or magnitudes (see Figure 6.26). Despite the maximal displacement of the models ranging between 0.59-3.07mm (0.98-5.03% PD), the deformation pertained to the triradiate cartilage. Once again, the structural deformation decreased with greater moduli, producing a maximal displacement range of 0.59-0.79mm (0.98-1.29% PD) when modelling with 30-50MPa.

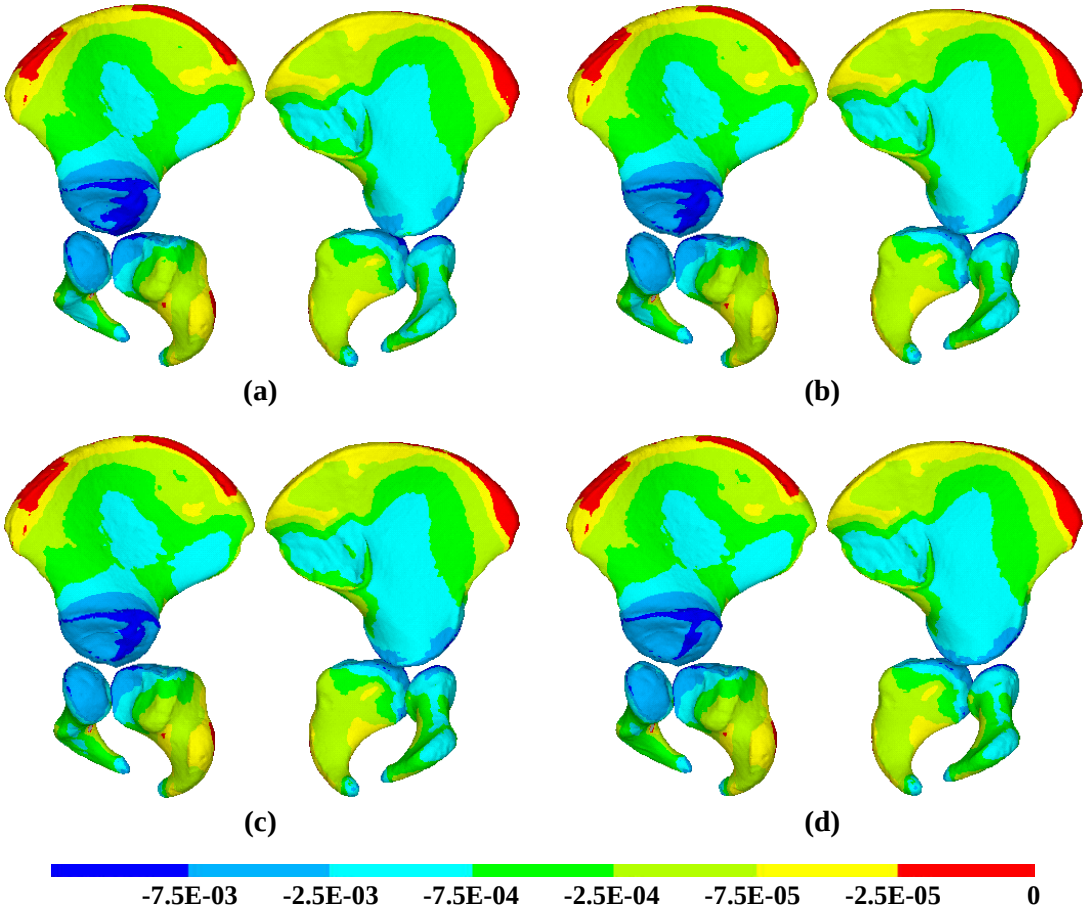

Figure 6.26. The trabecular minimum principal strain distribution of the 1yr old left hemi-pelvis produced by 5% of the MS forces associated with the 5th phase of the gait cycle and a triradiate cartilage modulus of (a) 5MPa, (b) 20MPa, (c) 30MPa and (d) 50MPa.

As illustrated in Figure 6.27(a), cumulative maximal muscle and hip joint forces (load regime 2 of Table 6.2) generated lower cortical von Mises stresses, although maximal concentrations were again observed at the SIJ and within the inferior ilium. The trabecular von Mises strain distribution displayed in Figure 6.27(b) was also similar to that predicted by load case 1 (see Figure 6.25(b)), although the magnitudes were generally lower. The maximal von Mises strains also dissipated much quicker to produce a lower strained superior ilium. Consequently, high strains remained directed in a superior column from the inferior ilium, and did not deviate towards the anterior or posterior regions of the hemi-pelvis.

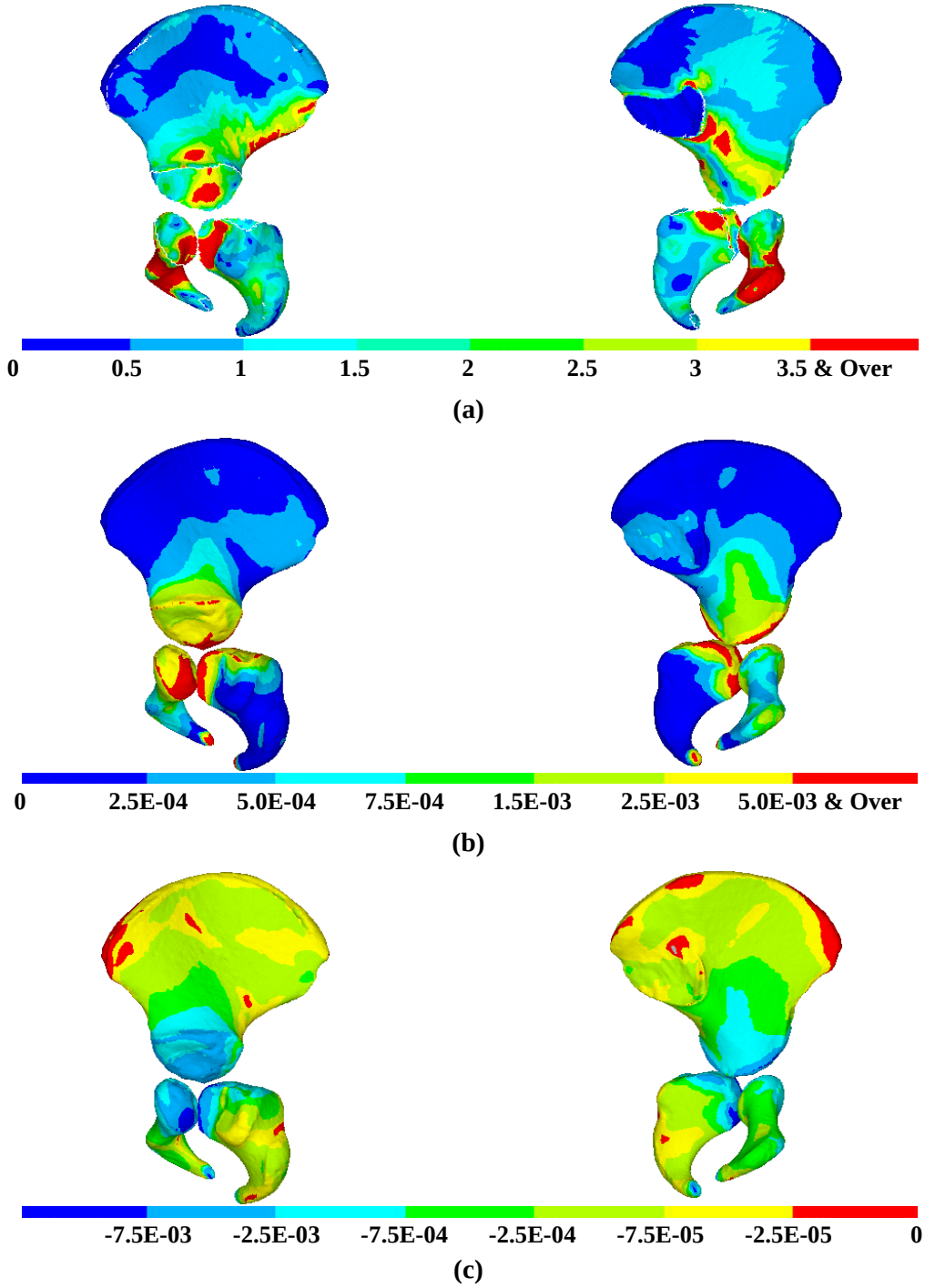

Figure 6.27. The mechanical response of the 1yr old left hemi-pelvis when loaded with 2% of the cumulative maximum muscle and joint forces associated with the gait cycle; showing, (a) cortical von Mises Stress (MPa), (b) trabecular von Mises strain and (c) trabecular minimum principal strain.

The compressive trabecular strains illustrated in Figure 6.27(c) produced a more varied distribution to those previously observed within the 19yr old and prenatal hemi-pelves. Although the highest strains again radiated from the inferior ilium, a

fairly randomised patterning was observed within the iliac fossa and along the iliac crest. Magnitudes exceeded 2500με in the regions of the ar, which is sufficient enough to instigate bone remodelling. However, the magnitudes reduced to a maximum of 750με within the location of the tc region, which was considered too low to correlate to the highly organised trabecular region. The strain dissipation also reduced the magnitudes around the greater sciatic notch to unfavourable levels for maintaining a high remodelling rate. The compressive strain dissipation throughout the ilium did not form any distributions to match the at or pt. Restricting the maximal muscular and joint forces to 2% of their actual values prevented excessive deformation of the hemi-pelvic structure, with a maximum displacement of 0.82mm (1.34% PD) produced.

As observed with the application of load regime 1, the variation of the triradiate cartilage modulus only served to deform the acetabulum and obturator foramen, and did not alter the strain distribution of the hemi-pelvic bone (see Appendix VI).

6.4.2. Stress and strain distribution associated with maximal isometric muscle forces

The cortical von Mises stresses generated through loading of muscle forces at 0.25% of their MIF's (load case 3 of Table 6.2) are illustrated in Figure 6.28(a). The maximal stresses again concentrated around the greater sciatic notch and inferior ilium laterally, and around the SIJ and along the ilio-pubic ridge medially. However the magnitude of the cortical stresses was higher than those previously observed through load regimes 1 and 2. Similarly, the maximal trabecular von Mises strain concentrations shown in Figure 6.25(b) were also larger in size within then inferior ilium. Although, the strains dissipated fairly rapidly and were contained to the

regions within the inferior ilium, thus loaded the superior ilium to similar magnitudes of those in Figure 6.25(b).

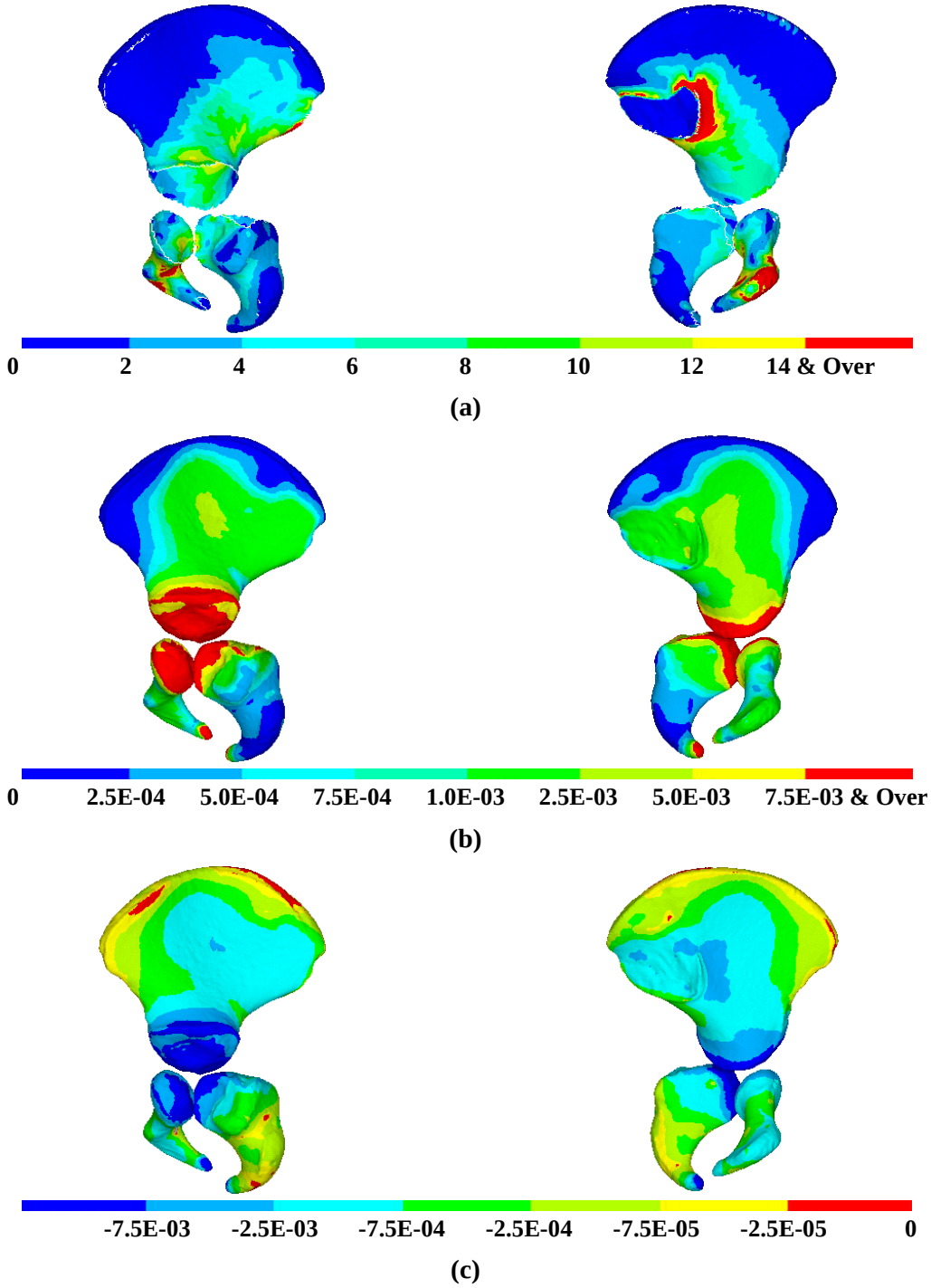

Figure 6.28. The mechanical response of the 1yr old left hemi-pelvis when loaded with 0.25% of the maximum isometric muscle forces and a hip joint force of 1x BW; showing, (a) cortical von Mises Stress (MPa), (b) trabecular von Mises strain and (c) trabecular minimum principal strain.

The trabecular compressive strain distribution illustrated in Figure 6.28(c) was also similar to that produced by load regime 1 (see Figure 6.25(c)). High strains radiated superiorly from the inferior ilium through to the iliac fossa, with a secondary concentration formed within the posterior ilium. Consequently, the strain magnitudes within the ar region were sufficient enough to instigate remodelling (at over 2500με), while within the tc regions they ranged between 750-2500με. The intensities lowered to between 250-750με around the greater sciatic notch, which was possibly too low to correlate to the high trabecular organisation within this region. A strain concentration matching the location of the pt trajectory contained sufficient magnitude to instigate bone remodelling. However, such magnitudes were also observed within the sm region, and were considered too high to be attributed to the low level of trabecular organisation in this location. There was no significant concentration to match the location of the at.

As observed within the prenatal hemi-pelvis, increasing the magnitude of BW loaded through the acetabulum caused a subsequent spread of high trabecular compressive strains throughout the structure (see Figure 6.29). Application of hip joint loading at 5 and 10 times BW dramatically increased the compressive strains to cause the majority of the ilium to be strained over 7500με. Through varying the hip joint loading the maximal displacement increased from 1.1mm (0 BW) to 12.59mm (10x BW), however the load regime displayed in Figure 6.29(b) generated the lowest displacement of 0.61mm (1% PD). This unexpected decrease was attributed to the hip joint loading at 1 times BW counteracting the forces of the pelvic muscles spanning the acetabulum, thus producing a more stable joint.

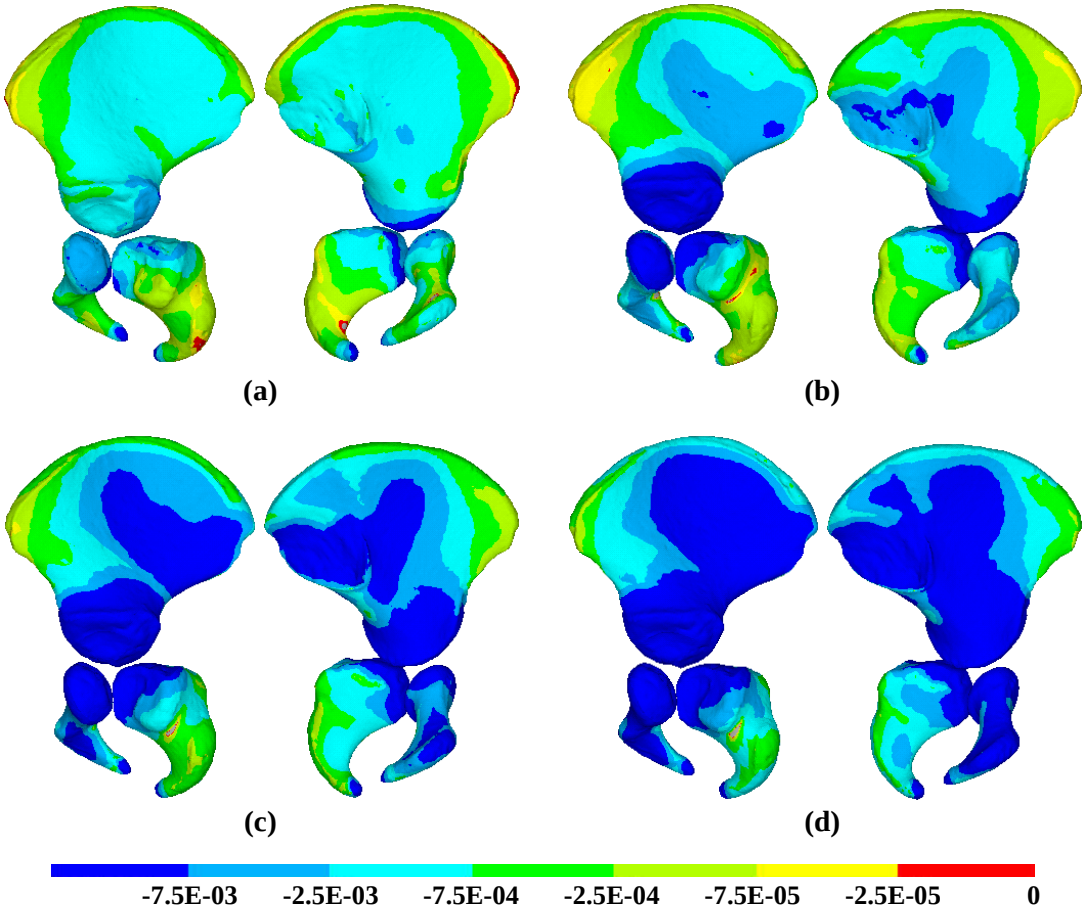

Figure 6.29. The trabecular minimum principal strain distribution of the 1yr old left hemi-pelvis produced by 0.25% of the maximum isometric muscle forces and a hip joint force of (a) 0x BW, (b) 1x BW, (c) 2x BW, (d) 5x BW and (e) 10x BW.

6.5. MODELLING OF THE 8 YEAR OLD HEMI-PELVIS

The 8yr old pelvis was modelled as a hemi-pelvic structure through 193,934 and 21,647 volumetric elements for trabecular bone and triradiate cartilage, respectively (see Figure 6.30). Cortical bone was modelled through 19,832 shell elements with a thickness of 1mm (Glorieux et al., 2000). The three load regimes detailed in Table 6.2 were applied to the FE model, while the average weight of an 8yr old was estimated at 25Kg. The MS forces of load regimes 1 and 2 were limited to 25% and 10% of their actual values respectively, while the maximum isometric muscle forces were limited to 1% (load regime 3). All models were constrained in all DOF at the

SIJ and in inferio-superior and posterior-anterior translation at the PS, and defined with a triradiate modulus of 40MPa (υ = 0.4), unless otherwise stated.

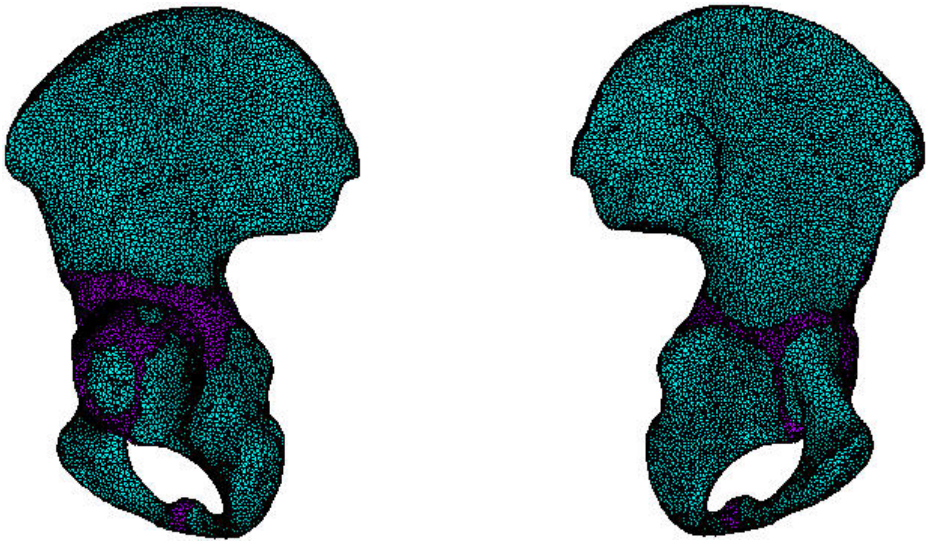

Figure 6.30. The FE model of the 8yr old left hemi-pelvis containing a total of 215,581 10-noded tetrahedral and 19,822 4-noded shell elements.

6.5.1. Stress and strain distribution associated with gait loading

As illustrated in Figure 6.31(a), load regime 1 generated the highest cortical von Mises stresses around the SIJ and ilio-pubic ridge, producing a similar distribution to that observed previously. However, the magnitudes of the cortical stresses were significantly increased from those witnessed within the 1yr old hemi-pelvis under the same loading (see Figure 6.25(a)). However, the ilio-pubic ridge and superior pubic ramus were significantly higher stressed in comparison to the other juvenile FE models, suggesting the degree of translation permitted at the pubic symphysis failed to stress relive the hemi-pelvis in this instance.

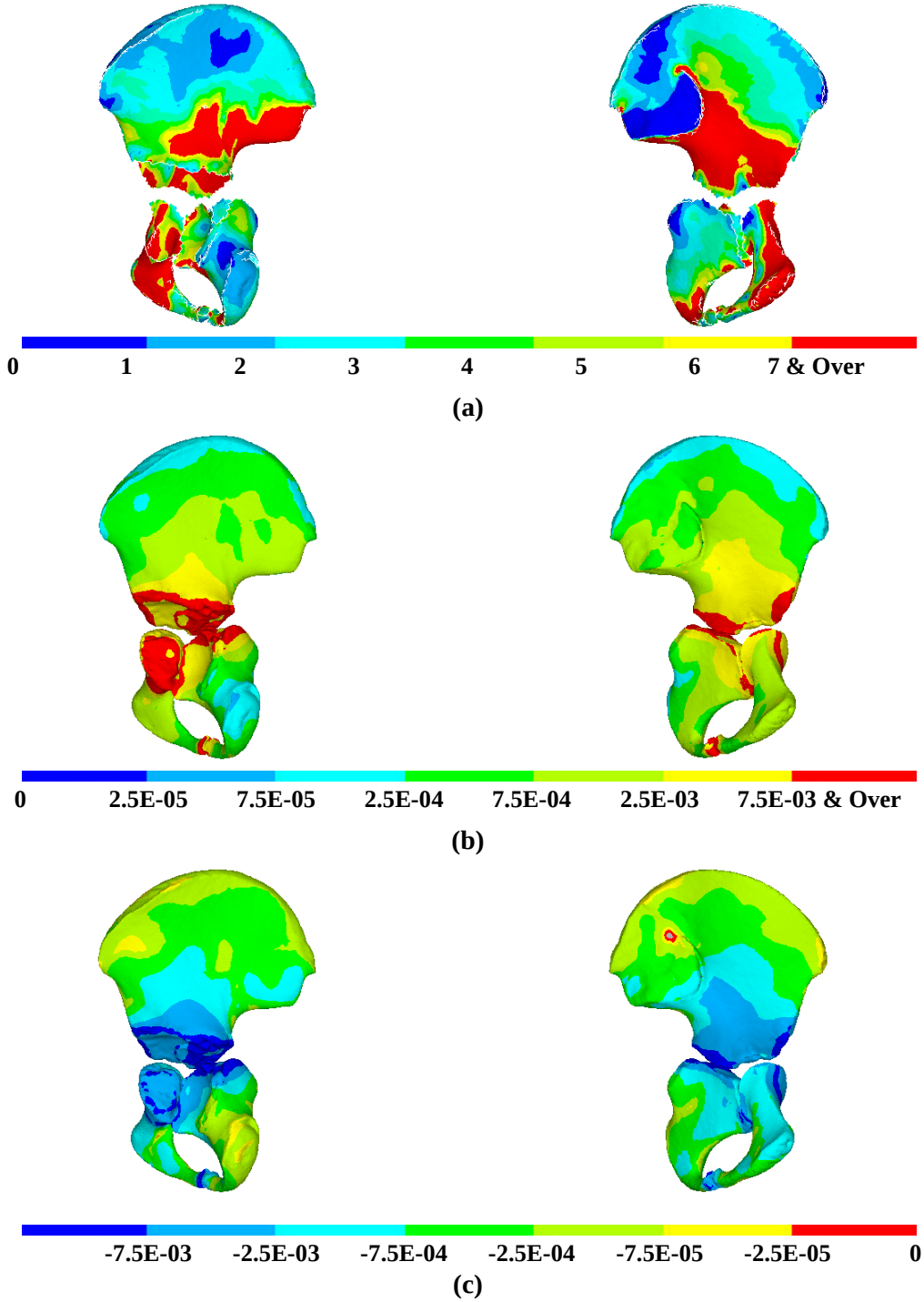

Figure 6.31. The mechanical response of the 8yr old left hemi-pelvis when loaded with 25% of the MS forces associated with the 5th phase of the gait cycle; showing, (a) cortical von Mises Stress (MPa), (b) trabecular von Mises strain and (c) trabecular minimum principal strain.

The von Mises strain distribution shown in Figure 6.31(b) displayed resemblances to that of Figure 6.25(b), where high strains radiated superiorly from the inferior ilium, although additional concentrations were also observed travelling posteriorly.

However, the von Mises strains dissipated more efficiently to produce a marginally lower loaded iliac fossa and crest. Compressive trabecular strains within the 8yr old hemi-pelvis (see Figure 6.31(c)) were slightly higher than those within the 1yr old (see Figure 6.25(c)), with magnitudes above 2500με in the ar region, and ranging between 750-2500με around the location of the tc. Compressive strains lowered near the greater sciatic notch to values of 250-750με, and dropped to lower levels in the sm location. A concentration was formed which loosely correlated to the pt, although no distribution was formed along the at. The restriction of the forces applied through load regime 1 to 25% of their actual values, was considered appropriate as a maximum displacement of 0.67mm (0.72% PD) produced a physiological deformation.

As observed within the prenatal and 1yr old hemi-pelves, the variation of the triradiate cartilage did not cause any variation of the trabecular compressive strain distribution (see Figure 6.32). Despite the maximal displacement ranging between 0.61-2.71mm (0.67-2.91% PD), the deformation remained solely within the triradiate cartilage, thus did not affect the pelvic bone mechanics.

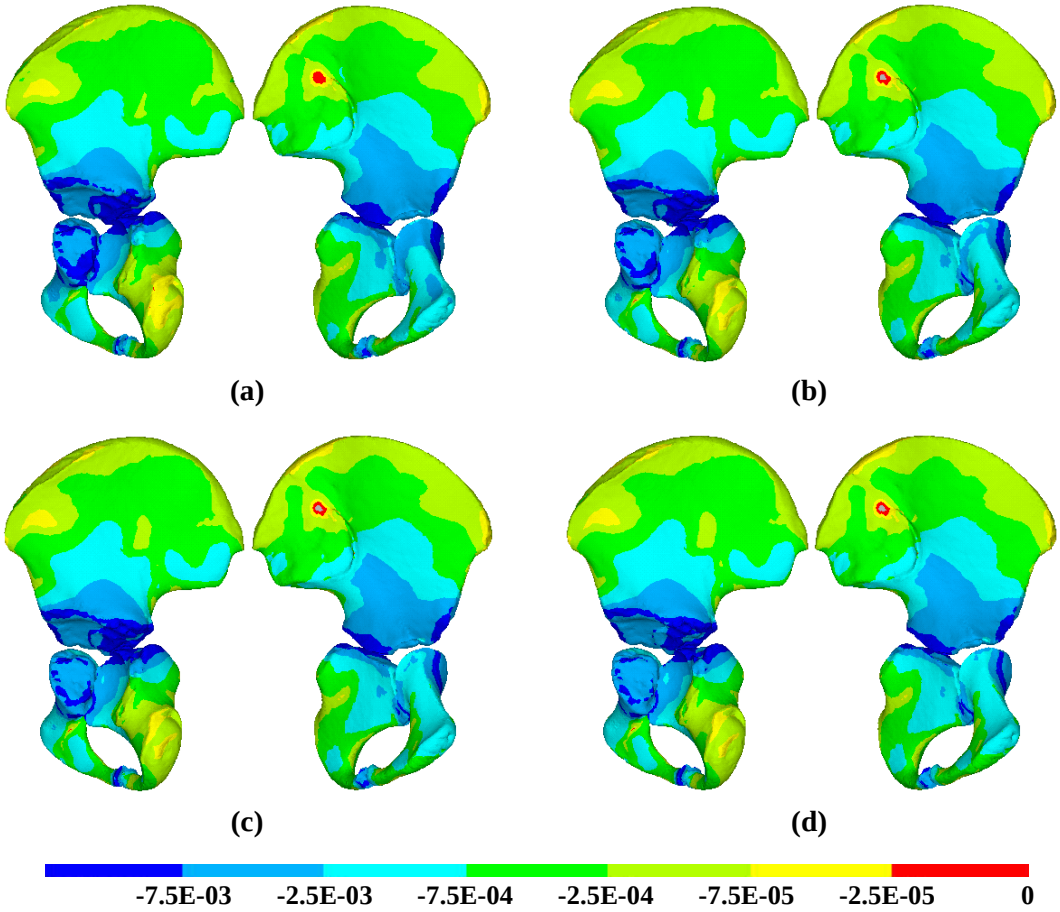

Figure 6.32. The trabecular minimum principal strain distribution of the 8yr old left hemi-pelvis produced by 25% of the MS forces associated with the 5th phase of the gait cycle and a triradiate cartilage modulus of (a) 5MPa, (b) 20MPa, (c) 30MPa and (d) 50MPa.

Load regime 2 also caused high cortical von Mises stresses to concentrate around the SIJ and ilio-pubic ridge, and within the inferior ilium (see Figure 6.33(a)). However, stress magnitudes were lower than those witnessed in Figure 6.31(a), producing a higher level of stress relieving along the superior pubic ramus. The von Mises strain distribution of Figure 6.33(b) was also similar to that produced by load regime 1 (see Figure 6.31(b)), although the high strains within the inferior ilium dissipated more efficiently. Therefore, load regime 2 produced a significantly lower strain superior ilium, while the previous large concentrations within the posterior hemi-pelvis became less prominent.

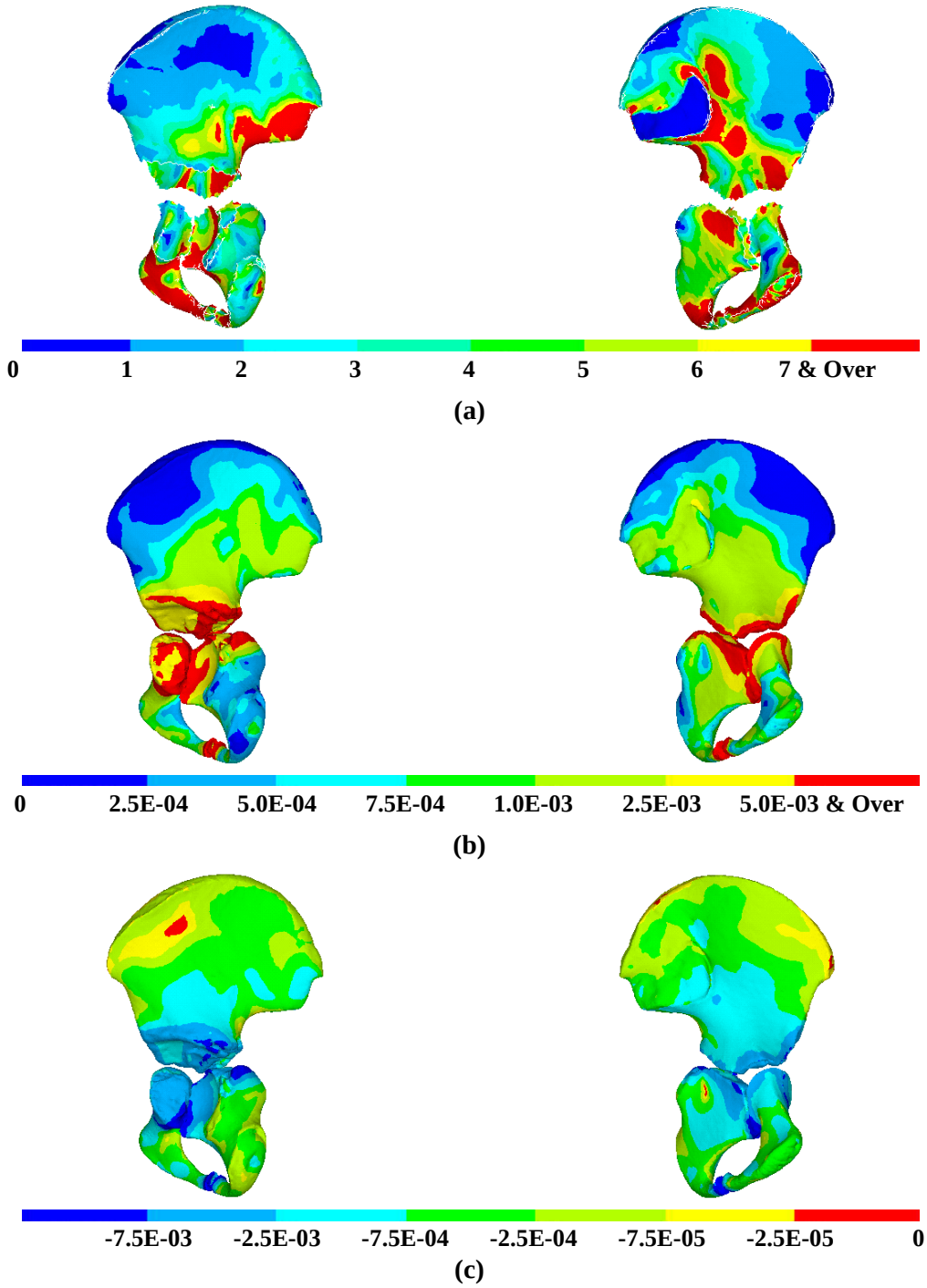

Figure 6.33. The mechanical response of the 8yr old left hemi-pelvis when loaded with 10% of the cumulative maximum muscle and joint forces associated with the gait cycle; showing, (a) cortical von Mises Stress (MPa), (b) trabecular von Mises strain and (c) trabecular minimum principal strain.

The trabecular compressive strain distributions were again similar to those observed in Figure 6.31(c), albeit with slightly lower maximal concentrations. The high strains located around the ar and tc regions and the pt, ranged between 750-2500με, which is

sufficient enough to cause the high level of remodelling evident in these regions. Magnitudes decreased around the sn region to 75-250με, which was considered too low to form the high trabecular organisation. Similar values were observed in the sm region, consistent with the low level of trabecular formation. No concentrations were observed in the region of the at. Restriction of the maximum forces associated with the gait cycle to 10% of their actual values, proved successful in maintaining a physiological displacement of 1.17mm (1.26% PD).

As witnessed previously, the variation of the triradiate cartilage only served to alter the deformation of the acetabulum, and not the mechanics of the pelvic bone (see Appendix VI).

6.5.2. Stress and strain distribution associated with maximal isometric muscle forces

Similar cortical von Mises stress distributions were generated through the application of load regime 3, although as observed within the 1yr old hemi-pelvis, the stresses were significantly larger (see Figure 6.34(a)). Therefore, the superior pubic ramus was once again highly stressed. The trabecular von Mises strains radiated from the maximal concentration within the inferior ilium, although a significant concentration was also formed posteriorly. The strains dissipated in a column like fashion superiorly, producing a fairly uniform strain distribution throughout much of the inferior ilium and iliac fossa (see Figure 6.34(b)). The trabecular compressive strains illustrated in Figure 6.34(c), generated a more uniform strain distribution that previously observed, loading the majority of the ilium within a range between 750-2500με. Although high strains were located around the ar and tc regions, no other distributions to match the other trabecular trajectories could be identified. Despite the

high levels of compressive strains throughout the structure, a physiological maximal displacement was still maintained at 1.13mm (1.21% PD).

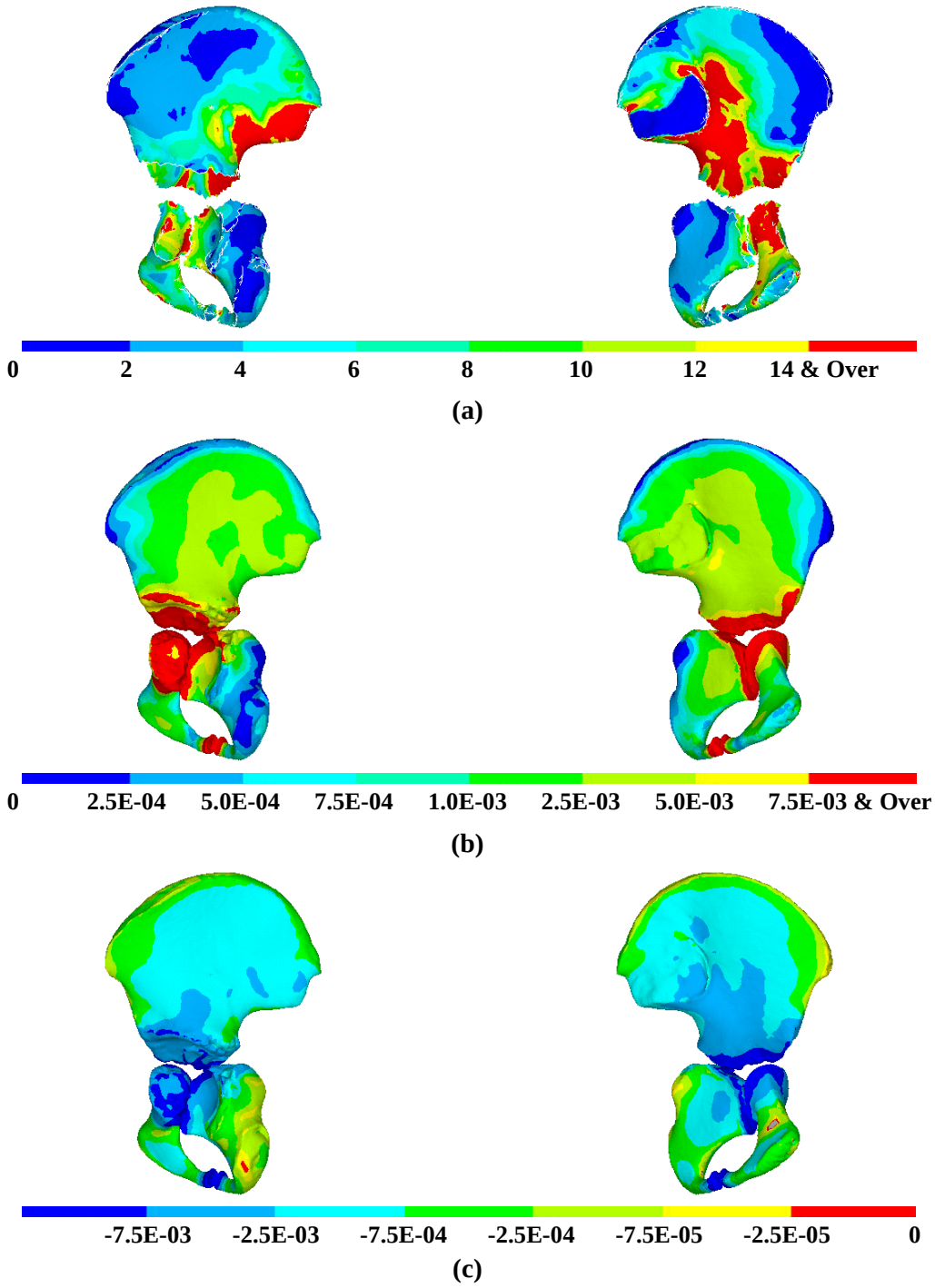

Figure 6.34. The mechanical response of the 8yr old left hemi-pelvis when loaded with 1% of the maximum isometric muscle forces and a hip joint force of 1x BW; showing, (a) cortical von Mises Stress (MPa), (b) trabecular von Mises strain and (c) trabecular minimum principal strain.

Similar to that observed within the 1yr old hemi-pelvis, hip joint loading with larger factors of BW caused a significant increase in the trabecular compressive strains throughout the whole ilium (see Figure 6.35). Despite the increased strain magnitudes inciting a variation in the distributions, no clearly correlation to the trabecular trajectories was observed. The maximum displacement produced by varying the BW factors ranged between 1.05–4.12mm (1.13–4.43% PD). However, when no acetabular loading was applied, a higher level of displacement was produced in comparison to the models in Figure 6.35(b) and Figure 6.35(c). This was once again attributed to the hip joint loading at 1 and 2 times BW counteracting the forces of the pelvic muscles spanning the hip joint.

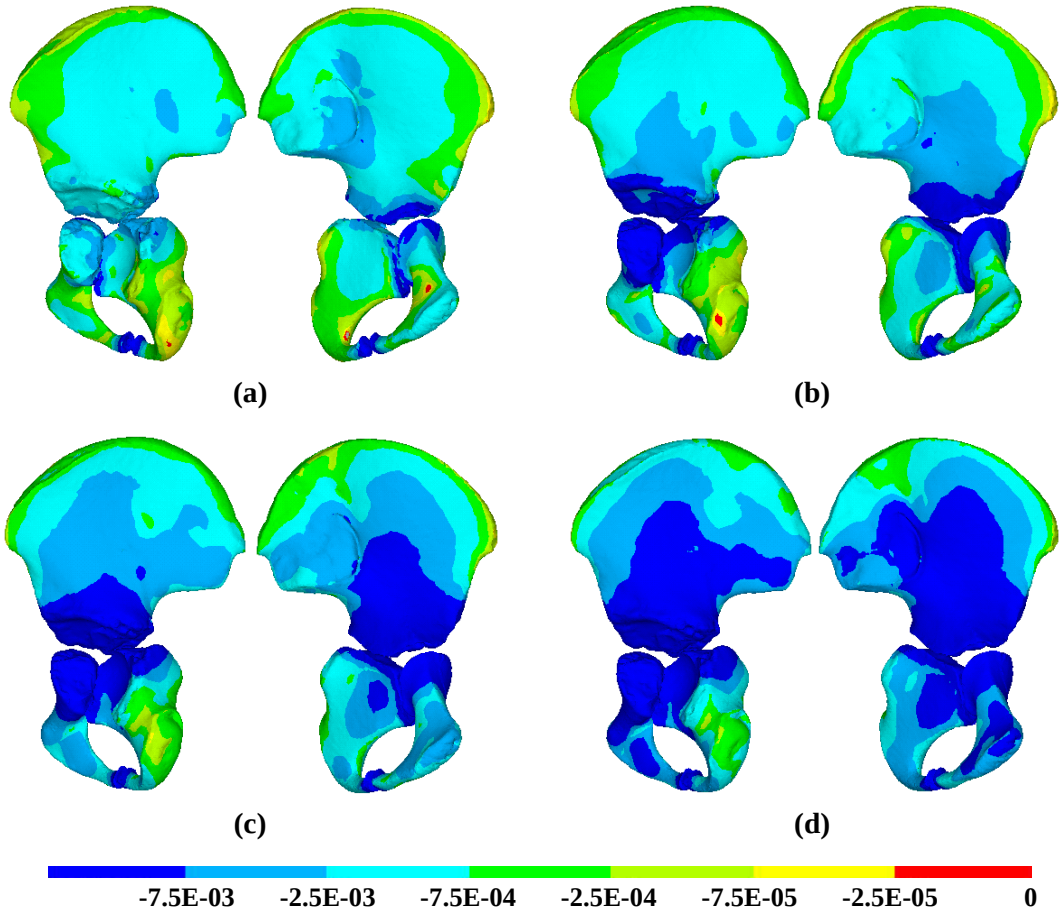

Figure 6.35. The trabecular minimum principal strain distribution of the 8yr old left hemi-pelvis produced when applying 1% of the maximum isometric muscle forces and a hip joint force of (a) 0% BW, (b) 1% BW, (c) 2% BW, (d) 5% BW and (e) 10% BW.

7. DISCUSSION

The predicted von Mises and compressive mechanical strains generally displayed similar distributions for the all juvenile ages analysed, characterised by a large concentrations within the inferior ilium which dissipated superiorly into the iliac fossa (see Chapter 6). In comparison to the trabecular trajectories illustrated in Figure 2.7, high strains were observed in the locations of the ar and tc. The maximal von Mises and compressive strain values exceeded 2500με within the former, significantly surpassing the reported thresholds suggested to instigate bone remodelling (Martin, 2000; Ward et al., 2009). Due to the superior radiation of the concentrations from the inferior ilium, strain magnitudes between 750-2500με were observed within the position of the tc, which again generally exceeded the remodelling threshold. In relation to the bone remodelling illustrated in Figure 2.3, this magnitude placed the tc in the overload range, while the ar region was within the pathological over load range. In instances when the strains dissipated rapidly from the inferior ilium, the majority of the iliac fossa and crest was relatively unloaded (see Figure 6.15, Figure 6.25 and Figure 6.31). The resulting strain distribution often caused a reduction in the magnitudes around the greater sciatic notch, to levels unfavourable with causing the high trabecular organisation within this region. Loading which caused an increase in the inferiorly located strain concentrations, often produced a more uniform distribution with a gradual strain dissipation (see Figure 18, Figure 22, Figure 25, Figure 28, Figure 33 and Figure 34). Consequently, high magnitude concentrations travelled along the ilio-pubic ridge and towards the superior regions of the SIJ articulation, creating a distribution loosely correlating to the pt. However, this concentration also expanded anteriorly to produce similar strain magnitudes within the central iliac blade, which were too high to be associated with

the low density sm region. There was no evidence of a distinct strain concentration directed anteriorly to correspond to the at. Consequently, comparisons between the predicted von Mises and compressive strain distributions of the prenatal, 1yr and 8yr old hemi-pelves and the trabecular trajectories described in literature (Macchiarelli et al., 1999; Rook et al., 1999; Cunningham and Black, 2009a, 2009b) were limited.

A slightly varied von Mises and compressive strain distribution was observed within the 19yr old pelvis, although larger magnitudes were once again concentrated within the inferior ilium (see Figure 6.8 and Figure 6.9). High strains radiated both superiorly into the ilium and inferiorly into the acetabulum, while a secondary concentration formed within the iliac fossa. This secondary concentration produced unreasonably high strain magnitudes to be associated with the location of the sm region. Unfortunately, literature reporting FE analyses of the adult pelvis under physiological loading (Dalstra and Huiskes, 1995; Majumder et al., 2005; Phillips et al., 2007) do not report strain distributions, therefore the validity of those predicted in this study was difficult ascertain. However, the cortical and trabecular stress distributions of the 19yr old hemi-pelvis (see Figure 6.6 and Figure 6.7) were comparable with those documented in literature. Although the stress magnitudes within this study were larger, this was attributed to the use of differing MS loading and the possible variations of the hemi-pelvic morphology. Therefore, it was concluded that the hemi-pelvis responded in a physiological manner under loading.

The contour plots displayed in Chapter 6 aimed to display the range of strains throughout the hemi-pelvis. Therefore, the strain contours did not reflect the strain threshold ranges reported by Martin (2000) (see Figure 2.3), thus failing to fully illustrate the hemi-pelvic regions which were homeostatic or undergoing bone formation. Figure 7.1 shows altered contours which correspond to the threshold

ranges for load regimes of the prenatal, 1yr and 8yr old hemi-pelves. Despite the distribution of the compressive strains being visually altered, they still provided the same general observations as described previously. Therefore, analysing strain distributions through contours which did not fully represent the bone threshold ranges, was presumed not to affect the observations and conclusions made.

The analysis of the hemi-pelvic strains was also limited to the von Mises and compressive states. The von Mises strains were recorded to observe if the distribution produced by the averaged strain magnitudes coincided with the known trabecular trajectories. The compressive strains were analysed in accordance with Wolff's law, which states that the trabecular trajectories align to principal trajectories. The minimum principal strain was deemed appropriate due to the nature of pelvic loading, which was expected to predominately place the structure in compression.

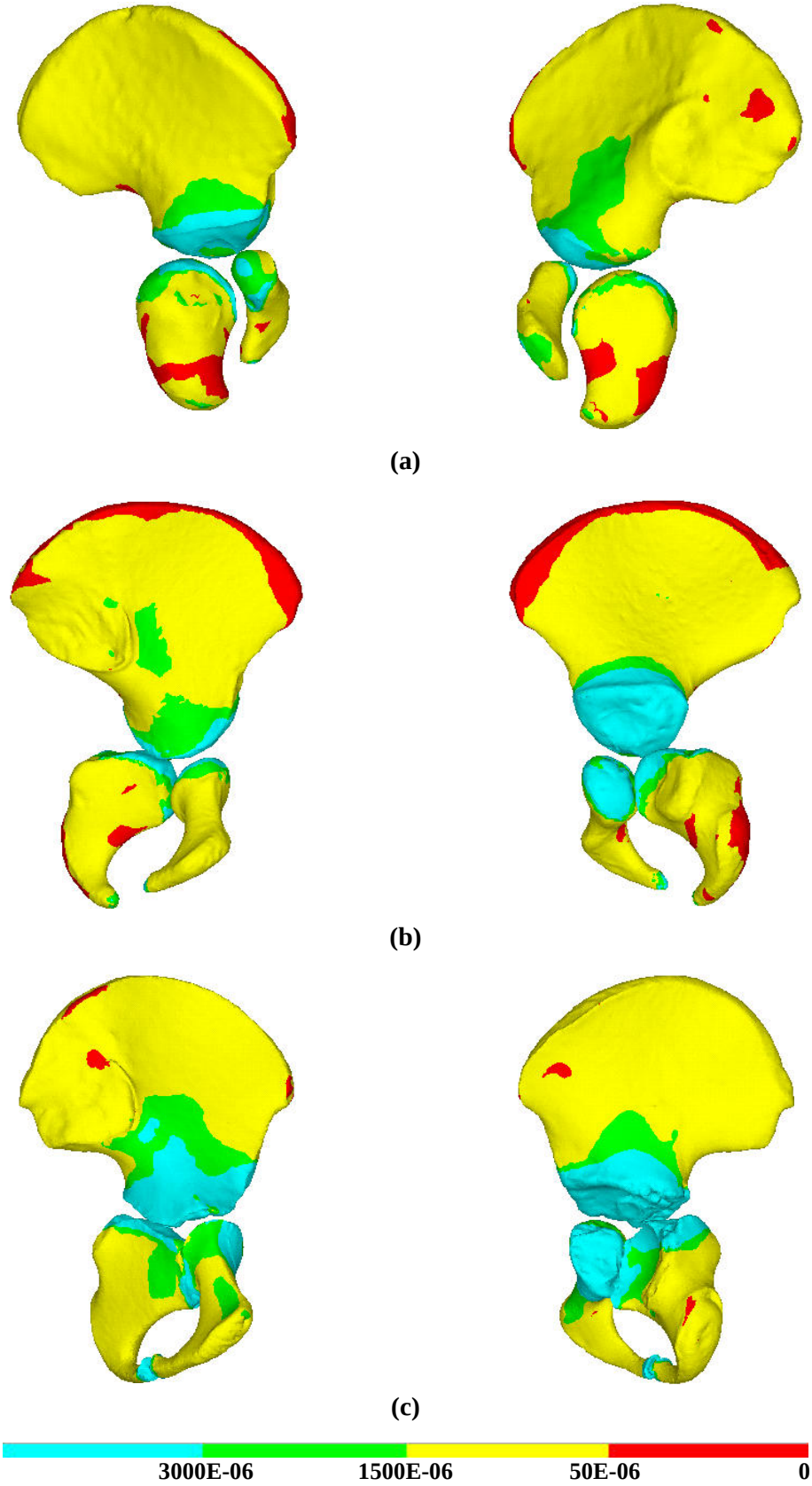

Figure 7.1. The minimum principal strain of the trabecular bone showing; (a) the prenatal hemi-pelvis under load regime 3 (see Table 6.1), and the (b) the 1yr old hemi-pelvis and (c) the 8yr old hemi-pelvis under load regime 1 (see Table 6.2).

7.1. VALIDITY OF PREDICTED STRAIN DISTRIBUTIONS

The validity of the predicted stress and strain distributions was dependent on the methods employed to construct the juvenile FE models. The areas considered for discussion are the replication of the physiological loading and mechanical interactions of the pelvis though FE methods, the predicted MS loading associated with *in utero* and bipedal movements, and the reconstruction of the juvenile hemi-pelvic geometry.

7.1.1. Validity of the finite element modelling

The validity of the methods used to replicate the pelvic constraints within the FE models was assessed through analysis of the 19yr old hemi-pelvis, where computed cortical and trabecular von Mises stress distributions were comparative to those within literature. Therefore, modelling of the MS anatomy through single lines of action per muscle (or segments in cases when muscles were split into regions) produced valid results. However, this was still considered a limitation of the modelling, as the forces applied to the nodes within an origin area were defined at the same angles. Consequently, this method did not fully replicate the fanning nature of the muscle fibres, as illustrated in Figure 2.17 and Figure 5.8. Landmarking of muscle origin sites on the pelvis was open to operator error, although they were identified with the aid of numerous anatomical texts (Scheuer and Black, 2000; Moore and Agur, 2002; Stobotta, 2006), which aimed to accurately define their location.

The constraints applied to the juvenile FE models may have influenced their mechanical response to the applied MS loading. Modelling the physiological

interaction between the pelvis and sacrum (Li et al., 2007; Majumder et al., 2007; Majumder et al., 2008b, 2009; Leung et al., 2009) is only possible with the availability of the CT data containing the pelvic girdle. However, due to the disarticulated nature of the specimens of the Scheuer collection, hemi-pelvic modelling was employed through making possible over estimations of the physiological structural constraints. Analysing numerous methods of constraining the 19yr old hemi-pelvis suggested that inclusion of the contralateral side, relieved high stresses along the superior pubic ramus (see section 6.1). An alternative method which permitted a degree of translation at the pubic symphysis also proved successful in relieving high pubic stresses, and formed similar distributions to those generated through the inclusion of the contralateral hemi-pelvis. Therefore, this method was applied to the other juvenile hemi-pelves, and aided in the formation of low stresses within the prenatal pubis (see section 6.3). Although, there were instances within the 1yr old (see Figure 6.25) and 8yr old (see Figure 6.31) hemi-pelves were the pubic stresses increased.

The results of section 6.1 also showed that modelling a layer of SIJ cartilage did not prove successful in achieving rotation of the pelvis. Sagittal rotation would have been produced through decreasing the SIJ cartilage modulus, although this was expected to have increased the pelvic deformation beyond a physiological magnitude. Modelling the hyperelastic material properties reported in literature (Li et al., 2006; Kim et al., 2009) would have increased the accuracy in modelling the soft tissue under loading. An attempt to perform such modelling was unsuccessful due to a high level of deformation which occurred within the SIJ cartilage elements. However, the limited rotation of the SIJ within the 19yr old hemi-pelvis did not produce significantly

altered pelvic stresses in comparison to those previously reported (Dalstra and Huiskes, 1995; Majumder et al., 2005; Phillips et al., 2007).

The analysis of the juvenile hemi-pelvic stress and strain distributions (see Chapter 6) was made with respect to the assumed material properties modelled. Cortical and trabecular bone was presumed to behave in a linear isotropic manner (Dalstra et al., 1993), while homogenous properties were modelled throughout the pelvis. Therefore, despite the range of the trabecular modulus and cortical thickness reported within the adult pelvis (Dalstra et al., 1995, Anderson et al., 2005), average values were defined for each material property. However, this method was employed primarily because element-specific material properties could not be determined from the μCT data of the original specimens. Although, both Dalstra et al. (1995) and Anderson et al. (2005) found that modelling homogeneous material properties produced a mechanical response which was similar to that created through element-specific values. Anderson et al. (2005) also concluded that predicted pelvic stresses were more sensitive to alterations in cortical thickness in comparison to trabecular modulus. Therefore, it would be reasonable to presume the validity of the predicted stress/strain distributions was mainly subject to the accuracy of representing the pelvic cortex. The influence of varying the cortical shell thickness within the prenatal model was examined, using the histomorphometric data reported by Cunningham and Black (2009c) (see Appendix VII). A homogenous cortical thickness was observed to produce comparative von Mises stress/strain distributions to instances when the cortex was modelled through eight separate regions of varying thickness. A more complex cortical structure which comprised of 64 separate regions, produced the most marked difference in the pelvic mechanics, although comparisons were still observed with the more simplistic modelling. Therefore, this provided evidence to

suggest that homogenous modelling of the cortical thickness was fairly valid in the case of the prenatal hemi-pelvis.

It is acknowledge that the histomorphometric data of Cunningham and Black (2009c) relates to the neonatal pelvis, and therefore is not fully applicable to the estimation of the prenatal morphology. However, due to the estimated gestational age of the prenatal specimen and the reduction in the MS loading after birth, the thicknesses applied were not presumed to overestimate the actual stiffness too excessively. The applied cortical thicknesses for the 1yr and 8yr old hemi-pelves was likely to be less valid, as they were based on the average thickness from bioposes taken from the region around the ASIS (Glorieux et al., 2000; Parfitt et al., 2000). Consequently, reported thicknesses were not representative of the whole pelvic structure. However, this remains to be the only literature detailing the histomorphometry of the juvenile pelvic cortex, albeit within a localised region. Modelling of the 19yr old cortical thickness was based solely on previous FE analyses (Cilingir et al., 2007; Coultrup et al., 2010).

As material properties of the juvenile pelvic bone is not extensively documented in literature, the trabecular and cortical moduli was defined using data from adult FE analyses (Dalstra and Huiskes, 1995; Majumder et al., 2005). Kim et al. (2009) reported that the trabecular and cortical moduli of a 10yr old pelvis was 64% and 70-80% of that modelled by Dalstra and Huiskes (1995), while the cortex was 70-80% of the thickness reported by Majumder et al. (2005). Therefore, this implies that the properties defined within Chapter 6 overestimated the stiffness of the pelvic structure. However, these findings were determined through optimising material properties through a series of FE analyses, until a predicted pelvic mechanical response matched that of one recorded experimentally. Consequently, the validity of

these results was dependent on the accuracy of the experimental data, and only related to the age of the specimen analysed. Therefore, although this indicates the degree to which juvenile bone is weaker compared to adults, its direct use within this study remained limited. Additionally, the levels of deflection observed within Chapter 6 were within physiological ranges. Decreasing the modelled bone strength would have caused the models to be too flexible and produced unphysiological responses. Material properties of triradiate cartilage are also sparse within literature, prompting the estimation of its modulus. Triradiate cartilage was presumed to be a linear elastic material, despite literature suggesting that cartilaginous material of the pubic symphysis and the SIJ is hyperelastic (Li et al., 2007; Majumder et al., 2007, 2008b, 2009; Leung et al., 2009). Although, Anderson et al. (2005) defined acetabular cartilage as a linear elastic material, therefore assuming triradiate acetabular cartilage modulus was between this and trabecular bone, was deemed appropriate. As shown in Chapter 6, variation of the modulus did not affect the predicted stress/strain distributions within the pelvis, and only served to deform the shape of the acetabulum. Altering the triradiate modulus also suggested that modelling between 30-50MPa produced similar maximal deflections, which were all considered to be within a physiological range. Therefore, the assumed modulus of 40MPa was deemed suitable, although modelling of hyperelastic properties may have proved more valid. However, a considerable amount of computation time would be required for modelling triradiate cartilage as a hyperelastic material, leaving linear modelling as a more viable option.

The convergence test detailed in Appendix VI concluded that modelling a mesh density of ~200,000 elements was sufficient to capture accurate hemi-pelvic mechanics. Although this was higher than previously reported within literature for

hemi-pelvic modelling (Kaku et al., 2004; Cilingir et al., 2007; Majumder et al., 2008; Zant et al., 2008), the additional nodal locations on the structural exterior was considered advantageous for defining muscle origins. The FE plots within Chapter 6 did not provide any evidence of disruptions to the stress/strain distributions, as would be expected if the modelled mesh density was inappropriate.

7.1.2. Validity of the musculoskeletal modelling

A major limitation of the prenatal MS model was the restriction of the kinematic movement to solely rotation in the sagittal plane. To faithfully replicate *in utero* movements, the hip joint should be modelled in all three degrees of rotation. However, the extent of the hip adduction/abduction and lateral rotation is difficult to ascertain, whereas an indication of the flexion can be estimated from Figure 5.1. Additionally, increasing the range of hip joint motion would increase the complexity of preventing the muscles from intersecting the pelvic bone and each other.

The predicted forces of the prenatal MS model were also dependent on the defined MIF's, which were based on previous modelling of an adult (Heller et al., 2001). This assumed that the physiology of the prenatal muscles was the same as those within the adult. The inverse dynamics was also influenced by the fetal weight determined from an age-to-weight growth chart (Ogden et al., 2002). This was subsequently dependent on the determination of the prenatal specimen gestation age, therefore inaccuracies in these estimations may have affected the MS modelling. Subject-specific MS modelling from a MRI scan, were the fetal age and weight can be estimated more accurately, would have reduced such validity issues. However, accessibility of such data is not freely available and has ethical considerations. Replicating the mechanical interactions between the prenatal limb and the womb wall was also simplified

through applying a resistive force to the kinematic motion. As shown in Table 2.4, applying a greater resistance to the hip joint movement served only to produce a relative increase in muscles forces, rather than incite different muscle activity combinations. Consequently, this could indicate that the simplifications made during construction of the prenatal model did not replicate the MS system accurately.

The validity of the prenatal MS loading was also related to the modelled muscular lines of action. Lenaerts et al. (2009) reported that the accurate definition of the HJC is required to correctly calculate joint kinetics, as incorrect joint centres subsequently influence the muscular paths spanning the hip. As the acetabulum of the original prenatal specimen was not fully intact and required reconstruction, functional methods of determining the HJC could not be utilised. Therefore, predictive methods were applied and the calculated joint coordinates averaged to estimate the joint centre. Although predictive methods contain a greater inaccurate in locating the HJC, the estimated joint centre estimates were closely positioned to each other within the acetabular labrum (see Figure 5.3). Estimating the HJC also provided evidence that the original prenatal specimen contained a correct physiological morphology.

The definition of the muscle lines of action of the prenatal model was also susceptible to operate variance, although the time expended during the construction of the muscular anatomy prohibited comparison between different operators. The method employed to replicate a femur to accompany the hemi-pelvis assumed comparative morphologies between adult and prenatal femurs. Therefore, this did not account for possible variations of regions such as the femoral neck (Tardieu and Damsin, 1997), which has been reported to effect inverse dynamics (Lenaerts et al., 2008, 2009a).

The load regimes applied to the 1yr and 8yr old FE models which were based on forces associated with the gait cycle (load regimes 1 and 2 of Table 6.2), were defined using the forces predicted from the adult MS model (see section 5.2). Although, this may be fairly plausible for the 8yr old as a mature gait is achieved close to this age (Sutherland, 1997), this would not be the case for the 1yr old hemi-pelvis. Unfortunately, the laborious nature of constructing a MS model of the 1yr old hip joint during crawling, rendered creating another model impractical. Additionally, such modelling would also have to consider the onset of early juvenile gait. Alteration of a generic MS model could have enabled estimation of MS forces during initial bipedalism, although gait and force plate data would be required for a 1yr old subject. Consequently, due to these complications, the MS loading from a mature gait pattern was applied. As the 1yr old pelvis was expected to contain a trabecular organisation related to a weight bearing function, it was deemed appropriate to apply MS loading from a mature gait.

The assessment into the validity of constructing subject-specific MS models from generic models proved inconclusive (see section 5.3). The differences between predicted and EMG measured muscle activities was attributed to possible inaccuracies within the experimental data. Therefore, it was concluded that further validation is required which analyses a larger number of subjects and makes greater attempts to record accurate experimental readings. This should be coupled with efforts to evaluate muscle forces through experiment methods, providing a greater means of comparison to the computed muscle function. Validation of this modelling technique paves the way for its application in the creation of subject-specific models of juveniles during the development of a mature gait.

7.1.3. Validity of the morphometric reconstructions

The digital modelling in Chapter 3 and section 4.2 aimed to create digital volumetric hemi-pelvic models which faithfully replicated the original articulated morphology. The GMM technique described in section 4.1 was successfully applied to reconstruct the articulated forms of the juvenile specimens. The validation of the modelling method suggested that a reconstructed 9yr old hemi-pelvis was close to the morphology of its original articulation (see section 4.2). The slight variation in form did not cause significant variation upon predicted strain distributions. However, the PCA results of Figure 4.7 showed that the original and reconstructed 9yr old hemi-pelves differed in morphology from those within the original morphometric data set, and that of the warped template. As the 9yr hemi-pelvic form was presumed to be accurate, this raised issues concerning the validity of the morphometric data set. This relates to the process of the manually reconstructing the disarticulated juvenile pelvic specimens, from which the original morphometric data was based. However, the even distribution of the data points of the original morphometric data set within Figure 4.7, suggests any possible misplacement within the manual reconstruction occurred with the same magnitude throughout the data set. Although this was considered to be unlikely, it did highlight the need for a morphological database generated through originally articulated juvenile hemi-pelves. The results of the validation were analysed with respect to the fact that only one reconstruction was compared to its original form, and that the 9yr old hemi-pelvis did not contain vast amounts of triradiate cartilage. In comparison, the 1yr hemi-pelvic bones were more difficult to rearticulate due to the lack of definition within the ilio-ischial, ilio-pubic and ischio-pubic articulation sites (see Figure 4.19). Consequently, a larger volume of triradiate cartilage was created, introducing greater inaccuracies when reconstructing its

articulated form. Therefore, additional modelling is required on younger specimens to fully analyse the validity of the technique. However, scan data containing the articulated juvenile pelves is not freely available, while cadaveric specimens are often dry and may have undergone morphological alterations.

The use of the landmark configuration illustrated in Figure 2.2 proved successfully in warping a range of differing adults pelves to warped templates of comparative morphologies. However, the analysis of the results in section 4.4 was made with respect to the unknown sex and age of the adult hemi-pelvic specimens used. Despite this, the use of the 19yr old hemi-pelvis from which to create the hemi-pelvic templates during the reconstruction process, was not considered to have any associated validity concerns.

8. CONCLUSION

This thesis aimed to investigate the influence of mechanical loading induced by the development of bipedal locomotion, upon the trabecular growth and remodelling within the human juvenile pelvis. It has been reported that the growth of trabecular bone within the adult pelvis aligns to the strain distribution produced during bipedal locomotion. Ontogenetic studies have observed the gradual optimisation of trabecular bone within the lower extremities, in response to juvenile locomotion. However, recent studies of the fetal and neonatal pelvis have observed organised trabecular structures comparative to those associated with a weight bearing function. The factors which cause such trabecular growth remain unknown, although a possible genetic blue print within the bone cells and the mechanical loading *in utero* provides a feasible explanation.

The issues related to performing biomechanical analyses based on cadaveric juvenile bone specimens were highlighted through the digitisation of the pelvis. The cadaveric dry pelvic specimens of the Scheuer Collection are mainly disarticulated, therefore a morphometric reconstruction technique was applied to reconstruct articulated structures. This technique demonstrated the ability to utilise morphometric datasets of juvenile landmark configurations, to estimate the complete morphologies of disarticulated bone specimens.

Evaluation of the muscular and joint forces produced during bipedal locomotion, highlighted the capabilities of simulation software packages to create subject-specific MS models. The personalisation of generic MS models provides an opportunity to perform juvenile modelling, and determine the loading associated with various stages during the development of a mature gait. The MS modelling of the prenatal hip joint

to replicate the *in utero* mechanical environment, demonstrated the possibilities to model other juvenile movements such as crawling.

Predicted von Mises and compressive mechanical strains from FE analyses of the prenatal, 1yr and 8yr old pelvis failed to display complete correlation to the trabecular histomorphometry within the ilium. A range of load regimes was applied which aimed to replicate the MS loading associated with the adult gait cycle, and the MIF that each muscle could exert on the pelvic cortex. The majority of the von Mises and compressive strain distributions produced by these load regimes displayed similar characteristics. Strains magnitudes exceeding threshold ranges suggested to instigate remodelling were generally concentrated within the inferior ilium, which did correspond to regions of high trabecular organisation. Although, these high strains generally dissipated superiorly in a column-like fashion, rather than travelling anteriorly or posteriorly as observed in the growth of pelvic trabecular bone. Therefore, no strain distribution correlated to the complex trabecular morphology in the ilium. Consequently, the results of this study imply that the trabecular growth witnessed within the prenatal and neonatal pelvis is predominately related to genetic influences, while mechanical loading provides a secondary system to further structural optimisation.

This study has only provided a primitive insight into the juvenile pelvic response under loading, and was subject to the validity of the applied modelling techniques. Further work is required to develop the methods of representing the pelvic MS system within biomechanical analyses. Employing a subject-specific modelling approach would enhance the accuracy of modelling procedures, initially enabling digitisation of complete anatomical features. Histomorphometric data of the juvenile pelvic bone properties could also be directly applied to FE analyses to define the

bone mechanics. Therefore, a subject-specific modelling should be adopted to investigate juvenile pelvic strains further.

9. FUTURE WORK

As this study failed to observe distinct correlations between computed mechanical strains and the complete trabecular organisation within the juvenile pelvis, further work is required to develop the applied modelling techniques. An initial study which involves the construction of a subject-specific MS model and a FE analysis of an adult patient, should be performed to analyse the validity of the employed modelling procedures. This should aim to analyse if applying subject-specific MS loading produces a close comparison between computed strains and the trabecular organisation within the pelvis. Observing a closer match between the two than that witnessed in this study, would provide further confidence in the modelling techniques and enable further work to apply the methods to the juvenile pelvis.

As a significant proportion of this study concerned the reconstruction of disarticulated juvenile pelves, future work should also concentrate on improving the reconstruction process and locating a source of articulated specimens. Although a morphometric reconstruction technique was created which facilitated the reconstruction of disarticulated bones, the method was dependent on the accuracy of the utilised morphometric dataset. Therefore, a dataset is required that contains a larger sample number and includes at least one specimen for each juvenile age. To eliminate the validity issues concerning the current dataset, juvenile landmark configurations should be taken from wet articulated pelvic specimens. This will enable greater accuracy in the estimation of juvenile landmark configurations based on anatomical measures, and provide a greater indication as the geometry of absent cartilaginous features.

The acquisition of wet articulated juvenile pelvic specimens also enables a more subject-specific approach to be employed, in instances when modelling the bones of disarticulated specimens is not essential. The direct modelling of wet samples also provides the opportunity to determine material properties from CT data, providing element-specific properties within FE analyses. This will facilitate greater accuracy in modelling the strength of the juvenile pelvis throughout ontogeny. In addition, mechanical testing of pelvic triradiate cartilage is necessary to establish if linear or hyperelastic modelling is more appropriate to represent its behaviour. However, this is dependent upon the nature of the wet specimens, as preservation methods can alter material properties. Alternatively, clinical CT scans could also be used, although the ethical implications of obtaining such data is problematic. Using specimens which contain an articulated pelvic girdle also permits accurate replication of the physiological interactions between the separate bones, rather than simplifying assumed joint motion. Experimental validation of the FE procedures employed is required to validate the assumptions made in the material modelling. However, due to the scarce availability of juvenile bone specimens and their often fragile nature, obtaining permission to perform experimentation on them is unlikely.

Locating a repository of articulated juvenile specimens would also aid the construction of MS models which replicate *in utero* and crawling movements. Modelling of specimens that maintain the complete structure of the acetabular labrum enables the use of functional methods to locate joint centres, in contrast to relying on predictive estimations. Juvenile pelvic specimens with accompanying femurs, would enhance the accuracy of created juvenile MS models, as muscle attachment sites could be identified. The complexity of the prenatal MS model should be increased further to consider adduction/abduction and rotation of the hip joint. Future work

could possibly investigate the use of ultrasonography as a means of quantifying the kinematics of fetal movement. Determining the MS loading associated with crawling will enable the analysis a greater range of juvenile ages, and analyse the strains induced through the first significant mechanical loading experienced during juvenile development.

The possibility of applying subject-specific MS modelling techniques to juveniles should also be investigating, as it provides the capabilities of determining muscle and joint forces associated the development of a mature bipedal gait. Initial work has already created MS models of juveniles based on experimentally recorded kinematic and kinetic data. However, the anthropometric scaling within AnyBody used to alter generic models, only adjusts the thigh and shank length and the pelvic width (see Figure 9.1). Therefore, to accurately model the juvenile anatomy, the complexity of the scaling requires increasing to optimise the pelvic height, and to a lesser extent, the radius of bones such as the femur.

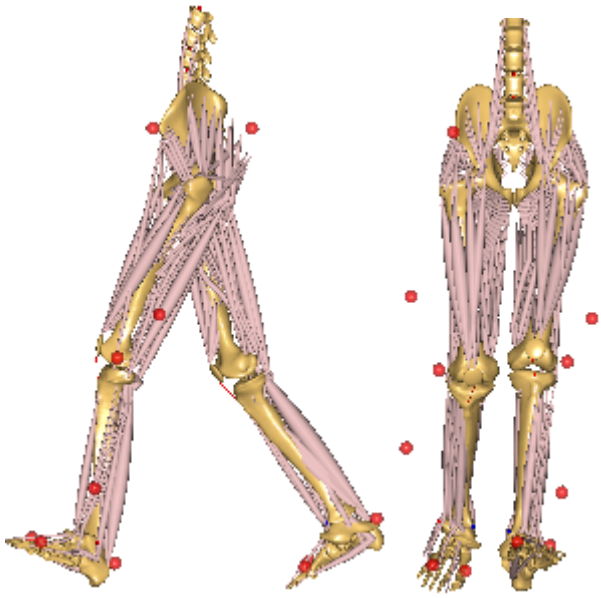

Figure 9.1. A MS model of a 7yr old within AnyBody.

Recent developments within AnyBody now provide the capabilities of importing a subjects skeletal geometry into the generic models, as determined from CT data. Identification of the muscle attachments from the scan data increases the accuracy of the subject-specific modelling. Therefore, upon the availability of such data for the juvenile, the representation of the actual juvenile anatomy significantly increases. The general method of the subject-specific modelling technique requires further validation, aimed at establishing a greater correlation between predicted and experimental muscle activity. This should be performed through analysing a greater number of participants, and devising a method of experimentally measuring a muscle force. Possible use of a isokinetic dynamometer to measure peak torques during voluntary contraction has been used to convert EMG signalling to a force, although this method needs further investigation.

REFERENCES

AFOKE, N. Y., BYERS, P. D. & HUTTON, W. C. 1987. Contact pressures in the human hip joint. *Journal of Bone and Joint Surgery - British Volume,* 69-B, 536-541.

AGOSTINI, V., NASCIMBENI, A., GAFFURI, A., IMAZIO, P., BENEDETTI, M. G. & KNAFLITZ, M. 2010. Normative EMG activation patterns of school-age children during gait. *Gait and Posture,* 32, 285-289.

ANDERSON, A. E., ELLIS, B. J., MAAS, S. A., PETERS, C. L. & WEISS, J. A. 2008. Validation of finite element predictions of cartilage contact pressure in the human hip joint. *Journal of Biomechanical Engineering,* 130.

ANDERSON, A. E., PETERS, C. L., TUTTLE, B. D. & WEISS, J. A. 2005. Subject-specific finite element model of the pelvis: development, validation and sensitivity studies. *J.Biomech.Eng,* 127, 364-373.

ANDERSON, F. C. & PANDY, M. G. 2003. Individual muscle contributions to support in normal walking. *Gait.Posture.,* 17, 159-169.

ANDERSSON, E. A., NILSSON, J. & THORSTENSSON, A. 1997. Intramuscular emg from the hip flexor muscles during human locomotion. *Acta Physiologica Scandinavica,* 161, 361-370.

ANDRIACCHI, T. P., ANDERSSON, G. B. J. & FERMIER, R. W. 1980. A study of lower-limb mechanics during stair-climbing. *Journal of Bone and Joint Surgery - Series A,* 62, 749-757.

ARNOLD, A. S., ANDERSON, F. C., PANDY, M. G. & DELP, S. L. 2005. Muscular contributions to hip and knee extension during the single limb stance phase of normal gait: a framework for investigating the causes of crouch gait. *Journal of Biomechanics,* 38, 2181-2189.

ARNOLD, A. S., BLEMKER, S. S. & DELP, S. L. 2001. Evaluation of a deformable musculoskeletal model for estimating muscle-tendon lengths during crouch gait. *Annals of Biomedical Engineering,* 29, 263-274.

ARNOLD, E. M., WARD, S. R., LIEBER, R. L. & DELP, S. L. 2010. A model of the lower limb for analysis of human movement. *Annals of Biomedical Engineering,* 38, 269-279.

AVISSE, C., GOMES, H., DELVINQUIERE, V., OUEDRAOGO, T., LALLEMAND, A., DELATTRE, J. F. & FLAMENT, J. B. 1997. Anatomic study of the pre- and neonatal hip. physiopathologic considerations on dysplasia and congenital dislocation of the hip. *Surgical and Radiologic Anatomy,* 19, 155-159.

BARRETT, R. S., BESIER, T. F. & LLOYD, D. G. 2007. Individual muscle contributions to the swing phase of gait: An EMG-based forward dynamics modelling approach. *Simulation Modelling Practice and Theory,* 15, 1146-1155.

BECKER, I., WOODLEY, S. J. & STRINGER, M. D. 2010. The adult human pubic symphysis: a systematic review. *Journal of Anatomy,* 217, 475-487.

BELL, A. L., BRAND, R. A. & PEDERSEN, D. R. 1989. Prediction of hip joint centre location from external landmarks. *Human Movement Science,* 8, 3-16.

BELL, A. L., PEDERSEN, D. R. & BRAND, R. A. 1990. A comparison of the accuracy of several hip center location prediction methods. *Journal of Biomechanics,* 23, 617-621.

BENAZZI, S., STANSFIELD, E., KULLMER, O., FIORENZA, L. & GRUPPIONI, G. 2009. Geometric morphometric methods for bone reconstruction: The mandibular condylar process of Pico della Mirandola. *Anatomical Record,* 292, 1088-1097.

BERGMANN, G., DEURETZBACHER, G., HELLER, M., GRAICHEN, F., ROHLMANN, A., STRAUSS, J. & DUDA, G. N. 2001. Hip contact forces and gait patterns from routine activities. *Journal of Biomechanics,* 34, 859-871.

BERGMANN, G., GRAICHEN, F. & ROHLMANN, A. 1993. Hip joint loading during walking and running, measured in two patients. *J Biomech,* 26, 969-90.

BERGMANN, G., GRAICHEN, F. & ROHLMANN, A. 2004. Hip joint contact forces during stumbling. *Langenbecks Arch.Surg.,* 389, 53-59.

BLANA, D., HINCAPIE, J. G., CHADWICK, E. K. & KIRSCH, R. F. 2008. A musculoskeletal model of the upper extremity for use in the development of neuroprosthetic systems. *Journal of Biomechanics,* 41, 1714-1721.

BLEMKER, S. S. & DELP, S. L. 2005. Three-dimensional representation of complex muscle architectures and geometries. *Annals of Biomedical Engineering,* 33, 661-673.

BLEMKER, S. S. & DELP, S. L. 2006. Rectus femoris and vastus intermedius fiber excursions predicted by three-dimensional muscle models. *J Biomech,* 39, 1383-91.

BOGDUK, N. 1997. Clinical Anatomy of the Lumbar Spine and Sacrum. 3rd ed. United States, Churchill Livingstone.

BOOKSTEIN, F. L. 1992. Principal warps: Thin-plate splines and the decomposition of deformations. *IEEE Transactions on Pattern Analysis and Machine Intelligence,* v, 567-585.

BOULAY, C., TARDIEU, C., BÉNAIM, C., HECQUET, J., MARTY, C., PRAT-PRADAL, D., LEGAYE, J., DUVAL-BEAUPÈRE, G. & PÉLISSIER, J. 2006. Three-dimensional study of pelvic asymmetry on anatomical specimens and its clinical perspectives. *Journal of Anatomy,* 208, 21-33.

BRAND, R. A., CROWNINSHIELD, R. D., WITTSTOCK, C. E., PEDERSEN, D. R., CLARK, C. R. & VAN KRIEKEN, F. M. 1982. MODEL OF LOWER EXTREMITY MUSCULAR ANATOMY. *J BIOMECH ENG TRANS ASME,* V 104, 304-310.

BRAND, R. A., PEDERSEN, D. R., DAVY, D. T., KOTZAR, G. M., HEIPLE, K. G. & GOLDBERG, V. M. 1994. Comparison of hip force calculations and measurements in the same patient. *J Arthroplasty,* 9, 45-51.

BUCHANAN, T. S., LLOYD, D. G., MANAL, K. & BESIER, T. F. 2005. Estimation of muscle forces and joint moments using a forward-inverse dynamics model. *Medicine and Science in Sports and Exercise,* 37, 1911-1916.

CAMOMILLA, V., CEREATTI, A., VANNOZZI, G. & CAPPOZZO, A. 2006. An optimized protocol for hip joint centre determination using the functional method. *Journal of Biomechanics,* 39, 1096-1106.

CAPPOZZO, A., CATANI, F., LEARDINI, A., BENEDETTI, M. G. & DELLA CROCE, U. 1996. Position and orientation in space of bones during movement: Experimental artefacts. *Clinical Biomechanics,* 11, 90-100.

CARTER, D. R., VASU, R. & HARRIS, W. H. 1982. Stress distributions in the acetabular region- II. Effects of cement thickness and metal backing of the total hip acetabular component. *Journal of Biomechanics,* 15, 165-170.

CHANG, W. N., LIPTON, J. S., TSIRIKOS, A. I. & MILLER, F. 2007. Kinesiological surface electromyography in normal children: Range of normal activity and pattern analysis. *Journal of Electromyography and Kinesiology,* 17, 437-445.

CILINGIR, A. C., UCAR, V. & KAZAN, R. 2007. Three-dimensional anatomic finite element modelling of hemi-arthroplasty of human hip joint. *Trends in Biomaterials and Artificial Organs,* 21, 63-72.

COULTRUP, O. J., HUNT, C., WROBLEWSKI, B. M. & TAYLOR, M. 2010. Computational assessment of the effect of polyethylene wear rate, mantle thickness, and porosity on the mechanical failure of the acetabular cement mantle. *Journal of Orthopaedic Research,* 28, 565-570.

CROWNINSHIELD, R. D. 1978. USE OF OPTIMIZATION TECHNIQUES TO PREDICT MUSCLE FORCES. *Journal of Biomechanical Engineering,* 100, 88-92.

CROWNINSHIELD, R. D. & BRAND, R. A. 1981. A physiologically based criterion of muscle force prediction in locomotion. *J Biomech,* 14, 793-801.

CUNNINGHAM, C. A. & BLACK, S. M. 2009a. Anticipating bipedalism: Trabecular organization in the newborn ilium. *Journal of Anatomy,* 214, 817-829.

CUNNINGHAM, C. A. & BLACK, S. M. 2009b. Development of the fetal ilium - Challenging concepts of bipedality. *Journal of Anatomy,* 214, 91-99.

CUNNINGHAM, C. A. & BLACK, S. M. 2009c. Iliac cortical thickness in the neonate - The gradient effect. *Journal of Anatomy,* 215, 364-370.

DALSTRA, M. & HUISKES, R. 1995. Load transfer across the pelvic bone. *J Biomech,* 28, 715-24.

DALSTRA, M., HUISKES, R., ODGAARD, A. & VAN ERNING, L. 1993. Mechanical and textural properties of pelvic trabecular bone. *Journal of Biomechanics,* 26, 523-535.

DALSTRA, M., HUISKES, R. & VAN ERNING, L. 1995. Development and validation of a three-dimensional finite element model of the pelvic bone. *J.Biomech.Eng,* 117, 272-278.

DAMSGAARD, M., RASMUSSEN, J., CHRISTENSEN, S. T., SURMA, E. & DE ZEE, M. 2006. Analysis of musculoskeletal systems in the AnyBody Modeling System. *Simulation Modelling Practice and Theory,* 14, 1100-1111.

DANIEL, M., IGLIC, A. & KRALJ-IGLIC, V. 2005. The shape of acetabular cartilage optimizes hip contact stress distribution. *J.Anat.,* 207, 85-91.

DAVIS, R. B., ÕUNPUU, S., TYBURSKI, D. & GAGE, J. R. 1991. A gait analysis data collection and reduction technique. *Human Movement Science,* 10, 575-587.

DAVY, D. T., KOTZAR, G. M., BROWN, R. H., HEIPLE, K. G., GOLDBERG, V. M., HEIPLE JR, K. G., BERILLA, J. & BURSTEIN, A. H. 1988. Telemetric force measurements across the hip after total arthroplasty. *Journal of Bone and Joint Surgery - Series A,* 70, 45-50.

DAWSON, J. M., KHMELNIKER, B. V. & MCANDREW, M. P. 1999. Analysis of the structural behavior of the pelvis during lateral impact using the finite element method. *Accid.Anal.Prev.,* 31, 109-119.

DELP, S. L., ANDERSON, F. C., ARNOLD, A. S., LOAN, P., HABIB, A., JOHN, C. T., GUENDELMAN, E. & THELEN, D. G. 2007. OpenSim: Open-source software to create and analyze dynamic simulations of movement. *IEEE Transactions on Biomedical Engineering,* 54, 1940-1950.

DELP, S. L., LOAN, J. P., HOY, M. G., ZAJAC, F. E., TOPP, E. L. & ROSEN, J. M. 1990. An interactive graphics-based model of the lower extremity to study orthopaedic surgical procedures. *IEEE Transactions on Biomedical Engineering,* 37, 757-767.

DRYDEN, I.L. & MARDIA, K.V. 1988. Statistical Shape Analysis. United Kingdom, John Wiley and Sons.

DOSTAL, W. F. & ANDREWS, J. G. 1981. A three-dimensional biomechanical model of hip musculature. *Journal of Biomechanics,* 14, 803-812.

DUBOWSKY, S. R., RASMUSSEN, J., SISTO, S. A. & LANGRANA, N. A. 2008. Validation of a musculoskeletal model of wheelchair propulsion and its application to minimizing shoulder joint forces. *Journal of Biomechanics,* 41, 2981-2988.

DUDA, G. N., BRAND, D., FREITAG, S., LIERSE, W. & SCHNEIDER, E. 1996. Variability of femoral muscle attachments. *J.Biomech.,* 29, 1185-1190.

EHRLICH, P. J. & LANYON, L. E. 2002. Mechanical strain and bone cell function: A review. *Osteoporosis International,* 13, 688-700.

EINHORN, T.A. 1996. The Bone Organ System: Form and Function. In. MARCUS, R., FELDMAN, D. & KELSEY, J. Osteoporosis. United States. Academic Press.

ENGLISH, T. A. & KILVINGTON, M. 1979. In vivo records of hip loads using a femoral implant with telemetric output (A preliminary report). *Journal of Biomedical Engineering,* 1, 111-115.

ERDEMIR, A., MCLEAN, S., HERZOG, W. & VAN DEN BOGERT, A. J. 2007. Model-based estimation of muscle forces exerted during movements. *Clin Biomech (Bristol, Avon),* 22, 131-54.

FAZEKAS, I.Gy. & KDSA, E. 1978. Forensic Fetal Osteology. Budapest: Akade~miai KiadS. FDI-F~d~ration Dentaire International.

FERGUSON, S. J., BRYANT, J. T., GANZ, R. & ITO, K. 2000. The influence of the acetabular labrum on hip joint cartilage consolidation: a poroelastic finite element model. *Journal of Biomechanics,* 33, 953-960.

FINLAY, J. B., BOURNE, R. B., LANDSBERG, R. P. D. & ANDREAE, P. 1986. Pelvic stresses in vitro-II. A study of the efficacy of metal-backed acetabular prostheses. *Journal of Biomechanics,* 19.

FROST, H. M. 1987. Bone 'mass' and the 'mechanostat': A proposal. *Anatomical Record,* 219, 1-9.

GAMBLE, J. G., SIMMONS, S. C. & FREEDMAN, M. 1986. The symphysis pubis. Anatomic and pathologic considerations. *Clin Orthop Relat Res,* 203, 261-72.

GARNER, B. A. & PANDY, M. G. 2001. Musculoskeletal model of the upper limb based on the visible human male dataset. *Computer methods in biomechanics and biomedical engineering,* 4, 93-126.

GAZENDAM, M. G. J. & HOF, A. L. 2007. Averaged EMG profiles in jogging and running at different speeds. *Gait and Posture,* 25, 604-614.

GIBSON, L. J. 1985. The mechanical behaviour of cancellous bone. *J Biomech,* 18, 317-28.

GLORIEUX, F. H., TRAVERS, R., TAYLOR, A., BOWEN, J. R., RAUCH, F., NORMAN, M. & PARFITT, A. M. 2000. Normative data for iliac bone histomorphometry in growing children. *Bone,* 26, 103-109.

GRAY, H. 1987. Gray's Anatomy. 15th ed. United Kingdom. Chancellor Press.

GOODE, A., HEGEDUS, E. J., SIZER, P., BRISMEE, J. M., LINBERG, A. & COOK, C. E. 2008. Three-dimensional movements of the sacroiliac joint: a systematic review of the literature and assessment of clinical utility. *J Man Manip Ther,* 16, 25-38.

GUNN, C. 1984. Bones and Joints. United States. Churchill Livingstone.

GOSMAN, J. H. & KETCHAM, R. A. 2009. Patterns in ontogeny of human trabecular bone from sunWatch village in the prehistoric ohio valley: General features of microarchitectural change. *American Journal of Physical Anthropology,* 138, 318-332.

HADJIDAKIS, D. J. & ANDROULAKIS, I. I. 2006. Bone Remodeling. *Annals of the New York Academy of Sciences,* 1092, 385-396.

HARRINGTON, M. E., ZAVATSKY, A. B., LAWSON, S. E. M., YUAN, Z. & THEOLOGIS, T. N. 2007. Prediction of the hip joint centre in adults, children, and patients with cerebral palsy based on magnetic resonance imaging. *Journal of Biomechanics,* 40, 595-602.

HELLER, M. O., BERGMANN, G., DEURETZBACHER, G., DURSELEN, L., POHL, M., CLAES, L., HAAS, N. P. & DUDA, G. N. 2001. Musculo-skeletal loading conditions at the hip during walking and stair climbing. *Journal of Biomechanics,* 34, 883-893.

HELLER, M. O., BERGMANN, G., KASSI, J. P., CLAES, L., HAAS, N. P. & DUDA, G. N. 2005. Determination of muscle loading at the hip joint for use in pre-clinical testing. *Journal of Biomechanics,* 38, 1155-1163.

HICKS, J. L. & RICHARDS, J. G. 2005. Clinical applicability of using spherical fitting to find hip joint centers. *Gait and Posture,* 22, 138-145.

HODGE, W. A., FIJAN, R. S., CARLSON, K. L., BURGESS, R. G., HARRIS, W. H. & MANN, R. W. 1986. Contact pressures in the human hip joint measured in vivo. *Proc.Natl.Acad.Sci.U.S.A,* 83, 2879-2883.

HOEK VAN DIJKE, G. A., SNIJDERS, C. J., STOECKART, R. & STAM, H. J. 1999. A biomechanical model on muscle forces in the transfer of spinal load to the pelvis and legs. *J Biomech,* 32, 927-33.

HOF, A. L., ELZINGA, H., GRIMMIUS, W. & HALBERTSMA, J. P. K. 2002. Speed dependence of averaged EMG profiles in walking. *Gait and Posture,* 16, 78-86.

HOLM, N. J. 1981. The development of a two-dimensional stress-optical model of the os coxae. *Acta Orthopaedica Scandinavica,* 52, 135-143.

IVANENKO, Y. P., POPPELE, R. E. & LACQUANITI, F. 2004. Five basic muscle activation patterns account for muscle activity during human locomotion. *Journal of Physiology,* 556, 267-282.

JACOB, H. A. C., HUGGLER, A. H., DIETSCHI, C. & SCHREIBER, A. 1976. Mechanical function of subchondral bone as experimentally determined on the acetabulum of the human pelvis. *Journal of Biomechanics,* 9, 625-627.

KAKU, N., TSUMURA, H., TAIRA, H., SAWATARI, T. & TORISU, T. 2004. Biomechanical study of load transfer of the pubic ramus due to pelvic inclination after hip joint surgery using a three-dimensional finite element model. *J Orthop Sci,* 9, 264-9.

KAMPEN, W. U. & TILLMANN, B. 1998. Age-related changes in the articular cartilage of human sacroiliac joint. *Anatomy and Embryology,* 198, 505-513.

KIM, J.-E., LI, Z., ITO, Y., HUBER, C. D., SHIH, A. M., EBERHARDT, A. W., YANG, K. H., KING, A. I. & SONI, B. K. 2009. Finite element model development of a child pelvis with optimization-based material identification. *Journal of Biomechanics,* 42, 2191-2195.

KIRKWOOD, R. N., CULHAM, E. G. & COSTIGAN, P. 1999. Radiographic and non-invasive determination of the hip joint center location: effect on hip joint moments. *Clinical Biomechanics,* 14, 227-235.

KLAUE, K., DURNIN, C. W. & GANZ, R. 1991. The acetabular rim syndrome. A clinical presentation of dysplasia of the hip. *Journal of Bone and Joint Surgery - Series B,* 73, 423-429.

KLEIN HORSMAN, M. D., KOOPMAN, H. F. J. M., VAN DER HELM, F. C. T., PROSÉ, L. P. & VEEGER, H. E. J. 2007. Morphological muscle and joint parameters for musculoskeletal modelling of the lower extremity. *Clinical Biomechanics,* 22, 239-247.

KORHONEN, R. K., KOISTINEN, A., KONTTINEN, Y. T., SANTAVIRTA, S. S. & LAPPALAINEN, R. 2005. The effect of geometry and abduction angle on the stresses in cemented UHMWPE acetabular cups - Finite element simulations and experimental tests. *BioMedical Engineering Online,* 4.

LAND, C. & SCHOENAU, E. 2008. Fetal and postnatal bone development: reviewing the role of mechanical stimuli and nutrition. *Best Practice and Research in Clinical Endocrinology and Metabolism,* 22, 107-118.

LANYON, L. E. & RUBIN, C. T. 1984. Static vs dynamic loads as an influence on bone remodelling. *Journal of Biomechanics,* 17, 897-905.

LAPEER, R. J. & PRAGER, R. W. 2000. 3D shape recovery of a newborn skull using thin-plate splines. *Comput.Med.Imaging Graph.,* 24, 193-204.

LEARDINI, A., CAPPOZZO, A., CATANI, F., TOKSVIG-LARSEN, S., PETITTO, A., SFORZA, V., CASSANELLI, G. & GIANNINI, S. 1999. Validation of a functional method for the estimation of hip joint centre location. *Journal of Biomechanics,* 32, 99-103.

LENAERTS, G., BARTELS, W., GELAUDE, F., MULIER, M., SPAEPEN, A., VAN DER PERRE, G. & JONKERS, I. 2009a. Subject-specific hip geometry and hip joint centre location affects calculated contact forces at the hip during gait. *Journal of Biomechanics,* 42, 1246-1251.

LENAERTS, G., DE GROOTE, F., DEMEULENAERE, B., MULIER, M., VAN DER PERRE, G., SPAEPEN, A. & JONKERS, I. 2008. Subject-specific hip geometry affects predicted hip joint contact forces during gait. *Journal of Biomechanics,* 41, 1243-1252.

LENAERTS, G., MULIER, M., SPAEPEN, A., VAN DER PERRE, G. & JONKERS, I. 2009b. Aberrant pelvis and hip kinematics impair hip loading before and after total hip replacement. *Gait and Posture,* 30, 296-302.

LEUNG, A. S. O., GORDON, L. M., SKRINSKAS, T., SZWEDOWSKI, T. & WHYNE, C. M. 2009. Effects of bone density alterations on strain patterns in the pelvis: Application of a finite element model. *Proceedings of the Institution of Mechanical Engineers, Part H: Journal of Engineering in Medicine,* 223, 965-979.

LEWIS, C. L., SAHRMANN, S. A. & MORAN, D. W. 2007. Anterior hip joint force increases with hip extension, decreased gluteal force, or decreased iliopsoas force. *J Biomech,* 40, 3725-31.

LEWIS, C. L., SAHRMANN, S. A. & MORAN, D. W. 2009. Effect of position and alteration in synergist muscle force contribution on hip forces when performing hip strengthening exercises. *Clin Biomech (Bristol, Avon),* 24, 35-42.

LI, Z., ALONSO, J. E., KIM, J. E., DAVIDSON, J. S., ETHERIDGE, B. S. & EBERHARDT, A. W. 2006. Three-dimensional finite element models of the human pubic symphysis with viscohyperelastic soft tissues. *Ann.Biomed.Eng,* 34, 1452-1462.

LI, Z., KIM, J. E., DAVIDSON, J. S., ETHERIDGE, B. S., ALONSO, J. E. & EBERHARDT, A. W. 2007. Biomechanical response of the pubic symphysis in lateral pelvic impacts: a finite element study. *J.Biomech.,* 40, 2758-2766.

LIONBERGER, D., WALKER, P. S. & GRANHOLM, J. 1985. Effects of prosthetic acetabular replacement on strains in the pelvis. *Journal of Orthopaedic Research,* 3, 372-379.

MACCHIARELLI, R., BONDIOLI, L., GALICHON, V. & TOBIAS, P. V. 1999. Hip bone trabecular architecture shows uniquely distinctive locomotor behaviour in South African australopithecines. *J.Hum.Evol.,* 36, 211-232.

MAJUMDER, S., ROYCHOWDHURY, A. & PAL, S. 2004. Dynamic response of the pelvis under side impact load - A three-dimensional finite element approach. *International Journal of Crashworthiness,* 9, 89-103.

MAJUMDER, S., ROYCHOWDHURY, A. & PAL, S. 2005. Biomechanical analysis of human pelvis under musculo-skeletal load using 3d finite element. *Applied Mechanics and Engineering,* 10, 647-6.

MAJUMDER, S., ROYCHOWDHURY, A. & PAL, S. 2007. Simulation of hip fracture in sideways fall using a 3D finite element model of pelvis-femur-soft tissue complex with simplified representation of whole body. *Medical Engineering and Physics,* 29, 1167-1178.

MAJUMDER, S., ROYCHOWDHURY, A. & PAL, S. 2008a. Effects of trochanteric soft tissue thickness and hip impact velocity on hip fracture in sideways fall through 3D finite element simulations. *Journal of Biomechanics,* 41, 2834-2842.

MAJUMDER, S., ROYCHOWDHURY, A. & PAL, S. 2008b. Experimental validation of three-dimensional finite element model of pelvis-femur-soft tissue complex under side impact loading. *International Journal of Vehicle Safety,* 3, 117-134.

MAJUMDER, S., ROYCHOWDHURY, A. & PAL, S. 2009. Effects of body configuration on pelvic injury in backward fall simulation using 3D finite element models of pelvis-femur-soft tissue complex. *Journal of Biomechanics,* 42, 1475-1482.

MARTIN, R. B. 2000. Toward a unifying theory of bone remodeling. *Bone,* 26, 1-6.

MARTINÓN-TORRES, M. 2003. Quantifying trabecular orientation in the pelvic cancellous bone of modern humans, chimpanzees, and the Kebara 2 Neanderthal. *American Journal of Human Biology,* 15, 647-661.

MANDERS, C., NEW, A. & RASMUSSEN, J. 2008. Validation of musculoskeletal gait simulation for use in investigation of total hip replacement, The 16th Congress of the European Society of Biomechanics, July, Lucerne, Switzerland.

MASSÓ, N., REY, F., ROMERO, D., GUAL, G., COSTA, L. & GERMÁN, A. 2010. Surface electromyography applications. *Aplicacions de l'electromiografia de superficieal esport,* 45, 127-136.

MCLAUCHLAN, G. J. & GARDNER, D. L. 2002. Sacral and iliac articular cartilage thickness and cellularity: relationship to subchondral bone end-plate thickness and cancellous bone density. *Rheumatology (Oxford),* 41, 375-80.

MILES, A. W. & MCNAMEE, P. B. 1989. Strain gauge and photoelatic evaluation of the load transfer in the pelvis in total hip replacement. The effect of the position of the axis of rotation. *Proceedings of the Institution of Mechanical Engineers, Part H: Journal of Engineering in Medicine,* 203, 103-107.

MILLER, M. E. 2005. Hypothesis: Fetal movement influences fetal and infant bone strength. *Medical Hypotheses,* 65, 880-886.

MOORE, K.L. & AGUR, A.M.R. 2002. Essential Clinical Anatomy. 2nd ed. United States. Lippincott Williams and Wilkins.

MOORE, K.L. & PERSAUD, T.V.N. 2007. The Developing Human, 8th ed. United States. Saunders.

MORLOCK, M., SCHNEIDER, E., BLUHM, A., VOLLMER, M., BERGMANN, G., MULLER, V. & HONL, M. 2001. Duration and frequency of every day activities in total hip patients. *Journal of Biomechanics,* 34, 873-881.

MOYER-MILEUR, L. J., BRUNSTETTER, V., MCNAUGHT, T. P., GILL, G. & CHAN, G. M. 2000. Daily physical activity program increases bone mineralization and growth in preterm very low birth weight infants. *Pediatrics,* 106, 1088-1092.

NENE, A., BYRNE, C. & HERMENS, H. 2004. Is rectus femoris really a part of quadriceps? Assessment of rectus femoris function during gait in able-bodied adults. *Gait and Posture,* 20, 1-13.

NEPTUNE, R. R., KAUTZ, S. A. & ZAJAC, F. E. 2001. Contributions of the individual ankle plantar flexors to support, forward progression and swing initiation during walking. *Journal of Biomechanics,* 34, 1387-1398.

NOWLAN, N. C., BOURDON, C., DUMAS, G., TAJBAKHSH, S., PRENDERGAST, P. J. & MURPHY, P. 2010. Developing bones are differentially affected by compromised skeletal muscle formation. *Bone,* 46, 1275-1285.

NOWLAN, N. C., MURPHY, P. & PRENDERGAST, P. J. 2007. Mechanobiology of Embryonic Limb Development. *Annals of the New York Academy of Sciences,* 1101, 389-411.

O'HIGGINS, P. 2000. The study of morphological variation in the hominid fossil record: Biology, landmarks and geometry. *Journal of Anatomy,* 197, 103-120.

O'HIGGINS, P. & JONES, N. 1998. Facial growth in Cercocebus torquatus: An application of three-dimensional geometric morphometric techniques to the study of morphological variation. *Journal of Anatomy,* 193, 251-272.

OBERHOFER, K., MITHRARATNE, K., STOTT, N. S. & ANDERSON, I. A. 2009. Anatomically-based musculoskeletal modeling: Prediction and validation of muscle deformation during walking. *Visual Computer,* 25, 843-851.

OGDEN, C. L., KUCZMARSKI, R. J., FLEGAL, K. M., MEI, Z., GUO, S., WEI, R., GRUMMER-STRAWN, L. M., CURTIN, L. R., ROCHE, A. F. & JOHNSON, C. L. 2002. Centers for Disease Control and Prevention 2000 growth charts for the United States: improvements to the 1977 National Center for Health Statistics version. *Pediatrics,* 109, 45-60.

OONISHI, H., ISHA, H. & HASEGAWA, T. 1983. Mechanical analysis of the human pelvis and its application to the artificial hip joint - by means of the three dimensional finite element method. *Journal of Biomechanics,* 16, 427-444.

PARFITT, A. M., TRAVERS, R., RAUCH, F. & GLORIEUX, F. H. 2000. Structural and cellular changes during bone growth in healthy children. *Bone,* 27, 487-494.

PATRIQUIN, M. L., LOTH, S. R. & STEYN, M. 2003. Sexually dimorphic pelvic morphology in South African whites and blacks. *HOMO,* 53, 255-262.

PEDERSEN, D. R., BRAND, R. A., CHENG, C. & ARORA, J. S. 1987. DIRECT COMPARISON OF MUSCLE FORCE PREDICTIONS USING LINEAR AND NONLINEAR PROGRAMMING. *Journal of Biomechanical Engineering,* 109, 192-199.

PEDERSEN, D. R., BRAND, R. A. & DAVY, D. T. 1997. Pelvic muscle and acetabular contact forces during gait. *Journal of Biomechanics,* 30, 959-965.

PEDERSEN, D. R., CROWNINSHIELD, R. D. & BRAND, R. A. 1982. An axisymmetric model of acetabular components in total hip arthroplasty. *Journal of Biomechanics,* 15, 305-315.

PETTY, W., MILLER, G. J. & PIOTROWSKI, G. 1980. In vitro evaluation of the effect of acetabular prosthesis implantation on human cadaver pelves. *Bulletin of Prosthetics Research,* 10, 80-89.

PHILLIPS, A. T. M., PANKAJ, P., HOWIE, C. R., USMANI, A. S. & SIMPSON, A. H. R. W. 2007. Finite element modelling of the pelvis: Inclusion of muscular and ligamentous boundary conditions. *Medical Engineering and Physics,* 29, 739-748.

PIERRYNOWSKI, M.R. 1995. Analytic representation of muscle line of action and geometry. In: ALLARD, P., STOKES, I.A.F. & BLANCHI, J.P. 1995, Human Kinetics, United States, Human Kinetics.

PONSETI, I. V. 1978. Growth and development of the acetabulum in the normal child. *The Journal of Bone and Joint Surgery,* 60, 575-585.

PORTINARO, N. M., MURRAY, D. W. & BENSON, M. K. 2001. Microanatomy of the acetabular cavity and its relation to growth. *J Bone Joint Surg Br,* 83, 377-83.

RAPPERPORT, D. J., CARTER, D. R. & SCHURMAN, D. J. 1985. Contact finite element stress analysis of the hip joint. *J.Orthop.Res.,* 3, 435-446.

RASMUSSEN, J., DAMSGAARD, M. & VOIGT, M. 2001. Muscle recruitment by the min/max criterion -- a comparative numerical study. *Journal of Biomechanics,* 34, 409-415.

RAUCH, F. & SCHOENAU, E. 2001. The developing bone: Slave or master of its cells and molecules? *Pediatric Research,* 50, 309-314.

RAUCH, F., TRAVERS, R. & GLORIEUX, F. H. 2006. Cellular activity on the seven surfaces of iliac bone: A histomorphometric study in children and adolescents. *Journal of Bone and Mineral Research,* 21, 513-519.

RIES, M., PUGH, J., AU, J. C., GURTOWSKI, J. & DEE, R. 1989. Cortical pelvic strains with varying size hemiarthroplasty in vitro. *Journal of Biomechanics,* 22, 775-780.

RODRIGUEZ, J. I., GARCIA-ALIX, A., PALACIOS, J. & PANIAGUA, R. 1988a. Changes in the long bones due to fetal immobility caused by neuromuscular disease. A

radiographic and histological study. *Journal of Bone and Joint Surgery - Series A,* 70, 1052-1060.

RODRIGUEZ, J. I., PALACIOS, J., GARCIA-ALIX, A., PASTOR, I. & PANIAGUA, R. 1988b. Effects of immobilization on fetal bone development. A morphometric study in newborns with congenital neuromuscular diseases with intrauterine onset. *Calcified Tissue International,* 43, 335-339.

RODRIGUEZ, J. I., PALACIOS, J., RUIZ, A., SANCHEZ, M., ALVAREZ, I. & DEMIGUEL, E. 1992. Morphological changes in long bone development in fetal akinesia deformation sequence: An experimental study in curarized rat fetuses. *Teratology,* 45, 213-221.

ROHRLE, H., SCHOLTEN, R. & SIGOLOTTO, C. 1984. Joint forces in the human pelvis-leg skeleton during walking. *Journal of Biomechanics,* 17, 409-424.

ROOK, L., BONDIOLI, L., KÖHLER, M., MOYÀ-SOLÀ, S. & MACCHIARELLI, R. 1999. Oreopithecus was a bipedal ape after all: Evidence from the iliac cancellous architecture. *Proceedings of the National Academy of Sciences of the United States of America,* 96, 8795-8799.

RYAN, T. M. & KETCHAM, R. A. 2002a. Femoral head trabecular bone structure in two omomyid primates. *Journal of Human Evolution,* 43, 241-263.

RYAN, T. M. & KETCHAM, R. A. 2002b. The three-dimensional structure of trabecular bone in the femoral head of strepsirrhine primates. *Journal of Human Evolution,* 43, 1-26.

RYAN, T. M. & KETCHAM, R. A. 2005. Angular orientation of trabecular bone in the femoral head and its relationship to hip joint loads in leaping primates. *Journal of Morphology,* 265, 249-263.

RYAN, T. M. & KROVITZ, G. E. 2006. Trabecular bone ontogeny in the human proximal femur. *J.Hum.Evol.,* 51, 591-602.

RYDELL, N. W. 1966. Forces acting on the femoral head-prosthesis. A study on strain gauge supplied prostheses in living persons. *Acta Orthopaedica Scandinavica,* 37, Suppl 88:1-132.

SALOMON, L. J., BERNARD, J. P. & VILLE, Y. 2007. Estimation of fetal weight: Reference range at 20-36 weeks' gestation and comparison with actual birth-weight reference range. *Ultrasound in Obstetrics and Gynecology,* 29, 550-555.

SALZAR, R. S., GENOVESE, D., BASS, C. R., BOLTON, J. R., GUILLEMOT, H., DAMON, A. M. & CRANDALL, J. R. 2009. Load path distribution within the pelvic structure under lateral loading. *International Journal of Crashworthiness,* 14, 99-110.

SARASWAT, P., ANDERSEN, M. S. & MACWILLIAMS, B. A. 2010. A musculoskeletal foot model for clinical gait analysis. *Journal of Biomechanics,* 43, 1645-1652.

SCHEUER, L. & BLACK, S. 2000. Developmental Juvenile Osteology. 1st ed. Academic Press. United Kingdom.

SCHEYS, L., VAN CAMPENHOUT, A., SPAEPEN, A., SUETENS, P. & JONKERS, I. 2008. Personalized MR-based musculoskeletal models compared to rescaled generic models in the presence of increased femoral anteversion: Effect on hip moment arm lengths. *Gait & posture,* 28, 358-365.

SCHNITZLER, C. M., MESQUITA, J. M. & PETTIFOR, J. M. 2009. Cortical bone development in black and white South African children: Iliac crest histomorphometry. *Bone,* 44, 603-611.

SCHOENAU, E. 2006. Muscular system is the driver of skeletal development. *Annales Nestle,* 64, 55-61.

SEIDEL, G. K., MARCHINDA, D. M., DIJKERS, M. & SOUTAS-LITTLE, R. W. 1995. Hip joint center location from palpable bony landmarks - A cadaver study. *Journal of Biomechanics,* 28, 995-998.

SEIREG, A. & ARVIKAR, R. J. 1973. A mathematical model for evaluation of forces in lower extremeties of the musculo-skeletal system. *J Biomech,* 6, 313-26.

SETH, A. & PANDY, M. G. 2007. A neuromusculoskeletal tracking method for estimating individual muscle forces in human movement. *Journal of Biomechanics,* 40, 356-366.

SHIM, V., BOHME, J., VAITL, P., KLIMA, S., JOSTEN, C. & ANDERSON, I. 2010. Finite element analysis of acetabular fractures-development and validation with a synthetic pelvis. *J Biomech*.

SHIM, V. B., PITTO, R. P., STREICHER, R. M., HUNTER, P. J. & ANDERSON, I. A. 2007. The use of sparse CT datasets for auto-generating accurate FE models of the femur and pelvis. *Journal of Biomechanics,* 40, 26-35.

SHIM, V. B., PITTO, R. P., STREICHER, R. M., HUNTER, P. J. & ANDERSON, I. A. 2008. Development and validation of patient-specific finite element models of the hemipelvis generated from a sparse CT data set. *Journal of Biomechanical Engineering,* 130.

SISTON, R. A. & DELP, S. L. 2006. Evaluation of a new algorithm to determine the hip joint center. *Journal of Biomechanics,* 39, 125-130.

SKERRY, T. 2000, Biomechanical influences on skeletal growth and development, In. O'HIGGINS, P. & COHN, M.J. Development, Growth and Evolution. United Kingdom. Academic Press.

STAGNI, R., LEARDINI, A., CAPPOZZO, A., GRAZIA BENEDETTI, M. & CAPPELLO, A. 2000. Effects of hip joint centre mislocation on gait analysis results. *Journal of Biomechanics,* 33, 1479-1487.

STANSFIELD, B. W. & NICOL, A. C. 2002. Hip joint contact forces in normal subjects and subjects with total hip prostheses: Walking and stair and ramp negotiation. *Clinical Biomechanics,* 17, 130-139.

STANSFIELD, B. W., NICOL, A. C., PAUL, J. P., KELLY, I. G., GRAICHEN, F. & BERGMANN, G. 2003. Direct comparison of calculated hip joint contact forces with those measured using instrumented implants. An evaluation of a three-

dimensional mathematical model of the lower limb. *Journal of Biomechanics,* 36, 929-936.

STEELE, K. M., SETH, A., HICKS, J. L., SCHWARTZ, M. S. & DELP, S. L. 2010. Muscle contributions to support and progression during single-limb stance in crouch gait. *Journal of Biomechanics,* 43, 2099-2105.

SOBOTTA, J. 2006. Sobotta Atlas of Human Anatomy Volume 2: Thorax, Abdomen, Pelvis, Lower Limb. 14th ed. Germany. Elsevier Urban & Fischer.

SU, J. C., ZHANG, C. C., CHEN, X. Q., WANG, B. H., WU, J. G. & DING, Z. Q. 2005. Three-dimensional finite element analysis of pelvis under static loading and its biomechanical significance. *Chinese Journal of Clinical Rehabilitation,* 9, 66-67.

SUTHERLAND, D. 1997. The development of mature gait. *Gait & posture,* 6, 163-170.

SUTHERLAND, D. H. 2001. The evolution of clinical gait analysis part 1: Kinesiological EMG. *Gait and Posture,* 14, 61-70.

TAN, V., SELDES, R. M., KATZ, M. A., FREEDHAND, A. M., KLIMKIEWICZ, J. J. & FITZGERALD JR, R. H. 2001. Contribution of acetabular labrum to articulating surface area and femoral head coverage in adult hip joints: an anatomic study in cadavera. *American journal of orthopedics (Belle Mead, N.J.),* 30, 809-812.

TARDIEU, C. & DAMSIN, J. P. 1997. Evolution of the angle of obliquity of the femoral diaphysis during growth -Correlations. *Surgical and Radiologic Anatomy,* 19, 91-97.

TAYLOR, S. J. G., PERRY, J. S., MESWANIA, J. M., DONALDSON, N., WALKER, P. S. & CANNON, S. R. 1997. Telemetry of forces from proximal femoral replacements and relevance to fixation. *Journal of Biomechanics,* 30, 225-234.

TAYLOR, S. J. G., WALKER, P. S., PERRY, J. S., CANNON, S. R. & WOLEDGE, R. 1998. The forces in the distal femur and the knee during walking and other activities measured by telemetry. *Journal of Arthroplasty,* 13, 428-435.

TURNER, C. H. 1992. On Wolff's law of trabecular architecture. *Journal of Biomechanics,* 25, 1-9.

TURNER, C. H. 1998. Three rules for bone adaptation to mechanical stimuli. *Bone,* 23, 399-407.

TURNER, C. H., COWIN, S. C., YOUNG RHO, J., ASHMAN, R. B. & RICE, J. C. 1990. The fabric dependence of the orthotropic elastic constants of cancellous bone. *Journal of Biomechanics,* 23, 549-561.

VAN DRONGELEN, S., VAN DER WOUDE, L. H., JANSSEN, T. W., ANGENOT, E. L., CHADWICK, E. K. & VEEGER, D. H. 2005. Glenohumeral contact forces and muscle forces evaluated in wheelchair-related activities of daily living in able-bodied subjects versus subjects with paraplegia and tetraplegia. *Archives of Physical Medicine and Rehabilitation,* 86, 1434-1440.

VAN SINT JAN, S. 2001. The VAKHUM project: presentation and preliminarily results, The 18th Congress of the International Society of Biomechanics, Zurich, Switzerland.

VASU, R., CARTER, D. R. & HARRIS, W. H. 1982. Stress distributions in the acetabular region I. Before and after total joint replacement. *Journal of Biomechanics,* 15, 155-164.

VAUGHAN, C.L., DAVIS, B.L. & O'CONNER, J.C. 1992. Dynamics of Human Gait, United States, Human Kinetics.

VAVERKA, M., NÁVRAT, T., VRBKA, M., FLORIAN, Z. & FUIS, V. 2006. Stress and strain analysis of the hip joint using FEM. *Technology and Health Care,* 14, 271-279.

VOLPATO, V. 2008. Bone endostructure morphogenesis of the human ilium. *Morphogenèse de l'endostructure osseuse de l'ilion humain,* 7, 463-471.

VOLPATO, V., VIOLA, T. B., NAKATSUKASA, M., BONDIOLI, L. & MACCHIARELLI, R. 2008. Textural characteristics of the iliac-femoral trabecular pattern in a bipedally trained Japanese macaque. *Primates,* 49, 16-25.

WALHEIM, G. G. & SELVIK, G. 1984. Mobility of the pubic symphysis. In vivo measurements with an electromechanic method and a roentgen stereophotogrammetric method. *Clin Orthop Relat Res,* 191, 129-35.

WALKER, J. M. 1992. The sacroiliac joint: a critical review. *Phys Ther,* 72, 903-16.

WARD, K. A., CAULTON, J. M., ADAMS, J. E. & MUGHAL, M. Z. 2006. Perspective: Cerebral palsy as a model of bone development in the absence of postnatal mechanical factors. *Journal of Musculoskeletal Neuronal Interactions,* 6, 154-159.

WARD, S. R., ENG, C. M., SMALLWOOD, L. H. & LIEBER, R. L. 2009. Are current measurements of lower extremity muscle architecture accurate? *Clinical Orthopaedics and Related Research,* 467, 1074-1082.

WATSON, P. J., O'HIGGINS, P., FAGAN, M. J. & DOBSON, C. A. 2011. Validation of a morphometric reconstruction technique applied to a juvenile pelvis. *Proc Inst Mech Eng H,* 225, 48-57.

WINTER, D.A. 1990. Biomechanics and Motor Control of Human Movement, 2nd ed. United States. John Wiley & Sons.

WOLFF, J. 1892. Das Gestz der Transformation der Knochen. Berlin. Hirschwald.

WOOD, J. M., LACHEREZ, P. F., BLACK, A. A., COLE, M. H., BOON, M. Y. & KERR, G. K. 2009. Postural stability and gait among older adults with age-related maculopathy. *Invest Ophthalmol Vis Sci,* 50, 482-7.

WU, G., SIEGLER, S., ALLARD, P., KIRTLEY, C., LEARDINI, A., ROSENBAUM, D., WHITTLE, M., D'LIMA, D. D., CRISTOFOLINI, L., WITTE, H., SCHMID, O. & STOKES, I. 2002. ISB recommendation on definitions of joint coordinate system of various joints for the reporting of human joint motion - Part I: Ankle, hip, and spine. *Journal of Biomechanics,* 35, 543-548.

WU, J. Z., CHIOU, S. S. & PAN, C. S. 2009a. Analysis of musculoskeletal loadings in lower limbs during stilts walking in occupational activity. *Annals of Biomedical Engineering,* 37, 1177-1189.

WU, J. Z., LI, Z. M., CUTLIP, R. G. & AN, K. N. 2009b. A simulating analysis of the effects of increased joint stiffness on muscle loading in a thumb. *Biomedical engineering online,* 8, 41.

WYLER, A., BOUSSON, V., BERGOT, C., POLIVKA, M., LEVEQUE, E., VICAUT, E. & LAREDO, J. D. 2007. Hyaline cartilage thickness in radiographically normal cadaveric hips: comparison of spiral CT arthrographic and macroscopic measurements. *Radiology,* 242, 441-9.

YOSHIOKA, Y. & SHIBA, R. 1981. A study on the stress analysis of the pelvis by means of the three-dimensional photoelastic experiments. *Journal of the Japanese Orthopaedic Association,* 55, 209-222.

ZAJAC, F. E., NEPTUNE, R. R. & KAUTZ, S. A. 2002. Biomechanics and muscle coordination of human walking. Part I: introduction to concepts, power transfer, dynamics and simulations. *Gait Posture,* 16, 215-32.

ZANT, N. P., HEATON-ADEGBILE, P., HUSSELL, J. G. & TONG, J. 2008. In vitro fatigue failure of cemented acetabular replacements: A hip simulator study. *Journal of Biomechanical Engineering,* 130.

ZELDITCH, M.L., SWIDERSKE, D.L., SHEETS, H.D. & FINK, W.L. 2004. Geometric Morphometrics for Biologists: a Primer. United States. Elsevier Academic Press.

ZHANG, Q. H., WANG, J. Y., LUPTON, C., HEATON-ADEGBILE, P., GUO, Z. X., LIU, Q. & TONG, J. 2010. A subject-specific pelvic bone model and its application to cemented acetabular replacements. *Journal of Biomechanics,* 43, 2722-2727.

APPENDIX I

This study uses the following terminology which is based on the reference frames of the body shown in Figure A. The four imaginary planes intersect the body through the following definitions:-

Median plane –	a vertical plane intersecting the body longitudally, dividing it into left and right halves;
Sagittal plane –	a vertical plane parallel to the median;
Frontal plane –	a vertical plane perpendicular to the median plane, dividing the body into anterior (front) and posterior (back) parts;
Transverse plane –	a horizontal plane passing through the body perpendicular to both the median and frontal planes, dividing the body into superior (upper) and inferior (lower) parts.

In addition, the following definitions are also used:-

Superior –	directed upwards towards the head;
Inferior –	directed downwards towards the feet;
Anterior –	directed towards the front of the body;
Posterior –	directed towards the back of the body;
Medial –	directed towards the mid line of the body;
Lateral –	directed away from the mid line of the body;
Proximal –	nearest to the point of attachment or origin;
Distal –	located away from the attachment or origin.

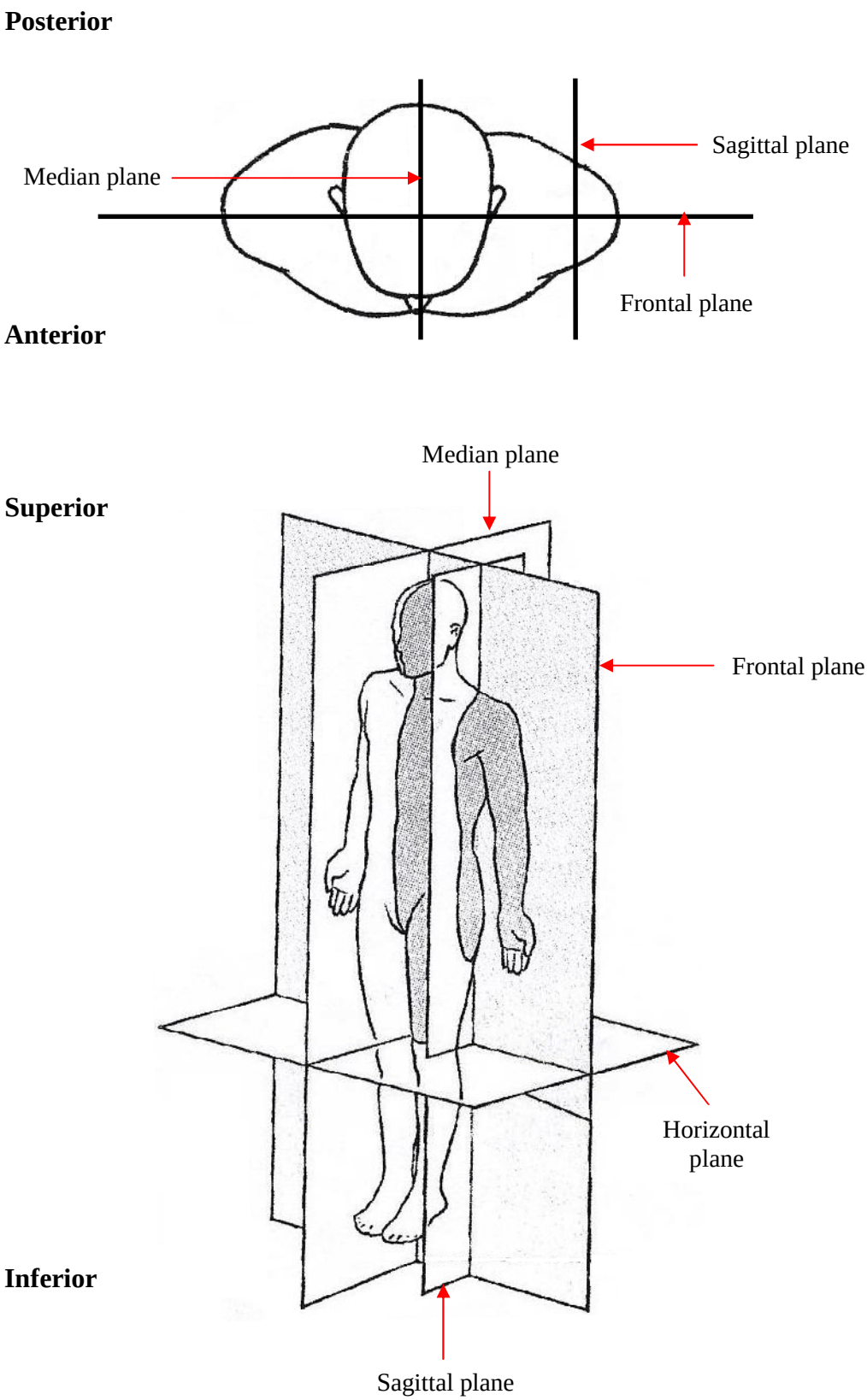

Figure A. A superior and anterio-lateral view of the reference planes of the body (adapted from Moore and Agur, 2002).

APPENDIX II

The extent to which the comparative hemi-pelvis created in section 4.3 varied from the originally articulated and reconstructed 9yr old forms, was observed through a PCA. The analysis was performed on the original morphometric dataset including the 9yr old forms, as shown in Figure B.

The close accuracy between the originally articulated and reconstructed hemi-pelves was again witnessed (particularly along PC2 and PC3), although with a slight decrease along PC1 (see Figure B). In contrast, the comparative hemi-pelvis displayed a greater variation in form along PC1 and this increased further within PC2. However, this variance decreased significantly along PC3, with the comparative hemi-pelvic morphology similar to that of the reconstructed form (see Figure B(b)). Therefore, although the comparative hemi-pelvis exhibited a larger morphological variance from the originally articulation than previously seen with the reconstructed model, it was still considered to maintain a general pelvic morphology.

As only the relative positioning between the pelvic bones was altered, and not their individual morphology, the comparative hemi-pelvis was considered to contain an appropriate variation in form for use within the FE validation.

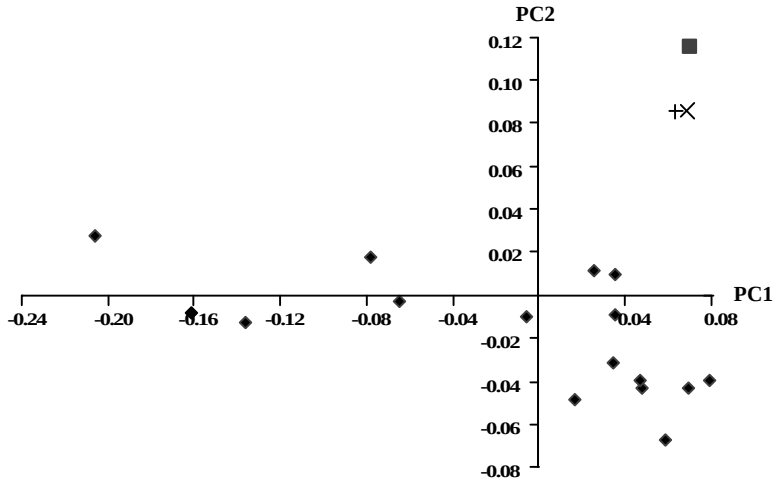

(a)

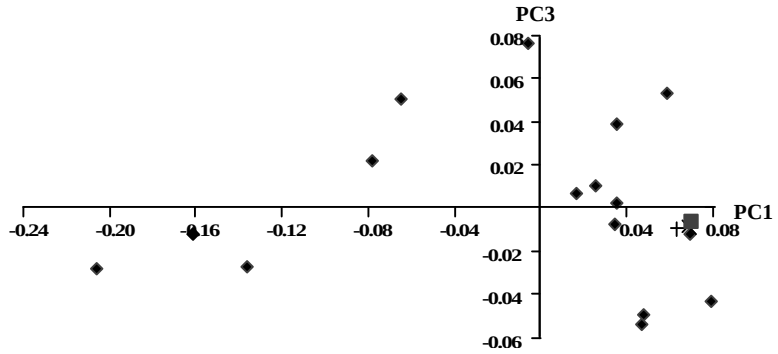

(b)

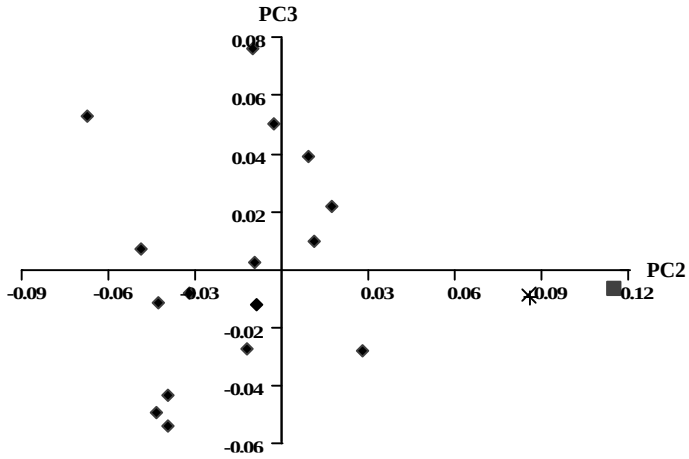

(c)

Figure B. Multivariate regression analysis of the original morphometric dataset (◆), including the originally articulated (+), reconstructed (×) and comparative (■) 9yr old hemi-pelvic forms; showing (a) PC1 vs PC2 (b) PC1 vs PC3 (c) PC2 vs PC3.

APPENDIX III

To determine if the meshes analysed throughout this study modelled a sufficient element density, a convergence test was performed on various meshes which ranged between ~117,000-2 million elements. All meshes were based on the digitised model of the originally articulated 9yr old hemi-pelvis (see section 4.3), and consisted of volumetric 10-noded tetrahedral elements (representing trabecular bone and triradiate cartilage) and 4-noded shell elements (for cortical bone). The tetrahedral element parameters of each mesh were adjusted to the recommended levels within AMIRA.

Material properties defined during the convergence testing were the same as those detailed within section 4.3.1. A simplistic loading regime was defined for each mesh, comprising of constraining four nodes within the superior ilium (two on the medial side; and two on the lateral side) in all DOF. A negative load of 12N was distributed evenly between four nodes positioned at roughly equal spacing along the obturator foramen, as illustrated within Figure C.

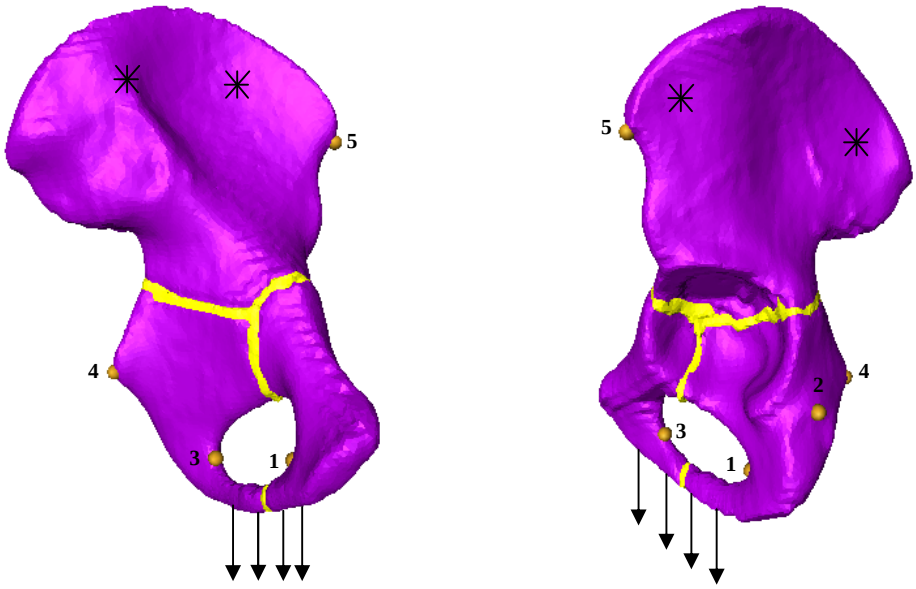

Figure C. The applied loading regime during the convergence testing which constrained four nodes within the superior ilium (2 lateral and 2 medial) and loaded the obturator foramen through four nodes (spheres show the five locations associated with elements on irregular profiles).

The level of convergence was analysed through an inter-mesh comparison of the cortical and trabecular von Mises strain distribution, and the nodal strains at specific locations. These locations were selected to include nodes associated with elements that followed regular and irregular surface profiles. As shown in Figure D, the locations of elements which were characterised by regular profiles included the iliac fossa and medial ischial body, where the surface remained fairly flat. In constrast, locations of irregular profiles were selected in regions such as the ASIS and ischial spine (see Figure C). This aimed to distinguish the level of convergence for nodes measuring a relatively even flow of strain distribution, and those experiencing a higher rate of strain change.

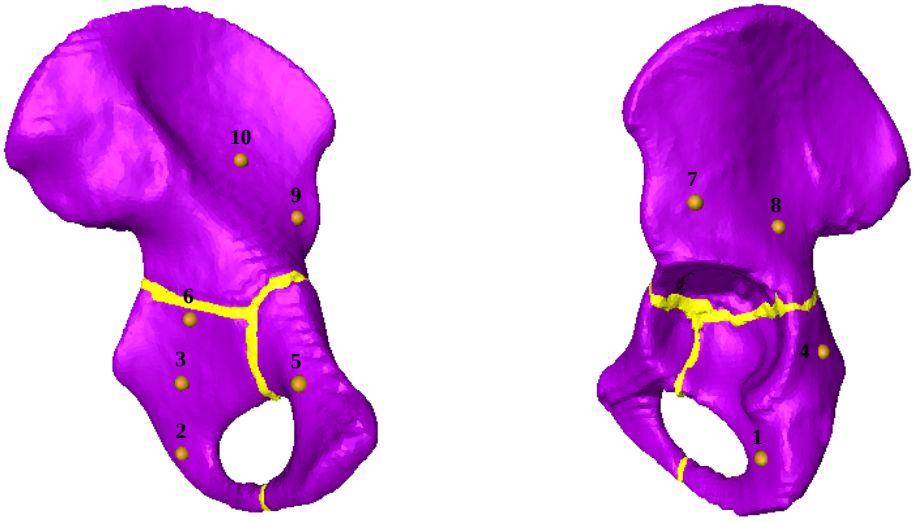

Figure D. The locations of ten nodes attached to elements on regular surface profiles.

As illustrated within Figure E and Figure F, minimal variation in the trabecular and cortical von Mises strain distribution was observed throughout the varying mesh densities. Within the trabecular bone, there was a slight increase in a concentration near the iliac crest (highlighted in Figure E(h)) when the mesh exceeded ~542,000 elements. There was also an emergence of a higher localised strain concentration within the superior iliac fossa (see Figure E(i)). It was also observed that the 2 million element mesh produced a region of a slightly increased strain within the

medial body of the ischium (highlighted within Figure E(j)). The most noticeable variation in the cortical von Mises strain distribution occurred within an iliac concentration or low magnitude (highlighted in Figure F(d)), which reduced in size between the mesh densities of ~175,000 and 250,000 elements. However, these minor variations in distribution only marginally altered the strain magnitudes and were localised to small areas. Therefore, when analysing the overall trabecular and cortical surface strains, a reasonable level of convergence was observed throughout all the meshes modelled.

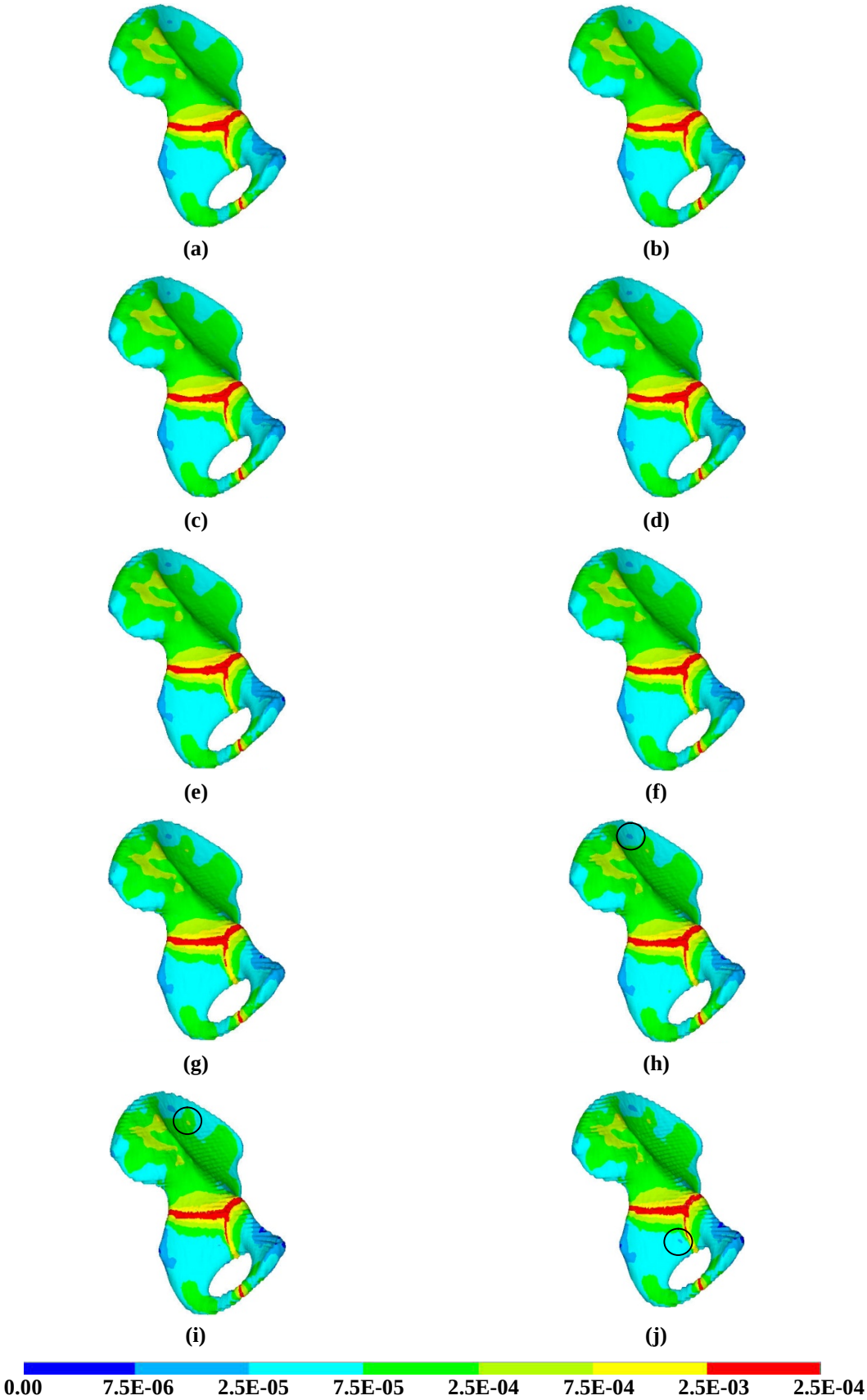

Figure E. The trabecular von Mises strain distribution produced by mesh densities containing around (a) 117,000, (b) 143,000, (c) 175,000, (d) 201,000, (e) 224,000, (f) 278,000, (g) 378,000, (h) 542,000, (i) 1million and (j) 2 million elements (the circles relate to locations of alter strain distribution).

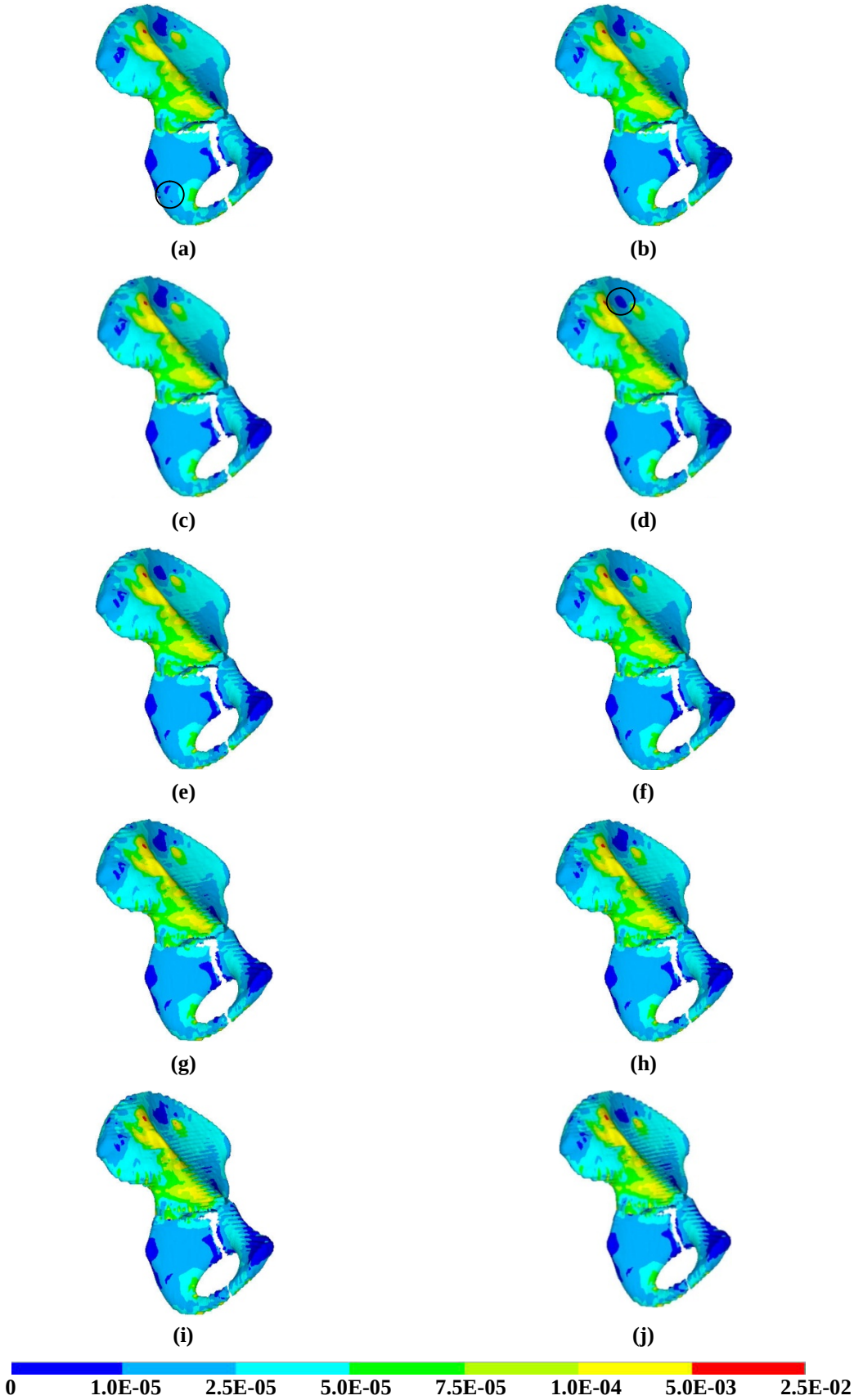

Figure F. The cortical von Mises strain distribution produced by mesh densities containing around (a) 117,000, (b) 143,000, (c) 175,000, (d) 201,000, (e) 224,000, (f) 278,000, (g) 378,000, (h) 542,000, (i) 1million and (j) 2 million elements (the circles relate to locations of alter strain distribution).

When analysing individual nodal von Mises strains, the trabecular bone displayed a high level of convergence for all mesh densities when experiencing magnitudes below 40με (see Figure G). However, more profound fluctuations were observed above this value, particularly for the mesh densities containing less than ~175,000 elements. Although, these fluctuations became less pronounced which an increasing element density. Figure G also shows that for some nodal strains above 40με, the level of convergence decreased once the total element number exceeed ~542,000 or 1 million. Such strain variation could suggest that the meshes had still not converged at the highest element densities modelled, although it was considered more plausible that these were anomalous results. This seemed a reasonable assumption, as in these instances the nodal strains remained fairly consistent for the mesh densities ranging between ~201,000 and 542,000 elements. Only two nodes produce erratic strain values between consecutive mesh densities, both of which related to elements lying on regular surface profiles. One node produced a significantly increased fluctuation between the mesh densities and was not included in Figure G.

No clear distinction was observed between the convergence of the nodes attached to elements on irregular profiles, and those associated with curved geometries. Figure G also illustrates that even low mesh densities were capable of capturing the mechanical response of the hemi-pelvic features.

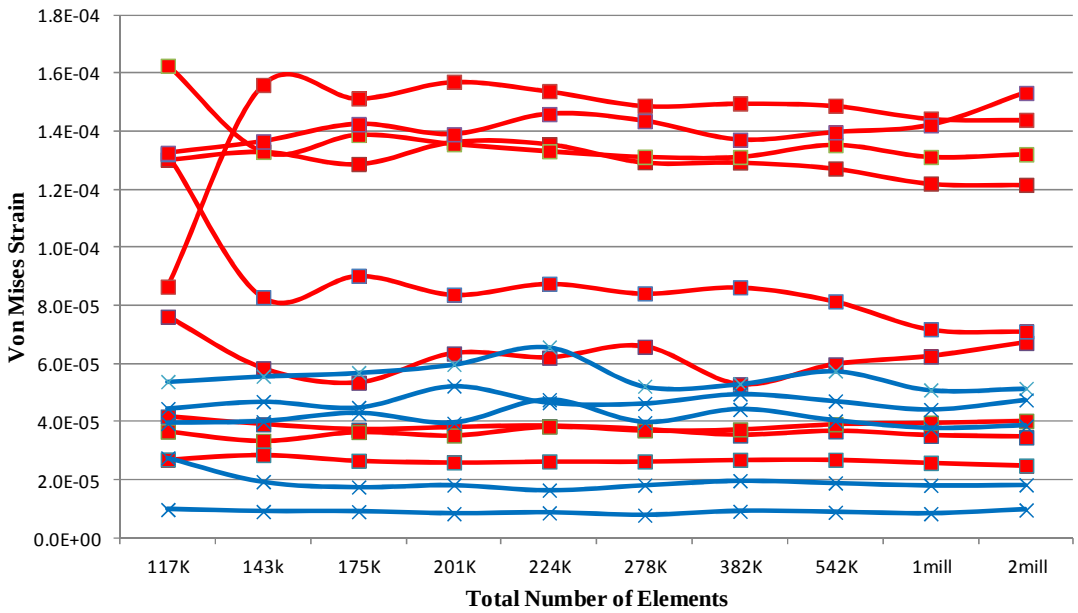

Figure G. The nodal von Mises strains of the trabecular bone produced by increasing mesh densities (red lines correspond to nodes attached to elements on regular profiles; blue lines correspond to nodes attached to elements on irregular profiles).

Similar observations were observed for the nodal results of the cortical von Mises strain, as illustrated in Figure H. Overall, a slightly higher level of convergence was observed in comparison to Figure G. However, as seen previously, the strain fluctuations increased for nodes recording higher strain magnitudes. Instances again occurred in which nodal strain variation increased upon modelling mesh densities exceeding 542,000 elements. Although, these fluctuations occurred after a relative plateau of nodal strains. Once again, there was little distinction between nodes laying on flat surfaces and those on curved geometries.

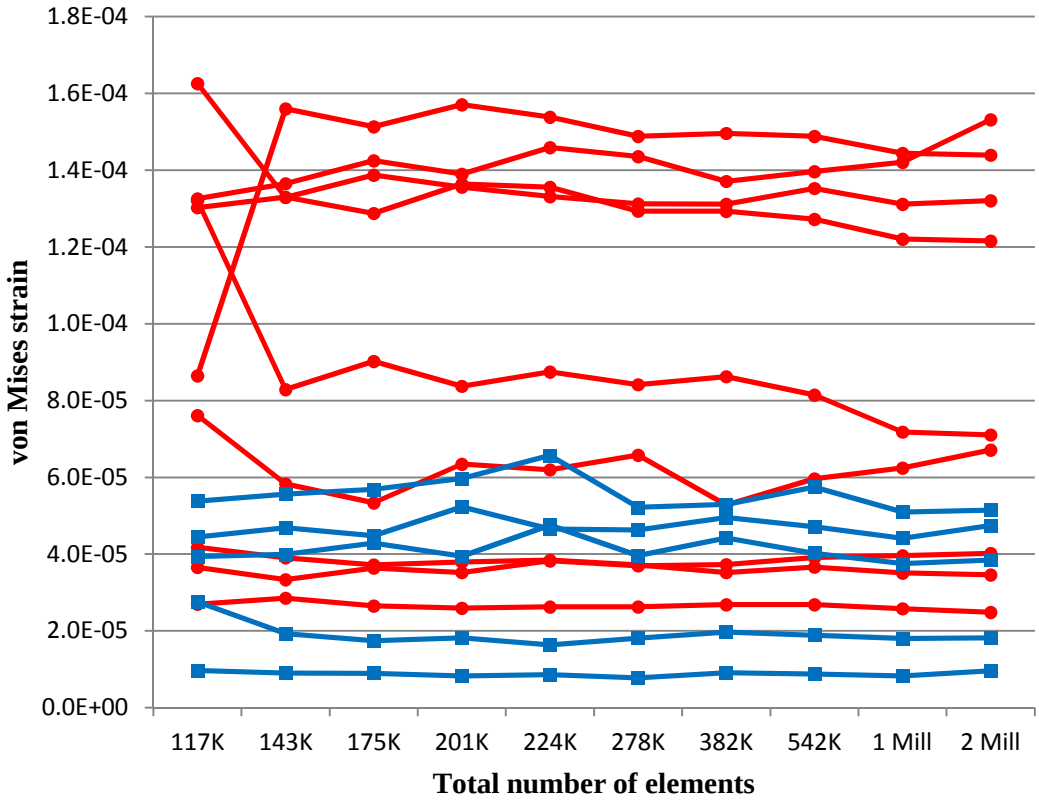

Figure H. The nodal von Mises strains of cortical bone produced by increasing mesh densities (red lines correspond to nodes attached to elements on regular profile; blue lines correspond to nodes attached to elements on irregular profiles).

To determine whether the fluctuation observed in Figure G and Figure H were anomalous data or representative of other structural regions, the average noded trabecular and cortical von Mises strains were calculated across the whole pelvic surface. As shown in Figure I, the average cortical strains converged throughout all the mesh densities modelled, producing a maximum relative variation of 2.75% (calculated as the range/the average strain). In comparison, averaged trabecular surface strains displayed an increased deviation, with a maximum relative variation of 13%. However, as shown within Figure I, the average trabecular surface strains decreased slightly once the mesh density exceeded ~542,000 elements. Therefore, when these results were discarded, the maximum relative variation reduced to 6.25%.

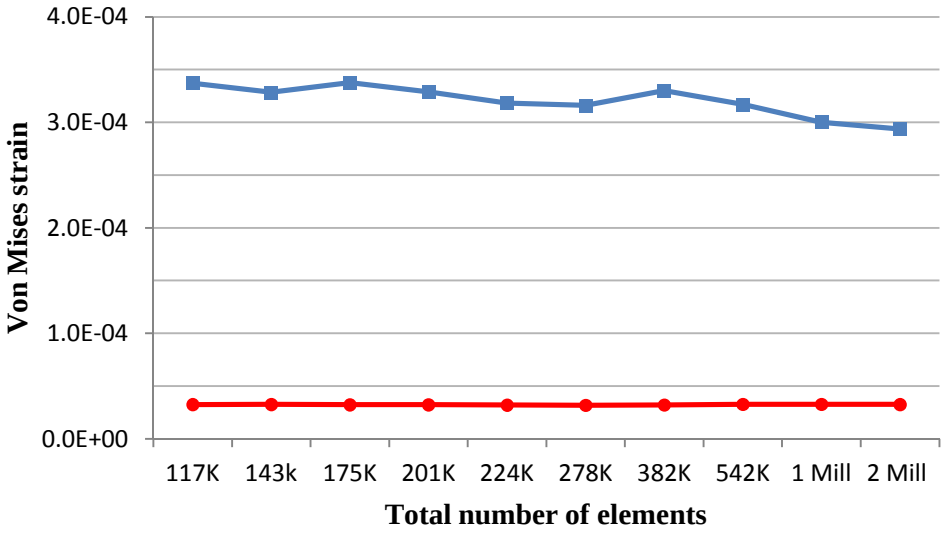

Figure I. The average surface nodal von Mises strain of the trabecular (blue) and cortical (red) bone produced by varying mesh densities.

As illustrated within Figure J, analysis of the maximum displacement throughout the pelvic structure displayed a high level of convergence. As observed previously, there was an increase in deformation with the higher density meshes, although the maximum relative variation was only 5%.

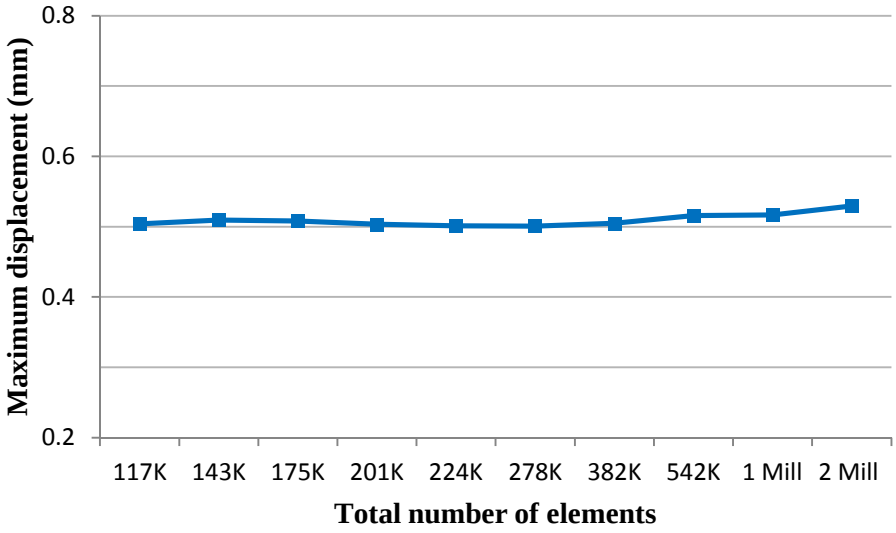

Figure J. The maximum displacement measured throughout the pelvic structure by the varying mesh densities.

The convergence testing displayed similar mechanical responses of the 9yr old hemi-pelvis between all of the meshes densities modelled (see Figure E and Figure F). However, analysis of nodal strains at specific locations did suggest that the lower dense meshes were more prone to calculating inaccurate values. Although Figure G and Figure H both displayed a small number of nodes which failed to show the level of convergence observed at other locations, it was predicted these were the cause of anomalous data, and not a common occurrence throughout the structure. This assumption was strengthened by a low level of variation observed within the average surface strains and deformation (see Figure I and Figure J), and the limited disruption to the distributions displayed in Figure E and Figure F. Therefore, when analysing the strain distribution across the whole surface, rather than at specific points, the lower density meshes were deemed suitable.

Although the above results highlighted slight inaccuracies within the less dense meshes, the total number of elements was higher than those reported within previous hemi-pelvic models, which typically contain less than ~60,000 elements (Kaku et al., 2004; Cilingir et al., 2007; Majumder et al., 2008; Zant et al., 2008). Therefore, despite been significantly increased from the total element numbers in literature, a mesh density closer to ~200,000 elements was chosen for this study. Although, this element total is similar to that of literature which has modelled the full pelvic girdle (Anderson et al., 2005, 2008; Majumder et al., 2008b), it was considered appropriate as the extra nodes enabled more accurate mapping of muscle attachments.

The conclusions regarding convergence are made with respect to the limited complexity of the applied loading, and the measure of only one stress state. The simplistic loading regime was selected based upon its ease of definition, and the increased accuracy of achieving identical loading between the various meshes.

Although modelling of physiological MS forces would be more representative of the forces used in this study, achieving identical loading between meshes would prove problematic, due to the operator interpretation in mapping muscle attachments.

APPENDIX IV

The moment of inertia for the prenatal femur was determined through the parameters of the segment mass (M), length (L), radius (R) and bone density (D). The segment R was calculated through the pre-defined equation within AnyBody (listed as Equation A), while the bone density was also taken from the software. Therefore, the following parameters were defined:-

$R = [M/(3.1416 \times L \times D)]^{0.5}$ Equation A

M = 0.2503Kg

L = 0.625m

R = 0.035704m

D = 1000Kg/m^3

The I_{XX}, I_{YY} and I_{ZZ} components of the moment of inertia were subsequently calculated through Equations B-D, producing the following values:-

$Ixx = (0.25 \times M \times R^2) + (1/(12 \times M \times L^2)$ Equation B

$Iyy = 0.5 \times M \times R^2$ Equation C

$Izz = Ixx$ Equation D

Ixx = 0.000161

Iyy = 0.00016

Izz = 0.000161

APPENDIX V

Definition of the MIF for each muscle in AnyBody is calculated through the product of the PCSA (Klein Horsman et al., 2007), a muscle stress of 0.27MPa and a strength leg index of 1.53. Consequently, calculated MIF's are reduced in magnitude compared to the method employed by Heller et al. (2001). Therefore, an analysis was performed to observe if the definition of differing MIF's within the prenatal MS model, would predict altered maximum muscle forces from those displayed in Table 5.3. A similar procedure to that detailed in section 5.1.5 was performed, whereby the hip joint performed a passive 120° flexion, and then a 120° extension back to a neutral position.

As shown in Figure K, identical maximum muscle forces to those in Table 5.3 were predicted when the MIF's were lowered to 1% of their original values. Differing muscle force combinations were only produced when the MIF's were restricted to 0.1%, although the gluteus medius, obturator internus and rectus femoris exceeded their maximal strengths. Therefore, as observed in section 5.1.5, reducing the MIF's to 1% of their original value was suggested to be a suitable strength from which to perform further modelling. Figure K also demonstrates that when modelling passive joint movements with MIF's at 1% of their original values, no difference was found in predicted maximal forces between the methods of Anybody and Heller et al. (2001).

		100%		10%		1%		0.1%	
	MIF (N)	Force (N)	% MIF	Force (N)	% of MIF	Force (N)	% MIF	Force (N)	% MIF
Adductor Brevis	145	0.22	0.152	0.22	1.52	0.22	15.2	0	0
Adductor Longus	624	0.78	0.125	0.78	1.25	0.78	12.5	0	0
Adductor Magnus	1004	0.6	0.059	0.6	0.59	0.6	5.9	9	89.6
Biceps Femoris	1124	0.67	0.059	0.67	0.59	0.67	5.9	1.7	152.8
Gemellus	169	0.35	0.207	0.35	2.07	0.35	20.7	0	0
Gluteus Maximus	2053	1.23	0.059	1.23	0.59	1.23	5.9	3.14	152.9
Gluteus Medius	2039	1.22	0.059	1.22	0.59	1.22	5.9	3.21	157.4
Gluteus Minimus	351	0.73	0.207	0.73	2.07	0.73	20.7	0	0
Gracilis	202	0.13	0.064	0.13	0.64	0.13	6.4	0	0
Iliacus	372	0.8	0.215	0.8	2.15	0.8	21.5	0	0
Ob Externus Ant	1016	2.05	0.201	2.05	2.01	2.05	20.1	0	0
Ob Externus Pos	1016	1.56	0.153	1.56	1.53	1.56	15.3	0	0
Ob Internus	1049	2.17	0.206	2.17	2.06	2.17	20.6	3.4	324.1
Pectineus	281	0.54	0.192	0.54	1.92	0.54	19.2	0	0
Piriformis	335	0.21	0.063	0.21	0.63	0.21	6.3	0	0
Quad Femoris	603	0.2	0.016	0.2	0.16	0.2	1.6	0	0
Rectus Femoris	1194	2.47	0.206	2.47	2.06	2.47	20.6	3.86	323.2
Sartorius	244	0.5	0.205	0.5	2.05	0.5	20.5	0	0
Semimembranosus	706	0.42	0.059	0.42	0.59	0.42	5.9	0	0
Semitendinosus	607	0.36	0.059	0.36	0.59	0.36	5.9	0	0
TFL	363	0.75	0.206	0.75	2.06	0.75	20.6	0	0

Figure K. The maximum muscle forces generated by the prenatal MS model when flexing the hip joint to 120° and then back to 0°. Maximum forces are displayed which were generated through reducing the MIF's to 10, 1 and 0.1% of their original values.

APPENDIX VI

As observed within the trabecular compressive strains of Figure 6.19, varying of the triradiate cartilage modulus within the prenatal hemi-pelvis did not disturb the cortical von Mises stresses (see Figure L) or trabecular von Mises strains (see Figure M). The stress and strain distributions were comparative to those in Figure 6.13(c) and Figure 6.14(b) respectively, again that showing that increased deformation related solely to the triradiate cartilage.

Application of load regime 7 (see Table 6.1) to the prenatal hemi-pelvis produced similar results when varying the triradiate cartilage modulus. The trabecular compressive strain distributions illustrated in Figure N were comparative to that in Figure 6.20(c), despite the maximal displacement ranging between 0.11-0.73mm (0.37-2.43% PD). As observed within section 6.3.1, the maximal displacement range significantly reduced when modelling moduli between 30-50MPa (0.11-0.16mm).

The minimal influence of varying the triradaite cartilage modulus on the predicted trabecular compressive strain distributions was also observed in the 1yr and 8yr old hemi-pelves. The strain distributions of the 1yr old hemi-pelvis showed in Figure O were similar to the one displayed in Figure 6.27(c), producing a maximal displacement range of 0.72-3.8mm (1.18-6.29% PD). Within the 8yr old hemi-pelvis, the strain distributions displayed in Figure P were comparative to those within Figure 6.33, although a maximal displacement range of 1.17-3.72 (1.26-3.89% PD) was recorded. As analysed in the prenatal FE models, both cases produced a reduction in the maximal displacement range when modelling moduli between 30-50MPa.

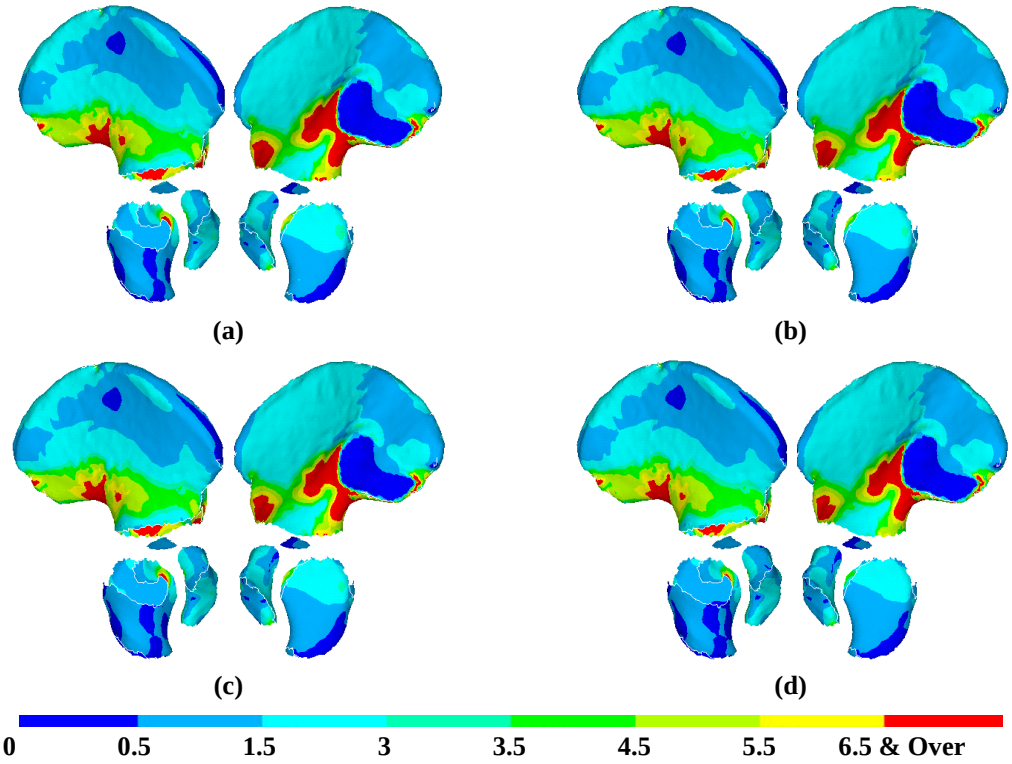

Figure L. The cortical von Mises stresses (MPa) of the prenatal right hemi-pelvis produced by the cumulative maximal force loading of the passive hip joint movement and varying the triradiate modulus to (a) 5MPa, (b) 20MPa, (c) 30MPa and (d) 50MPa.

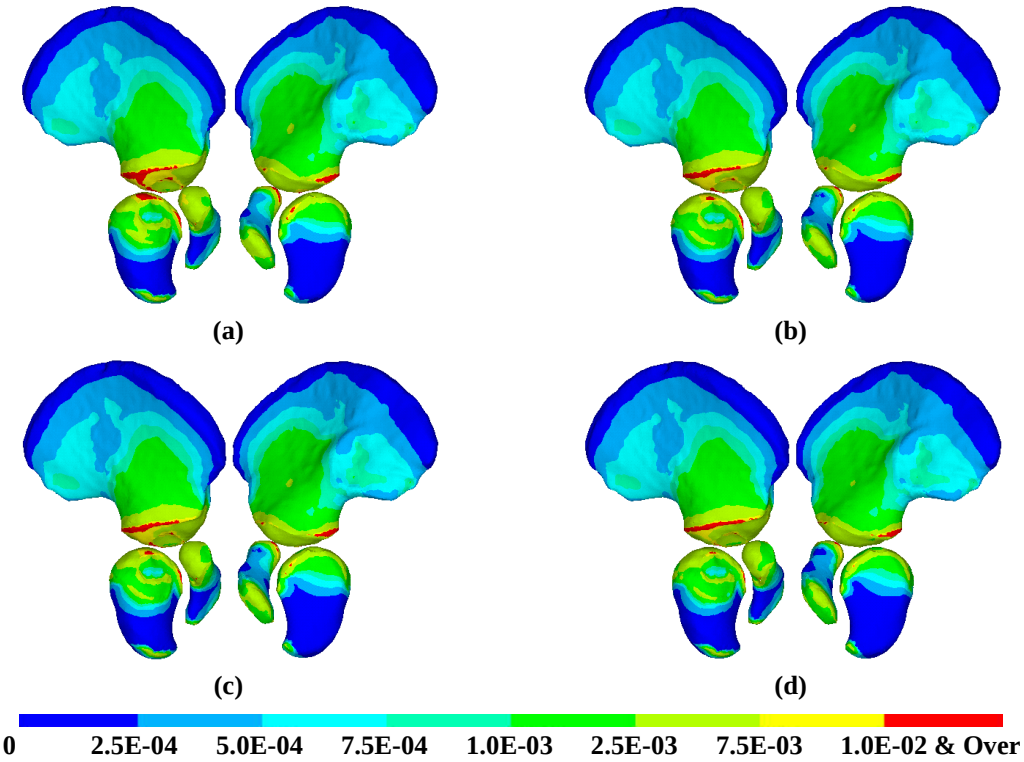

Figure M. The trabecular von Mises strains of the prenatal right hemi-pelvis produced by the cumulative maximal loading regime of the passive hip joint movement through varying the triradiate modulus to (a) 5MPa, (b) 20MPa, (c) 30MPa and 50MPa.

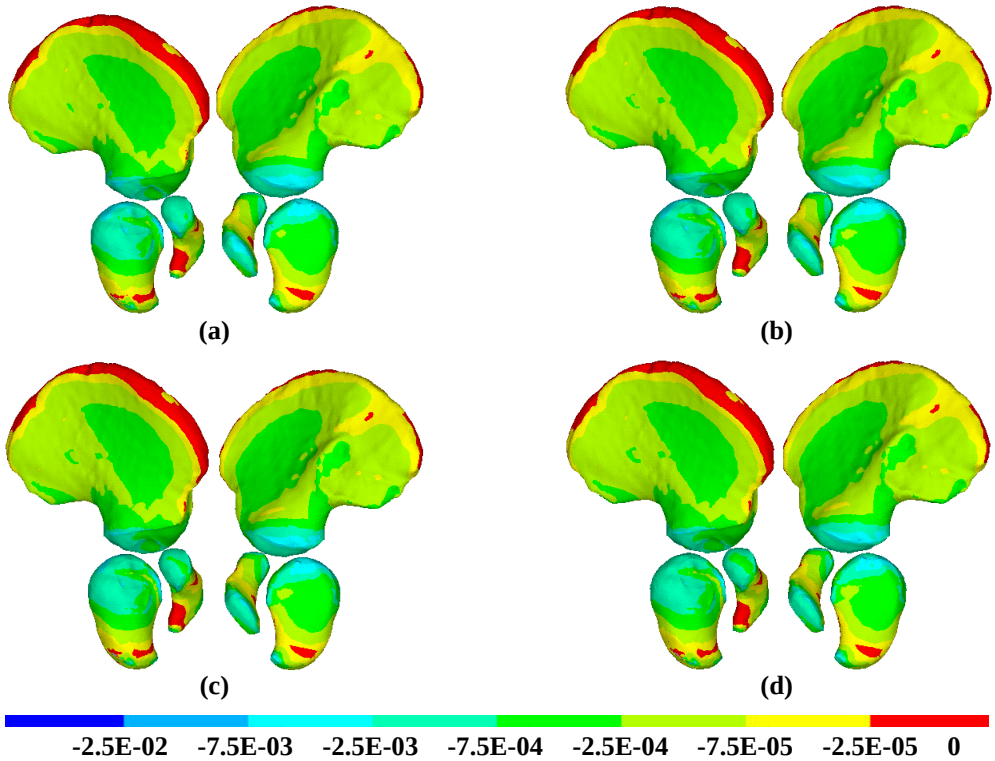

Figure N. The trabecular minimum principal strains of the prenatal right hemi-pelvis produced by 1% of the cumulative maximum forces associated with the gait cycle and varying the triradiate modulus to (a) 5MPa, (b) 20MPa, (c) 30MPa and 40MPa.

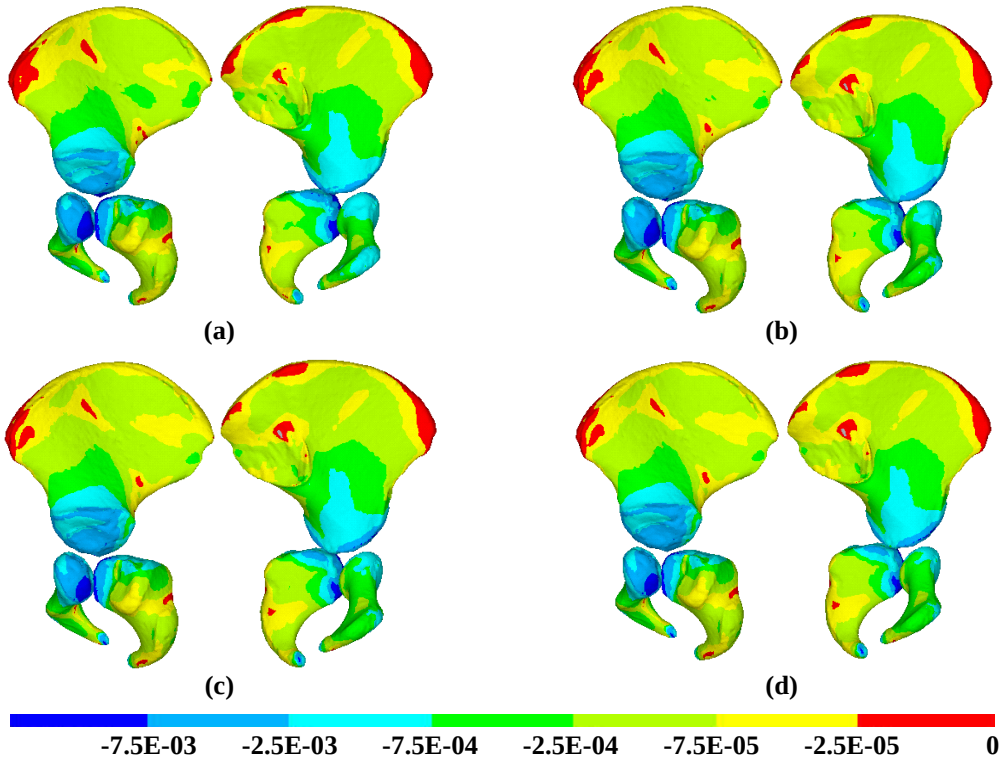

Figure O. The trabecular minimum principal strain distribution of the 1yr old left hemi-pelvis produced by 2% of the maximum forces associated with the gait cycle and varying the triradiate modulus to (a) 5MPa, (b) 20MPa, (c) 30MPa and (d) 50MPa.

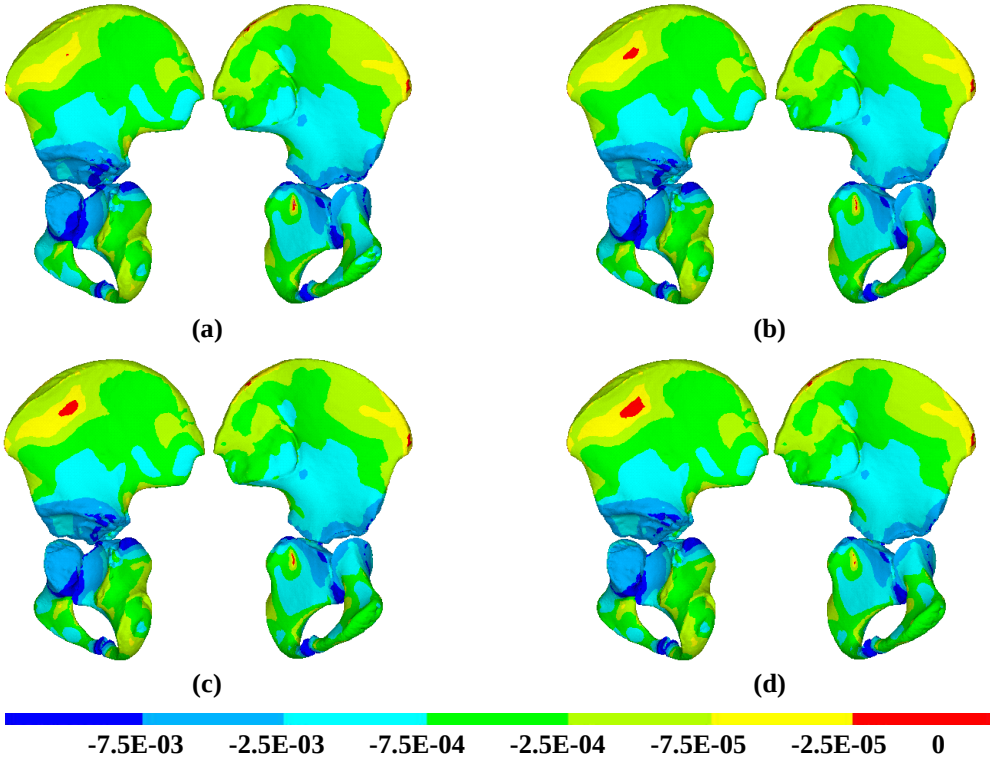

Figure P. The trabecular minimum principal strain distribution of the 8yr old left hemi-pelvis produced by 10% of the maximum forces associated with the gait cycle and varying the triradiate modulus to (a) 5MPa, (b) 20MPa, (c) 30MPa and (d) 50MPa.

APPENDIX VII

The validity of modelling a homogenous cortical thickness was analysed through altering the complexity of the cortex morphology within the prenatal FE model. Four additional models were created which split the cortical bone into separate regions, thus enabling definition of thicker cortices within specific areas (such as the gluteal surface). The separate regions were defined through mapping out grids on the pelvic cortex in a symmetrical manner between the medial and lateral sides. The four models were defined through the following characteristics:-

Model 1 - 2 grids (one grid medially and one laterally);

Model 2 - 4 grids (see Figure Q(a));

Model 3 - 8 grids (see Figure Q(b));

Model 4 - 64 grids (see Figure Q(c)).

Model 4 was created to match the location of the 64 square grid used in the histomorphometric analysis performed by Cunningham and Black (2009c). The thicknesses of the cotical bone within each grid were defined using the data of Cunningham and Black (2009c). The cortical modulus and the material properties of the trabecular bone and triradiate cartilage were the same as those detailed in Chapter 6.

All models were loaded within the cumulated maximal muscular and joint forces predicted by the prenatal MS model during the passive hip joint movement (load case 3 of Table 6.1). Identical constraints to those detailed in section 6.3 were applied.

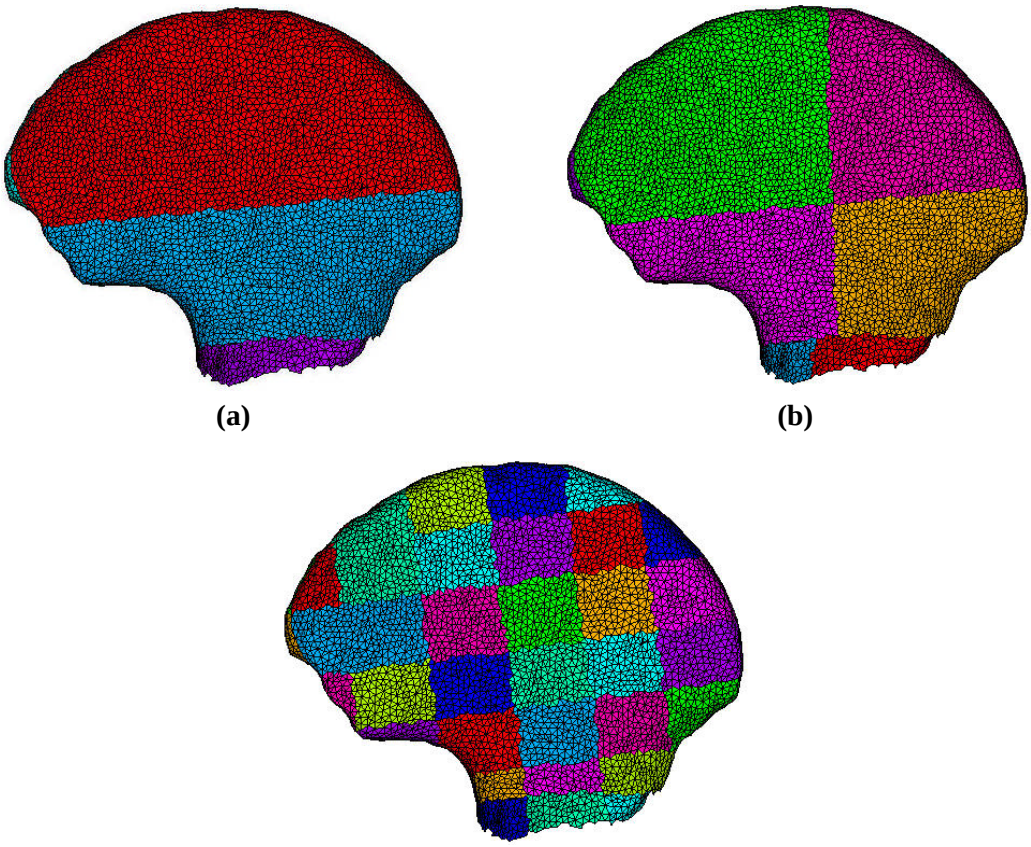

(a) **(b)**

(c)

Figure Q. Modelling of the prenatal pelvic cortex through (a) 4 grids (model 2), (b) 8 grids (model 3) and (c) 64 grids (model 4).

The cortical von Mises stress distributions illustrated in Figure R, were all similar to the one created through modelling a homogenous cortical thickness (see Figure 6.13(c)). Variations between the cortical stresses of models 1 – 3 were minimal, where slight deviations in the distributions generally related to the lower stress magnitudes. However, model 4 displayed a greater fluctuation in the distribution, producing increased stresses within the inferior ilium on the medial side (see Figure R(d)). Therefore, a more accurate representation of the cortical shell, produced a mechanical response which deviated the most from modelling a homogeneous thickness.

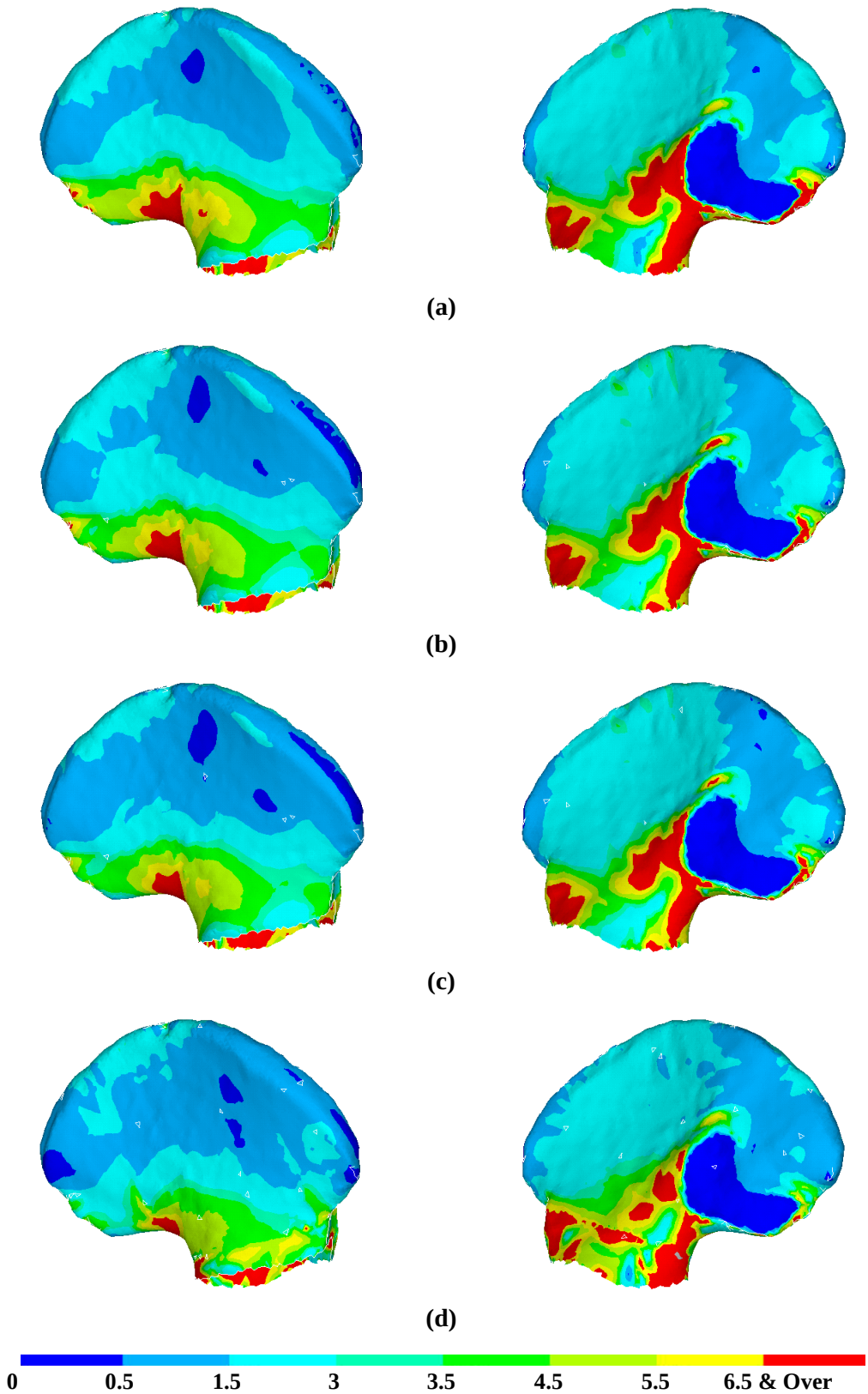

Figure R. The cortical von Mises stress distribution (MPa) of the prenatal right ilium when modelling the cortex through (a) 2 grids, (b) 4 grids, (c) 8 grids and (d) 64 grids.

The distribution of the trabecular compressive strains displayed a slightly greater variation (see Figure S). Once again, the distributions of models 1-3 produced the greatest similarities, although their comparison to strains in Figure 6.15(c) was not as close as observed within the cortical bone. The most noticeable variations in the distributions occurred in the concentrations of low strains, although models 1-3 predicted a large area within the posterior ilium on the medial side to be in tension. This was not captured in Figure 6.15(c) or by model 4 (see Figure S(d)). Therefore, despite the increasing number of grids used to replicate the pelvic cortex slightly increasing the model flexibility, fairly comparative compressive distributions were created in regions strained near or above the remodelling limit.

The similarities between the predicted cortical von Mises stresses of the complex and homogenous cortical modelling, was in agreement with the findings of Dalstra and Huiskes (1995) and Anderson et al (2005). However, these results were analysed with respect to the fact that an exact cortical morphology was not examined, as only grids were modelled. Additionally, the cortical thickness values were taken from literature which examined a neonatal morphology rather than that of a prenatal (Cunningham and Black, 2009c). Although a small influence on the compressive strains within the trabecular bone observed, a larger degree of fluctuation may have occurred if non homogeneous material properties for the trabecular bone had been defined.

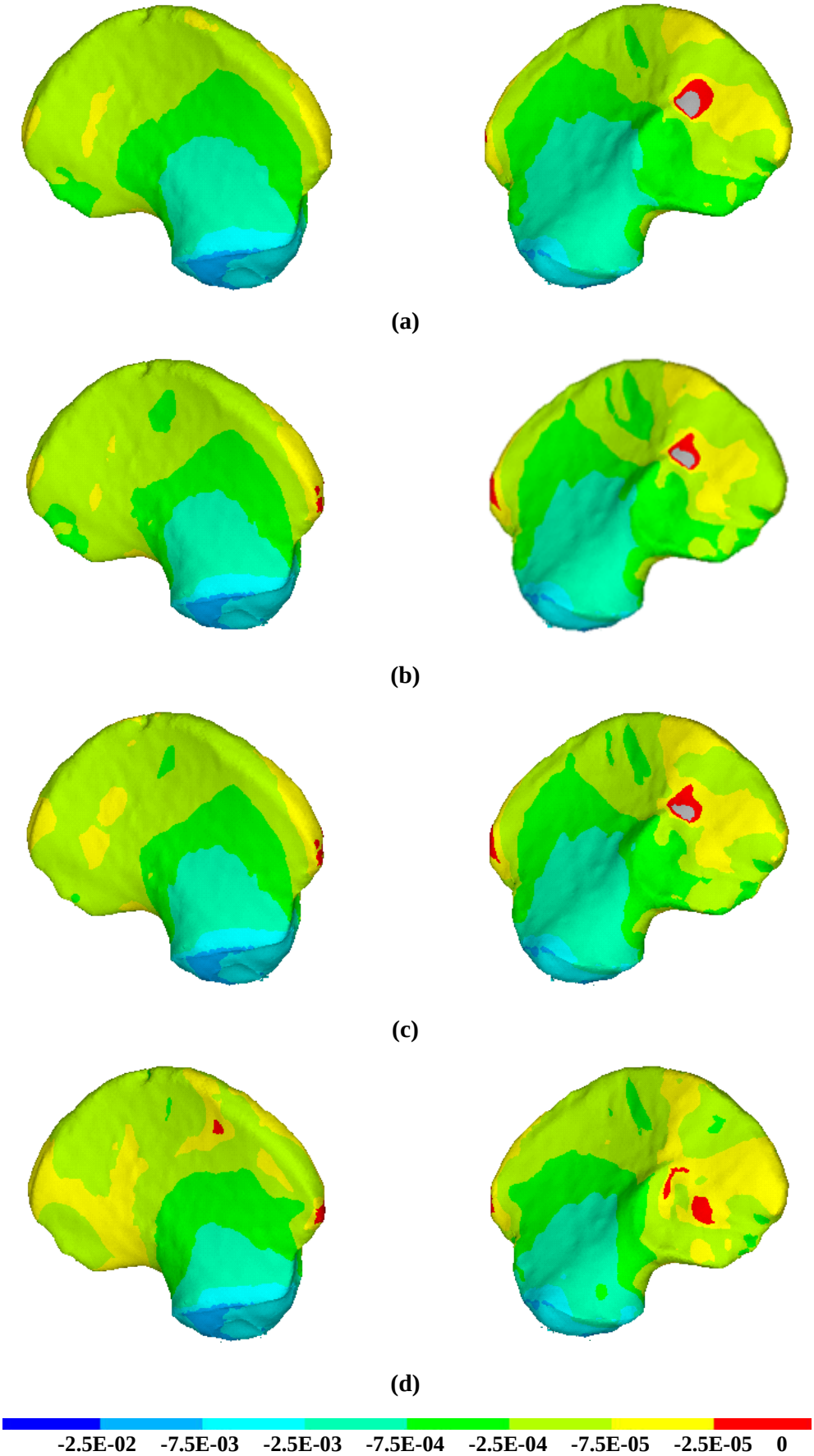

Figure S. The trabecular minimum principal strains of the right prenatal ilium when modelling the cortex through (a) 2 grids, (b) 4 grids, (c) 8 grids and (d) 64 grids.

APPENDIX VIII

Published Papers

WATSON, P. J., O'HIGGINS, P., FAGAN, M. J. & DOBSON, C. A. 2011. Validation of a morphometric reconstruction technique applied to a juvenile pelvis. *Proc Inst Mech Eng H,* 225, 48-57.

Conferences

LUNN, D.E., WATSON, P.J., O'HIGGINS, P., FAGAN, M.J. & DOBSON, C.A. 2009. New method using warped gait data to create subject-specific musculoskeletal modles for cadaveric bone samples. The 4th International Conference on Computational Bioengineering. September. Bertinoro. Italy.

WATSON, P.J., O'HIGGINS, P., FAGAN, M.J. & DOBSON, C.A. 2009. A morphometric reconstruction of a disarticlated juvenile pelvis, The 4th International Conference on Computational Bioengineering. September. Bertinoro. Italy.

WATSON, P.J., FAGAN, M.J. & DOBSON, C.A. 2010. Finite element modelling of a prenatal human hemi-pelvis. The 17th congress of the European Society of Biomechanics. July. Edinburgh. United Kingdom.

WATSON, P.J., O'HIGGINS, P., FAGAN, M.J. & DOBSON, C.A. 2010. Geometric morphometric methods: Assessing the sensitivity of the final warped form to the geometry of the original. The 17th congress of the European Society of Biomechanics. July. Edinburgh. United Kingdom.

WATSON, P.J., LUNN, D.E., ALCOCK, L., VANICEK, N. & DOBSON. C.A. 2010. The reliability of kinetic data in musculoskeletal models during gait. The 17th congress of the European Society of Biomechanics. July. Edinburgh. United Kingdom.

WATSON, P.J., FAGAN, M.J. & DOBSON, C.A. 2010. Validation of a morphometric reconstruction technique through the use of finite element analysis. The 17th congress of the European Society of Biomechanics, July. Edinburgh. United Kingdom.